NONLINEAR WAVE DYNAMICS OF CONTINUUM PHONONIC MATERIALS WITH PERIODIC ROUGH CONTACTS

BY

GANESH U. PATIL

DISSERTATION

Submitted in partial fulfillment of the requirements
for the degree of Doctor of Philosophy in Mechanical Engineering
in the Graduate College of the
University of Illinois Urbana-Champaign, 2023

Urbana, Illinois

Doctoral Committee:

Associate Professor Kathryn H. Matlack, Chair and Director of Research
Professor Alexander F. Vakakis
Associate Professor Alison C. Dunn
Associate Professor Ahmed Elbanna

Abstract

Controlling mechanical wave propagation is crucial for addressing technological and environmental challenges. These include preventing the vibration-induced structural failure of civil and energy infrastructure, enhancing noise-cancellation and imaging technologies, and developing novel acoustic devices for protective gears and nondestructive evaluation. Phononic materials, which are engineered materials with periodic building blocks, exhibit wave characteristics superior to that of traditional materials and therefore have the potential to revolutionize our ability to control waves. However, the current understanding of their functionality is primarily limited to the linear regime, despite the prevalent occurrence of large deformations and nonlinear mechanical responses in real-world materials. Recent research has explored the nonlinear behavior of phononic materials through granular crystals and soft metamaterials, extending the analysis beyond the linear regime. However, these studies primarily examined either *discrete* nonlinearity in the form of spring-mass chains or *continuous* nonlinearities in continuous periodic materials. Consequently, there remains an open fundamental question of how waves propagate in continuum phononic materials with discrete (or local) nonlinearities. Addressing this question may reveal new opportunities to control the global nonlinear wave response of phononic materials via local nonlinearities and discrete-continuum coupling.

This dissertation introduces and investigates nonlinear continuum phononic materials featuring geomaterial microstructures, particularly, micro-cracks as local nonlinearities. The nondestructive evaluation of geomaterials has shown that micro-cracks display highly nonlinear responses because of rough features on their contacting surfaces, known as rough contacts. Despite their rich nonlinear responses, rough contacts have not yet been explored in the context of engineered periodic media. Thus, this research develops a fundamental understanding of (1) the influence of the periodic arrangement of rough contacts on wave propagation and (2) the role of local contact nonlinearity between successive continuum layers in shaping nonlinear wave responses. To achieve this, extensive numerical analyses were conducted to study wave responses in these phononic materials for varying levels of contact nonlinearity, from weak to strong, including friction. Additionally, pilot experimental studies of acoustic characterization of base materials and ultrasonic wave propagation through rough contact have been conducted, which serves as a foundation for the future realization of these materials.

The research reveals atypical wave signatures with no analogs in linear theory and provides insight into the underlying physics behind their emergence. Specifically, the study reports energy transfer between frequencies through harmonic generation, self-demodulation, and wave mixing, propagation of localized traveling waves in the form of stegotons, energy localization through acoustic resonances, and generation of eigenstrains from memory-dependent responses. These properties are further exploited to demonstrate novel wave propagation control via tunable vibration filtering, tunable spectral energy transfer, broadband nonreciprocal wave propagation, adaptive energy absorption, compact energy propagation, and acoustically-governed programmability, and surface reconfigurability. Preliminary measurements suggest that complex mechanisms at rough contacts such as nonlinear normal force-displacement relationship due to asperity deformation, and eigenstrain generation and energy dissipation due to interface sliding in a physical system may be captured through ultrasonic measurements. Overall, this dissertation offers a new perspective on the potential of nonlinear continuum phononic materials with local nonlinearity for wave control and manipulation, which could have significant implications for enhancing structural integrity and innovations in acoustic technology.

Acknowledgments

I am profoundly grateful to the numerous individuals who have supported, guided, and assisted me throughout the completion of this dissertation. I owe a tremendous debt of gratitude to each and every one of you.

First and foremost, my Ph.D. advisor, Prof. Katie Matlack. Your unwavering support and guidance throughout my graduate school adventure have immensely shaped me as both a researcher and an individual. I mean, not only did you guide me through my Ph.D. dissertation, but you also let me dive into all sorts of cool side projects like acoustic cloaking, pentamode, and auxetic lattices. Those experiences really expanded my horizons in ways that I can't even put a price on. Your patience and understanding during my research on nonlinear phononic materials were crucial as a newcomer to the field. I used to look at nonlinearity as nothing but trouble, but now I look at it as a golden opportunity. This positive shift in my perspective is a testament to your exceptional mentorship. The pandemic was a major curveball, but your flexibility and support helped me navigate through those challenging times. Your wholehearted backing of my research ideas, including the work on phononic diodes and friction-driven programmability, has inspired me to push boundaries and explore new frontiers. Your genuine care for my aspirations and career objectives has helped me make well-informed decisions about my future plans. I cannot thank you enough for the significant impact you have had on my journey so far.

The esteemed members of my dissertation committee: Prof. Alexander Vakakis, Prof. Alison Dunn, and Prof. Ahmed Elbanna, thank you for your crucial role in steering my research direction. You created an environment for both my preliminary and final examinations that fostered thought-provoking discussions. Your constructive feedback has been invaluable in refining my work, with Prof. Vakakis providing insightful comments on considering the effects of disorder in my system, and Prof. Dunn offering valuable feedback on emphasizing the hypothesis-driven discussion. Your suggestions for future research directions have opened up exciting avenues for exploration, especially Prof. Elbanna's input on considering fractal surfaces and rate-dependent frictional effects. I also extend my heartfelt thanks to the members of my candidacy committee: Prof. Alexander Vakakis and Prof. Nikhil Chandra Admal.

To my collaborators, thank you for your priceless contributions to my research journey. A big shout-out to Dr. Alfredo Fantetti. Our long discussions on frictional contacts have truly shaped my understanding of this field. Because of your insights, I was able to troubleshoot and improve my samples and contact interfaces. A special thanks to Prof. Sanjiv Sinha and his students for collaborating on an interdisciplinary project of multifunctional lattices. Although this work falls outside the scope of my Ph.D. dissertation, it has been a remarkable experience that has broadened my research horizons and allowed me to explore new domains.

I feel incredibly privileged to have been a part of the prestigious University of Illinois Urbana-Champaign (UIUC) and the Department of Mechanical Science and Engineering (MechSE). The Grainger College of Engineering at UIUC provided unique opportunities such as the Mavis Future Faculty Program and WYSE/GBAM Summer Programs that broadened my horizons and prepared me for a successful future in academia. The MechSE department consistently supported my success through the MechSE Teaching Fellowship in Summer 2020, the Schaller Travel Award in Summer 2022, and the James O. Smith Outstanding Theoretical and Applied Mechanics Teaching Assistant Award in Spring 2020. The departmental seminars, given by leading researchers from diverse fields, further enhanced my professional growth. I am also grateful to the staff, especially Kathy Smith, the MechSE graduate program coordinator, for her prompt responses and assistance. I also appreciate the staff at the MechSE and Civil machine shops, as well as the Material Research Lab staff, for their patient guidance in sample fabrication and characterization.

I would also like to express my sincere gratitude to the US Army Research Office for their generous financial support during my Ph.D. research. I also acknowledge the National Science Foundation and the Ford University Research Program for their partial financial support in the early phase of my Ph.D. research. My travel to European Nonlinear Oscillator Conference in Summer 2022 was partially supported by Schaller Travel Award from MechSE and Conference Presentation Award through Graduate College at UIUC.

I must say, I am super grateful for the camaraderie of my lab members. These folks have been more than just colleagues to me – they've become cherished friends. First up, Chaitanya Nimmagadda, whose invaluable assistance helped me acclimate to life in the USA during my early days. Ignacio Arretche and Changgong Kim, you two have transcended the role of mere officemates to become close friends. We've had so many deep discussions about our research and personal life, sharing the ups and downs along the way. Thank you for providing that social support and bringing so much fun and joy to our workplace. Connor Pierce, I salute your insane attention to detail. Your meticulous approach has been a huge inspiration for my research. By the way, those Thanksgiving and Super Bowl meals were straight-up epic. Oh, and can we talk about those legendary memes? I'm telling you, the meme train won't stop even after I graduate. Betsy Smith, you've been the ultimate project partner and unofficial companion at conferences. Thank you for your insights on ultrasonic experiments that saved me countless headaches. And I will never forget those delicious Apple Pies and S'mores. Itay Grinberg, thanks for laying the foundation of nonlinear phononic materials in our lab. Your thoughtful explanations and smooth transition of material have helped me initiate my Ph.D. research without any issues. I am immensely appreciative of my mentees as well: Aditya Shedge, Songyuan Cui, Thomas Block, Mark Guo, and Edgar Becerra. Your out-of-the-box ideas and boundless enthusiasm accelerated my research and ignited new inspiration within me. Lastly, I extend my thanks to all other lab members, both past and present, whose contributions have enriched my lab experience. Together, we have cultivated a nurturing, and warm micro-community that has profoundly impacted my growth as a researcher.

I have also been fortunate to receive invaluable mentorship from several professors during my Ph.D. My mentors during my role as teaching assistants: Prof. Mariana Silva, Prof. Matt West, Prof. Katie Matlack, Prof. Elif Ertkin, Prof. Chia-Fon Lee, Prof. Wayne Chang, Prof. Blake Johnson, and Prof. Srinivasa Salapaka. Your guidance has been instrumental in helping me understand how instructors create dynamic educational environments in their classrooms. Your mentorship has provided me with invaluable insights into effective teaching practices and has contributed significantly to my growth as an educator. I would also like to express my gratitude to my instructors, particularly, Prof. Petros Sofronis, Prof. Martin Ostoja-Starzewski, and Prof. John Lambros. You have taught me the nitty-gritty of solid mechanics and wave propagation, which have built a rock-solid technical foundation for my research. A special mention to Prof. Amy Wagoner Johnson for her enlightening "Science Communication" course, which instilled in me the ability to effectively communicate intricate research to a wider audience.

Several individuals have played a pivotal role in my journey into graduate school. I am deeply indebted to my professors from my diploma and undergraduate college, Veermata Jijabai Technological Institute (VJTI):

Prof. Sachin Barve, Prof. Arvind Deshpande, Prof. Sampatkumar Gunadal, and Prof. Mandar Tendolkar. Prof. Barve, your engaging lectures and practical examples in the Mechanical Vibration course sparked my passion for the field. Prof. Gunadal, your emphasis on fundamental mechanics ensured that I developed a strong technical background for graduate school. Prof. Deshpande, your teaching and mentoring on finite difference methods during my B.Tech thesis shaped my path in computational analysis. Prof. Tendolkar and Prof. Barve, thank you for reaching out to me during a challenging period in my life and inspiring me to persevere and pursue my goals despite the obstacles. I was also lucky to have awesome colleagues at Bajaj Auto Ltd: Nitin Gavali, Miling Wagh, Vaibhav Sabade, Sumit Galpalli, and Sarang Kulkarni. Your belief in me and encouragement to pursue my academic dreams have been invaluable, and I am profoundly thankful for this incredible support.

Last but not least, I gotta give a big shout-out to my amazing friends and family who have had my back through thick and thin. MechSE crew, Yashraj Bhosale, Chaithanya Kondur, and Tejaswin Parthasarthy, you guys are the real MVPs. Those epic road trips we took to national parks all over the USA will forever hold a special place in my heart. And let's not forget my roommate, Vipul Satone, my go-to person to vent, discuss, and troubleshoot any problem that came my way. That Fish Fillet with Green Chillies always reminds me of you, Vipul. To my ride-or-die best friends, Anish Biwalkar, Saurabh Jadhav, Giridhar Jambare, and Suraj Pawar, who has been my biggest cheerleaders, pushing me to chase my dreams and giving me the motivation to put in the grind that made all of this happen. It's crazy how being spread out across the US has actually brought us even closer. Fingers crossed, we'll make that long-awaited meet-up happen soon! And now, it's time for some serious gratitude. My dear mother, Pushpa Patil, and my warrior brother, Salil (Bunty) Patil, I owe you the world. Your unwavering love and belief in me have kept me going, especially during the toughest of times. Mom, I'll never forget how you single-handedly raised Bunty and me, and the sacrifices you've made are truly unparalleled. The only reason I've been able to put in so much effort is because I know you've done it all for me. Every success I achieve is a gift to you. And Bunty, thank you for taking heavy responsibilities on your shoulders at such a young age, granting me the freedom to learn and pursue my career. With your strength and eternal optimism, you've always been my pillar of support. You both are my superheroes, and I'm forever grateful for you.

Table of contents

List of Tables

List of Figures

List of Abbreviations

1D	One-dimensional
2D	Two-dimensional
BC	Boundary condition
COV	Coefficient of variance
CT	Computed tomography
FFT	Fast Fourier transform
FIB	Focused ion beam
IA	Inertial amplification
RMS	Root mean square
SEM	Scanning electron microscopy
SHG	Second harmonic generation

List of Symbols

α	Attenuation coefficient
α_c	Attenuation correction
β	Exponent of contact power-law nonlinearity
β_0	Exponent of contact power-law nonlinearity of ideal phononic material
Γ_L	Semi-infinite bulk layer to the left of phononic material
Γ_R	Semi-infinite bulk layer to the left of phononic material
Δ	Eigenstrain
$\Delta\Omega$	Bandwidth of normalized frequency
$\Delta\phi$	Phase difference of propagating frequencies
Δ_I	Eigenstrain in inner layers
Δ_O	Eigenstrain in outer layers
Δf	Bandwidth of frequency
Δq	Difference in wavenumber of fundamental and harmonic waves
Δt	Time step
Δu	Normal contact displacement
Δx	Mesh element size
Δx_1	Mesh element size based on wavelength
Δx_2	Mesh element size based on layer dynamics
δ	Rough asperity size
δ_0	Predeformation from external precompression
δ_1	Deformation of spring left endpoint
δ_2	Deformation of spring right endpoint
δ_b	Tangential displacement increment
δ_c	Clearance offset
$\bar{\delta}$	Average deformation of embedded contacts

ε	Strain
ϵ	Degree of disorder
ζ	Mean of Gaussian function
η	Normalized precompression
κ_1	Linear term of the normal contact stiffness per unit area
κ_2	Quadratic term of the normal contact stiffness per unit area
κ_t	Tangential contact stiffness per unit area
Λ	Normalized wavelength
λ	Wavelength
$\lambda^{(L)}$	Lame's first parameter
λ_{ff}	Wavelength corresponding to free-free acoustic resonance of layer
μ	Coefficient of friction
$\mu^{(L)}$	Lame's second parameter
μ_I	Coefficient of friction at inner contacts
μ_O	Coefficient of friction at outer contacts
ξ	Normalized shear wave excitation
ρ	material density
σ	Normal stress
σ_0	pre-stress
τ	Shear or tangential stress
τ_c	Friction limit
τ_i	Maximum incident shear stress
$\dot{\tau}$	rate of change of shear stress
Φ_t	Wave function
ϕ_t	Phase shift
χ	Rectangular function
ψ	Standard deviation of Gaussian function
Ω	Normalized frequency
Ω_1	Normalized frequency of probe wave
Ω_2	Normalized frequency of pump wave
Ω_+	Normalized sum-frequency component
Ω_-	Normalized difference-frequency component
Ω_{NR}	Normalized frequency of nonreciprocal waves

Ω_r	Normalized resonance frequency of layer
ω	Radial frequency
A_0	Spectral amplitude of DC component
A_1	Spectral amplitude of fundamental wave
A_2	Spectral amplitude of second harmonic wave
A_E	Spectral amplitude of excited wave
a	Actual contact area
b	Tangential contact displacement
b_I	Inner contact deformation
b^*	Maximum tangential contact displacement before the first sliding
$\dot{b}$	Tangential velocity
C	Proportionality constant of contact power-law nonlinearity
c_L	Dilatational wave speed
c_p	Phase velocity of wave
c_s	Shear wave speed
c_w	Wave speed in water
D	Diameter of transducer element
D_L	Lommel diffraction correction
E_1	Energy of layer 1
E_2	Energy of layer 2
E_L	Energy in layers
E_D	Dissipated energy
E_R	Reflected energy
E_S	Energy in stegotons
E_T	Total energy
E_T^P	Transmitted energy in periodic contact system
E_T^S	Transmitted energy in a single contact system
E_{cr}	Critical energy limit of weakly nonlinear system
E_i	Energy in ith layer
$\bar{E}$	Normalized energy
F	Force
F_s	Spring force
f	Frequency

f_1	Frequency of probe wave
f_2	Frequency of pump wave
f_{r1}	Frequency of layer 1 resonance
f_{r2}	Frequency of layer 2 resonance
$f_{fixed-free}$	Frequency of fixed-free acoustic resonance
$f_{free-free}$	Frequency of free-free acoustic resonance
G	Shear modulus
G_f	Gaussian function
H	Height
H_c	Hurst exponent
h	Height of double array embedded contacts
h_0	Height of transducer
h_1	Height of waveguide enlarged section
h_2	Height of waveguide
i	indices
j	Order of layer acoustic resonance
K	Constant beam divergence factor
K_N	Absolute contact stiffness in the normal direction
K_t	Absolute contact stiffness in the tangential direction
k	Number of stegotons
k_r	Resonator stiffness
L	Length of finite phononic material
L_c	Length of single array embedded contacts
L_s	Thickness of sample
L_w	Distance between sample and transducer in an immersion tank
l_1	Length of waveguide enlarged section
l_2	Length of waveguide
m_r	Resonator mass
N	Normal force
N_1	Near-field distance
N_2	Beam spread at far-field distance
n	Number of elastic layers
n_1	Starting point of the rectangular window function

n_2	Ending point of the rectangular window function
p	Contact pressure
p_0	External precompression
q	Wavenumber
$R(\omega)$	Reflection coefficient at a contact
R_a	Average roughness
R_q	RMS value of surface roughness
R_{ws}	Reflection coefficient at water-sample interface
r	Array of normally distributed values
S_0	Surface echo
S_1	First back-wall reflection
S_2	Second back-wall reflection
S_A	Wave incident to contact
S_B	Wave transmitted through contact
s	Unit cell constant (or size) of phononic material
T	Tangential force
$T(\Omega)$	Transmission of phononic material
$T(\omega)$	Transmission coefficient at a contact
t	Time
U	Wave displacement amplitude
$\bar{U}$	Normalized wave displacement
u	Wave displacement
u_i	Input wave displacement
v	Particle velocity of wave
v_0	Particle velocity of wave in an ideal system
v_1	Amplitude of primary stegotons in terms of particle velocity
v_2	Amplitude of secondary stegotons in terms of particle velocity
W	Weight of sample
x_1	Stable equilibrium point of weakly nonlinear system
x_2	Unstable equilibrium point of weakly nonlinear system
z	Acoustic impedance

Chapter 1

Introduction

This chapter introduces the research motivation, scope, and objectives of the dissertation. It emphasizes the importance of developing phononic materials to control mechanical wave propagation in engineering applications. Additionally, it provides an overview of the existing knowledge and state-of-the-art in the phononic materials field. The primary gap in this area is identified as the question of how waves propagate in continuum phononic material with discrete nonlinearity. To address this question, the dissertation examines continuum phononic material with rough contacts, which represents the system in question. Finally, the chapter concludes by highlighting the research objectives and corresponding key accomplishments along with the structure of the dissertation.

1.1 Motivation

Waves permeate our daily existence, manifesting themselves throughout nature in diverse forms. They are disturbances that carry energy through space and time, encompassing electromagnetic and mechanical variations. Electromagnetic waves, such as visible light, X-rays, and radio waves, traverse vacuums, while mechanical waves, like sound, oceanic, and seismic waves, necessitate a medium—be it fluid or solid—to propagate. Among these, the propagation of waves through solid materials is of particular significance in addressing current engineering and societal challenges. Such challenges include environmental noise, component failure due to vibrations, and the loss of life caused by catastrophic disasters and earthquakes. Understanding the interactions between waves and materials is also crucial for various technologies, including ultrasonic inspection and biomedical imaging. Hence, this dissertation research concentrates on wave propagation through solid materials as it is highly relevant to addressing these challenges and advancing related technologies.

The ability to control and manipulate mechanical waves holds the utmost importance in addressing critical engineering problems. These problems include a range of objectives, such as ensuring comfort and safety, improving energy and cost efficiency, and preventing signal interference for enhanced technologies. For instance, excessive noise and vibration can cause discomfort and health problems, particularly in occupational and residential environments. By exerting control over wave propagation, we gain the capability to regulate noise and vibration levels in engineering applications like vehicles, machinery, and buildings. Similarly, controlling the propagation of seismic waves can lead to the design of protective structures that can withstand earthquakes and other natural disasters. Waves, such as sound or vibration, can also be harnessed to generate energy, and controlling their propagation enables the design of devices that can convert mechanical energy into electrical energy. This is particularly useful in powering devices in remote areas or in places where accessing traditional sources of energy is challenging. Additionally, controlling noise and vibration in turbines and engines can improve their life and cost efficiency. Moreover, controlling wave propagation can enhance medical imaging by reducing noise from signal interference and improving image quality. By directing waves with precision to target specific tissues in the body, we can potentially enhance the efficacy of therapeutic treatments for diseases like cancer. Therefore, controlling these waves is critical to addressing problems in various industries, including aviation, transportation, materials, healthcare, and energy.

Wave propagation control has been historically achieved through both active and passive methods. Active control involves a sensor-actuator system, where the sensor detects the state of wave propagation, and the actuator alters the system or structure's behavior based on the feedback received. An example of this method is piezoelectric materials, which tune their properties to alter wave or vibrational responses [1]. Passive methods rely on materials with different acoustic properties [2], and structures that can dissipate or absorb waves, such as vibration dampers and resonators in mechanical systems [3]. However, despite the advantages and widespread use of these active and passive methods, they suffer from certain limitations. Active methods are complex, expensive, require maintenance and calibration, and can be less reliable due to their dependence on sensors and actuators. Passive methods, on the other hand, are less flexible and limited in their functional range, especially in highly fluctuating dynamic environments. Therefore, this dissertation aims to study novel engineered materials with tailored and tunable properties, offering more flexible and precise control over wave propagation.

1.2 Phononic materials

Phononic materials, also known as "metamaterials", are a class of engineered materials designed to control wave propagation. They are constructed using periodic building blocks of "unit cells", such as material properties, geometries, and/or boundary conditions [Fig. 1.1(a)]. Due to these periodic architectures, phononic materials exhibit nonlinear dispersion, which is the relationship between frequency and wavenumber, and result in band gaps [4], [5] over specific frequency ranges [Fig. 1.1(b)]. Within these band gaps, waves cannot propagate and are reflected due to the material's heterogeneity [refer to mode shape associated with star marker in Fig. 1.1(b)]. This unique property has direct applications in vibration mitigation [6]–[8], noise isolation [9], and waveguiding [10], [11], making material design an effective way to control wave propagation, the primary focus of this dissertation.

1.2.1 Linear phononic materials

Phononic materials have been extensively studied with linear constitutive laws where stresses are linearly proportional to strains or forces are linearly proportional to displacement. The linearity simplifies the mathematical analysis and enables the design of phononic materials with specific band gaps for controlling wave propagation. In-depth background on the mathematical analysis of dispersion and band gap formation in linear phononic materials and metamaterials can be found in the review articles by Hussein et al. [12] and Zhou et al. [13]. The Bragg-scattering mechanism dictates the formation of band gaps, which arises from the interference of waves scattered by the periodic structure. Therefore, the frequencies at which band gaps form correspond to wavelengths of the order of size of the unit cell of the phononic materials. Since the wavelength and frequency of waves are inversely related, waves at low frequencies have high wavelengths. Thus, phononic

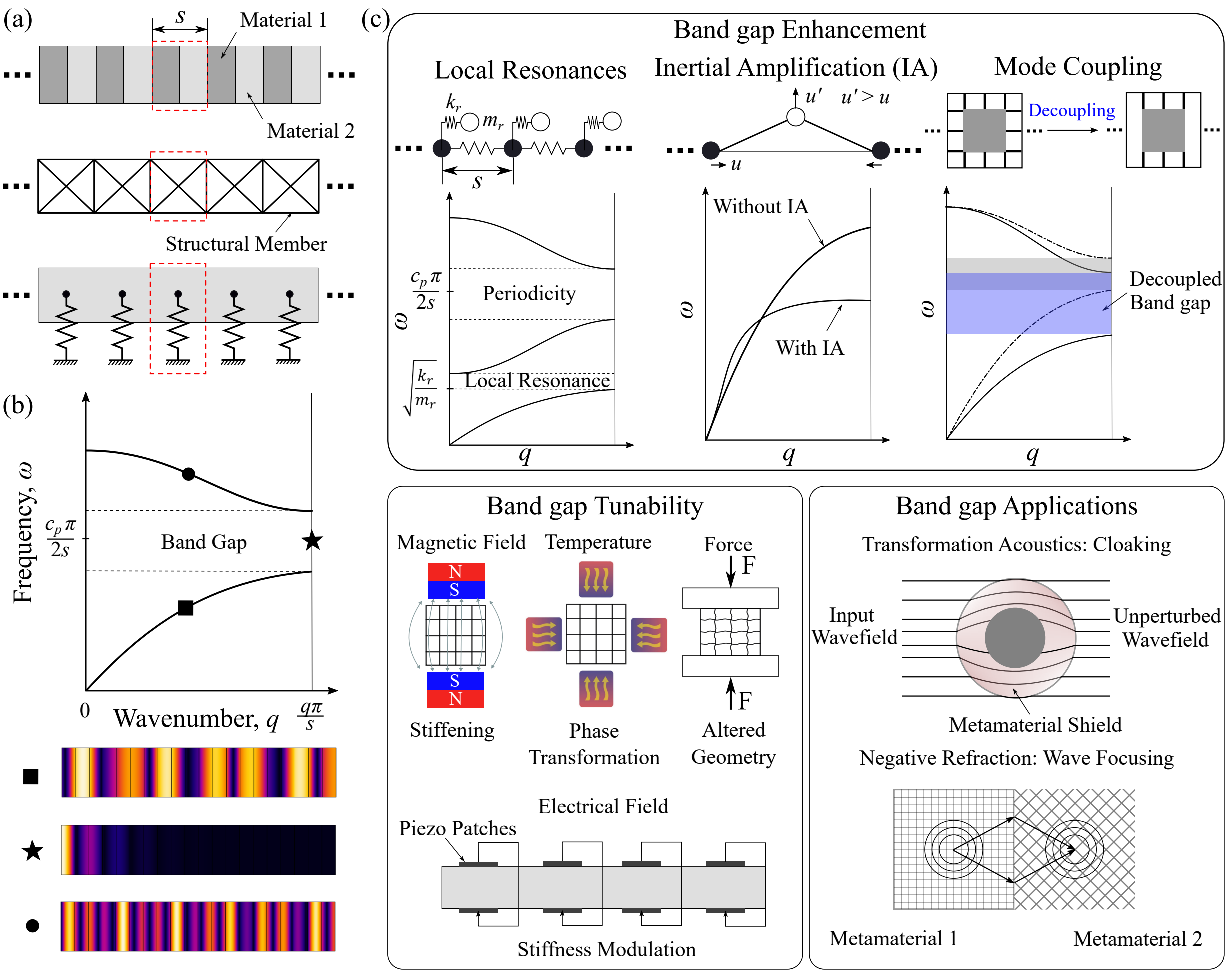

Figure 1.1: Phononic materials offer promising prospects to control wave propagation. (a) The periodic nature of phononic materials is exemplified by the presence of periodic building blocks, depicted by red dashed rectangles, with a unit cell length denoted as s. Periodicity can arise from variations in material properties, geometries, and/or boundary conditions. (b) Typical dispersion characteristics of phononic materials with a Bragg scattering-induced band gap, which is influenced by both the unit cell size and the phase velocity (c_p) of the bulk wave. Mode shapes of three representative cases, namely the acoustic band (square), the band gap (star), and the optical band (circle), illustrate the frequency-dependent nature of wave propagation. (c) The field of linear phononic materials encompasses diverse research domains. Schematic illustrations depict various mechanisms explored for enhancing band gaps, the utilization of external stimuli for tunability, and demonstrated acoustic applications.

materials require unrealistically large sizes to form band gaps at low frequencies. As a result, significant efforts have been dedicated to enhancing the band gaps, which involves lowering the center frequency and widening the width, over the last decade [Fig. 1.1(c)]. For example, mechanisms such as local resonances [14] and inertial amplification [15] have been developed to reduce the band gap frequency without increasing the size of the unit cell. The architecture of the unit cell, which governs the effective mechanical and wave propagation properties [16]–[18], has also been exploited to enhance band gaps. This includes developing novel lattice structures [6], optimizing their mass and volume distribution [6], [19], and nodal connectivities [6], [19] that have been shown to lower the band gap frequency and widen their width.

Researchers have also utilized the band gap properties of phononic materials to enable unique and exotic phenomena such as mode conversion [20] and negative refraction [21]. Within the band gap frequency range, it is possible to achieve a negative refractive index, which leads to fascinating effects such as wave focusing below the diffraction limit [22], [23] and invisibility cloaking [24]. Furthermore, phononic materials based on their geometry, specifically their lattice structure, exhibit anisotropic properties due to the architecture of their unit cells. This enables directional control of wave propagation [16], [17], wave beaming [25], and anomalous wave polarization [16], [17]. However, phononic materials have fixed dispersion and band gap characteristics once they are designed, making them unsuitable for applications that require adaptable properties in fluctuating environmental conditions. Thus, recent years have seen extensive research on tuning the properties of phononic materials in situ through stiffening, phase transformation, or geometry modulation [26]. Various external stimuli, such as magnetic [27], electrical [28], optical [29], thermal [30], and mechanical forces [31], have been used to tune the dispersion characteristics of phononic materials.

Although there have been significant studies on phononic materials, as reviewed in recent articles [32] and [33], most of the current research has been limited to the linear regime of wave propagation, which only considers infinitesimal displacements and deformations. However, many materials and structures undergo large deformations and exhibit nonlinear mechanical responses. This restriction to linear regimes further hinders the exploration of complex, intertwined dynamic responses that could arise in nonlinear regimes. Thus, there is a need to better understand and design nonlinear phononic materials. This would enable the exploration of novel avenues for the control of wave propagation, leading to new acoustic applications.

1.2.2 Nonlinear phononic materials

Nonlinearity is pervasive across diverse disciplines of physics, spanning optics [34], chemistry [35], biology [36], thermodynamics [37], material science [38], and even cosmology [39], operating at various length scales. These physical nonlinearities enable advanced functionalities in engineering applications [40], [41] and have recently garnered significant attention in enhancing the dynamics of periodic media [42], [43]. From the perspective of mechanical systems, real materials and structures often undergo larger deformations than what can be captured by linear analysis. Therefore, it is critical to understand how phononic materials respond to waves with amplitudes that surpass the linear regime. Further, expanding the analysis of phononic materials into the nonlinear regime allows even more control over the distribution of energy of a mechanical wave in time and space as it propagates through the material. This is because nonlinearity can achieve behaviors that are inaccessible and potentially superior to their linear counterparts [44]. These richer wave responses include amplitude-dependent material responses, energy transfer between frequencies, modal mixing, irreversibility, and localization, among others. Incorporating nonlinearity can also manifest passive material response, eliminating the need for external stimuli. Overall, comprehending the nonlinear behavior of phononic materials is vital for optimizing their performance and unlocking new behaviors.

Studies on nonlinear bulk wave propagation have a rich history dating back to the 1960s [45]–[49], when researchers first considered higher-order elasticity laws in the context of elastic wave propagation. These early studies provided a solid foundation for further exploration of nonlinear bulk waves, which were later extensively documented [50]–[52]. Nonlinear dispersive waves in waveguides [53], [54] and surface waves [55] were also investigated. Nonlinear wave propagation in bulk materials offers unique opportunities, such as amplitude dependence [47] and energy transfer between frequencies [47], [49], [54], which inform potential opportunities to exploit nonlinearity in phononic media. Furthermore, classical perturbation approaches [56], such as the Lindstedt–Poincaré method, the method of multiple scales, the method of averaging, and approximation techniques [56] such as the method of harmonic balance, were developed and applied to general

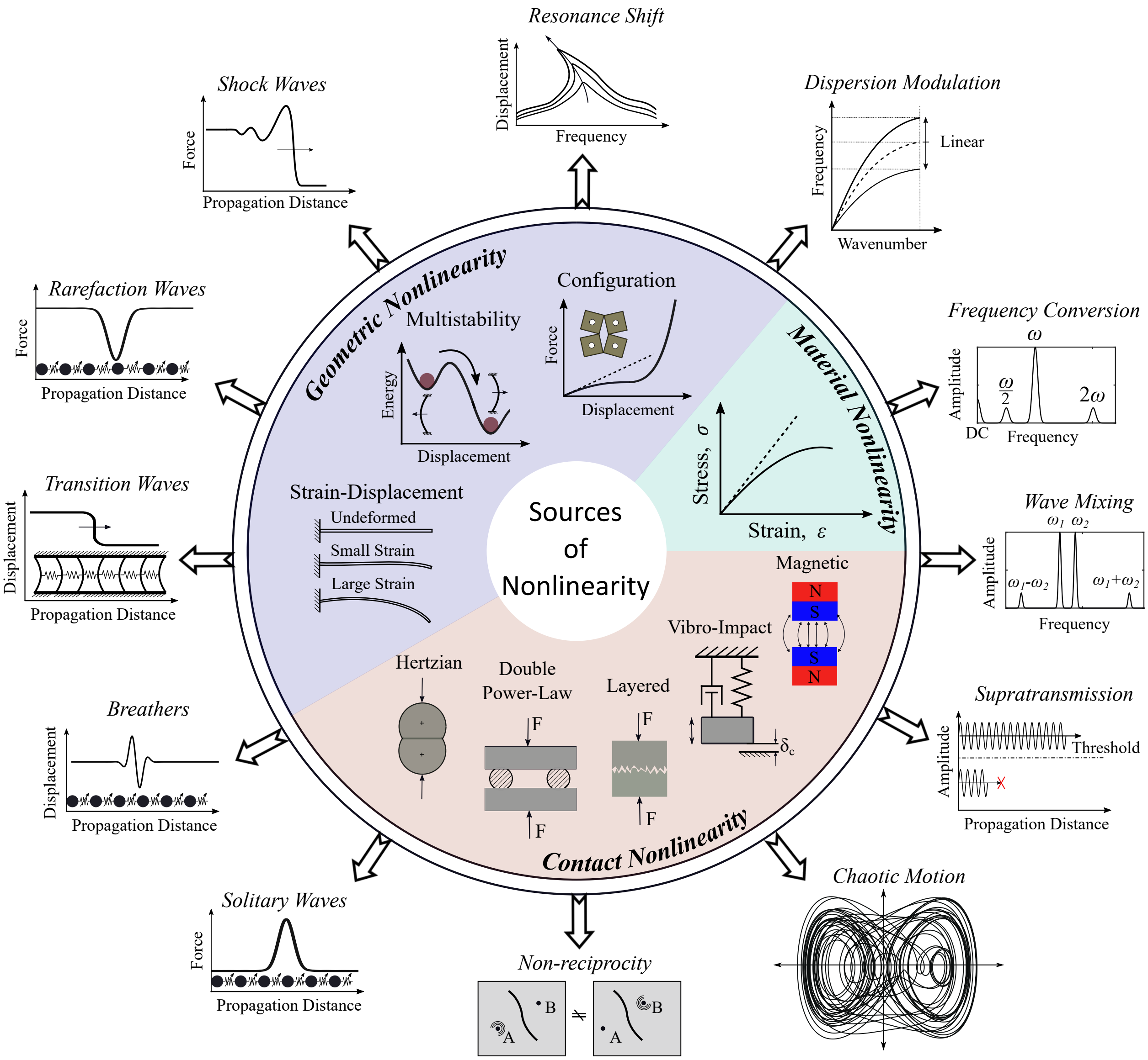

Figure 1.2: Novel wave responses arising from the incorporation of nonlinearity in phononic materials. Figure adapted with permission from [44], © Springer Nature 2021.

continua, providing foundational tools to reformulate and study nonlinear wave propagation in phononic media.

Despite several advantages offered by nonlinearity, its complexity has often discouraged researchers from exploring its potential in phononic materials. However, recent advances in analytical methods and the increasing availability of computational power have enabled the intentional design of nonlinearity in phononic materials for enhanced functionalities [44]. Initial studies in the field were focused on developing approximate analytical, numerical, or computational tools to analyze nonlinear wave propagation through phononic media due to the absence of exact closed-form analytical solutions for most nonlinear systems. These efforts were largely confined to simple one-dimensional (1D) discrete systems, such as periodic chains coupled with nonlinear springs [57]–[59], linearly coupled spring-mass system with locally connected nonlinear oscillators [60], and continuous systems such as a homogeneous bar under finite strain with periodically attached linear local resonators [61]. These studies showed amplitude-dependent dispersion and band gaps of nonlinear periodic systems. Building on these fundamental studies, recent research efforts have exploited physics-driven sources of nonlinearity in phononic materials to achieve unique nonlinear wave responses (see review by Patil and Matlack [44]). Additional review articles have highlighted key contributions to different aspects of nonlinear phononics [12], granular crystals [62], [63], nonlinear lattice materials [64], flexible metamaterials [65], and nonreciprocal acoustic and elastic materials [66]. In the following paragraphs, a high-level summary of some of the key advances in nonlinear phononic materials is provided. However, readers are advised to refer to the aforementioned review papers for a more in-depth summary.

Granular phononic crystals or granular crystals are a class of nonlinear phononic materials, where an ensemble of particles interacting through Hertzian contact gives rise to nonlinear responses. Remarkably, the mechanical response of granular crystals can be tuned from the linear to nonlinear regimes by controlling the precompression and wave amplitude. Moreover, the nonlinear response can be categorized as weak or strong. The absence or presence of contact loss under dynamic excitation governs the weak or strong nonlinearity, respectively. Weak nonlinearity exists when the excitation amplitude is smaller compared to static precompression, whereas strong nonlinearity exists when the excitation amplitude is larger than the precompression or when the precompression itself is zero. Thus, Hertzian contact nonlinearity is not a continuous function when strong nonlinearity exists. Over the years, various analytical approaches such as continuum approximations [67], binary collision approximation [68], and reduced-order models with periodic boundary conditions [69] have been developed to solve wave propagation through strongly nonlinear granular crystals, whereas weakly nonlinear granular crystals are typically approximated up to quadratic order via asymptotic expansion [62]. Using these models and several experimental demonstrations, nonlinear wave propagation through granular crystals has been researched extensively. These materials have also shown exceptional wave propagation properties such as solitary waves [67], [70], discrete breathers [71], second harmonic generation [72], [73], and modal mixing [74].

Over the past decade, several other phononic material systems with nonlinearity have been introduced and studied. These include tensegrity structures [75], [76], bistable periodic networks [77], [78], flexible metamaterials [79], and origami metamaterial [80]. Tensegrity structures are assemblies of rigid bars connected by prestressed cable-like elements that only support tensile loads, all constrained between rigid masses. Similar to granular crystals, they have a tunable nonlinearity, exhibiting a nonlinear force–displacement power law relation that is softening, hardening, or a combination thereof, depending upon the local pre-strain (i.e., the pretension of tensile elements) and global prestress (i.e., external axial force) [75], [76]. Phononic materials with bistable or multistable elements exploit the transition of structural members from one stable state to another as waves propagate [77], [78]. Flexible metamaterials exploit the configurational nonlinearity of rotating rigid squares coupled by flexible ligaments thus coupling both translational and rotation degrees of freedom [79]. Finally, origami metamaterials exploit the large deformation of origami-inspired linkages [80]. All these systems are studied analytically through reduced-order models, numerically, and experimentally to demonstrate unique wave propagation properties. Some of these notable properties consist of solitary waves in tensegrity structures [75], [76], transition waves [77] and supratransmission [78] in bistable phononic materials, vector solitons in flexible metamaterials [79], and transition of compressional waves to rarefaction in origami metamaterials [80].

In summary, exploiting several forms of nonlinearities, including material, finite strains, multistability, configuration, and contact in phononic materials enabled wave responses not achievable in corresponding linear counterparts [Fig. 1.2]. These responses are not just limited to the passive tuning of the acoustic

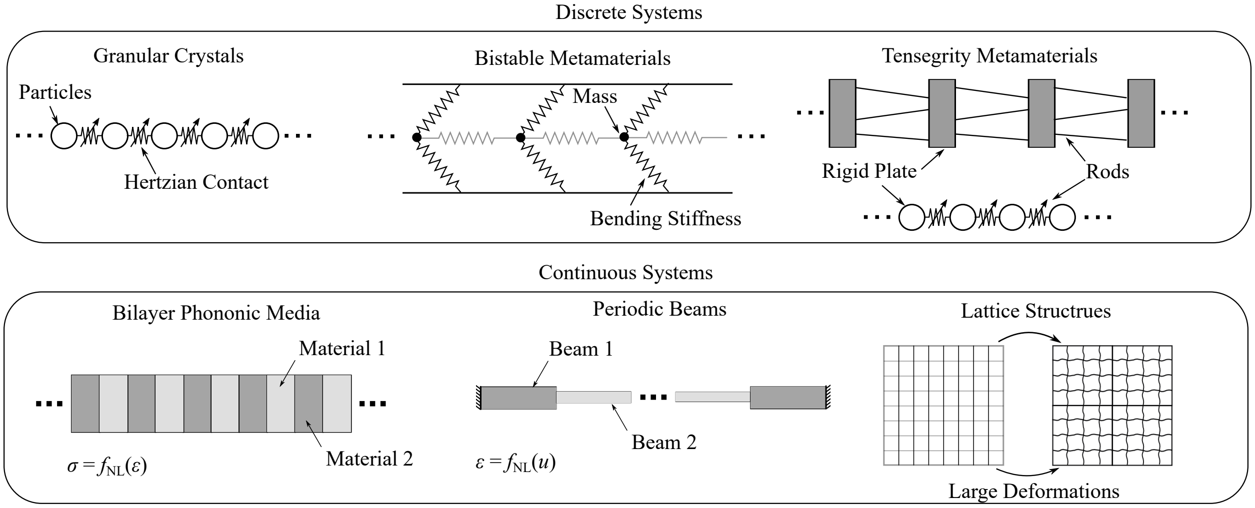

Figure 1.3: Nonlinear phononic materials as either (a) discrete systems with discrete nonlinearity or (b) continuous systems with continuous nonlinearity.

characteristics but include the propagation of localized waves such as solitary and transition waves, localization of energy such as discrete breathers, abrupt energy transmission within band gap through supra transmission, and nonreciprocal wave propagation [44].

1.2.3 Knowledge gap

The potential of nonlinear phononic materials for advanced engineering material design is underscored by their superior wave propagation properties, which arise from the combination of periodicity and nonlinearity. Yet, the nonlinear phononic materials studied so far have either considered discrete nonlinearity in discrete chains (purely discrete form) or continuous nonlinearity in continuous materials (purely continuous form) [Fig. 1.3]. *It remains an open question of how waves propagate in continuum phononic materials with discrete (or local) nonlinearities.* More importantly, what role does a continuum play on nonlinear responses generated at discrete locations, and how does the distribution of discrete nonlinearities within a continuum govern energy transfer between frequencies and wave evolution through the material? By addressing these questions, new opportunities for wave propagation control through the local coupling of discrete–continuum elements can be unlocked.

For example, studies of granular crystals are focused on frequencies having timescales of the dynamic disturbances much larger than the timescales of the modal frequencies of individual beads. Thus, elastic deformations were assumed to be concentrated only at the contacts while the beads were under the action of quasi-static deformation, making it reasonable to model granular crystals as discrete spring-mass chains. However, such treatment lacks the prospect of manipulating wave propagation through the dynamic response of the elastic media between nonlinear contacts. Moving away from the particle mechanics, the continuous modeling of beads has highlighted vibration-energy trapping [81], pulse propagation through an elastic–acoustic interface [82], and the effect of localized plastic dissipation on solitary waves [83]. Notably, a comparative study highlighted substantial differences in the dispersion of soft granular crystals obtained through continuous and discrete modeling of beads [84]. Despite this progress, the impact of the continuum between nonlinear contacts on wave propagation, specifically on the interactions between continuously propagating and discretely generated waves, is not studied. Such understanding can help improve the dynamic response of granular crystals at frequencies close to the modal frequencies of individual beads.

Even in the case of other nonlinear phononic media, the effects of vibrational modes of structural members are not explored. For example, beams in bistable periodic media [77], [78], rotating discs in configuration-based metamaterials [65], and rods and discs in tensegrity structures [75], [76] are considered rigid elements. Consequently, there also exists a lack of fundamental understanding of how local nonlinearity surrounded by deformable media leads to global nonlinear dynamic behavior. This further restricts the development of new platforms and strategies that exploit the local coupling of discrete-continuum elements to design phononic materials.

1.3 Local nonlinearities of geomaterial microstructures

Geomaterials are naturally formed materials characterized by their granular, heterogeneous, porous, and fractal nature [Fig. 1.4(a)]. These materials exhibit strong nonlinear elastic properties and rate-dependent effects due to their micro- and mesoscopic elements [85] [Figs. 1.4(b)-(d)]. Over the past few decades, various measurement techniques have been developed to characterize the nonlinear acoustic properties of geomaterials. These include nonlinear resonant ultrasound [86]–[88], nonlinear elastic wave spectroscopy [89], dynamic acoustoelastic testing [86], [90], [91], and time reversal diagnostic techniques [92], [93]. Additionally, researchers have developed multiscale mechanics models to better understand these nonlinear and rate-dependent effects [87], [94], [95].

Berea sandstone, one of the well-studied geomaterials, also exhibits nonlinear elastic properties (Fig. 1.4). Its matrix primarily consists of quartz grains with characteristic length scales ranging from 10s to 100s of microns. The sandstone contains inclusions, cracks, other mineral phases, and both dry and fluid-filled pores [96], [97]. Another interesting feature of these sandstones is their fractal geometry [98] - a complex geometric shape or pattern that exhibits self-similarity at different scales. Thus, a geometric feature of these sandstones resembles the whole structure when viewed at different levels of magnification. By combining imaging techniques like micro-computed tomography (CT) with numerical simulations, researchers have predicted the mechanical properties of rocks of Berea sandstones with different microstructures [97], [99]. Through 3D micro-CT and Focused Ion Beam (FIB) Scanning Electron Microscopy (SEM) imaging, a network of larger voids connected with smaller channels of pores has been revealed in Berea sandstone [100]. However, some digital reconstructions based on micro-CT have overpredicted the effective elastic properties of Berea sandstone, suggesting a loss of information at the smaller scale of grain-to-grain contacts, cracks, and small pores [97], [99]. These findings provide insights into the microstructural features that potentially contribute to nonlinear mechanisms, such as harmonic generation [101] and resonant frequency shifts [89] due to contacting faces of microcracks, nonclassical nonlinearity in consolidated granular media [87], and softening effects resulting from interactions between interfaces of hard and soft phases in cracks [86], [94] of geomaterials.

Clearly, numerous studies have examined the micro- and mesoscale features of Berea sandstone [96], [97], [99], [100], and others have explored its nonlinear mechanical and acoustic properties extensively [95]. *Yet, there remains a gap in exploiting the micro- or mesoscale features of geomaterials and their nonlinear responses in designing wave-tailoring materials.* Berea sandstone possesses diverse microstructures, such as porosities, hard-soft boundaries, and multiphase interfaces, among others. Among these microstructures, microcracks have been widely investigated in the field of nondestructive evaluation due to their role in failure mechanisms under dynamic loads. Therefore, several studies have leveraged nonlinearities to detect damage in

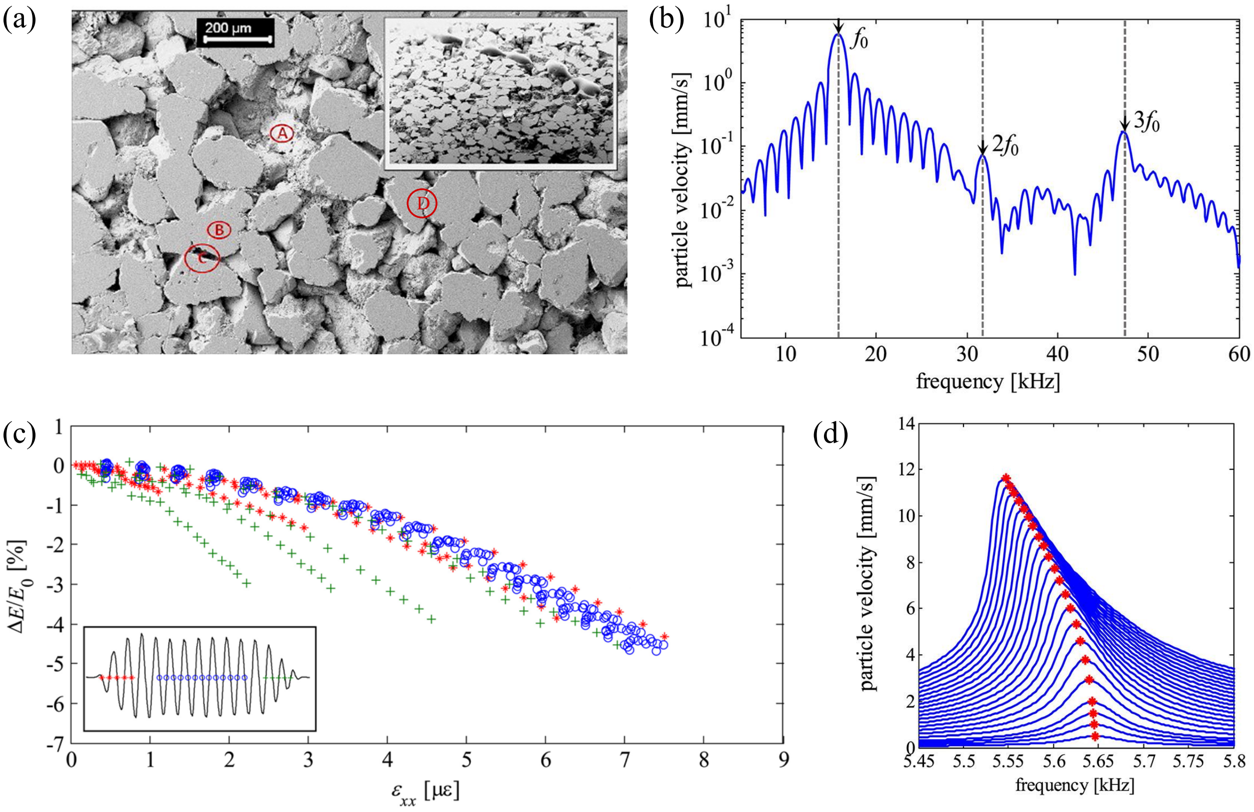

Figure 1.4: Nonlinear responses from the microstructures of Berea sandstone. (a) FIB-SEM image of a milled Berea sandstone sample. The image illustrates several microstructural features including (A) crater surrounded by (B) matrix, (C) voids, and (D) microcracks. Figure adapted with permission from [100], © 2010 Elsevier Ltd. These microstructural features give rise to nonlinear mesoscopic wave response including (b) higher harmonic generation, (c) slow dynamics leading to change in elasticity with strains, and (d) amplitude-dependent resonance shift. Figures adapted from [87], under the Creative Commons license CC BY-NC-ND 4.0.

geomaterials and improve the characterization of wave propagation. But what makes these cracks interesting is that they act as localized sources of nonlinearity. Yet, microcrack-induced nonlinearities have not been used in the context of periodic media.

1.4 Objectives and accomplishments

This dissertation aims to investigate wave propagation in continuum phononic materials with discrete nonlinearities, focusing on understanding the role of the continuum and distribution of such nonlinearities in governing energy propagation. Drawing inspiration from geomaterials, the research primarily explores microcracks as a local source of nonlinearity. Specifically, it investigates 1D nonlinear continuum phononic materials that incorporate microcracks (or rough contacts) as discrete nonlinearities (Fig. 1.5). It aims to develop a fundamental understanding of two key aspects: (1) the influence of the periodic arrangement of rough contacts on wave propagation and (2) the role of local contact nonlinearity between successive continuum layers in shaping nonlinear wave responses. To achieve these goals, a comprehensive numerical analysis is employed, considering various levels of contact nonlinearity ranging from weak to strong, including friction. Through careful examination of wave evolution in the material, the research aims to uncover the underlying physics behind the emergence of novel nonlinear responses. Moreover, it aims to demonstrate the potential for controlling and manipulating wave-energy propagation using these novel wave responses. Preliminary measurements of ultrasonic wave propagation through single rough contact are also conducted to establish an experimental foundation for future studies on these materials. The specific research objectives are as follows:

Objective 1: Understanding longitudinal wave propagation through weakly-nonlinear continuum phononic materials with rough contacts [102], [103].

This objective investigates longitudinal wave propagation in nonlinear phononic materials with external precompression. Finite element simulations are conducted to study two phenomena: wave self-interactions and wave-wave interactions. Wave self-interactions focus on the generation of zero (DC), self-demodulated low, and second harmonic frequencies, considering finiteness and embedded contacts. Results provide insights into the influence of dispersion zones on nonlinear wave amplitudes and their evolution through the phononic material. Additionally, controlling and tuning energy propagation between frequencies through external precompression is also explored. Wave-wave interactions investigate the generation of sum and difference frequencies, leading to the development of a contact-based phononic diode enabling nonreciprocal wave propagation. This diode offers control over broadband frequency, mode, and direction of energy propagation.

Objective 2: Understanding longitudinal wave propagation through strongly-nonlinear continuum phononic materials with rough contacts [104], [105].

This objective investigates longitudinal wave propagation in nonlinear phononic materials without precompression, specifically examining the effects of wave-induced contact clapping. Finite element simulations explore elastodynamic effects resulting from the strong nonlinear coupling between layers. Results capture remarkable phenomena, including energy transfer in the frequency domain from the acoustic resonances of the layers. The study also presents the interplay of strong nonlinearity and dispersion, giving rise to stegotons, which are solitary-like localized traveling waves exhibiting spatial profile variations due to layers. It also examines the influence of rough contact nonlinearity on stegoton parameters and the generation of secondary stegotons through the collision of counterpropagating waves. Additionally, the effects of physical constraints, such as light precompression, disorder, and finite lateral size, are studied to understand their influence on the ideal system's behavior.

Objective 3: Understanding shear wave propagation through hysteretically-nonlinear continuum phononic materials with rough contacts [106].

This objective explores the untapped potential of hysteretic nonlinearity in nonlinear phononic materials, specifically focusing on shear wave-induced friction and its role in enabling superior wave responses and programmable functionalities for acoustic devices. A hybrid analytical-numerical approach is employed to solve the strongly nonlinear problem of shear wave propagation through a single and periodic array of contacts. Frictional effects, captured using the Jenkin friction model with experimentally-obtained properties, account for the stick-slip transition behavior at the contacts. Results show the generation of shear-polarized eigenstrains, which are residual static deformations within the system, resulting from friction. These eigenstrains are further exploited for smart functionality, including mechanical switches, precision actuation, and surface reconfigurability. Additionally, energy dissipation from contact sliding is also studied and exploited to form amplitude-dependent wide-band attenuation zones.

Objective 4: Developing experimental foundation by measuring ultrasonic wave propagation through a single rough contact.

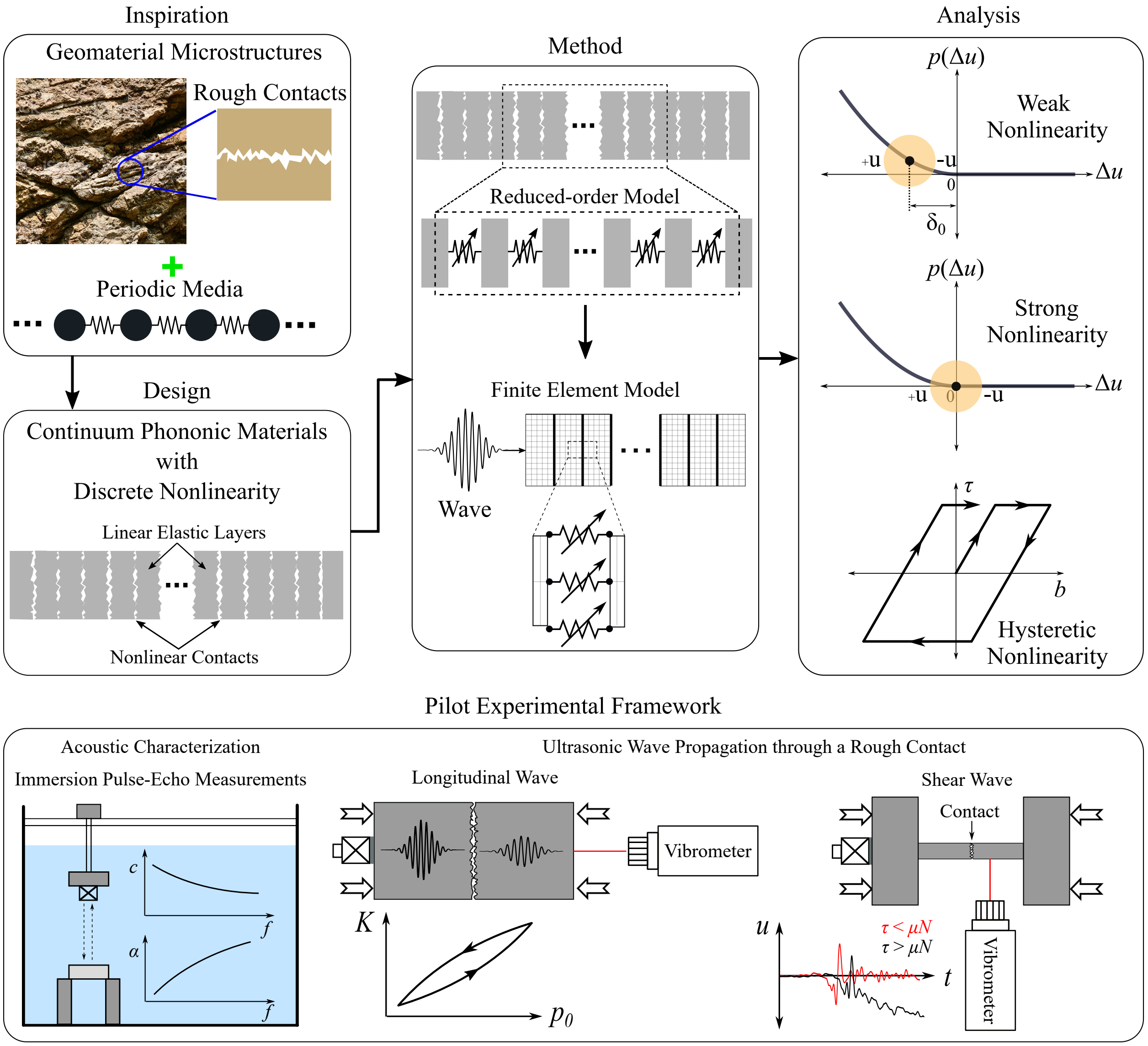

Figure 1.5: Dissertation Overview

This objective aims to develop an experimental framework to study ultrasonic wave propagation through rough contacts. To achieve this, preliminary measurements are conducted to characterize the acoustic properties of the base materials and analyze longitudinal and shear wave propagation through a rough contact. Acoustic characterization involves using ultrasonic pulse-echo measurements in an immersion tank, which provides wave speed and frequency-dependent attenuation coefficient of the parent material. Measurements of wave propagation through a rough contact suggest that complex mechanisms at contacts, such as nonlinear normal force-displacement relationship due to asperity deformation, and eigenstrain generation and energy dissipation due to interface sliding may be observed in a physical system. These experiments outline the challenges and guidelines for future experimental work, establishing the groundwork for realizing phononic materials with periodic rough contacts.

1.5 Organization of the dissertation

The rest of the dissertation is organized as follows: Chapter 2 focuses on the nonlinear laws at rough contacts and introduces different configurations of continuum phononic materials with contacts studied in the dissertation. Chapter 3 presents the modeling details of nonlinear wave propagation through these materials. It includes an analytical model for linear dispersion analysis and comprehensive details of finite element models for weakly and strongly nonlinear phononic materials. It also introduces a hybrid model to capture the hysteresis effect resulting from frictional instability. These initial chapters lay the foundation for subsequent chapters, which delve deeper into specific aspects of nonlinear wave responses. Chapter 4 investigates wave dynamics of the phononic materials under strong external precompression (weak nonlinearity), while Chapter 5 focuses on the same materials under zero or light external precompression (strong nonlinearity). Chapter 6 examines nonlinear shear wave propagation in these materials while capturing the effects of hysteretic nonlinearity from frictional effects.

Chapter 7 presents the experimental results of ultrasonic wave propagation through rough contacts. It includes immersion pulse-echo measurements for acoustic characterization of materials and investigates wave-contact interaction for longitudinal and shear wave propagation. Finally, Chapter 8 concludes the dissertation by summarizing the major results, research outputs, and the significance of the study. It also provides recommendations for future work in this area, emphasizing potential avenues for further research and development.

Chapter 2

Continuum phononic materials with rough contacts

This chapter introduces nonlinear laws for rough contacts and different configurations of continuum phononic materials studied in this dissertation. It starts by discussing the nonlinear relationships used at the contacts in both normal and tangential directions, along with the underlying assumptions and their physical interpretation. The generalized formulation and deduction of nonlinear laws for specific cases, in line with the Hertzian contacts formulation, are also presented. Subsequent sections delve into the exploration of different phononic material systems. The contents of this chapter have been adapted from various sections of my published articles, [102], [104], [106], which were written as part of the research for this dissertation.

2.1 Rough contact nonlinearity

Inspired by the presence of microcracks in geomaterials, rough contacts represent interfaces characterized by surface roughness or microscale asperities (unevenness of rough surfaces) [Fig. 2.1(a)]. These interfaces exhibit a nonlinear mechanical response due to the deformation of the contact asperities. Such nonlinear responses manifest in both the normal and tangential directions. When subjected to compressive loads, the asperities undergo significant deformation, leading to a change in the contact area and thereby resulting in a nonlinear response. Similarly, under tangential loads, the asperities initially deform, but once the applied tangential load surpasses the friction limit, sliding occurs, thus demonstrating a nonlinear tangential response.

The modeling of rough contacts and the determination of their mechanical response have been subjects of interest for decades. Hertz investigated frictionless contact between elastic solids with smooth surface profiles, approximating them as parabolic near the contact area [107]. According to this theory, the contact area exhibits a nonlinear increase with the squeezing force, following a power-law relationship with an exponent of 2/3. Although this model can approximate a randomly rough but nominally flat surface composed of spherical bumps with uniform radii of curvature and height [108], it is not suitable for practical calculations due to its idealized representation of real surfaces. Alternatively, more comprehensive models have been developed. Some include models incorporating hierarchical asperities [109], a Gaussian distribution of spherical bumps [110], models utilizing paraboloids with random height distributions [111], and numerous others [112]. However, these models have limitations. Firstly, they neglect the interactions between neighboring asperities and the bulk material. Secondly, these models are only applicable to small asperity deformations and contact

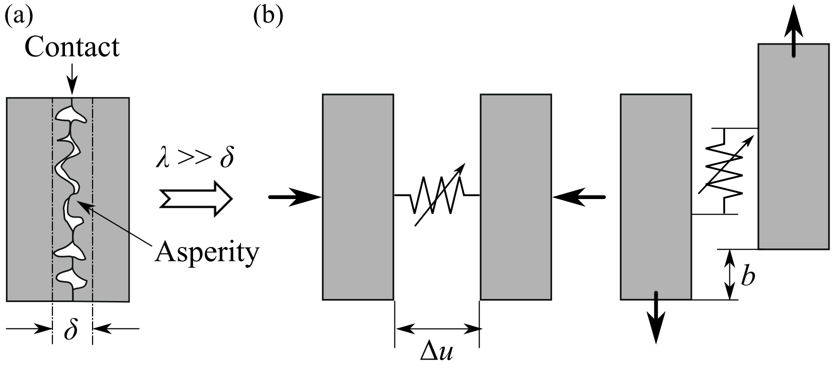

Figure 2.1: (a) Physical rough contacts and (b) the reduced-order models of their normal and tangential interactions for wavelength larger than asperity size.

areas significantly smaller than the nominal area.

In this research, the contact laws are informed by experimental studies that consider the effects of actual roughness, real deformations, and multi-asperity interactions. By incorporating these factors, the research aims to overcome the limitations of idealized models and provide a more accurate representation of the mechanical response of rough contacts. The surfaces in focus, however, are idealized and assumed to be non-fractal, i.e. there is no repeating pattern on the contacting surfaces at length scales other than the microscale asperities. This dissertation, specifically, focuses on wave interactions with rough contacts at wavelengths (λ) much larger than the size of individual asperities (δ). In other words, the interest lies in studying the effective nonlinear response of a collection of asperities, which includes the normal as well as lateral interactions between adjecent asperities along with local sliding between them. To investigate such mesoscale interactions, a reduced-order model is employed, treating the contacts as nonlinear springs with experimentally-derived effective contact properties [Fig. 2.1(b)]. This approach enables the modeling of force continuity and displacement discontinuity across the contacts while incorporating realistic nonlinear contact laws. The study does not account for interfacial mass or inertia at the contact, as the effects of gap resonances or cavities are negligible at wavelengths significantly larger than the rough asperities [113].

2.1.1 Normal contact law

The normal contact law utilized in this research is derived from a combination of ultrasonic experiments [113], a micromechanics contact model [114], and asymptotic analysis [115]. A normal stiffness-pressure ($K_N - p_0$) relation at the pre-compressed interface of two aluminum blocks with rough surfaces was obtained experimentally based on the quasi-spring model [113]. This relationship was later expanded asymptotically to eventually derive a nonlinear relationship between the contact pressure, $p(\Delta u)$, and normal contact displacement, Δu [115]. This nonlinear relation follows a power-law dependence [115] as given by

$$p(\Delta u) = \begin{cases} [p_0^{1-\beta} - (1-\beta)C(\Delta u - \delta_0)]^{1/(1-\beta)}, & \beta \neq 1, \\ p_0 \exp\left[-C(\Delta u - \delta_0)\right], & \beta = 1, \end{cases} \tag{2.1}$$

where C, β are curve fitting parameters of the experimental data of contact stiffness and pressure, and δ_0 is the initial static deformation corresponding to external precompression, p_0. C and β depend on the base material and roughness topography such as asperity size, shape, and height distribution. As a result, a wide range of β is reported in the literature based on roughness distribution [116], [117]. Theoretically, β for a contact between rough fractal surfaces is such that $\beta = 1/(1 + H_c)$ in the interval $H_c \in (0, 1)$, where H_c is an Hurst exponent [116]. Physically, β tends to be towards unity for roughness having statistical (or non-uniform) height distribution, whereas it tends to 0.5 for uniform roughness [115]. Further, the value of β for a rough contact changes if the asperities undergo plastic deformation; this has been experimentally observed, but only during the first loading cycle [113]. This research uses β corresponding to elastic deformations of rough contacts after the first loading cycle (i.e. after hysteresis has been removed) and considers wave amplitudes much smaller than the maximum deformation of asperities caused by the loads in the experimental work of [113]. Therefore, the rough contacts in this study do not undergo any plastic deformation during wave propagation and as a result, energy dissipation at the contacts from plasticity is neglected.

In a weakly nonlinear regime, where the contacts are *initially precompressed* and contact deformations from waves are smaller than predeformation ($\Delta u < \delta_0$), the leading terms of the series expansion of Eq. (2.1) are considered to obtain the nonlinear force-displacement relation as

$$p(\Delta u) = \kappa_1 \Delta u - \kappa_2 \Delta u^2, \tag{2.2}$$

where κ_1 and κ_2 are linear and quadratic contact stiffness per unit area, respectively, as given by

$$\kappa_1 = C p_0^{\beta}, \ \kappa_2 = 0.5 C^2 \beta p_0^{2\beta - 1}. \tag{2.3}$$

In a strongly nonlinear regime, where contacts are *initially uncompressed*, the relationship of Eq. (2.1) for compressive loads exhibits essential nonlinearity as

$$p(\Delta u) = [(1 - \beta) C \Delta u]^{1/(1-\beta)}. \tag{2.4}$$

This dissertation considers $C = 6 \times 10^{10} \sqrt{Pa}/m$ and exponent $\beta = 0.5$, which results in a quadratic dependence of pressure on displacement, a similar approximation made in the micromechanics model of rough contact [114] owing to the fitting of experimentally acquired data [115]. This means the rough contact model in this dissertation corresponds to rough surfaces with uniform height distribution of asperities. Thus, the nonlinear force-displacement relation at the rough contacts in this research is,

For weakly nonlinear contacts [Fig. 2.2(a)]:

$$p(\Delta u) = C \sqrt{p_0} \Delta u - \frac{C^2}{4} \Delta u^2. \tag{2.5}$$

For strongly nonlinear contacts [Fig. 2.2(b)]:

$$p(\Delta u) = \begin{cases} 0, & \Delta u > 0, \\ \frac{C^2 \Delta u^2}{4}, & \Delta u \leq 0. \end{cases} \tag{2.6}$$

The potential energy corresponding to weakly nonlinear Eq. (2.5) shows two distinct features - asymmetry and anharmonicity - near the stable equilibrium point, x_1 [Fig. 2.2(a)]. Asymmetry results in the generation of DC while second harmonic frequencies are generated due to anharmonicity. The model given by Eq. (2.5) is not valid beyond critical energy, E_{cr}, however, this research is focused within the weakly nonlinear regime, i.e. below E_{cr}. On the other hand, Eq. (2.6) indicates that the dynamics of rough contacts is non-smooth as contacting surfaces can collide and separate [Fig. 2.2(b)]. As a result, the dynamics of rough contacts are strongly nonlinear (in fact, not even linearizable) when no precompression is applied. This strong nonlinearity

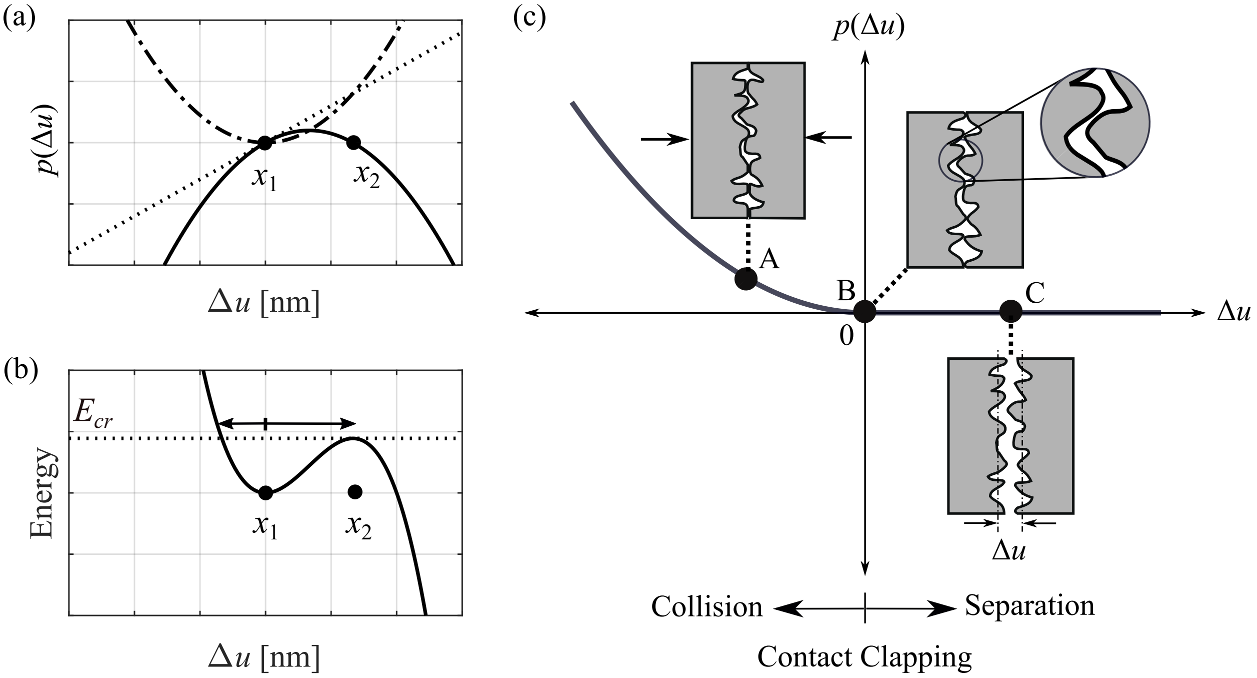

Figure 2.2: Normal contact law corresponding to (a)-(b) weakly and (c) strongly nonlinear regime. (a) The pressure-displacement relationship (solid) along with linear (dotted) and quadratic (dashed–dotted) force components. (b) Potential energy corresponding to the pressure-displacement relationship in (a). The arrow indicates the asymmetric potential well around the stable equilibrium point, x_1, and the dotted line is a critical energy limit at the unstable equilibrium point, x_2. The energy plot is scaled up for better visualization. (c) The pressure-displacement relationship with three contact configurations: (A) contact under compressive load undergoing flattening of rough asperities, (B) contact under no load, and (C) contact loss. The inset in (B) shows undeformed rough asperities and thin black lines in (C) indicate nominal surfaces.

is in addition to the nonlinear power-law interaction between rough asperities.

The nonlinear laws discussed above are obtained through a generalized formulation, which can be applied to any values of β. However, for $\beta \neq 1$, an alternative formulation also leads to the same nonlinear law and draws an analogy with that of Hertzian contacts in granular crystals. In this alternate method, the stiffness-pressure relation at a rough contact obtained experimentally can be fitted to a power law [115] such that:

$$\frac{dp}{du} = -Cp^{\beta}. \tag{2.7}$$

To obtain a pressure-displacement relationship, integrate Eq. (2.7) within the interval 0 to p_0 as

$$\int_0^{p_0} \frac{1}{p^{\beta}}\, dp = -C \int_0^{\delta_0} du, \tag{2.8}$$

$$p_0^{1-\beta} = -(1-\beta)C\delta_0 \text{ and } p_0 = [-(1-\beta)C\delta_0]^{\frac{1}{1-\beta}} \tag{2.9}$$

Eq. (2.9) is the strongly nonlinear form of the rough contact nonlinearity and is consistent with Eq. (2.4). To deduce the above relationship to weakly nonlinear form, taking the Taylor series expansion up to the first two terms such that,

$$p(u) = [-(1-\beta)C(\delta_0 \pm u)]^{\frac{1}{1-\beta}}, \tag{2.10}$$

$$p(\Delta u) = p'(\delta_0)\Delta u + \frac{p''(\delta_0)}{2!}\Delta u^2, \tag{2.11}$$

where

$$p'(\delta_0) = -C[-(1-\beta)C\delta_0]^{\frac{\beta}{1-\beta}}, \text{ and } p''(\delta_0) = C^2\beta[-(1-\beta)C\delta_0]^{\frac{2\beta-1}{1-\beta}}. \tag{2.12}$$

This effectively leads to

$$K_1 = -C[-(1-\beta)C\delta_0]^{\frac{\beta}{1-\beta}}, \text{ and } K_2 = \frac{1}{2}C^2\beta[-(1-\beta)C\delta_0]^{\frac{2\beta-1}{1-\beta}}, \tag{2.13}$$

which informs the nonlinear dependencies of contact stiffness with predeformation.

For $\beta = 0.5$, Eq. (2.13) reduces to Eq. (2.5).

2.1.2 Tangential contact law

The Jenkins friction model [118] is considered to account for frictional effects and tangential compliance of roughness [Fig. 2.3(a)]. This model captures stick-slip transition at the contacts and further assumes that the compliance at real contacts is governed by the stiffness corresponding to the elastic deformation of the micro-asperities at the contact interfaces [119] and the bulk elastic deformation at the macroscopic contact scale[120]. Accordingly, the tangential interaction at the contacts is,

$$\tau(t) = \begin{cases} \tau(t-\Delta t) + \kappa_t \Delta b(t), & \text{stick}, \\ \operatorname{sgn}[\dot{b}(t)]\tau_c, & \text{slip}, \end{cases} \tag{2.14}$$

where τ is shear stress at the contact, b is corresponding tangential contact deformation, and $\dot{b}$ $(= db/dt)$ is tangential velocity. t is time variable and Δt is time step such that displacement increment, $\Delta b(t) = b(t) - b(t-\Delta t)$. κ_t is tangential contact stiffness per unit area and τ_c $(= \mu\sigma_0)$ is the friction limit at which the contacts start to slide. The contact is under the state of normal pre-stress, σ_0. The static and kinematic coefficient of friction are treated the same, i.e. no abrupt jump in the friction force on the onset of sliding. From Eq. (2.14), it can be seen that the contact law is history-dependent and follows different loading-unloading paths due to contact sliding [Fig. 2.3(a)]. While an intermediate state of micro-slip (or partial slip) exists in real contacts, no such state is assumed in this research, i.e. all asperities slide simultaneously once the friction limit is reached.

Experiments were conducted to inform the contact properties, κ_t and μ, to be used as input parameters in the tangential contact law of Eq. (2.14). Specifically, friction hysteresis loops were measured on a high-frequency friction rig [refer to the experimental schematics of Fig. 2.3(b) and [121] for more details]. The setup consists of an electrodynamic shaker that applies a harmonic sinusoidal excitation in the tangential direction to two contacting specimens while two laser Doppler vibrometers and a force transducer measure relative motion between the specimens, b, and friction (or tangential) force, T, respectively. Experiments were conducted on two aluminum (AL6061-T6511) specimens, which were roughened to an RMS surface roughness of $R_q \sim 1.1$ μm using P1200 grit sandpaper. The loading conditions for hysteresis measurements were: $N = 60$ N and $b = 15\mu$m at an excitation frequency of 100 Hz at room temperature, which is commonly used for reliable measurements on the friction rig.

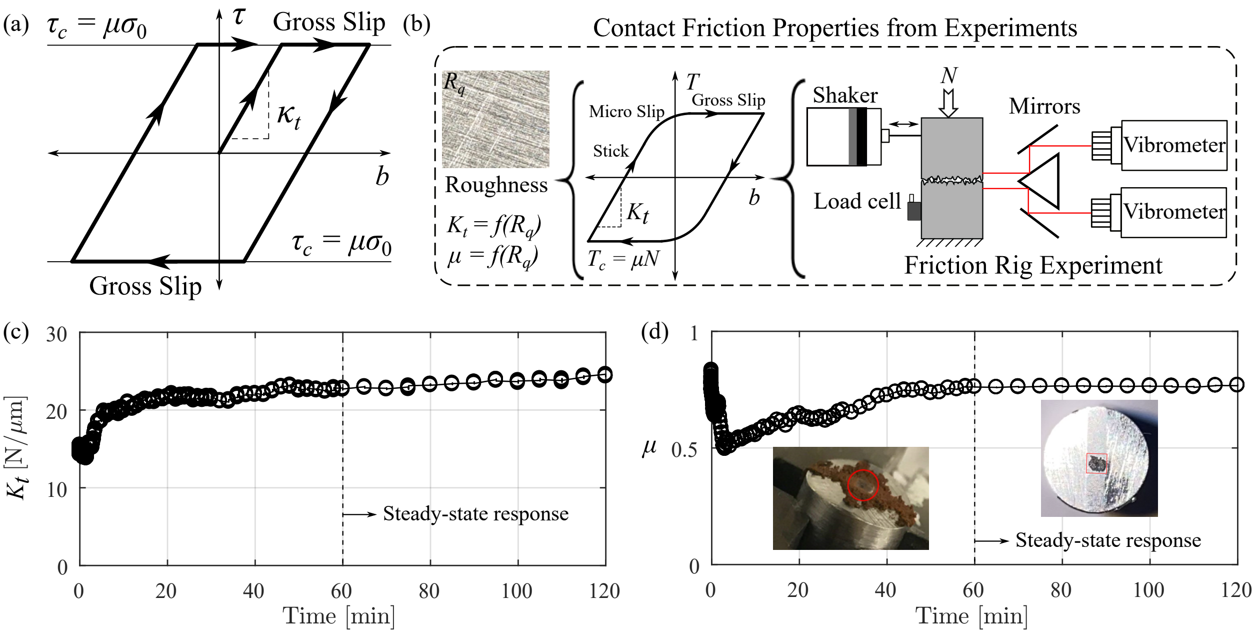

Figure 2.3: Tangential contact law. (a) Jenkins friction law. (b) Schematic of friction rig experiments to obtain realistic hysteresis loop and contact properties of rough surfaces. Experimentally obtained (c) absolute contact stiffness, K_t, and (d) coefficient of friction, μ, as contacting surfaces evolve. Insets in (d) highlight wear during surface evolution and the actual area of contact (shaded black patch) during the steady-state response.

The hysteresis loops ($T - b$ relation) were recorded and absolute contact stiffness, K_t, was evaluated as the slope of the stick portion of the loop and coefficient of friction as, $\mu = T_c/N$ [schematics of Fig. 2.3(b)]. These values are evaluated while the surface texture evolved from wear until a steady-state response was reached [Figs. 2.3(c)-(d)]. The steady-state properties are listed in Table 2.1. Microscopic measurements were also used to determine the actual contact area [shaded black patch in the inset of Fig. 2.3(d)], from which the contact stiffness per unit area ($\kappa_t = K_t/a$, where a is the actual contact area) was obtained and used as input for the friction law of Eq. (2.14) along with the coefficient of friction.

Parameters	Obtained Values
Normal load, N	60 N
Actual worn-out area, a	1.2 mm^2
Prestress, $\sigma_0 = N/a$	50 MPa
Displacement amplitude, b	15 μm
Coefficient of friction, μ	0.77
Absolute stiffness, K_t	22 N/μm
Stiffness per unit area, $\kappa_t = K_t/a$	18.33e12 N/m^3

Table 2.1: Friction rig experimental parameters and evaluated steady-state contact frictional properties

To ensure that the contact properties evaluated experimentally can be applied in the wave propagation analysis, identical loading conditions and sample material was employed in the numerical model. Additionally, the following assumptions are made:

1. The contacts are already in a steady-state condition from surface wearing, i.e. frictional properties do not change with time as waves propagate through the contact.

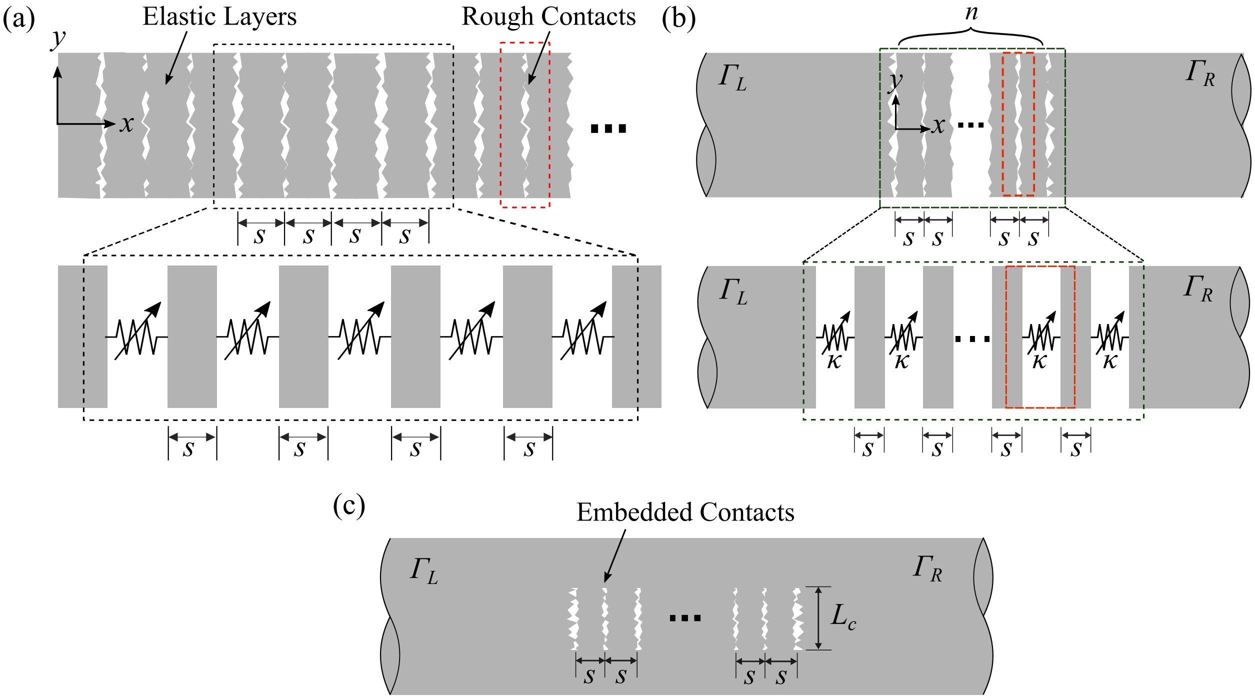

Figure 2.4: Phononic materials with periodic rough contacts. (a) Semi-infinite and (b) a finite number of layers and (c) embedded contact configurations. Red dashed rectangles indicate the unit cell of the phononic material.

2. Both the coefficient of friction and tangential stiffness are rate independent, i.e. independent of the frequency of excitation. This is a reasonable assumption since the coefficient of friction obtained from quasi-static and frequency-dependent approaches differ insignificantly [122]. Further, contact stiffnesses obtained through the quasi-spring model are frequency-independent for frequencies that correspond to wavelengths much larger than asperity size [113]. Thus, the frictional properties of contacts with a roughness of the orders of $\sim \mu$m obtained at 100 Hz through friction rig can be reasonably applied to study wave propagation up to ultrasonic frequencies (i.e. up to a few MHz).

3. Based on the parametric measurements of hysteresis loops on friction rig, it is assumed that both coefficient of friction and tangential stiffness do not (or negligibly) depend upon the tangential displacement amplitude.

2.2 Phononic materials with rough contacts

This dissertation introduces 1D phononic materials by periodically arranging nonlinear rough contacts. As a result, the system is a multilayered configuration with elastic layers coupled through rough contact nonlinearity [Fig. 2.4(a)]. These layers are linear and have identical thicknesses, s. Consequently, the unit cell of the phononic materials includes a contact and adjacent half layers [red rectangle in Fig. 2.4(a)]. While the focus of the study is on wavelengths larger than rough asperities, the wavelengths are still of the order of layer thickness. Thus, significant elastic deformation occurs in this system - both at the rough contacts and within the layers. This differs from granular crystals, where elastic deformations are limited to the contacts, and the elastic body between successive contacts is considered a rigid dimensionless point. To model these mechanical deformations in this dissertation, the layers are treated as a continuous material, while the contacts are represented as nonlinear springs. The nonlinear relationship for weakly nonlinear normal interaction is given by Eq. (2.2), whereas strongly nonlinear normal interaction is described by Eq. (2.4), and tangential interaction is characterized by Eq. (2.14). Although the main focus is on understanding wave propagation through semi-infinite $x-$directional phononic materials, the effects of finiteness are also examined in selected cases. Various configurations of phononic materials studied in this dissertation are categorized in Table 2.2.

Type of Nonlinearity	Semi-infinite	Finite	Embedded Contact
Weak Nonlinearity	✓	✓	✓
Strong Nonlinearity	✓	-	-
Hysteretic Nonlinearity	-	✓	-

Table 2.2: Different configurations of continuum phononic materials investigated in this dissertation based on geometry.

Semi-infinite phononic materials [Fig. 2.4(a)] are considered to be infinite in the $+x$ direction, while the other end (the left at $x = 0$) is treated as an excitation boundary. Both the layers and contacts are assumed to be infinite in the $y-$direction. On the other hand, *finite phononic materials* [Fig. 2.4(b)] are introduced such that a finite number of elastic layers are present in-between semi-infinite bulk layers, (Γ_L, Γ_R). The left bulk layer, Γ_L, occupies the space $x < 0$ while the right one, Γ_R, occupies the space $x > ns$, where n is the number of layers in the phononic material. The semi-infinite layers, (Γ_L, Γ_R), have rough surfaces at the finite ends ($x = 0$ and $x = ns$). Thus, finite phononic material with n layers has $n + 1$ contacts. Again, the layers are assumed to be infinite in the y-direction while two different systems of contacts are studied $-$ infinite-length [Fig. 2.4(b)] and embedded [Fig. 2.4(c)] contacts of finite length, L_c.

The strength and type of nonlinearity of rough contacts in these phononic materials rely on external boundary conditions (BCs) and the excitation type. When an external precompression, p_0, is applied, rough contacts do not induce contact clapping for longitudinal wave excitation with amplitudes smaller than the pre-deformation, indicating a weakly nonlinear phononic material. Additionally, this same material enables the propagation of shear waves due to non-zero normal stress at the contact. Therefore, externally precompressed phononic material is studied to examine the effects of weak nonlinearity in rough contacts and hysteretic nonlinearity from friction. On the contrary, a strongly nonlinear phononic material refers to one with no or significantly smaller precompression compared to wave excitation. Table 2.3 classifies the boundary conditions and wave excitation types, corresponding to their respective nonlinearity analyses.

Type of Nonlinearity	External Precompression	Wave Polarization
Weak Nonlinearity	✓	Longitudinal
Strong Nonlinearity	-	Longitudinal
Hysteretic Nonlinearity	✓	Shear

Table 2.3: Different configurations of continuum phononic materials investigated in this dissertation based on boundary condition and excitation type.

2.3 Summary

This chapter explored the modeling of rough contacts and presented different phononic material configurations studied in this dissertation. The analysis in this dissertation is restricted to wavelengths much larger than the size of asperities at contact, while being on the order of the size of layers of phononic material. Therefore, the contacts were treated as nonlinear springs to capture the effective behavior of the collection of asperities, overcoming the limitation of existing and simplified analytical models. Specifically, the laws incorporated in the analysis are -

1. In normal direction, contacts followed a power-law relationship between pressure and displacement. The coefficient and exponents of power law are derived from experimental data obtained from contact interfaces with uniform roughness. Under external precompression and relatively smaller wave amplitudes, these contacts display weak nonlinearity as the power-law relationship can be asymptotically reduced. However, for zero or light precompression and high wave amplitudes, the contacts exhibit strong nonlinearity due to collision and separation of the contacting interface.
2. In tangential direction, the Jenkins friction model is used. This model accounts for the finite stiffness of contact asperities and captures the stick-slip transition during frictional sliding. The coefficient of friction and tangential contact stiffness is derived from the hysteresis loops measured on a friction rig. These properties are evaluated when the contact response is steady-state.

These laws, derived from experimentally-informed contact properties, accurately depict the realistic and physical behavior of rough contacts.

Next, the chapter presented phononic material with periodic contacts and several different configurations studied in this dissertation. These configurations are based on geometry, boundary condition, and type of wave excitation. Specifically, designs include semi-infinite and finite systems along with infinite-length and embedded contacts. These configurations are developed to capture the effects of periodicity, finiteness, and surrounding continuum. Additionally, configurations with and without precompression and for longitudinal and shear wave excitation were considered for a thorough understanding of the nonlinear wave propagation through the phononic material.

Chapter 3

Modeling of wave propagation

This chapter provides an overview of modeling nonlinear wave propagation in continuum phononic material with rough contacts. It begins with a concise review of existing approaches in the literature. Next, an analytical model for linear dispersion analysis of unit cells is presented, followed by comprehensive details of finite element models for wave propagation in both weakly and strongly nonlinear phononic materials. Lastly, a hybrid model combining an analytical friction model and a finite element model for shear wave propagation is introduced to capture the hysteresis effect resulting from frictional instability at contacts. The contents of this chapter have been adapted from various sections of my published articles, [102], [104], [106], which were written as part of the research for this dissertation.

3.1 Background on modeling nonlinear phononic materials

Phononic materials are commonly represented as spring-mass chains [12], which allows for a reduced-order formulation of the wave propagation problem. Despite this simplification, the underlying physics of wave propagation through these materials can still be studied. Additionally, phononic materials based on continuous structural members, such as rods and beams, have facilitated the formulation of wave propagation through them [61]. Previous studies have employed various methods, such as harmonic balance [60], multiple scales [58], perturbation theory [57], [59], [123], and transfer matrix [61] techniques, to approximate the solution for nonlinear wave propagation problems in periodic chains with discrete nonlinearity and homogeneous waveguides with continuous nonlinearity. Granular crystals with contact nonlinearity have also been analyzed using different methods [62]. However, these approaches mainly provide insights into simpler nonlinear systems and face challenges when applied to complex configurations involving multidimensional multi-degrees of freedom systems. Recent advancements in phononic materials, such as bistable metamaterials [77], flexible metamaterials [65], tensegrity structures [75], and origami materials [80], have also been simplified as spring-mass systems to facilitate the use of approximate methods mentioned above. However, there is limited availability of methods that can simultaneously incorporate continuum systems with local nonlinearities, especially for dynamic problems.

To address this, the present research adopts a finite element approach, which not only accommodates complex geometries but also allows the simulation of amplitudes that are not achievable with perturbation methods. This approach enables the analysis of phononic materials with strong and hysteretic nonlinearity. The 1D phononic materials are modeled within a two-dimensional (2D) plane strain framework using the

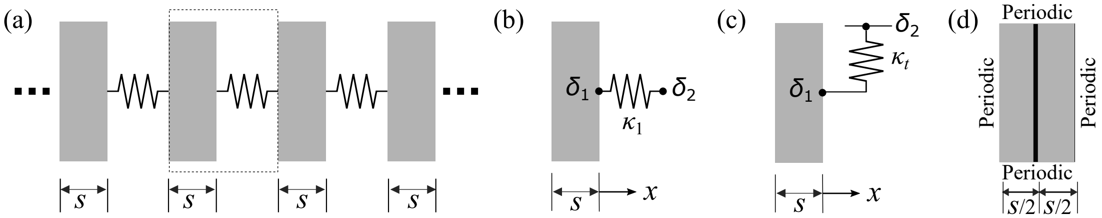

Figure 3.1: (a) Reduced-order model of phononic materials with periodic rough contacts considering linear contact stiffness only. The unit cell of the phononic material [Dashed rectangle in (a)] with (b) normal and (c) shear interactions only. (d) Finite element setup of Bloch analysis on a different form of the unit cell of (a).

commercial finite element package COMSOL Multiphysics 5.5. The layers are modeled as aluminum (Young's modulus = 69 GPa, Poisson's ratio = 0.33, density = 2700 kg/m^3) to align with experiments of rough contacts [106], [113].

3.2 Analytical modeling of linear dispersion

Phononic material with zero precompression does not support the propagation of linear waves and thus is referred to as a "sonic vacuum" [67]. However, externally compressed phononic material can support the propagation of harmonic waves - both longitudinal and shear. In the context of longitudinal wave propagation, the contact nonlinearity in the normal direction, as governed by Eq. (2.2), is fundamentally asymmetric in nature with softening and hardening effects in tension and compression, respectively [Fig. 2.2(a) – solid black]. Due to this asymmetry, the effective nonlinearity may be of hardening or softening type depending upon the competing effects in tension-compression, i.e. the dominant behavior may dictate the nature of effective nonlinearity. Thus, increasing excitation amplitude may increase or decrease dispersion curves. Nevertheless, the amplitude-dependent dispersion correction for weak quadratic nonlinearity is negligible [124]. Therefore, the linear dispersion of these phononic materials is evaluated without considering the nonlinear stiffness. This is sufficient to inform different zones of dispersion and facilitate the selection of appropriate input frequencies for nonlinear analysis. Concerning shear wave propagation, the dispersion, and therefore the band gaps of the phononic material are expected to depend on wave amplitude due to strong nonlinearity. Thus, the effects of wave amplitude on shear band gaps are studied by considering linear dispersion as a reference. In that case, the contact is assumed to be in the stick state, corresponding only to the tangential contact stiffness.

Next, the analytical model for dispersion calculation of pure longitudinal and shear waves is presented, followed by the finite element setup as an alternate method. The unit cell of the phononic material consists of a contact and two half layers [Fig. 2.4(a)]. However, for the simplified analytical formulation, the unit cell can also be represented as a layer and a contact where the contact is treated as a linear spring [Fig. 3.1(a)]. The spring characteristics are defined by the linear terms of Eq. (2.2) and Eq. (2.14) for normal and tangential interactions, respectively. To obtain dispersion relations of longitudinal waves, a Bloch analysis is performed on the unit cell [Fig. 3.1(b)-(c)] as follows:

By applying a uniaxial strain wave equation for the layer as,

$$\frac{\partial^2 u}{\partial t^2} = c_L^2 \frac{\partial^2 u}{\partial x^2}, \tag{3.1}$$

where u is the displacement, c_L is the dilatational wave speed of the bulk material, and x and t are spatial and temporal variables, respectively. The force per unit area (contact pressure) on the contact spring element is

$$p(\Delta u) = \kappa_1(\delta_2 - \delta_1), \tag{3.2}$$

where, δ_1, δ_2 are the displacements of the spring endpoints such that $\Delta u = \delta_2 - \delta_1$. Now, applying force continuity boundary condition per unit area at $x = 0$ as

$$(\lambda^{(L)} + 2\mu^{(L)})\frac{du}{dx}\Big|_{x=0} = \kappa_1(\delta_2 - \delta_1), \tag{3.3}$$

where $\lambda^{(L)}$, $\mu^{(L)}$ are the Lame parameters of the bulk materials. To simulate the infinite periodic material, the Bloch boundary condition is applied on the end faces of the unit cell as

$$u(x = -st) = \delta_2 e^{iqs}, \tag{3.4}$$

where q is the wavenumber. After solving Eqs. (3.1) to (3.4), the dispersion relation is obtained as

$$\cos(qs) = \frac{1}{2}\left\{2\cos\left(\frac{\omega}{c_L}s\right) - \left[\left(\frac{\lambda^{(L)} + 2\mu^{(L)}}{\kappa_1}\right)\frac{\omega}{c_L}\right]\sin\left(\frac{\omega}{c_L}s\right)\right\}. \tag{3.5}$$

This dispersion relation is solved for the wave vector for a given value of angular frequencies while relaxing the wave vectors to be either real or imaginary to distinguish the propagating and evanescent waves, respectively. Similarly, the equation for shear wave dispersion is obtained as,

$$\cos(qs) = \frac{1}{2}\left\{2\cos\left(\frac{\omega}{c_s}s\right) - \left[\left(\frac{G}{\kappa_t}\right)\frac{\omega}{c_s}\right]\sin\left(\frac{\omega}{c_s}s\right)\right\}, \tag{3.6}$$

where G is shear modulus and κ_t is tangential stiffness of contact.

These linear dispersions can also be evaluated using the finite element approach, where the unit cell can be modeled as half-elastic layers with a contact-equivalent spring in between them [Fig. 3.1(d)]. By applying periodic boundary conditions at all sides, the modes of the system can be obtained through eigenfrequency analysis. The analytical results are validated through this method by sweeping the wavevector in the $x-$direction for the first 100 frequencies. To obtain dispersion curves of 1D wave propagation, pure longitudinal and shear wave modes are isolated by evaluating the modal mass along the x and y directions for each frequency-wavenumber combination. For longitudinal dispersion, only combinations with non-zero modal mass in the x-direction and zero modal mass in the y-direction are selected, while vice versa applies for shear wave dispersion. This filtering condition considers pure modes and disregards mixed modes of the 2D system.

3.3 Numerical modeling of nonlinear wave propagation

3.3.1 Longitudinal wave propagation

3.3.1.1 Semi-infinite phononic material

Nonlinear wave propagation through semi-infinite phononic materials with periodic contacts [Fig. 2.4(a)] was studied using a time-dependent finite element analysis at specific frequencies. Symmetry boundary conditions are applied on the top and bottom edges of the finite element model [Fig. 3.2(a)], which ensured a perfect impedance match for longitudinal waves at these edges (i.e. no side reflections) to best approximate an infinite medium in the $y-$direction. The height of the geometry is considered the same as the wavelength

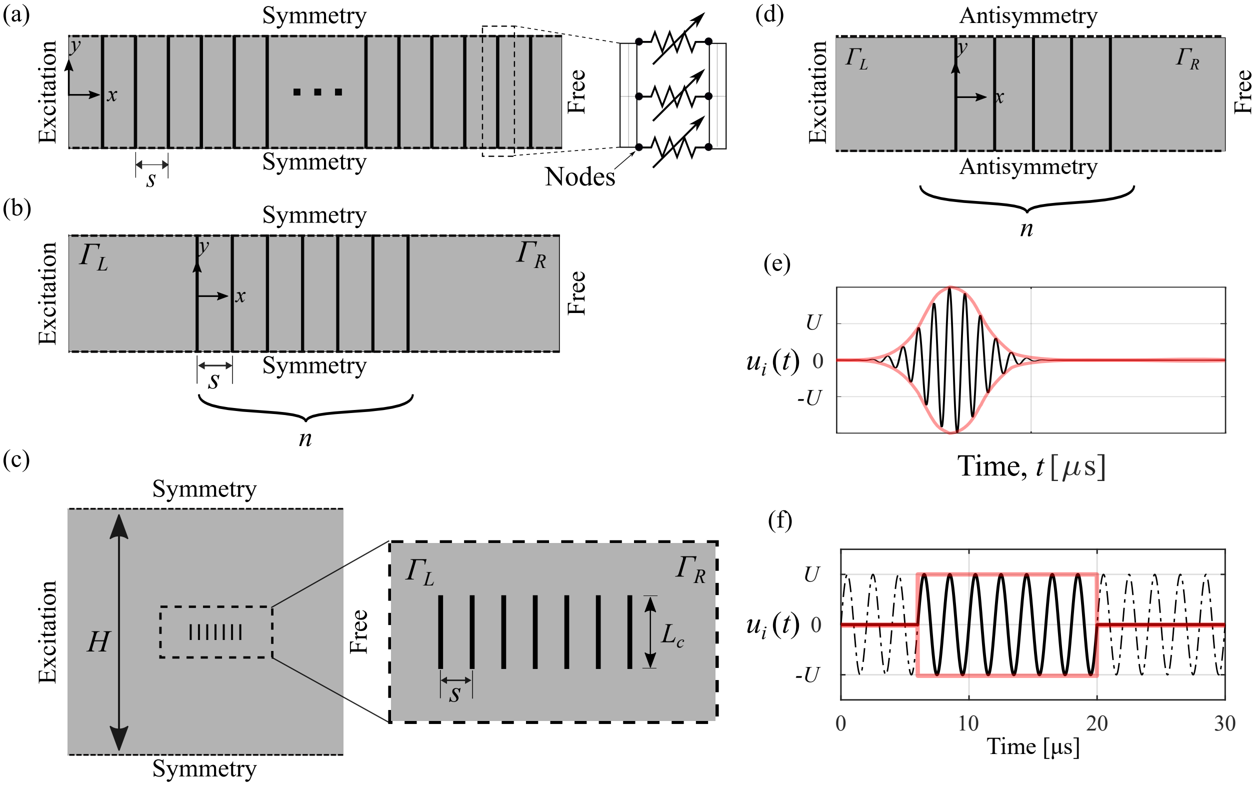

Figure 3.2: Finite element models of nonlinear wave propagation through phononic materials with rough contacts. Longitudinal wave propagation model for (a) semi-infinite, (b) finite, and (c) finite with embedded contacts phononic material. The inset in (a) illustrate contact boundary conditions as nonlinear springs decoupling adjacent layers at mesh nodes. (d) Shear wave propagation through finite phononic materials. Excitation of (e) longitudinal waves as Gaussian-modulated tone bursts and (f) shear waves as wave packets with a finite number of cycles of equal amplitude. Red curves in (e) and (f) denote Gaussian and rectangular modulation of harmonic waves, respectively.

of the fundamental (input) wave to help visualize wave propagation color plots in post-processing software; however, any finite height with symmetric boundary conditions would suffice. While a large number of layers (a few hundred) are considered in the model, the simulation was conducted until the wave reaches the right-most layer with a traction-free boundary condition. However, the wave propagation is analyzed within the first few layers only, to avoid the influence of any reflections from the right-end boundary, approximating $x-$directional wave propagation in an infinite phononic material. The contacts are modeled through nonlinear thin elastic layers, which are spring-equivalent zero-thickness boundary conditions that decouple adjacent elastic layers [inset of Fig. 3.2(a)]. These boundary conditions are in-built into COMSOL with nonlinear spring characteristics explicitly specified as Eq. (2.2) for weakly nonlinear and Eq. (2.3) for strongly nonlinear analysis.

3.3.1.2 Finite phononic material

Nonlinear wave propagation through finite phononic materials is also modeled [Fig. 3.2(b)], in particular, phononic materials with $n = 100$ and 10. The total length of the phononic materials with 100 layers is larger than the spatial length of the excited tone burst used in the finite element simulation, and therefore explicitly clarifies the individual effects of nonlinearity and finiteness. The phononic material with 10 layers, which is smaller than the spatial length of the excited tone burst, is studied to understand the overlapping effects of nonlinearity and finiteness, i.e. how boundary reflections interact with the incident wave inside the phononic material. A special case of a single contact between semi-infinite layers is also studied to understand the effect of periodic contact arrangement on wave propagation. The lengths of semi-infinite bulk layers (Γ_L, Γ_R) are carefully chosen such that the reflections from the left and right boundaries of the finite element model do not re-enter the phononic material, i.e. the model is simulated until the wave reaches the ends of the geometry. An excitation signal from the left boundary is used as an incident wave entering the finite phononic material, as there is no damping, diffraction, or dispersion in Γ_L such that the amplitude and shape of the input signal are retained up until the first contact in the phononic material.

3.3.1.3 Finite phononic material with embedded contacts

The finite element setup of nonlinear wave propagation through finite phononic materials with embedded contacts of length, L_c, is the same as Section 3.3.1.2, except the height, H, is increased to avoid wave reflections from the top and bottom boundaries [Fig. 3.2(c)]. This is because the interaction of the incident wave with the edges of the embedded contacts generates scattered waves, which could reflect and re-enter the phononic material obscuring the analysis of generated nonlinear amplitude. Different arrangements of embedded contacts are also studied to explain the effect of the surrounding continuum on wave propagation.

3.3.1.4 Numerical parameters

The finite element parameters such as mesh size, time step, and type of excitation in the above phononic material models are selected based on the type of analysis conducted and the nature of nonlinearity studied.

The mapped quad-meshing with quadratic serendipity shape function is used. The mapping generates uniform meshing throughout the model avoiding any localized effect from sudden changes in mesh distribution. In weakly nonlinear analysis, the maximum element size in the model is kept at least eight times smaller than the smallest wavelength of interest [125], i.e. $\Delta x_1 = c_p/(8 \times 2f)$, where the smallest wavelength is defined by the second harmonic frequency, $2f$ (i.e. the largest frequency of interest in the simulations) and the corresponding phase velocity, c_p, of the dispersive system at $2f$. The phase velocity is evaluated as the secant of the dispersion curve of the linear phononic material at a given frequency. When $2f$ is in the band gap, the minimum phase velocity of the linear dispersive system is used, which occurs at the lower band edge frequency of the first band gap. At least four elements per layer are also ensured to capture layer deformation, i.e. $\Delta x_2 = s/4$. In strongly nonlinear analysis, the element size in the model is determined based on the minimum number of elements required to capture: 1) wave propagation results and 2) elastodynamics effects of layers. To satisfy the first criteria, the element size in the model was kept eight times smaller than the smallest wavelength of interest [102], i.e. $\Delta x_1 = \lambda_{ff}/8$, where the smallest wavelength, λ_{ff}, is defined by the first free-free acoustic resonance of the layers, $f_{free-free}$ (i.e. the largest frequency of interest in the simulations) and the bulk phase velocity, c_L. To satisfy the second criterion, at least four elements per layer were ensured, i.e. $\Delta x_2 = s/4$. Thus the element size, Δx, in both the model is min $(\Delta x_1, \Delta x_2)$. It is confirmed that there is a negligible increase in the accuracy of the numerical results with a further increase in the number of elements per wavelength.

The PARDISO direct time-dependent solver with generalized alpha time stepping is implemented, and the Courant–Friedrichs–Lewy (CFL) number of 0.2 is used to achieve convergence while solving the partial differential equations numerically [126]. The time step, Δt, according to CFL in the simulations is $\Delta t = [CFL\times$

$\min(s/4, \Delta x)]/c_p$. Damping in the model is ignored, given the metal material and short wave propagation distance. Further, diffraction was neglected as a plane wave is excited in these models.

A Gaussian-modulated longitudinal tone burst at a center frequency, f, is excited [Fig. 3.2(e)] from the entire left edge of the model. This type of excitation is common in experiments at ultrasonic frequencies where internal rough cracks have been studied [127]. Further, the modulation ensures the excitation is narrow-band, which is useful for studying additional frequencies generated due to contact nonlinearity. The wave excitation in the form of Gaussian modulated burst is defined as

$$u_i(t) = U \sin(2\pi f t) G_f(t), \tag{3.7}$$

where U is displacement excitation amplitude, t is time, and G_f is the Gaussian function in time domain such that,

$$G_f(t) = \exp\left[-\left(\frac{t-\zeta}{\psi}\right)^2\right], \tag{3.8}$$

where ψ, and ζ are the Gaussian parameters controlling the length and mean of the time-domain tone burst, respectively (i.e. controlling the number of cycles in the tone burst). In weakly nonlinear analysis the number of cycles is crucial as it determines the band of excited frequencies, Δf, and therefore of the nonlinearly generated frequencies. In the strongly nonlinear regime, this governs the number of collisions of rough surfaces (discussed later in Chapter 6).

3.3.2 Shear wave propagation

To study 1D strongly nonlinear shear wave propagation through rough contacts, a coupled analytical-finite element model [Fig. 3.3] is employed, as adopted from [114], [128]. Specifically, the Jenkins friction law - an analytical model with experimentally-informed properties [refer to Fig. 2.3 and Eq. (2.14)] - is externally solved in MATLAB and linked to finite element analysis of wave propagation in commercial software COMSOL Multiphysics. The wave propagation is analyzed as a time-dependent study. Effectively, the boundary conditions required at the contact interfaces in a time-dependent study are obtained externally through the friction model at each time step. To capture the effects of hysteresis, the force history is stored and re-used at each time step to evaluate the current forces.

The finite element model is similar to the one for nonlinear longitudinal waves through finite phononic materials (Section 3.3.1.2) but modified to carefully account for the effects of friction-induced nonlinear responses [Figs. 3.2(d)]. Two different configurations of this system are studied: (1) with a single rough contact and (2) with an array of n contacts spaced apart at a distance of s from each other (referred to as phononic material). To model a 1D shear wave propagation, a two-dimensional (2D) plane strain framework is employed by applying antisymmetry boundary conditions on the top and bottom edges of the model. These conditions ensured a perfect impedance match for shear waves propagating in the $x-$direction at these edges (i.e. no side reflections). The simulations were ended even before the transmitted and reflected waves reaches the right and left boundaries of the model to avoid the influence of any reflections, eventually making the waveguides (Γ_L, Γ_R) act as infinite in the $x-$direction. The contact deformation and force information is coupled to the Jenkins friction model through MATLAB Livelink at each time step.

Again, the mapped quad-meshing with the quadratic serendipity shape function is used. The element size, Δx, in the model is determined based on the minimum number of elements required to capture (1) nonlinear wave propagation results and (2) elastic deformation in-between array of contacts. To satisfy the first criterion,

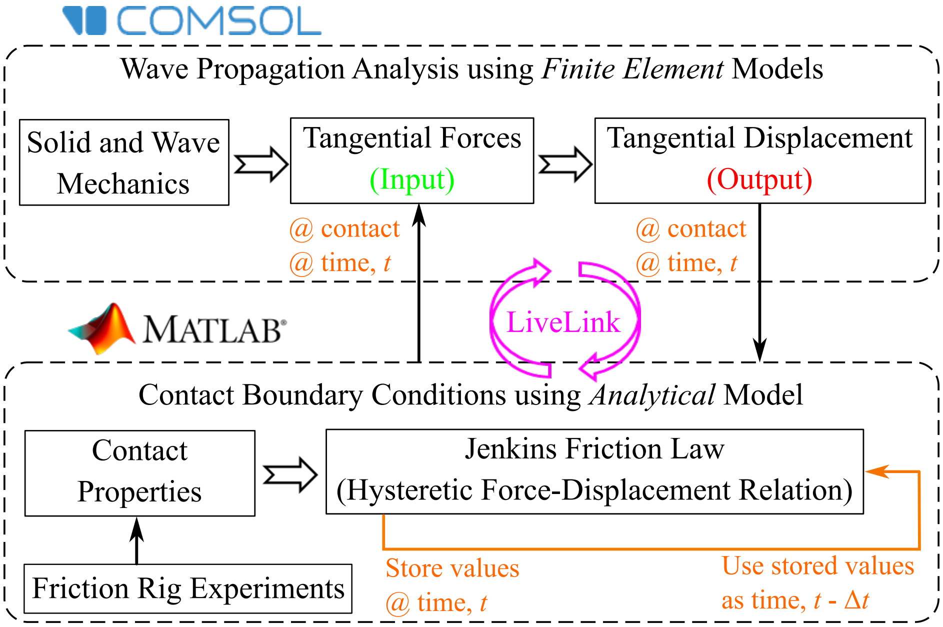

Figure 3.3: Coupled finite element-analytical model informed by experimental contact properties for nonlinear shear wave propagation through periodic contacts.

the element size in the model was kept eight times smaller than the smallest wavelength of interest [102], i.e. $\Delta x_1 = \lambda_{3f}/8$, where the smallest wavelength, $\lambda_{3f} = c_p/3f$, is defined by the third harmonic frequency, $3f$, and the shear phase velocity, c_p, of the system. c_p is the phase velocity of the shear bulk wave (c_s) for the non-dispersive system (i.e. of a single and two contacts) and taken at the band gap edge frequency for the dispersive system (i.e. of an array of contacts), where $c_p(f)$ is minimum. The third harmonic is the strongest higher harmonic generated from friction and can affect the amplitudes of fundamental (originally-excited) frequencies, hence it is used as a criterion to depict the accuracy of the model to capture nonlinear frequency conversion. To satisfy the second criterion of the element size, at least four elements between successive contacts are considered, i.e. $\Delta x_2 = s/4$. Effectively, the element size in the model is $\min(\Delta x_1, \Delta x_2)$. The solver and time step are selected based on the criteria listed in Section 3.3.1.4 but evaluated by taking into account the mesh size required for shear wave propagation. This time step is enough to capture nonlinear wave responses and stick-slip transition of the contacts with reasonable computational time. Further decrease in time step changes the third harmonic amplitude and energy dissipation by $< 0.1\%$ only. No inherent damping is assumed in the model due to the metal material and short wave propagation distance. Further, diffraction was neglected as a plane wave is excited in the model. Overall, the only source of damping and hysteresis in the model is the frictional behavior of the contact.

The contact interfaces are assumed to be in a state of constant normal stress, σ_0, such that $\sigma_0 < 0$, before the incident shear wave strikes the interface. Shear wave packets at a frequency, f, is excited from the entire left edge of the FE geometry. This type of excitation is common in experiments, where shear wave interactions with internal cracks have been studied [122], [129]. The wave excitation in the form of a wave packet [Fig. 3.2(f)] is defined as

$$u_i(t) = U \sin(2\pi f t)\chi(t), \tag{3.9}$$

where U is displacement excitation amplitude, and χ is the rectangular function in time-domain expressed as,

$$\chi(t) = \begin{cases} 1, & n_1/f \leq t \leq n_2/f, \\ 0, & t < n_1/f, t > n_2/f, \end{cases} \tag{3.10}$$

where n_1 and n_2 dictate the wave packet start and end time instants such that $n_2 - n_1$ corresponds to the number of cycles in the packet. Simulations with both a single and finite number of cycles are conducted. Single-cycle pulse facilitates the demonstration of programmable functionality as it enables the excitation of a number of pulses in sequence over a short duration of time. Single-cycle excitation also corresponds to wide-band frequencies, which allow the study of transmission characteristics of the phononic material. In contrast, a finite number of cycles facilitates the selection of a steady-state portion of the signal for better signal post-processing and even ensures a narrow-band frequency excitation that can reveal additional frequencies generated due to the contact nonlinearity. Thus, a finite number of cycles are used while illustrating the underlying mechanics of wave-contact interactions. A smoothing window over a short time interval is applied at the start and end of the wave packet to suppress any transient effects from the sudden wave excitation.

3.4 Summary

This chapter presented modeling of linear and nonlinear wave propagation through continuum phononic material with rough contacts. Specifically,

1. Linear dispersion relations of both pure longitudinal and shear waves were obtained through Bloch analysis. Both analytical and finite element approach for dispersion calculation is presented.
2. Finite element model of nonlinear longitudinal wave propagation and hybrid analytical-finite element model of nonlinear shear wave propagation through these phononic materials is also presented.
3. To ensure accurate simulations of nonlinear phenomena, several crucial numerical parameters such as mesh size, time step, solver type, and excitation type were carefully considered and discussed.

Chapter 4

Weakly nonlinear wave dynamics

This chapter presents nonlinear longitudinal wave propagation through continuum phononic materials when rough contacts are strongly precompressed (weakly nonlinear). It begins by examining wave-self interactions and subsequently explores wave-wave interactions. In wave-self interaction, the linear dispersion and band gaps of the material are presented first. Then, the evolution of propagating nonlinear waves is illustrated, emphasizing the generation of zero (DC), self-demodulated low, and second harmonic frequencies for excitation in different zones of the dispersion. The combined effects of nonlinearity, periodicity, and finiteness on wave amplitudes are also reported. Furthermore, the impact of discrete-continuum coupling on nonlinear wave propagation is demonstrated through the study of various arrangements of embedded contacts. Moving on to wave-wave interaction, the chapter delves into the nonlinear effects resulting from wave mixing in phononic materials. Finally, a contact-based phononic diode is designed as an application of wave mixing, and its broadband nonreciprocal characteristic is presented. The contents of this chapter have been adapted from various sections of my published articles, [102] (associated with wave-self interactions) and [103] (associated with wave-wave interactions), which were written as part of the research for this dissertation.

4.1 Wave self-interactions

In contrast to linear materials, nonlinear materials exhibit properties where the response is not directly proportional to the applied stimulus. Consequently, the interaction of waves with these nonlinear materials can give rise to additional waves through nonlinear processes, known as "wave self-interactions". A typical feature of wave self-interaction is the generation of higher harmonics. In a material with quadratic nonlinearity, both even and odd-order harmonics are generated while cubic nonlinearity generates odd harmonics only. This research introduces a continuum phononic material that possesses distinct characteristics, including local nonlinearity arising from contacts and the presence of layers between successive contacts, which create alternative linear-nonlinear media. Therefore, the subsequent sections of this study (Section 4.2 to 4.6) investigate the wave-self interaction within these phononic materials, and the role of these unique features on nonlinearly generated frequencies.

A normalized precompression parameter, η, is introduced as the ratio of the linear contact stiffness, κ_1, to the stiffness per unit length of the layer, $(\lambda^{(L)} + 2\mu^{(L)})/s$, where $\lambda^{(L)}$ and $\mu^{(L)}$ are the Lame parameters of the material. Consequently, η increases with precompression. This study focuses on systems where $\eta > 1$, indicating that the layer stiffness (for layer width, $s = 3.175$ mm) is smaller than the contact stiffness. Such

Ω	f [MHz]	ψ	ζ	Δf [MHz]
0.153	0.10	$2.5/f$	$7.5/f$	± 0.04
0.384	0.25	$2.5/f$	$7.5/f$	± 0.09
0.614	0.40	$5/f$	$15/f$	± 0.08
1.228	0.80	$5/f$	$15/f$	± 0.15

Table 4.1: Gaussian parameters of the simulated tone burst. Ω is the excitation frequency normalized by the lower edge frequency of the first band gap for $\eta = 1.863$.

a case allows for non-trivial deformation in the elastic layers and enables the examination of the effects of discretely-generated nonlinear waves on the modes of the linearly elastic layer. It is worth noting that the wave propagation is studied within the weakly nonlinear regime, specifically, $U < \delta_0$. Throughout this chapter, all presented cases correspond to $U/\delta_0 = 0.15$ (i.e. $U = 5$ nm). Finite element analyses, as detailed in Section 3.3.1 of Chapter 3, are performed to extract the wave displacement, $u(x, t)$, for all times, spatially at $y = 0$ and along discrete positions x, specifically at five equally-spaced locations within each layer. The results are sampled at the same rate as the time step, Δt, which ensures the sampling frequency is more than twice the Nyquist frequency to avoid aliasing. The discrete fast Fourier transform (FFT) of the extracted time signal is taken in MATLAB to study the frequency content of the signal. Table 4.1 summarizes Gaussian parameters of the simulated tone burst. The amplitudes of nonlinearly-generated frequencies are extracted from these FFT plots. To filter out the specific frequency components in the analysis, a Chebyshev Type-II filter with ripple values of 10dB for the pass band and 50dB for the stop band are used.

4.2 Linear dispersion

The dispersion curves of the phononic material for precompression, $\eta = 1.863$ (i.e. $p_0 = 1$ MPa), $\eta = 5.892$ (i.e. $p_0 = 10$ MPa), and $\eta = 58.92$ (i.e. $p_0 = 1$ GPa) are shown in Fig. 4.1. Non-dimensional frequency, Ω, is obtained by normalizing frequencies by the lower edge frequency of the 1st band gap at $q = \pi/s$ for $\eta = 1.863$ (i.e. $f = 0.65$ MHz). There exist pass bands, for example, $\Omega < 1$ as well as band gaps, for example, $1 < \Omega < 1.49$ for $\eta = 1.863$. These band gaps result from Bragg scattering, which is triggered due to the periodic arrangement of contacts. It is worth noting that granular crystals as dictated by Hertzian law exhibit band gaps at frequencies two orders smaller than these phononic materials for the same length scale and bulk material [71]. Further, the high-frequency end of both acoustic and optical modes of the phononic material shifts upwards with an increase in precompression while reducing the width of the band gap. Physically, this dependence corresponds to the variable contact area. An increase in precompression increases the overall contact area due to the deformation of the asperities, which subsequently reduces the impedance mismatch at the contacts and decreases the band gap width. At extreme precompression ($\eta = 58.92$), band gap width narrows significantly. Eventually, the band gaps vanish at an infinite precompression since complete deformation of the asperities results in perfect contact between the adjacent layers. Thus, there exists both stress and displacement continuity across the interface and the phononic material effectively behaves as a homogeneous continuum. These results show the filtering capability of rough contact-based phononic materials that can be tuned through applied precompression. The zones of exact [$\Delta q = q(2\Omega) - 2q(\Omega) = 0$] and approximate [$\Delta q \neq 0$ but smaller] phase matching between the fundamental and second harmonic waves due to the dispersive acoustic passband are also observed [Fig. 4.1(b)]. The effect of these dispersive regimes and band gaps on nonlinear wave propagation is discussed in the following sections of the chapter.

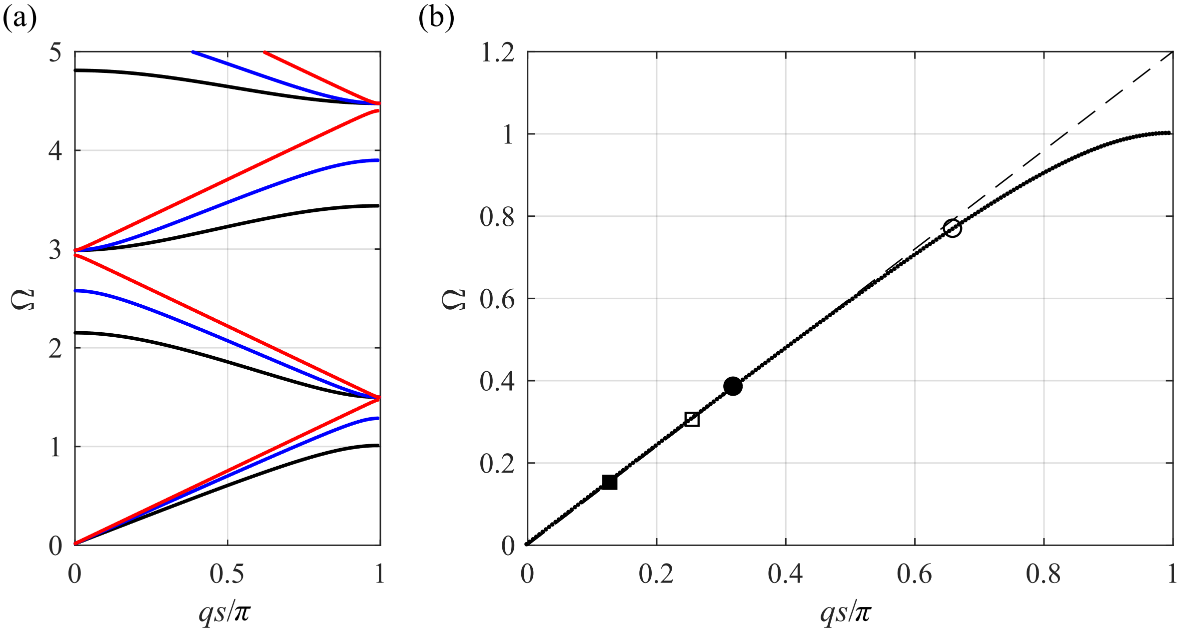

Figure 4.1: (a) Linear band diagrams for precompression, $\eta = 1.863$ - black, $\eta = 5.892$ - blue, and $\eta = 58.92$ - red. (b) Zoomed view of the acoustic passband of (a) for $\eta = 1.863$. Fundamental frequency (filled markers) and corresponding second harmonic (empty markers) show two cases: exact (square) and approximate (circle) phase matching. The dashed line is a long-wavelength asymptote.

4.3 Wave evolution with propagation distance

In this section, how a wave packet evolves through semi-infinite and finite phononic materials is studied. This evolution is presented for precompression, $\eta = 1.863$ and excitation frequency, $\Omega = 0.384$ corresponding to the acoustic passband (Fig. 4.2). One of the main characteristics observed here is an increase in the static offset of a propagating harmonic wave.

In semi-infinite phononic materials, the static offset increases with increasing propagation distance [Fig. 4.2(a)]. This offset is generated due to the asymmetric potential [Fig. 2.2(b)] at the contact, i.e. the nonlinear springs representing contacts have larger deformation under tension than compression for a given force. Thus, when the propagating wave interacts with the contacts, the tensile force causes expansion (static repulsive movement) of the contacting surfaces resulting in a positive offset in the wave [Fig. 4.2(a)]. This offset is much smaller than δ_0 and does not result in complete separation (or opening) of contacts. As the wave propagates in the positive direction, the interaction with the next contact further increases the offset in the same way. Thus, the asymmetry of the wave increases monotonically as it propagates through the phononic material [Fig. 4.2(a) $t_1 - t_2 - t_3$]. This asymmetry, attributed to the contact expansion, also counteracts the external precompression and results in spatially varying contact pressure. Further, the asymmetry that locally shifts the average position of each layer in this phononic material is reminiscent of "acoustic dilation", i.e. constant strain produced in a periodic chain as observed in the α-Fermi-Pasta-Ulam lattice [130]. Importantly, the offset travels with the wave while the layers retain their initial equilibrium position.

In finite phononic materials, the wave packet evolution in terms of the static offset is more complex. The boundaries of the phononic materials, which are also rough contacts, give rise to multiple nonlinear reflections [Fig. 4.2(b) $t_1 - t_3$]. For example, the reflected wave from the first contact contains a negative offset [zoomed view of Fig. 4.2(b) t_1, t_2] as a competing effect of the positive offset in the transmitted wave. These offsets

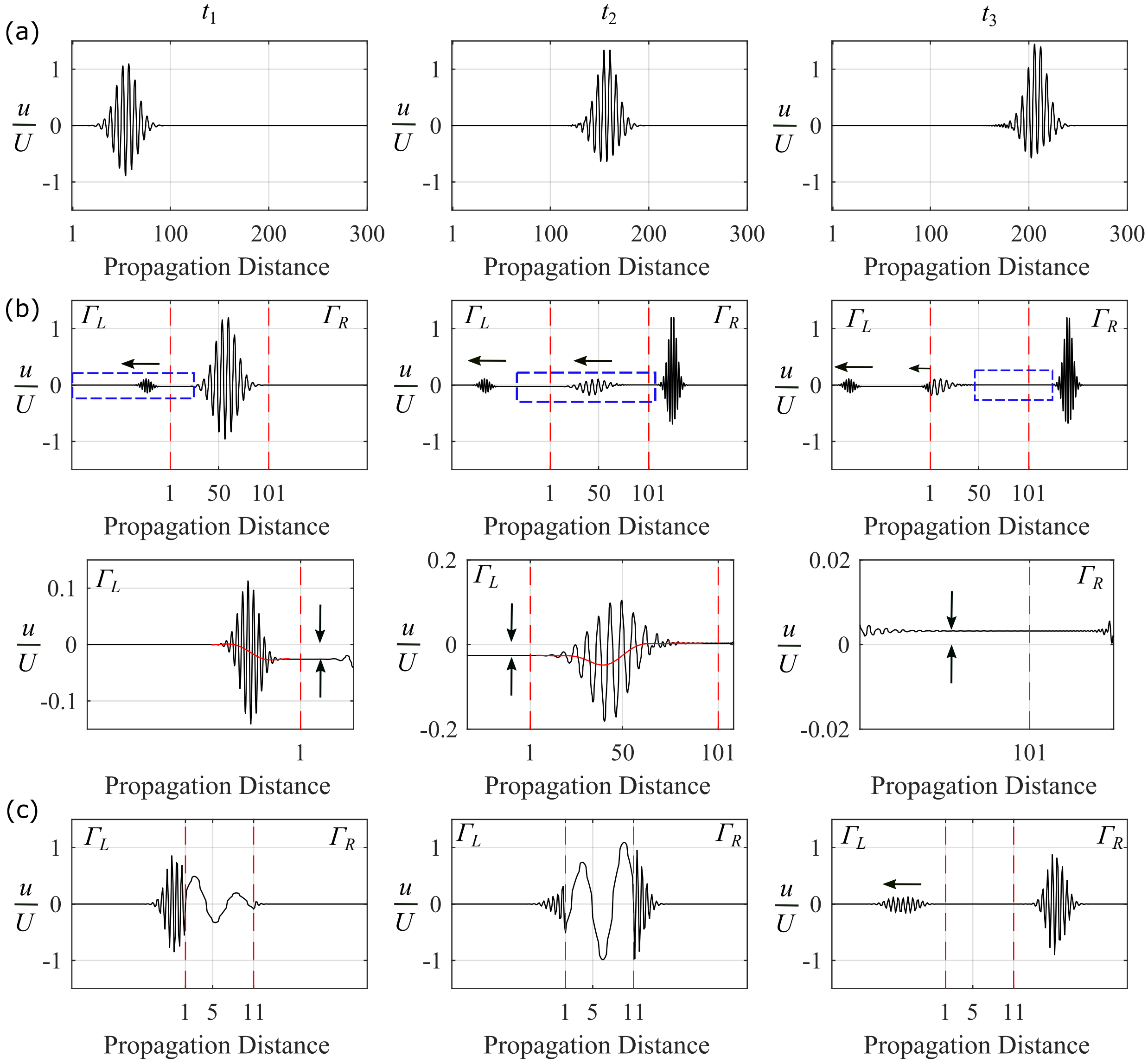

Figure 4.2: Normalized wave displacements, u/U, inside (a) semi-infinite, and finite phononic materials with (b) 100 and (c) 10 layers at three different time instants ($t_1 - t_3$ column-wise), when excitation frequency is in the acoustic passband. Red dashed lines are the boundaries of the finite phononic materials while the $x-$labels correspond to the contact indices. Zoomed images of the blue rectangles are shown below the plots. The effect of finiteness and nonlinearity on the wave packet can be seen through the generation of reflected waves (indicated by horizontal arrows), static offset (indicated by vertical arrows), and long-wavelength spatial wave (solid red line). Note: the horizontal axis scales of semi-infinite layers (Γ_L, Γ_R) and phononic materials are different in (b) and (c) to visualize the entire finite phononic material.

can be considered as a spatially-dependent long-wavelength component [solid red line in Fig. 4.2(a)-(b), a feature of nonlinear wave propagation useful to estimate the contact power-law via inverse problem [131]. Further, the layers do not retain their original equilibrium position once the wave propagates through them [zoomed view of Fig. 4.2(b) t_1 – note the negative displacement inside the phononic material]. This effect of wave interactions with the finite boundaries of the phononic material can be understood in the following way: The right boundary of the left semi-infinite bulk layer, Γ_L, (i.e. $x = 0$) moved to the left (i.e. at $x < 0$) due to the negative offset formed by the backward propagating reflected wave. This creates a gap between the semi-infinite layer, Γ_L, and the first layer of the phononic material. When the propagating wave interacts with the second contact, the contact expansion pushes the first layer towards the semi-infinite layer, Γ_L. As a result, the first layer settles to an equilibrium position that is different from its original position, and specifically in the negative $x-$direction. This re-positioning happens successively for each layer [shown in zoomed views of Fig. 4.2(b) t_1] as the wave propagates. At the same time, the positive offset of the forward propagating wave increases as discussed in the previous paragraph. A complementary case happens at the interface between the phononic material and semi-infinite bulk layer Γ_R (i.e. at $x = ns$ with $n = 100$), where the generated reflection travels back into the phononic material leaving behind a positive offset [Fig. 4.2(b) t_3]. Multiple wave interactions happen within and at the ends of the phononic material until the energy completely travels out of the phononic material, however, the effects of later reflections and offsets are smaller. Waves propagating through both semi-infinite layers, Γ_L, Γ_R, remain unchanged due to the absence of nonlinearity in these layers. A similar case would happen in phononic material with 10 layers; however, the effect of finiteness and nonlinearity cannot be easily separated since the length of the phononic material is smaller than the excited signal [Fig. 4.2(c)]. These effects are explained in terms of nonlinear interactions of low-frequency components in the following sections. Apart from static offsets, propagated wave exhibits two effects – 1) a wider envelope due to dispersion, and 2) reduced oscillation amplitude as a portion of the input energy traveled back with the reflected wave. However, these two effects are not visible due to weaker dispersion around $\Omega = 0.384$ [Fig. 4.1(a)] and relatively smaller reflections.

4.4 Nonlinearly-generated frequencies in passbands

In addition to evolving waveform, the contact nonlinearity also give rise to new frequencies, specifically, DC, low frequencies in the vicinity of DC, and a second harmonic. This section presents how the amplitudes of these nonlinearly-generated frequencies depend on propagation distance when they are in the acoustic passband. Key effects from the elastic layers in combination with the discrete nonlinear contacts are elucidated. Further, the role of dispersion on energy transfer between fundamental and second harmonic frequency is also illustrated.

4.4.1 Zero frequency generation

Fig. 4.3 shows the dependence of the DC spectral amplitude, A_0, normalized by the excitation spectral amplitude, A_E, on propagation distance for semi-infinite and finite phononic materials at an excitation frequency, $\Omega = 0.384$ and normalized precompression, $\eta = 1.863$.

4.4.1.1 Semi-infinite phononic materials

For semi-infinite phononic material, A_0 depends linearly on the propagation distance [Fig. 4.3(a)]. This dependence corresponds to the monotonic increase in wave asymmetry (or offset) with propagation distance as discussed in Section 4.3. A similar A_0 dependence is observed in granular crystals with weak quadratic nonlinearity [73], however, the incorporation of the continuum between the contacts in these phononic materials drives an additional dependence of A_0 locally, i.e. within the layers. A_0 decreases gradually inside each layer and then increases again at the next contact [insets of Fig. 4.3(a)]. Such competing effects on A_0 can be attributed to the compressive deformation of the layers due to contact expansion. This local elastic

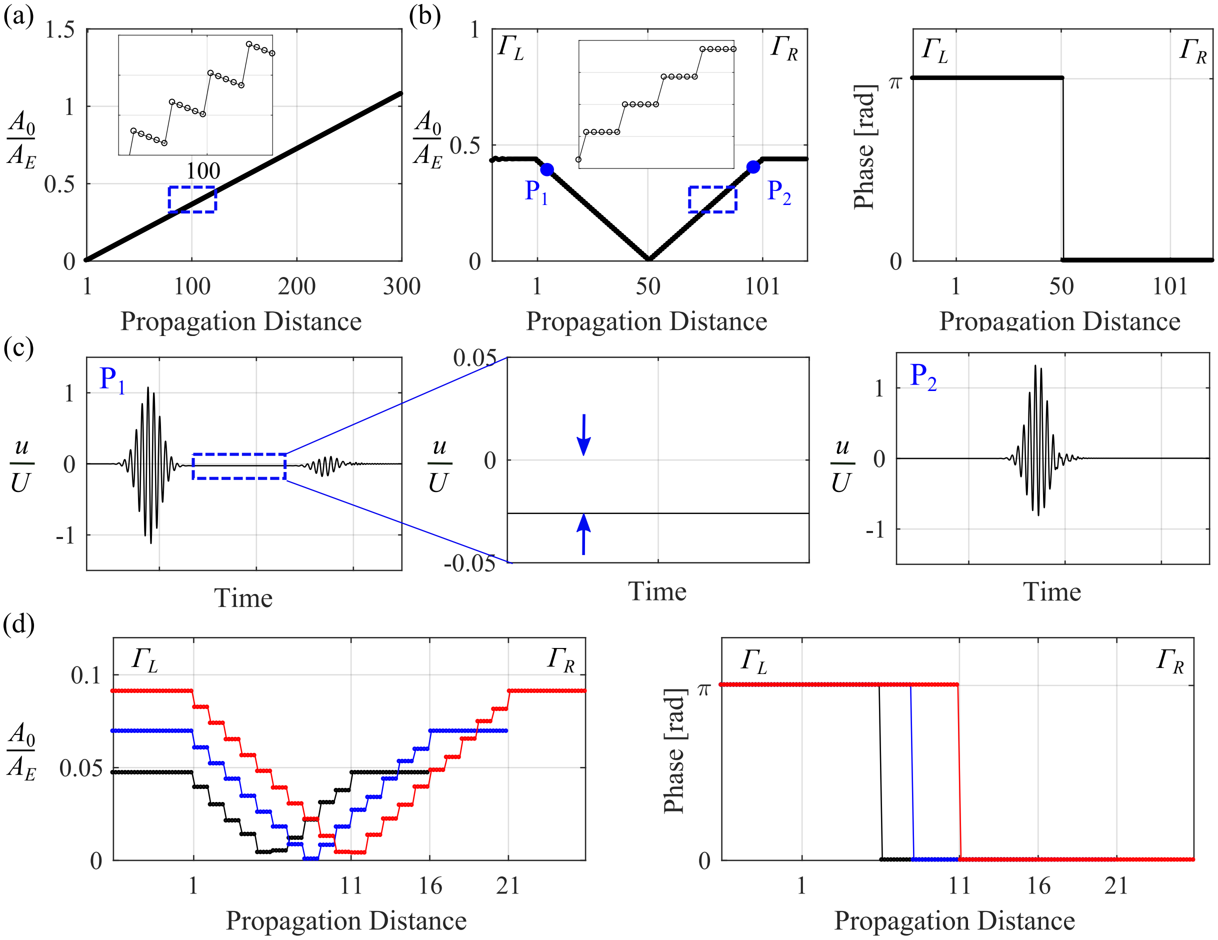

Figure 4.3: Dependence of normalized A_0 on the propagation distance in (a) semi-infinite, and finite phononic materials with (b) 100 and (d) 10 (black), 15(blue), 20(red) layers when excitation frequency is in the acoustic passband. $x-$labels correspond to the contact indices. Insets are zoomed views of blue rectangles indicating the variation of A_0 within layers. Phase (b) and (d) are evaluated at zero frequency. (c) Normalized time-domain wave displacements at representative locations, P_1 and P_2, as shown in (b).

effect is not seen in other phononic materials that assume discrete masses and nonlinear springs, such as granular crystals.

4.4.1.2 Finite phononic materials

The dependence of A_0 on the propagation distance is significantly different for finite phononic materials, as A_0 is maximum at the boundaries of the phononic material [Figs. 4.3(b)-(d)]. This dependence, along with a phase difference of π rad, is equivalent to the linear dependence of A_0 for semi-infinite phononic materials [Fig. 4.3(a)]; however, A_0 takes different value at the first contact i.e. A_0 is negative (since the phase is π rad) for finite phononic materials while $A_0 = 0$ for the semi-infinite phononic materials. We note that A_0 for finite phononic materials is a combined effect of the static offsets of the propagating and reflected waves (as discussed in Section 4.3). To explain this, Fig. 4.3(c) shows the time-signals of the two representative locations ($P_1 - P_2$) of the zones $A_0 < 0$ and $A_0 > 0$ of Fig. 4.3(b), respectively. For the first half of the phononic material, the negative offset generated by the reflected wave dominates the positive offset of the propagating wave resulting in $A_0 < 0$ [P_1 time signal in Fig. 4.3(c)]. However, a monotonic increase in the positive offset with propagation distance eventually dominates in the second half, thus $A_0 > 0$ [P_2 time signal in Fig. 4.3(c)]. A_0 is consistently maximum at the ends and minimum at the center of the phononic materials irrespective of the number of contacts [Fig. 4.3(d)]. As expected, A_0 remains constant outside the phononic material [i.e. inside Γ_L, Γ_R in Figs. 4.3(b) and (d)] due to the absence of nonlinearity in the semi-infinite layers. Interestingly, unlike the semi-infinite phononic material, A_0 is constant within the layers of the finite phononic materials [insets of Fig. 4.3(b)]. This indicates that the layers do not experience compressive deformation, because they re-position themselves to account for the contact expansions.

4.4.2 Self-demodulated low-frequency generation

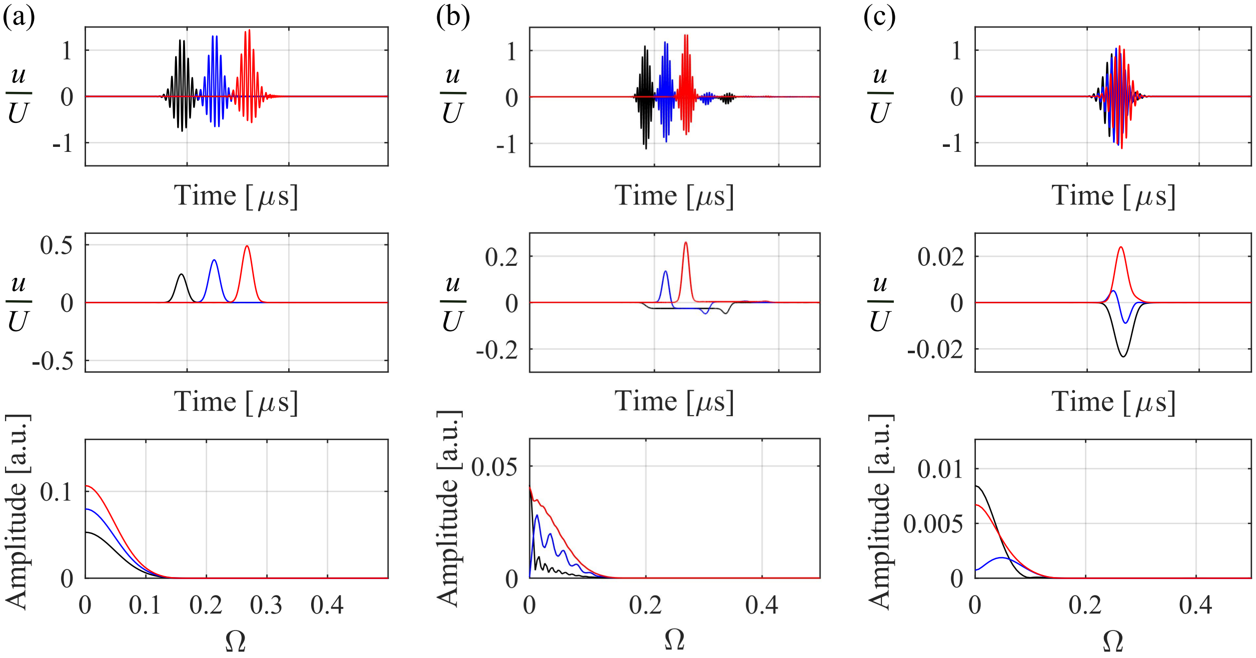

Figure 4.4: Dependence of low-frequency components on the propagation distance in (a) semi-infinite, and finite phononic material with (b) 100 and (c) 10 layers for excitation in the acoustic passband. Top row: normalized time-domain wave displacements recorded at 3 different locations in semi-infinite phononic materials and near the 1st (black), center (blue), and last (red) contacts for finite phononic materials. Middle row: low-frequency filtered normalized time-domain signal with only long-wavelength components. Bottom row: FFT of the filtered signal.

An energy transfer from the fundamental wave to very low frequencies in the vicinity of the DC component is also observed in these phononic materials. This energy transfer is due to the wave self-demodulation effect [132], [133], which is a nonlinear wave mixing between the neighboring frequencies of the narrow yet finite-band (Δf) frequency excitation in the simulations. Due to the proximity of the waves within the excited bandwidth, their mixing generates difference-frequency components at very low frequencies. The propagation of these low-frequency components is analyzed by separating them from the main wave using a low-pass Chebyshev filter (Fig. 4.4). Similar to A_0, this low-frequency amplitude increases monotonically with propagation distance within the semi-infinite phononic materials [Fig. 4.4(a)], highlighting continuous energy transfer to low-frequencies. In the case of finite phononic materials, the recorded signal also contains a reflection from the $x = ns$ boundary of the phononic material, which are the small (secondary) wave packets in Fig. 4.4(b) – top row. Even these reflected waves from the finite boundaries of the phononic material contain low-frequency components, which are the small (secondary) negative humps in Fig. 4.4(b) - middle row. Interestingly, for phononic material with 10 layers, reflected low-frequency components interact with the propagating low-frequency components inside the phononic material [Fig. 4.4(c) – solid blue line]. This interaction results in a low-frequency component that dominates A_0 at certain locations inside the finite phononic material. Recall that the larger spatial width of the wave packet relative to the overall size of the phononic material [Fig. 4.3(c)] enables this interaction that is otherwise absent in the phononic material with 100 layers. This highlights that the wave interaction inside finite phononic materials also depends upon the relative spatial size of the phononic material and excitation signal. These observations will be significant in interpreting experimental wave propagation where finite-band frequency excitation is commonly employed.

4.4.3 Second harmonic generation

To study the second harmonic generation (SHG) and its amplitude dependence on propagation distance, two excitation frequencies, $\Omega = 0.153$ and $\Omega = 0.384$, with normalized precompression, $\eta = 1.863$, are investigated. In both of these cases, the fundamental, as well as the second harmonic waves, are in the acoustic passband since $\Omega < 1$ and $2\Omega < 1$ [Fig. 4.1(a)], however, $\Omega = 0.153$ is associated with the exact phase matching while $\Omega = 0.384$ is an approximate phase match case [Fig. 4.1(b)].

4.4.3.1 Semi-infinite phononic materials

Figs. 4.5(a) and 4.5(b) shows the dependence of the normalized fundamental (A_1) and second harmonic (A_2) wave amplitudes on the propagation distance for the semi-infinite phononic material. For $\Omega = 0.153$ (exact phase matching), a continuous increase in A_2 with propagation distance is observed [Fig. 4.5(a)]. This is an effect of internal resonance (or constructive interference) between the SHG at each contact and the propagating second harmonic wave from prior contacts due to equal phase velocities of the fundamental and second harmonic waves. As a result, there is a continuous energy transfer to the second harmonic frequency. Note that the drop in fundamental amplitude is relatively small due to the weak nonlinearity in the model. For $\Omega = 0.384$ (approximate phase matching), there is a distance-dependent beating of A_2 [Fig. 4.5(b)], due to a phase mismatch between fundamental and second harmonic frequency. Since $V_p(\Omega) \neq V_p(2\Omega)$ [refer Fig. 4.1(b)], the SHG at a contact occurs from the fundamental wave that is propagating with a velocity of $V_p(\Omega)$, however, that generated second harmonic wave then travels to the next contact at $V_p(2\Omega)$. As a result, the forward propagating second harmonic wave interacts with discretely generated second harmonic wave efficiently, but only up to a certain distance. The continuous change in the relative phase between generated and propagating second harmonic waves eventually results in destructive interference and thus a beating of second harmonic frequency.

Interestingly, both A_1 and A_2 are higher inside the layers and gradually drop near the contacts [insets of Figs. 4.5(a) and (b)], possibly a case of wave interference inside the layers. Note that the amplitude variations within layers are higher compared to the amplitude variations across the contacts. This indicates that the elastic deformations of the layers influence the nonlinear waves generated at the contacts, even though the layers themselves do not contain nonlinearities. Such spatial variations in the nonlinear amplitude have not been observed in other nonlinear phononic materials where only discrete masses are considered, such as granular crystals, e.g. [134].

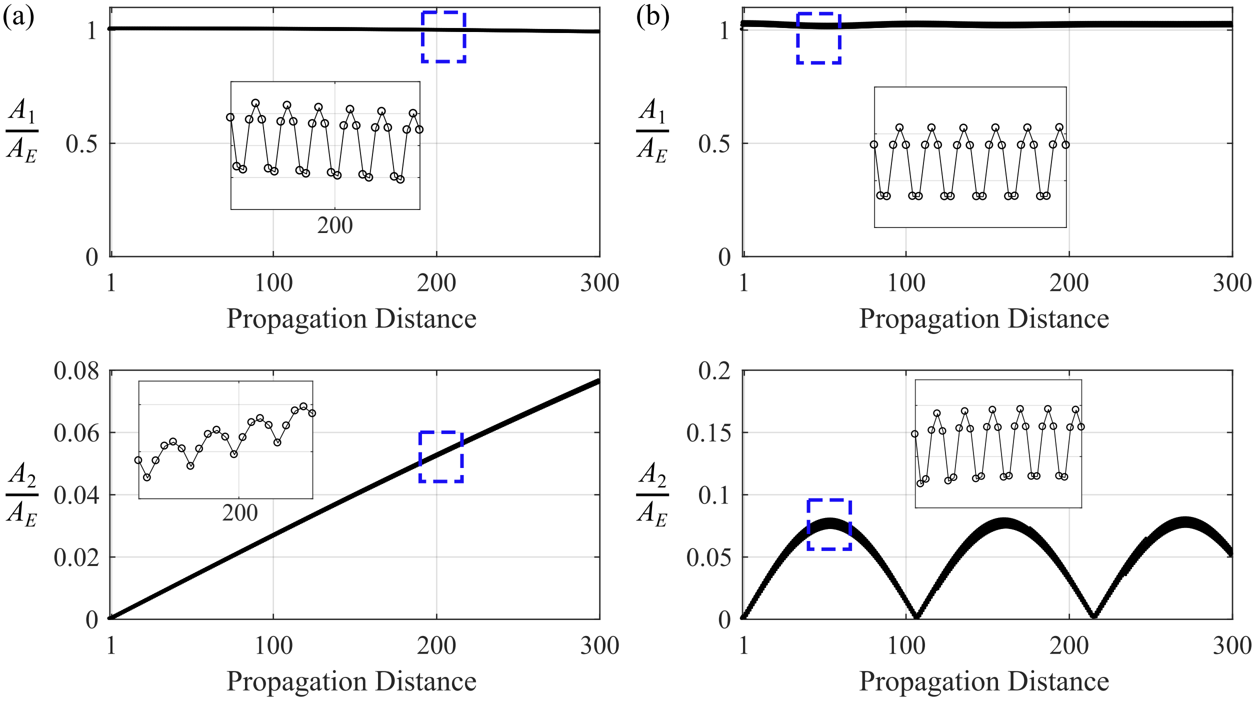

Figure 4.5: Dependence of normalized A_1 and A_2 on propagation distance in semi-infinite phononic material for excitation frequency (a) $\Omega = 0.153$ – exact phase match and (b) $\Omega = 0.384$ – approximate phase match condition. Both the excitation and second harmonic frequencies are in the acoustic passband. The $x-$labels correspond to the contact indices. Insets are zoomed views of blue rectangles showing amplitude variation within layers.

Importantly, these phononic materials can tune the second harmonic amplitude as well as the location where they are maximum or minimum through applied precompression. As discussed, the distance-dependent beating of A_2 is a combined effect of the nonlinear interaction and dispersive nature between the fundamental and second harmonic frequency. Since the dispersion of these phononic materials depends on applied precompression, the beating periods, $2\pi/\Delta q$ of the second harmonic wave can be modulated by controlling the condition of phase matching between the fundamental and second harmonic waves (Fig. 4.6). For example, for precompression, $\eta = 1.863$, A_2 beating is observed in the 108th, 216th, . . . layers whereas, for $\eta = 2.635$, the beating is in the 168th, 336th, . . . layers for $\Omega = 0.384$.

4.4.3.2 Finite phononic materials

For finite phononic material with 10 layers, normalized A_1 and A_2 are related to mode shapes of the phononic material at corresponding frequencies (Fig. 4.7). The dependence of A_1 on propagation distance reveals the structural mode of the finite phononic material at Ω. The dependence of A_2 on propagation distance reveals the combined effect of SHG from the contact nonlinearity plus the structural mode of the finite phononic material at 2Ω. Since this finite phononic material is small compared to the beating length, i.e. $\Delta q L \ll 2\pi$, where L $(= ns)$ is the length of the finite phononic material, there is a cumulative increase in A_2 even for the case of approximate phase matching. Unlike granular crystals, A_1 and A_2 also depend on the individual modes of the layers; note this effect is more visible at higher frequencies, e.g. at $\Omega = 0.384$ [Fig. 4.7(b)]. The elastic deformation of the layers becomes significant when the wavelength is comparable to the layer

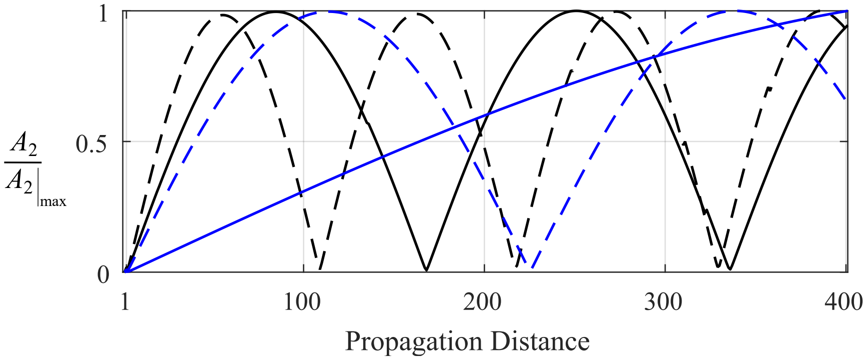

Figure 4.6: Second harmonic amplitude beating for precompression of $\eta = 1.863$ – dashed black, $\eta = 2.282$ – solid black, $\eta = 2.635$ - dashed blue, and $\eta = 5.893$ – solid blue for fundamental frequency $\Omega = 0.384$. $X-$labels are layer indices.

thickness. As a result, we observe noticeable amplitude variation when a discretely generated wave propagates through the continuum for $\Omega = 0.384$. This further confirms the significance of the continuum between successive contacts at frequencies close to the modal frequencies of individual layers. The dependence of A_2 on propagation distance within the finite phononic material with 100 layers (not shown) is a combination of modal behavior and beating.

4.5 Nonlinearly-generated frequencies in band gaps

With an understanding of DC, low, and second harmonic frequency generation and their propagation in the acoustic passband, this section presents their characteristics for two other cases: (1) when the fundamental frequency is in the pass band but the second harmonic in the band gap, i.e. $\Omega = 0.614$ and (2) when both fundamental and second harmonic frequencies are in the band gap, i.e. $\Omega = 1.228$. Semi-infinite and 10-layer finite phononic material with normalized precompression, $\eta = 1.863$ is considered.

4.5.1 Semi-infinite phononic materials

For, $\Omega = 0.614$ (i.e. Ω in passband but 2Ω in the band gap), the fundamental wave propagates through the phononic material. Thus, it interacts with contacts and generates A_0 that depends linearly on propagation distance [Fig. 4.8(a)]. This indicates that A_0 generation primarily depends upon the fundamental wave propagation and its interaction with contacts. Interestingly, the dependence of A_2 on propagation distance is different from that of the exact or approximate phase match condition: there is neither a linear increase nor beating of the second harmonic wave, rather, A_2 increases only in the first few unit cells and then remains constant [Fig. 4.8(a)]. This is because the second harmonic frequency is in the band gap. The fundamental wave interacts with each contact, generating a second harmonic wave; however, these nonlinear waves are blocked from propagating beyond the unit cell as they lie in the band gap. Remarkably, the second harmonic amplitude in these phononic materials is maximum inside the first few layers and gradually decreases to a constant mean value, unlike granular crystals where A_2 is reported to increase to a value and then remain constant [73]. This difference in A_2 characteristics is because the phononic material here contains continuum elastic layers between the discrete nonlinear contacts. For $\Omega = 1.228$ (i.e. both Ω and 2Ω in band gaps), there exist only evanescent waves, causing energy localization within the first few unit cells of the phononic

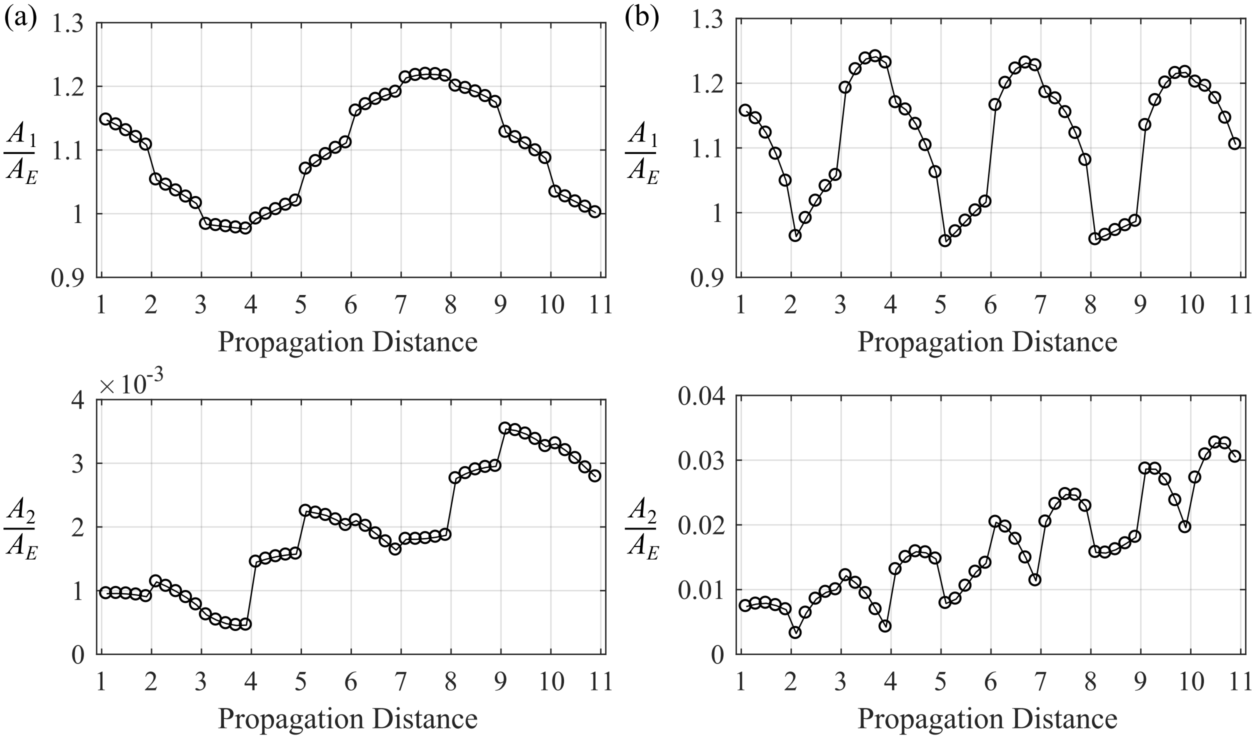

Figure 4.7: Dependence of normalized A_1 and A_2 on propagation distance in a finite phononic material with 10 layers for excitation frequency (a) $\Omega = 0.153$ – exact phase-match and (b) $\Omega = 0.384$ – approximate phase-match condition, and normalized precompression, $\eta = 1.863$. $X-$labels indicate contact indices.

material [Fig. 4.8(b)]. These localized fundamental waves still generate A_0 that causes static deformation through the phononic material. This result shows that these phononic materials with dynamic excitations in the band gap can still experience static deformation. Note that there is no further generation of A_0 at later contacts due to the decayed fundamental wave.

Similar to A_0, low-frequency generation depends upon the propagation and interaction of the fundamental wave. Thus, the low-frequency component increases monotonically with propagation distance for $\Omega = 0.614$ [Fig. 4.8(c)]. However, for $\Omega = 1.228$, the self-demodulation effect and therefore low-frequency generation occurs only in the first few contacts. This low frequency can still propagate through the phononic material as it lies in the pass band [Fig. 4.8(d)]. No further generation (or monotonic increase in amplitude) of low-frequency components is seen due to the decayed fundamental wave.

4.5.2 Finite phononic materials

For $\Omega = 0.614$ (i.e. Ω in pass band but 2Ω in band gap), A_0 is generated at all contacts due to the propagating fundamental wave. Its dependence on propagation distance is similar to the case when both the fundamental and the second harmonic waves are in pass bands: A_0 is maximum at finite ends [Fig. 4.9(a)]. On the contrary, A_2 remains trapped in the unit cell, and no cumulative increase with propagation distance is observed. However, energy propagation through the phononic material at 2Ω (which is in band gap) is still possible up to a certain extent due to the propagation of the second harmonic waves generated at the last few contacts. For $\Omega = 1.228$ (i.e. both Ω and 2Ω in band gaps), neither the fundamental nor second harmonic waves propagate, but A_0, generated at the first few contacts, causes deformation throughout the phononic

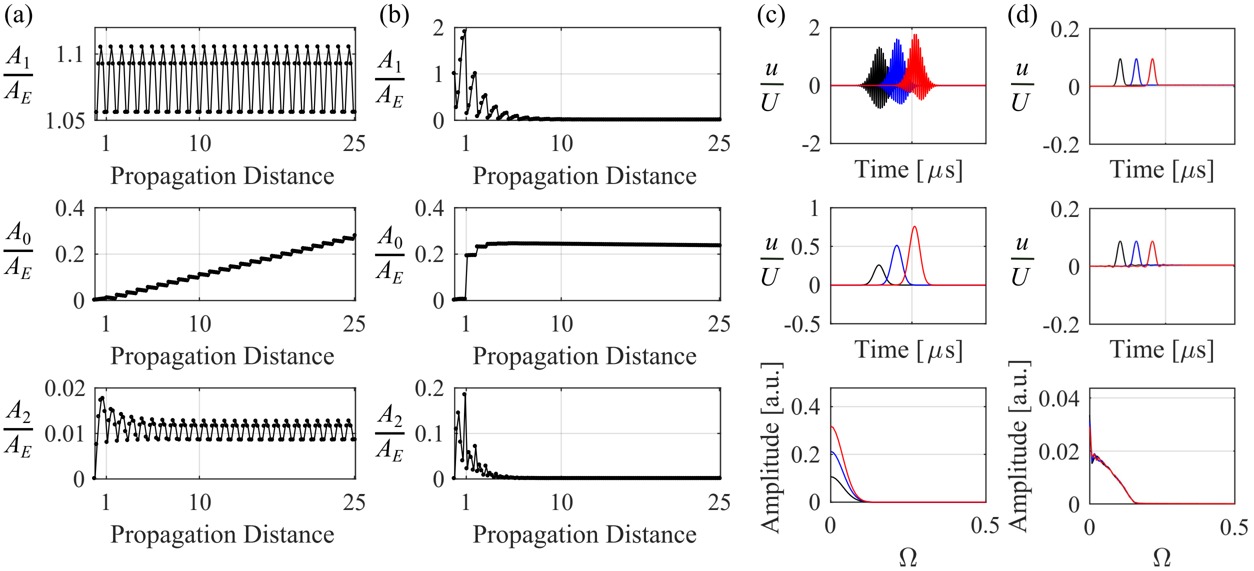

Figure 4.8: Dependence of normalized A_1, A_0, and A_2 on propagation distance in semi-infinite phononic material when (a) Ω in pass band but 2Ω in band gap and (b) both Ω and 2Ω in the band gap. $X-$labels indicate contact indices. Results are shown only up to the first 25 contacts. Dependence of low-frequency components on the propagation distance in semi-infinite phononic material for (c) Ω in pass band but 2Ω in band gap and (d) both Ω and 2Ω in the band gap. Top row: normalized time-domain wave displacements recorded at 3 different locations in semi-infinite phononic material. Middle row: low-frequency filtered normalized time-domain signal with only long-wavelength components. Bottom row: FFT of the filtered signal.

material [Fig. 4.9(b)]. Further, A_0 is maximum when the fundamental wave has fully decayed, unlike previous cases where A_0 is maximum at finite boundaries of the phononic material. Interestingly, the dependence of A_0 on propagation distance is similar for both semi-infinite and finite phononic materials only when both Ω and 2Ω are in the band gap [Figs. 4.8(b) and 4.9(b)]. This is because the right-side finite boundaries are trivial for finite phononic material when the wave is in a band gap. Thus, the finite phononic material effectively behaves similarly to that of semi-infinite phononic material.

Similar to the case when $\Omega < 1$ and $2\Omega < 1$, the interaction between propagating and reflected nonlinear waves results in low-frequency components higher than A_0 at certain locations inside phononic materials, even for the case of $\Omega = 0.614$ [Fig. 4.9(c) − solid blue]. However, for the same locations, such interaction does not exist when the fundamental wave is in the band gap as it can not propagate through the phononic material, and therefore no reflected wave exists [Fig. 4.9(d) − solid blue]. More interestingly, we observe that the locations inside the first few layers [e.g. solid black in Fig. 4.9(d)] show a dominant low-frequency component, probably a result of the nonlinear interactions of the trapped fundamental and generated low-frequency waves. The generated low-frequency wave propagates through the phononic material as it lies in the pass band. This nonlinear frequency down-conversion in these phononic materials enables energy transmission from band gap frequencies at low amplitudes; such transmission is typically not possible in linear material, and only possible in nonlinear material at high amplitudes due to supratransmission [78].

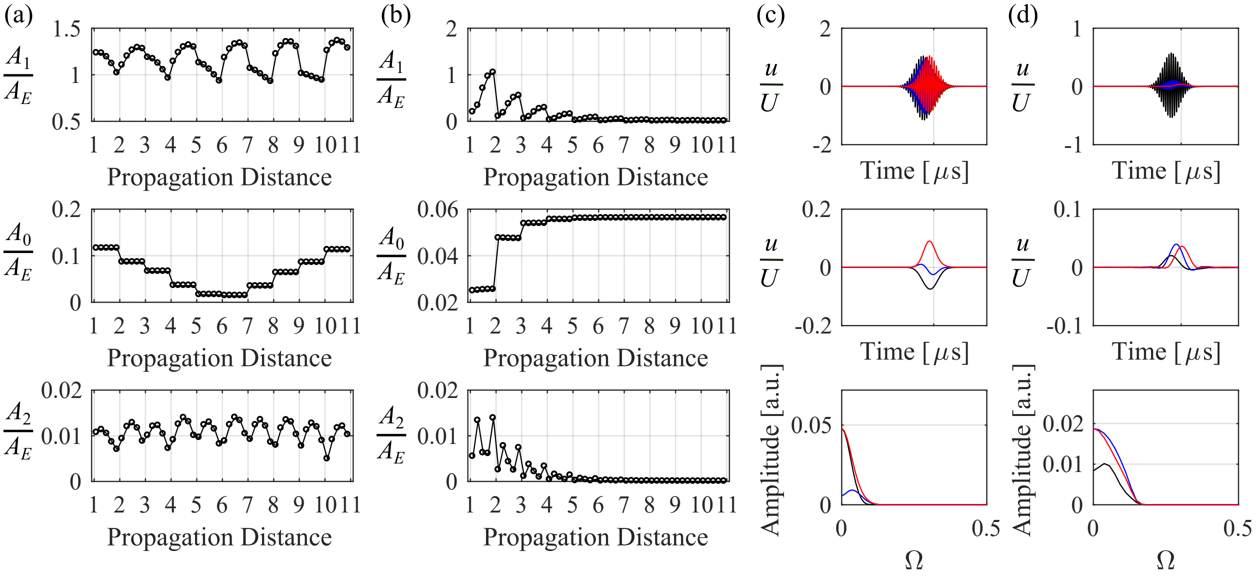

Figure 4.9: Dependence of normalized A_1, A_0, and A_2 on propagation distance in a finite phononic material with 10-layers when (a) Ω in passband but 2Ω in band gap and (b) both Ω and 2Ω in band gap. $X-$labels indicate contact indices. Dependence of low-frequency components on the propagation distance in finite phononic material for (c) Ω in passband but 2Ω in band gap and (d) both Ω and 2Ω in band gap. Top row: normalized time-domain wave displacements recorded near the 1st (black), center (blue), and last (red) contacts. Middle row: low-frequency filtered normalized time-domain signal with only long-wavelength components. Bottom row: FFT of the filtered signal.

4.6 Wave propagation through embedded contacts

The nonlinear phononic materials discussed so far assumed infinite-length contacts within the model. Such an arrangement couples adjacent layers solely through contact-equivalent stiffness, resulting in uniform deformation along the contact length. However, finite-sized contacts (or those embedded in a continuum) are anticipated to exhibit spatially varying deformation. In particular, the elastic media would be decoupled at the center of the contact interfaces but merged at the contact endpoints. Consequently, the separation of contact interfaces would encounter resistance not only from contact tensile forces but also from compressive forces exerted by the surrounding continuum. As a result, the deformation of the contacts and the nonlinear wave responses emerging from them are expected to differ from infinite-length contacts. Consequently, embedded contacts would allow additional design parameters in the form of their spatial arrangement within an elastic media while retaining the capability to generate additional frequency components from the discrete nonlinearity. This section explains how embedded contacts couple with the neighboring elastic continuum by exploring the dependence of nonlinearly-generated A_0 and A_2 on different representative arrangements of embedded contacts.

4.6.1 Phononic materials with different contact arrangements

While there are many conceivable arrangements of embedded contacts, the goal here is to (1) demonstrate the local coupling of contacts with surrounding elastic media and (2) understand how the spatial distribution of contacts influences the global nonlinear response of the material. Thus, selected but representative configurations of embedded contacts, limited to 1D periodicity, are studied. Fig. 4.10(a) shows the studied

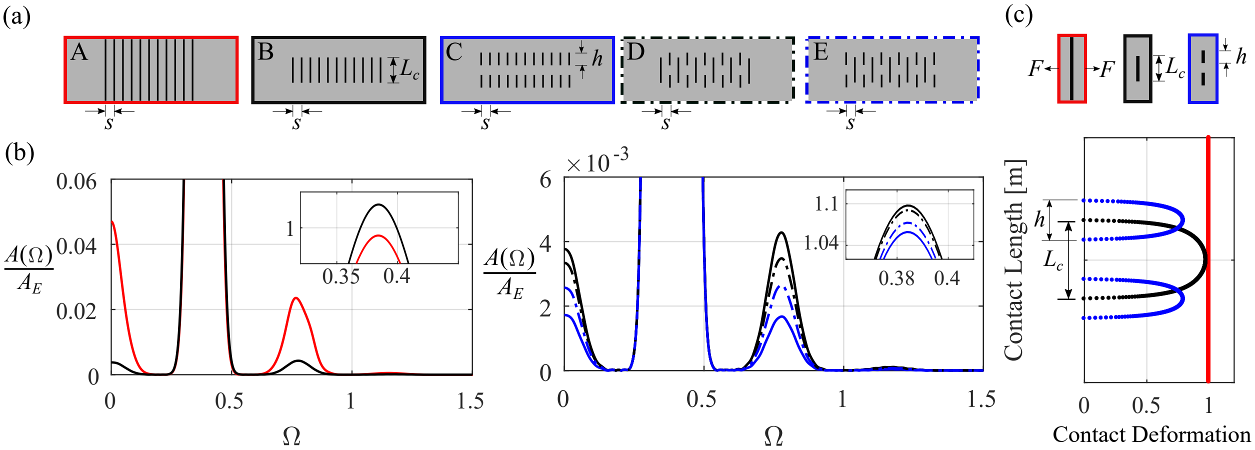

Figure 4.10: (a) Finite phononic materials with infinite-length contact (A), single array (B), two parallel arrays (C), and staggered arrays (D-E) of embedded contacts, where $h = L_c/2$. (b) Zoomed views of normalized FFT of transmitted nonlinear waves. The lines in the plots correspond to the boundary style of the system schematics in (a). Insets are zoomed views of fundamental amplitude. (c) Infinite-length vs embedded contact deformation under tensile force illustrates the effect of the neighboring continuum. Contact deformations are evaluated as the spring extension and normalized by the deformation of infinite-length contacts.

finite phononic materials with 11 contacts arranged in different configurations. The phononic material with infinite-length contacts is defined as system “A”, while systems “B-E” contain embedded contacts. Note that system A corresponds to all cases explored thus far. The total length of the embedded contacts, L_c, at any given spatial location, x, as well as the periodicity constant, s, are kept the same for all embedded contact configurations (systems “B-E”). So, the only difference among systems B-E is the spatial arrangement of contacts. System B corresponds to a single horizontal array of periodic contacts, each with length L_c, while system C has two parallel periodic arrays, where the length of each contact is $h = L_c/2$. In systems D and E, the contacts are arranged in a staggered pattern of alternating one- and two-array contacts, such that they are a combination of systems B and C. It is worth noting that the total number of contacts with individual lengths, L_c, in systems D and E are 6 and 5, respectively. It is assumed that the contact length does not grow as waves propagate through them. By investigating these configurations, insights can be gained into the role of separating contacts into multiple arrays and the proximity of contacts on nonlinear wave propagation. While the global symmetry of contact arrangements is preserved in this study, asymmetric arrangements are expected to support additional nonlinear behavior of nonreciprocity.

A precompression of $\eta = 1.863$ and excitation frequency $\Omega = 0.384$ is considered, such that both the fundamental and second harmonic waves are in the pass bands for all the systems. Although systems A-E have different dispersions, the phase mismatch between the fundamental and second harmonic waves for these systems is trivial since only short propagation distances are probed, meaning the generated and propagating second harmonic waves interact constructively in all simulations. The embedded contact length is $L_c = \lambda/6$, where λ is the wavelength at the excitation frequency, Ω, in system A, i.e. the wavelengths of the fundamental and second harmonic waves are both larger than the contact length, L_c. This condition is true for all other systems as well since their phase velocity at Ω is larger than that of system A. Note that $A_1/A_E < 1$ for system A but $A_1/A_E > 1$ for system B-E [see insets of Fig. 4.10(b)]. For system A, energy transfer from the fundamental to the second harmonic frequency results in $A_1/A_E < 1$. However, for systems B-E, in addition to the energy transfer, scattered waves from the edges of the embedded contacts interfere with the propagating fundamental wave and increase its amplitude.

4.6.2 Dependence of nonlinear wave propagation on contact arrangement

Fig. 4.10(b) shows the FFT of the transmitted wave signal for systems A-E. Comparing first the case of infinite-length (system A) to embedded contacts (system B), there is clearly a smaller A_0 and A_2 for the phononic material with embedded contacts. This can be understood by considering the deformation along the length of a single contact in system A vs. system B. Unlike the infinite-length contacts where the layers are coupled purely through nonlinear elements, the embedded contacts are surrounded by an elastic continuum. This neighboring elastic material prevents the embedded contacts from expanding and restricts the deformation close to the edges of the contact. As a result, the deformation along the length of an embedded contact is reduced compared to an infinite-length contact [Fig. 4.10(c) – red and black]. The results indicate that this smaller contact deformation is the cause of the reduced amplitudes of the nonlinearly-generated waves. As L_c increases, the nonlinear response of system B approaches that of system A's [Fig. 4.11(b)], as the effect of contact edges on overall contact deformation becomes less significant [Fig. 4.11(a)].

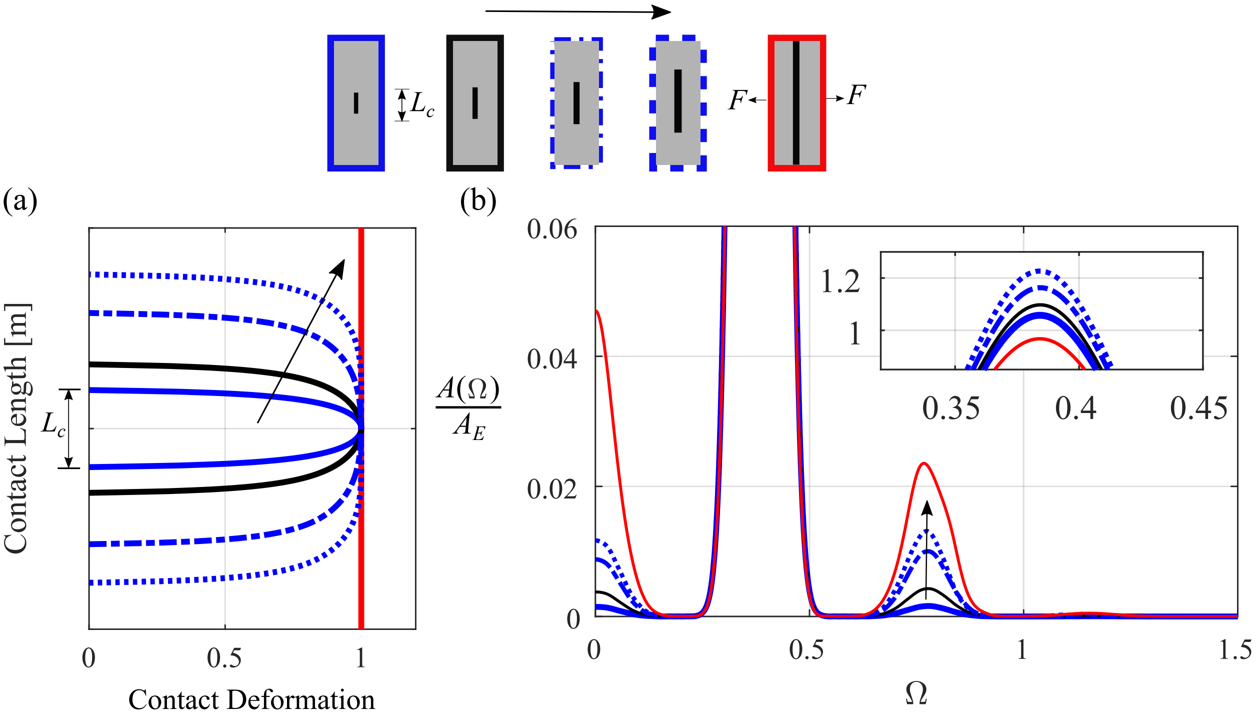

Figure 4.11: Response of system B for increasing contact length. (a) Contact deformation under tensile force. Contact deformations are evaluated as the spring extension and normalized by the maximum deformation. (b) Zoomed views of normalized FFT of transmitted nonlinear waves. Inset is zoomed view of the fundamental amplitude. The lines in the plots correspond to the boundary style of the system schematics shown above the plots. Arrows indicate the direction of increasing contact length.

Results also show that A_0 and A_2 depend on the arrangement of the embedded contacts (systems B-E) [Fig. 4.10(b)]. This is despite the fact that the total contact length at a given x-position in all systems is the same. The influence of the single vs. double array of contacts on nonlinear wave propagation can be understood as follows: the longer contacts in system B deform more compared to the shorter contacts in system C [Fig. 4.10(c) – black and blue], due to the influence of the surrounding elastic continua. The coupling between the elastic media on either side of the contact reduces from the contact edges to the center. This is because the surrounding elastic media merge into each other at the contact edges but they are separated through contact-equivalent springs away from the contact edges. As a result, longer contacts (system B) exhibit weaker coupling, i.e. they exhibit weaker resistance to expansion under tensile force, resulting in higher deformation; and vice versa for shorter contacts (system C). Subsequently, A_0 and A_2 are larger in system B compared to system C. The amplitudes of the DC and second harmonic waves in the staggered patterns (systems D and E) can be understood similarly. Fig. 4.10(b) shows that A_0 and A_2 in systems D and E are higher than system C, yet lower than system B. This is because the combination of the longer and shorter contacts in continua shows deformation that is smaller than a single array of longer contacts but higher than a double array of shorter contacts. Further, the number of continuous contacts with length L_c in the staggered pattern determines whether the response of the system will be skewed more towards system B or system C. For example, system D with 6 continuous contacts has nonlinear amplitudes much closer to system B than system E.

To further clarify the dependence of the nonlinear amplitudes on embedded contact arrangement, the average deformation of all contacts, $\bar{\delta}$, in a given arrangement, is compared to A_0 and A_2. Fig. 4.12(a) shows the deformation profile for each contact in system B and its corresponding $\bar{\delta}$, as an example. The contact deformation for each arrangement is obtained by imposing a uniaxial tensile force on the phononic material, and $\bar{\delta}$ is evaluated as the average deformation of all contacts. Fig. 4.12(b) shows there may be a quadratic dependence of both A_0 and A_2 on $\bar{\delta}$ for systems A-E, however further studies are needed to confirm this. This is particularly interesting since it suggests that the nonlinear wave amplitudes can be informed by the deformation profiles of a given contact arrangement. Further analysis of other arrangements is needed to fully understand this dependence and its applicability.

Finally, the simulation results are compared to recent analytical wave propagation models to further clarify the dependence of the nonlinear response of these phononic materials on dispersion and contact deformation. For example, Biwa et al. [115] introduced a contact model for wave propagation through a single rough contact, which predicts that the transmitted A_0 and A_2 depends on parameters such as the excitation amplitude (A_E), frequency (ω), contact stiffness (κ_1, κ_2), material density (ρ), and phase velocity (c_p) by:

$$A_0 = \frac{\kappa_2 A_E^2}{\kappa_1[1 + \frac{4\kappa_1^2}{\rho^2 c_p^2 \omega^2}]} \tag{4.1}$$

$$A_0 = \frac{\kappa_2 A_E^2}{\rho c_p \omega[1 + \frac{4\kappa_1^2}{\rho^2 c_p^2 \omega^2}]\sqrt{1 + \frac{\kappa_1^2}{\rho^2 c_p^2 \omega^2}}} \tag{4.2}$$

To apply these relations to systems A and B, all parameters would be the same except the phase velocity, due to the differences in their dispersion relation. Note that this model is only for a single contact whereas the phononic material system has periodic contacts, but it is conceivable that the dependence of A_0 and A_2 on phase velocity could be similar. For the frequency probed in this work, $\Omega = 0.384$, the phase velocity of system B is higher than that of system A. As a result, Eqs. (4.1) and (4.2) predicts A_0 and A_2 of system B to be higher than system A, whereas simulation results show the opposite [Fig. 4.10(b) – red and black]. Clearly, this model does not predict the response of phononic material with embedded contacts, indicating that the observed nonlinear response is an effect of dispersion, periodic nonlinearity, or contact deformation. This

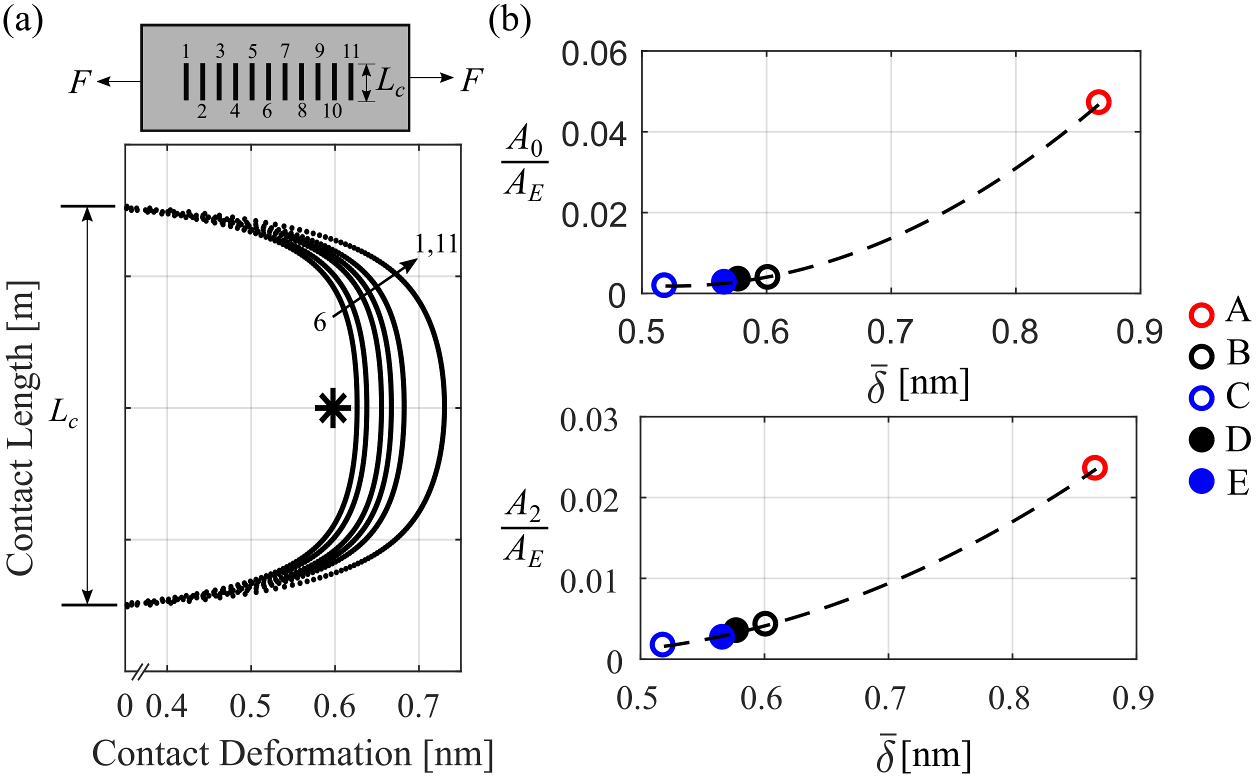

Figure 4.12: (a) System B contact deformation profiles under uniaxial tensile force. Black dots are the deformation of each contact; contact deformation increases from the center contact (6) towards the outermost contacts (1, 11). The asterisk shows the average value of all contact deformations, i.e. $\bar{\delta}$. (b) Dependence of normalized A_0 and A_2 on $\bar{\delta}$ for system A-E. The dashed line is a quadratic polyfit function.

model may predict nonlinear amplitudes of system A if combined with a dynamic homogenization method that represents the periodic contacts of these systems as a single contact with effective contact stiffness.

Alternatively, an analytical model of wave propagation through multiple nonlinear interfaces proposed in [135] can be considered. In addition to the parameters in Eqs. (4.1) and (4.2), this model also considers superimposed reflections and transmissions of nonlinear waves at each successive interface, as given by Eq. (53) in [135]. Thus, this model does capture the dispersion and periodic discrete nonlinearity of these systems, but it does not capture the effects of contact deformation specific to the embedded contact systems (systems B-E). This analytical model predicts a 28% increase in A_2 from system A to B, however, the FE model predicts an 80% decrease of A_2 from system A to B. This sharp contrast in the nonlinear response indicates that the effect of neighboring elastic media on contact deformation, the only aspect of embedded contact systems not considered in the recent analytical model, has a much more significant effect on the nonlinear response than dispersion, at least for the frequencies and systems considered here.

In summary, the results indicate that the surrounding continuum of embedded contacts significantly influences the nonlinear wave propagation, altering the response of the contacts. Consequently, phononic materials featuring embedded contacts demonstrate the ability to manipulate the overall nonlinear wave response of the material by employing a spatial distribution of local nonlinearity within a continuum.

4.7 Wave-wave interactions

The presence of nonlinearity within the material causes another interesting wave signature, which is the mixing of two (or more) waves of different frequencies, also known as "wave-wave interactions". This mixing causes the generation of new waves whose frequencies correspond to the sum or difference between the frequencies of the original propagating waves. This enables control of the frequencies of the generated waves by selecting the frequencies of the mixing waves. This is particularly explored for defect detection in nondestructive evaluation of structural components [126], [136]. In this section, the effects of wave-wave interaction in phononic material with contacts are studied, which are then leveraged to design a phononic diode for broad-band nonreciprocal wave propagation in Section 4.8.

Similar to wave self-interaction studies, a phononic material with periodic rough contacts is studied [Fig. 4.13(a)]. Dispersion results for $p_0 = 1$ MPa (i.e. $\eta = 1.863$, where $\eta = \kappa_1/[(\lambda^{(L)} + 2\mu^{(L)})/s]$), as an example are presented [Fig. 4.13(b)]. To study how nonlinearity causes waves at distinct frequencies to mix in this phononic material, finite element simulations of nonlinear wave propagation are conducted as presented in Chapter 3, but using an excitation that is the sum of two equal-amplitude Gaussian pulses, each at a different frequency - probe (Ω_1) and pump (Ω_2). The wave excitation, $u_i(t)$, is:

$$u_i(t) = UG_f(t)[\sin(2\pi f_1 t) + \sin(2\pi f_2 t)], \tag{4.3}$$

where U is the excitation amplitude, f_1 and f_2 are the absolute probe and pump frequencies, and $G_f(t)$ is the Gaussian function. To simulate such wave mixing, relevant numerical parameters were carefully modified. For example, mesh size was determined based on the largest second harmonic frequency (smallest wavelength), and Gaussian function parameters were adjusted to excite frequencies with bandwidth enough to avoid overlapping with adjacent nonlinearly generated frequencies. When input frequencies are in the pass band ($\Omega_1 < 1, \Omega_2 < 1$), energy is transferred to additional frequencies [Fig. 4.13(c)] from nonlinear wave mixing, specifically to (1) second harmonics of each input frequency ($2\Omega_1, 2\Omega_2$), (2) DC and self-demodulated frequency ($\Omega \sim 0$), and (3) sum ($\Omega_+ = \Omega_1 + \Omega_2$) and difference ($\Omega_- = |\Omega_1 - \Omega_2|$) frequencies. Similar to wave self-interactions, the DC component is generated in the system's response due to the quadratic nonlinearity of rough contacts [refer to Section 4.4.1]. This component physically corresponds to the gap opening (i.e. separation of contacting surfaces) at the contacts; however, due to weak nonlinearity, the contacts do not open completely [102]. This is because the wave displacements are smaller than the predeformation caused by external precompression, and the generated DC component itself is an order of magnitude smaller than the wave displacement within a weakly nonlinear regime.

When both Ω_1 and Ω_2 are in the band gap, for example, $\Omega_1 = 1.15$ ($f = 0.75$ MHz) and $\Omega_2 = 1.30$ ($f = 0.85$ MHz), the nonlinearity-induced waves are still generated. However, this generation ceases after the first few unit cells as the amplitude of the excitation decays - the amplitudes at the nonlinearly-generated frequencies stop increasing beyond layer indices ~ 5, when $A(\Omega_1)$ and $A(\Omega_2)$ are almost zero [Fig. 4.13(d)]. The corresponding harmonics ($2\Omega_1 = 2.30$ and $2\Omega_2 = 2.60$) as well as the sum frequency ($\Omega_+ = 2.45$) are also within the band gap, and therefore their amplitudes decay exponentially after initial generation [Fig. 4.13(d)]. Only the difference frequency is in the pass band ($\Omega_- = 0.15$, i.e. < 1). Unlike other frequency waves, the amplitude of the difference-frequency wave remains constant with propagation distance [Fig. 4.13(d)]. This is because no further Ω_- is generated once excitation frequencies have decayed and the Ω_- generated near the excitation boundary propagates through the phononic materials. This specific case, where the input frequencies, their harmonics, and sum-frequencies are in the band gaps, is used to demonstrate nonreciprocal wave propagation. However, other possible scenarios are also discussed later.

4.8 Leveraging wave-mixing for nonreciprocal wave propagation

4.8.1 Nonreciprocity: State-of-the-art research

Wave propagation in conventional materials is inherently reciprocal between two points due to time-reversal symmetry. This means the wave transmission is identical if the source and receiver of the wave are interchanged. However, breaking this reciprocity holds the potential for novel applications since nonreciprocity can avoid backscattering, wave interference from reflection, and even enable direction-dependent responses. This has inspired extensive research in recent years to design materials supporting nonreciprocal wave propagation [66]. These materials, often termed as "diodes" [137], have been used in sound isolation [138], [139], lithotripsy [140], and for designing advanced acoustic devices such as switches and rectifiers [141].

Nonreciprocal acoustic devices were initially designed using an external energy source [138] and recently, through periodic media [141]–[145]. Periodic media exhibit exceptional wave propagation properties such as band gaps [12], [19], anomalous polarization [16], [17], topological insulators [146] and many more [12], [147] by virtue of their engineered architecture. Recent studies further incorporated spatiotemporal property modulation [142]–[144] and nonlinearity [44], [141], [145] to enable nonreciprocal wave propagation through them. Specifically, nonlinearity allows passive and amplitude-dependent control over nonreciprocal response of the system [145]. Moreover, nonlinearity supports nonlinear signatures such as second harmonic generation (SHG) [148], [149], self-demodulation [133], frequency shift [150], [151], and supratransmission [152], all of which have been explored to design phononic diodes made of non-linear and linear media [44], [148]–[152]. Despite these unique mechanisms, the frequency of the nonreciprocal waves is not generally tunable. For example, the acoustic diode can enable energy propagation along one direction but only at a second harmonic frequency (i.e. only above the excitation frequency) in Liang *et al.* [148], [149] and at a self-demodulated frequency (i.e. only below the excitation frequency) in Devaux *et al.* [133]. Diode of Zhou *et al.* [150] and Kulkarni and Manimala [151] can allow one-way energy propagation but only in the narrow regions where frequency shifts are observed, limiting the frequency of operation for nonreciprocity. Further, diodes based on supratransmission enable nonreciprocal waves within band gap frequency ranges only [152].

To enable broadband nonreciprocal wave transport, phononic materials with unique but highly complex configurations have been presented. Fang et al. [153] and Zhang et al. [154] exploited *strong* nonlinearity to achieve broadband nonreciprocal frequencies. Specifically, Fang et al. [153] studied one-dimensional (1D) triangle-shaped asymmetric unit cell topology along with strong nonlinearity to enable nonreciprocal wave behavior. Zhang et al. [154] studied a two-dimensional granular channel composed of a main homogeneous lattice with several pairs of side granules such that side granules are in contact with the main lattice only on one side while there exists a clearance on the other side. Such topological asymmetry, combined with Hertzian contact nonlinearity between granules, enabled nonreciprocal wave propagation in this system. Some other studies have presented compact (thinner) nonreciprocal devices with a relatively broadband range of nonreciprocal frequencies [155], [156]. Zhai et al. [155] designed diodes based on an active linear Willis material. However, the functionality of their device is valid within a small wave amplitude regime only due to the linearity assumption. Popa and Cummer [156] designed metamaterial with an attached electronic circuit such that the nonlinearity is generated by the electronics and not by the physical structure. Thus, their compact devices could be prone to extensive heating and mechanical deformation under strong and

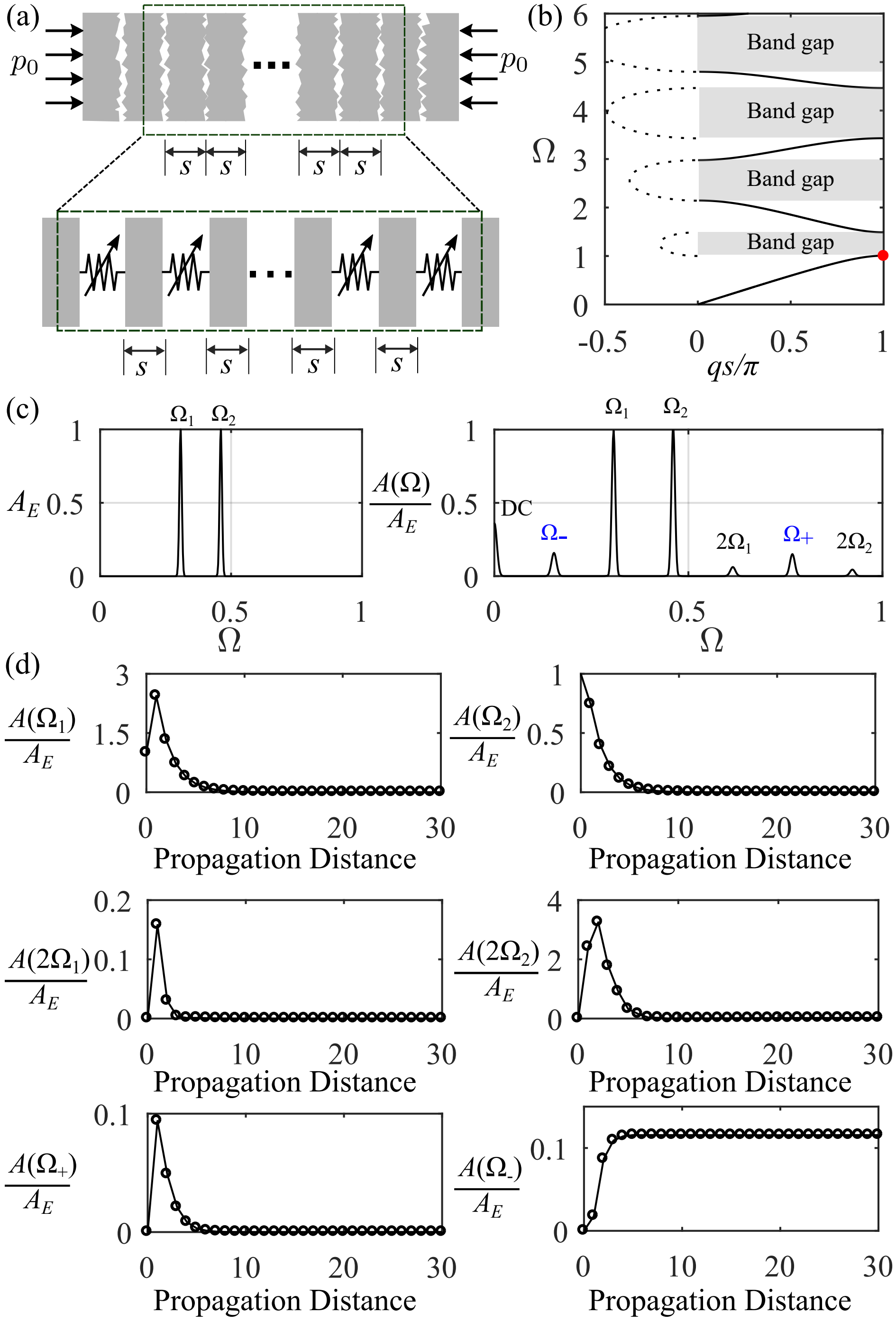

Figure 4.13: Nonlinear wave mixing in phononic material. (a) Phononic material with periodic rough contacts precompressed externally, and the corresponding model. (b) Linear dispersion showing propagating modes (solid) and multiple Bragg-scattering induced band gap regimes (dotted) for $\eta = 1.863$. Ω is band frequency normalized by the lower edge frequency of the 1st band gap at $q = \pi/s$ (red marker). (c) Frequency content of the input waves (left) and waves inside the 50th layer of the phononic material (right) when both Ω_1 and Ω_2 are in the acoustic pass band. (d) Dependence of wave amplitudes of input waves and nonlinearly-generated frequency waves on propagation distance when only the difference-frequency wave is in the pass band. Propagation distance is marked as layer indices from the excitation boundary.

prolonged mechanical vibrations.

4.8.2 Objective: Wave-mixing for nonreciprocity

Wave mixing in elastic nonlinear media along with harmonic generation was recently used to demonstrate proof of concept of a frequency-preserved diode [157]. This diode only allows unidirectional energy propagation and works for specific input frequencies by virtue of its design principle for frequency preservation. Wave mixing, however, has only been explored in nonlinear phononic media and for mechanical wave propagation control in a limited capacity: Li *et al.* [158] developed acoustic switches and logic elements using wave mixing in granular media, and recently Zhang *et al.* [159] explored mixing-induced mode conversion in granular crystals with coupled motions. In this dissertation, wave mixing of double-frequency (*pump* and *probe*) waves in nonlinear phononic materials is exploited to design a diode that can control the frequency, mode, and direction of energy propagation of the broadband nonreciprocal waves.

This concept is demonstrated by proposing a phononic diode based on the concept of global asymmetry of the system as adopted from Liang *et al.*'s acoustic diode [148], [149], but combined with the extrinsic nonlinearity in the form of rough contacts, and dispersive nature from their periodic arrangement. Nonlinear wave mixing of double-frequency (*pump* and *probe*) input waves and band gaps of the phononic material are exploited together to enable nonreciprocal wave propagation. A wave whose frequency is controlled to achieve tunability is referred to as a "pump" wave while the other input wave as a "probe". By controlling the frequency of the "pump" wave, the manipulation of the dispersion branch associated with the wave that exhibits nonreciprocal behavior is demonstrated. Results show that nonreciprocity can occur at lower or higher frequencies than the excitation, overcoming the limitations of the existing literature [133], [148]–[152]. Further, the flexibility of the diode to allow either one-way (unidirectional) or two-way (bidirectional [160]) energy propagation through a suitable selection of pairs of frequencies is highlighted. Finally, the contact nonlinearity in these diodes also offers an opportunity for *in-situ* tuning of wave propagation via external precompression.

The proposed diode also addresses an open question in the field of how to achieve nonreciprocity over broadband frequencies using a simpler diode design. As discussed, the diode is based on contact nonlinearity, which stems from the roughness on contacting surface. Thus, it could offer an excellent platform to tune contact response through surface texture while at the same time simplifying the overall design of the nonreciprocal device without needing any external electronic device. Due to pure mechanical construction, these diodes built on phononic material with contacts could also be useful even in harsh and extreme environments.

4.8.3 Concept of phononic diode

To enable nonreciprocal wave propagation using nonlinear wave mixing, a phononic diode is designed by assembling two sets of rough contact-based phononic materials in series (Fig. 4.14) - one with large and the other with small asperities. Note that the nonlinearity of rough contacts arises from the nonlinear mechanical deformation of asperities. For a given amplitude, small asperities undergo nonlinear deformation (large strain) such that both κ_1 and κ_2 exist, while large asperities undergo small strain exhibiting only κ_1. Further, the linearized dispersion of both phononic materials is the same. Two propagation directions are studied for the case when input waves are in band gaps: (1) from linear to nonlinear phononic material (forward) and (2) from nonlinear to linear phononic material (backward). In forward propagation, input waves do not propagate through the linear phononic material as they fall in band gaps. However, for backward propagation,

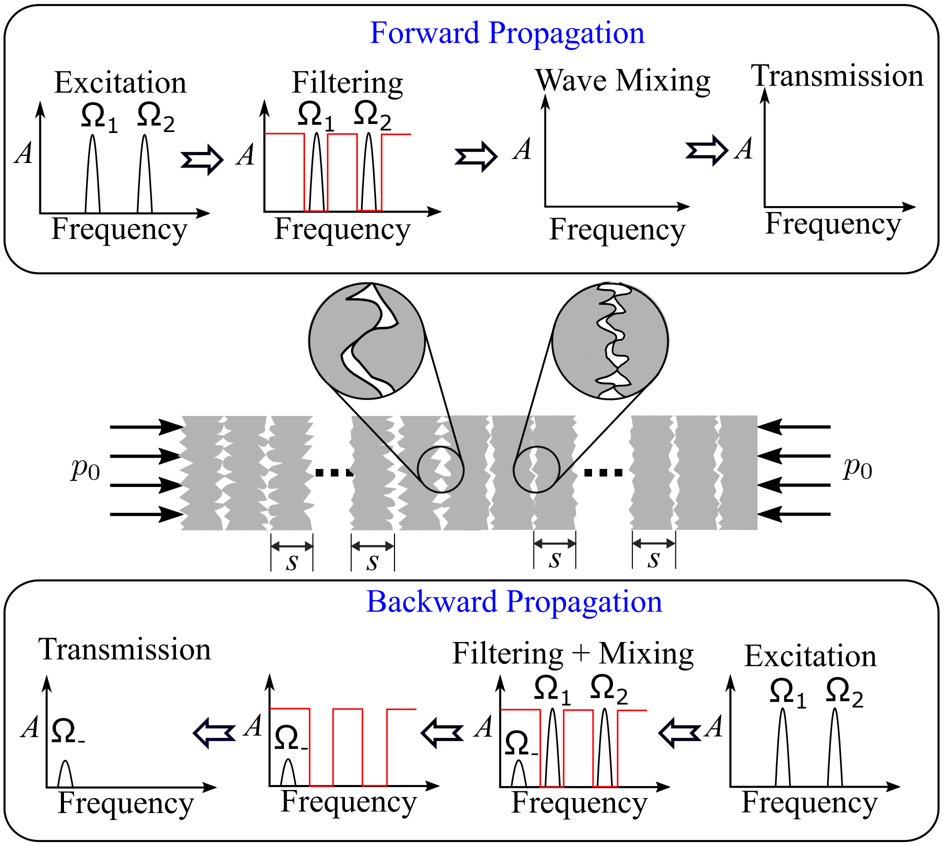

Figure 4.14: Phononic diode design based on nonlinear wave mixing. Diode consists of contacts with large and small asperities on the left and right side, respectively.

input waves mix nonlinearly and generate a difference-frequency wave within a pass band. Thus, energy propagates only in the backward direction but not in the forward, enabling unidirectional nonreciprocal wave propagation.

4.8.4 Numerical demonstration of diode functionality

Numerical demonstrations are carried out to confirm the concept of wave mixing-based diode, and illustrate how to tune the frequency and mode of nonreciprocal wave propagation by controlling the pump frequency while keeping the probe frequency the same. Two representative cases are discussed - first, when both the pump and probe frequencies are in the same band gap [Figs. 4.15(a) and 4.15(b)] and second, when they are in different band gaps [Figs. 4.15(c) and 4.15(d)]. For both cases, input waves do not propagate in the forward direction and no additional frequencies are generated due to the lack of nonlinearity [Figs. 4.15(b) and 4.15(d)]. For backward propagation, the input waves are again trapped within the first few unit cells, however, they do generate additional waves in the first few unit cells from their self-interactions [as discussed in Section 4.5] and nonlinear mixing. Importantly, the generated difference-frequency wave propagates into the linear phononic material [Figs. 4.15(b) and 4.15(d)], demonstrating nonreciprocal propagation. When the pump frequency is in the first band gap [Fig. 4.15(a)], the difference-frequency component lies in the acoustic band and nonreciprocity is achieved at a frequency lower than the probe frequency [Fig. 4.15(b)]. In contrast, when the pump frequency is in the second band gap [Fig. 4.15(c)], the difference-frequency component lies in the optical band and nonreciprocity is achieved at a frequency higher than the probe frequency [Fig. 4.15(d)]. Clearly, the frequency at which nonreciprocal energy propagates can be controlled, and it is even possible to enable mode hopping [161] of nonreciprocal waves between the acoustic and optical modes [Fig. 4.15] by controlling the pump frequency yet without altering the probe frequency. This is particularly useful in multi-dimensional diodes, where tuning the mode of the nonreciprocal waves can open applications of mode-converted diodes.

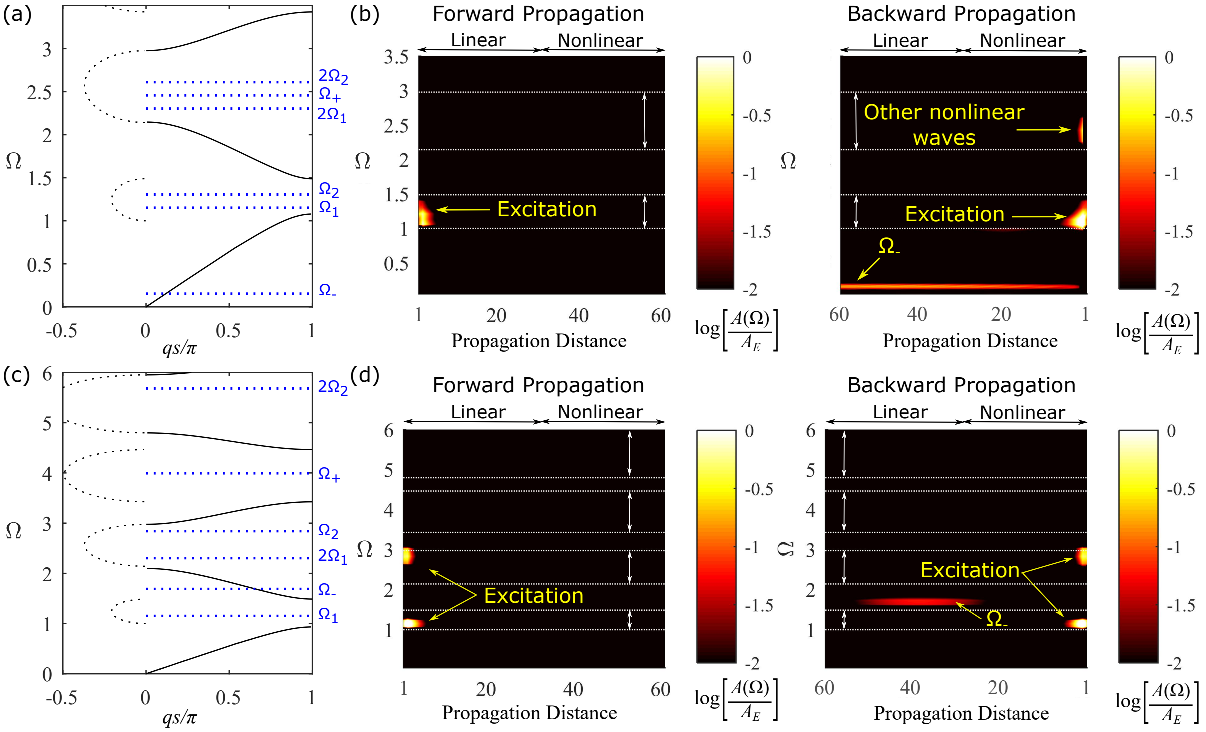

Figure 4.15: Nonreciprocal wave propagation due to nonlinear wave mixing, when the pump frequency is in [(a) and (b)] the same and [(c) and (d)] different band gaps as that of probe frequency. (a) and (c) Dispersion of the phononic material. (b) and (d) Frequency-space-amplitude of the waves propagating through the diode (plotted for the same time instant for both forward and backward propagation). Propagation distance is marked as layer indices from the excitation boundary with 30 layers each for linear and nonlinear phononic material. White dotted lines and arrows are band gap edges and widths, respectively.

For simplicity, pairs of input frequencies for which only the difference frequency is in a pass band were illustrated. However, a wide range of frequencies can be paired to achieve nonreciprocal wave propagation in this diode [Fig. 4.16(a)]. Particularly, the diode can allow nonreciprocal wave propagation (which can cause unidirectional or bidirectional energy propagation), fully reciprocal wave propagation, or no propagation at all, by carefully selecting pump and probe frequencies. For the diode to support unidirectional energy propagation, the required conditions are - (1) both pump and probe frequencies are in band gaps and (2) at least one of the nonlinearly-generated frequencies is in a pass band. While two such representative cases were discussed [Fig. 4.15], many other frequencies can also support such behavior [Fig. 4.16(a) - yellow]. For the diode to support bidirectional energy propagation but still exhibit nonreciprocity, the required conditions are - (1) one of the input frequencies should be in a pass band while the other is in a band gap and (2) at least one of the frequencies out of Ω_+, Ω_- and second harmonic (of the input frequency that is in a band gap) is in a pass band [Fig. 4.16(a) - blue]. For these conditions, forward propagation enables harmonic generation only while backward propagation causes both harmonic generation and wave mixing, enabling nonreciprocity. For certain cases, the transmitted wave in the forward and backward directions contains the same frequencies but different energy. These cases correspond to (1) when one of the input frequencies is in the pass band, while the other input frequency and all nonlinearly-generated frequencies are in band gaps, and (2) when one of the input frequencies and corresponding harmonic is in pass band while all other frequencies in band gaps. However, these cases are considered fully reciprocal as their energy difference is negligible due to weak nonlinearity. Moreover, the diode will be fully reciprocal if both the input waves are in pass bands [Fig. 4.16(a) - green], irrespective of dispersion zones in which nonlinearly-generated frequencies lie. This is because the generation and propagation of additional frequencies will be the same in either direction. Finally, there are frequency ranges over which the input and nonlinearly-generated frequencies, all fall within band gaps. This eventually prohibits energy propagation in either direction [Fig. 4.16(a) - red].

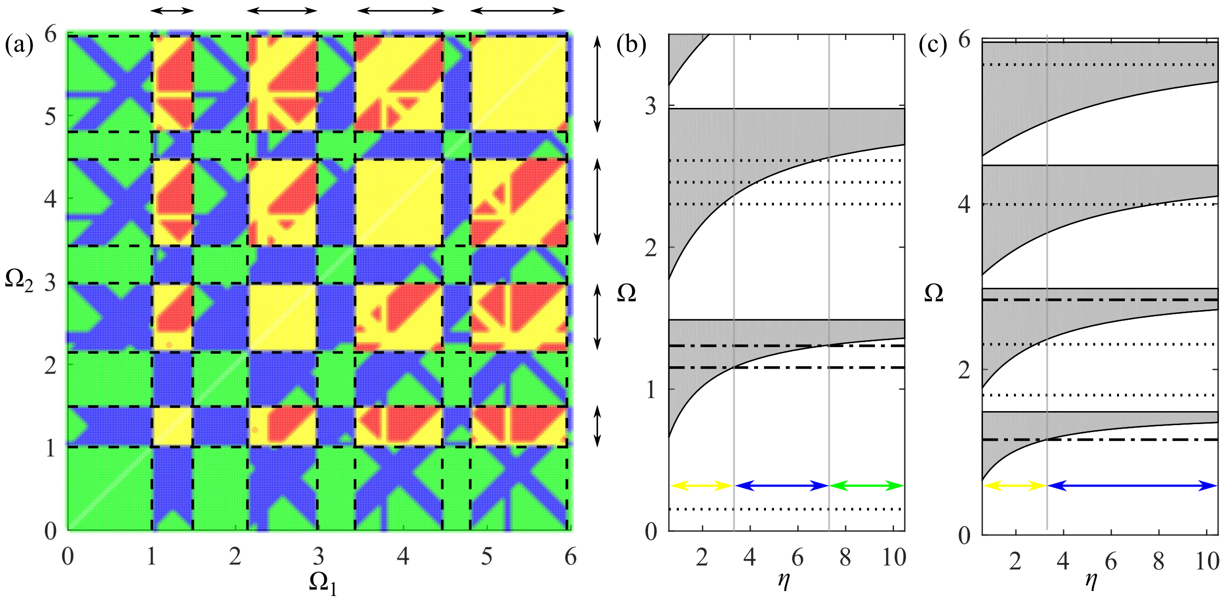

Figure 4.16: Tunability of nonreciprocal waves through (a) frequency pairing and (b)-(c) precompression. (a) The nature of wave propagation through the diode - reciprocal (green), unidirectional nonreciprocal (yellow), bidirectional nonreciprocal (blue), and no propagation at all (red) at Ω_1, and Ω_2 pairs for $\eta = 1.863$. Plot is discretized in 200 X 200 points. Dashed lines and arrows are band gap edges and widths, respectively. (b)-(c) Switching the nature of wave propagation in diode through precompression for a pair of pump and probe frequencies, when both waves are in the (b) same and (c) different band gaps. Gray regions are band gaps. Dash-dotted and dotted lines are input and nonlinearly-generated frequencies, respectively. Colored arrows indicate precompression ranges and the corresponding nature of wave propagation.

Further, the state of energy propagation (reciprocal, unidirectional, and bidirectional nonreciprocal) through the diode can be switched via external precompression, without changing the input frequencies [Figs. 4.16(b) and (c)]. Such tunability is possible since the dispersion of the phononic material depends upon the precompression (Eq. 3.5). Therefore, the input frequencies can be forced to fall in the band gaps, pass bands, or one each in a pass band and band gap, simply by changing the precompression. For example: For $\Omega_1 = 1.15$ and $\Omega_2 = 1.30$, both pump and probe frequencies are inside the 1$^{\text{st}}$ band gap for $\eta = 1.863$ [Fig. 4.16(b)], and Ω_- is in the pass band. Thus, the diode supports unidirectional nonreciprocal waves [Fig. 4.16(b)]. As precompression increases, the band gap narrows. Eventually, Ω_1 comes out of the band gap and lies in the acoustic pass band for $\eta = 3.29$ ($p_0 \sim 3.1$ MPa). Now, the diode supports bidirectional energy

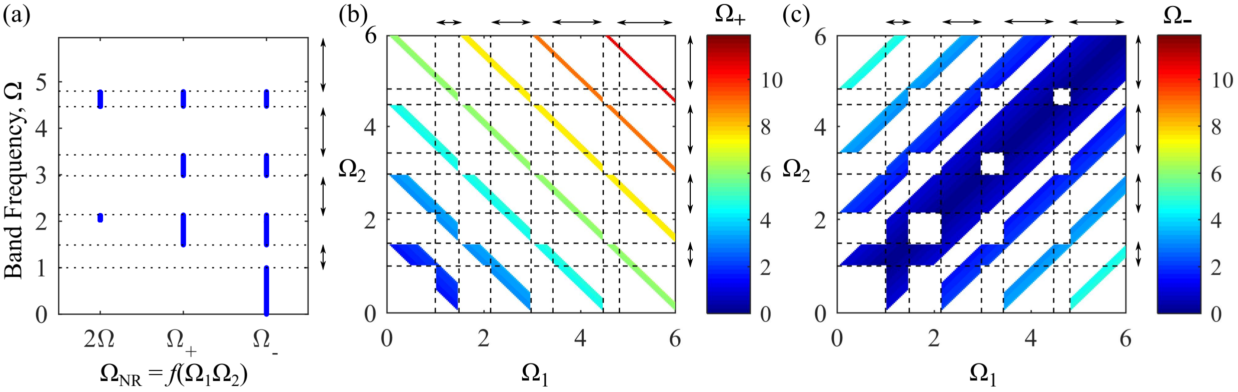

Figure 4.17: Frequencies of nonreciprocal waves in wave mixing-based diode. (a) Markers show resulting nonreciprocal frequencies and their relation with respect to input frequencies. (b)-(c) Colorbars show nonreciprocal frequencies in the form of (b) Ω_+, and (c) Ω_- for different pairs of input frequencies. Dashed lines and arrows are band gap edges and widths, respectively.

propagation, which is still nonreciprocal due to different frequency content in the forward and backward directions. A further increase in precompression to $\eta = 7.08$ ($p_0 \sim 14.4$ MPa) causes Ω_2 to also fall in the acoustic pass band. Thus, for $\eta \geq 7.08$, waves propagate reciprocally, causing the system to no longer operate as a diode. Similar tunability can be seen when input frequencies are in different band gaps ($\Omega_1 = 1.15$, $\Omega_2 = 2.85$) [Fig. 4.16(c)]. The system supports unidirectional nonreciprocity for $\eta < 3.29$, which switches to bidirectional nonreciprocity at $\eta = 3.29$, when Ω_1 comes outside the band gap. These results depict a unique feature of the proposed diode to achieve tunable nonreciprocity without altering the input frequencies.

While nonreciprocity in this diode can be enabled by pairing a range of input frequencies (Fig. 4.16), the nonreciprocity itself can be achieved over a wide range of frequencies (Fig. 4.17). In fact, the resulting nonreciprocal frequencies in this diode can be two times, the sum, or difference of input frequencies [Fig. 4.17(a)], overcoming the limitations of existing diodes [133], [148]–[152]. For example, diodes exploiting SHG can enable nonreciprocity for frequencies where input frequency is in band gap but the second harmonic in pass band [148], [149], which restricts the range of frequencies for nonreciprocity [refer 2Ω in Fig. 4.17(a)]. On the other hand, the complexities associated with nonlinear wave mixing in this diode provide additional opportunities to enable nonreciprocal waves at (1) frequencies higher [Fig. 4.17(b)] or lower [Fig. 4.17(c)] than the input frequency, and (2) more than one frequency (for example, $1 < \Omega_1 < 1.48$ and $0.5 < \Omega_2 < 0.62$ support nonreciprocity at both Ω_+ and Ω_-). All these results shed light on the flexibility of this diode to achieve robust control over nonreciprocal wave propagation.

4.9 Summary

In this chapter, weakly nonlinear results of continuum phononic material with rough contacts are presented. Both wave self-interaction, which is an interaction of propagating narrow band frequency wave with contact nonlinearity, and wave-wave interaction, which is an interaction of two waves of distinct narrow band frequencies at contact nonlinearity are studied.

Wave self-interaction gave rise to DC component, low-frequency wave in the vicinity of DC, and second harmonic wave due to quadratic nonlinearity of contacts. The effects of dispersion, finiteness, and surrounding continuum on wave propagation are studied. Noteworthy observations are:

1. The treatment of elastic layers as continua changes the response of the nonlinearly-generated waves, e.g. they locally reduce the DC component and cause variations in second harmonic amplitudes inside the layers, even though the layers are linear.
2. Second harmonic amplitude exhibit spatial beating due to phase mismatch between fundamental and second harmonic wave. Thus, second harmonic amplitudes and the spatial location where they are maximum or minimum can be controlled through external precompression. This is because precompression changes the dispersion relation and thus the phase mismatch between the fundamental and second harmonic waves.
3. Deformation of contact asperities under external precompression leads to tunable band gaps.
4. The interplay between periodicity, nonlinearity, and finiteness causes the DC amplitude to be maximum at the finite boundaries of the phononic materials, and the second harmonic amplitude depends on the individual mode of elastic layers.
5. The finite bandwidth of the wave excitation causes energy transfer to low frequencies at the contacts via nonlinear self-demodulation effects. The low frequencies generated at each contact interact nonlinearly with those reflected from finite boundaries of the phononic materials.
6. The coupling between the contact and surrounding continuum changes the nonlinear contact response; DC and second harmonic wave amplitudes depend on the arrangement of embedded contacts in a continuum.

Wave-wave interactions generate new frequencies as sums or differences of the propagating frequencies. This phenomenon is utilized in phononic materials, combining wave-mixing with band gaps for achieving broadband nonreciprocity. A phononic diode based on the global asymmetry, local nonlinearity, and periodicity of precompressed rough contacts was designed. Numerical demonstration confirmed nonreciprocal wave propagation upon excitation of a frequency pair. The primary features observed in the wave propagation were:

1. The frequency and propagating mode of nonreciprocal waves can be tuned through an appropriate selection of a pair of input frequencies, surpassing the limitation of existing diodes.
2. Wave propagation can be switched to support either reciprocity or nonreciprocity, and can allow unidirectional, bidirectional, or no propagation of energy at all.
3. The presence of contact nonlinearity further allows *in situ* control of energy propagation through precompression.

Chapter 5

Strongly nonlinear wave dynamics

This chapter presents nonlinear longitudinal wave propagation through continuum phononic materials with rough contacts under zero external precompression (strongly nonlinear). The strong nonlinearity arises from the nonlinear mechanical deformation of contact asperities under compressive loads as well as their inability to support tensile loads. The chapter begins with a concise literature review of solitary waves in strongly nonlinear phononic media, followed by a detailed investigation of novel wave responses observed in continuum phononic materials with rough contacts. These include acoustic resonances of layers, propagation of distinctive solitary waves with their unique characteristics, and collision dynamics. Additionally, it examines the influence of physical constraints, such as light precompression, disorder, and finite lateral size on wave transformation within the ideal system. The contents of this chapter have been adapted from various sections of my published article, [104] (associated with zero precompression) and conference proceeding, [105] (associated with light precompression), which were written as part of the research for this dissertation.

5.1 Background: Strong nonlinearity and solitary waves

One of the revolutionary strongly nonlinear behaviors studied in periodic media is the propagation of solitons or solitary waves [162], which are localized traveling waves, meaning they have a spatially localized (or compact) profile that travels through the system. Following John Scott Russell's observation of shallow-water waves [163] that maintained their shape and speed for a very long distance, characteristics of solitary waves have been extensively studied across various domains of science [67], [164]–[166]. Solitary waves form as a result of the delicate interplay between nonlinearity and dispersion. In materials with nonlinearity, waves of greater amplitude propagate faster. Consequently, the peak value of a wave pulse tends to surpass lower values, leading to a steepening and eventual breakage of the pulses. Conversely, dispersion in the material causes a localized distribution to disperse or spread out. Hence, a solitary wave emerges when the nonlinear steepening is counterbalanced by the dispersive spreading, resulting in a localized disturbance that propagates without distortion. Recent progress in realizing these waves in phononic materials has led to numerous applications such as diodes [167], sound bullets [168], impact mitigators [169], robotic motion [170], and sensors [171]. Solitary waves have been studied in granular crystals [62], [67], [70], [162], [172], tensegrity structures [75], [76], bistable [173], and soft architecture [79], [167], [170], all of which were assumed as lumped-mass periodic systems, i.e. discrete nonlinearity connecting discrete particle masses. A few studies have explored the propagation of solitary waves in bilayered phononic media with material [174] or geometric

[175] nonlinearity. Yet, it is an open question whether solitary waves exist in a continuum with periodic and discrete nonlinearity.

Moreover, the system architecture itself governs the nature of solitary waves that propagate through it. For example, phononic media supporting single-polarization forms scalar [162] solitary waves whereas media with coupled polarization support propagation of vector [79], [167], [174] solitary waves. A couple of other studies on nonlinear phononic materials have reported the formation and propagation of nanopteron [176] and stegotons [177]. These two solitary-like localized traveling waves arise from a unique interplay of the underlying periodic system and nonlinearity, and exhibit different characteristics than classical solitons. For example, nanopteron are solitary waves on top of small oscillations as observed in stacked woodpile structures with Hertzian contact nonlinearity [176] whereas stegotons are solitary waves with a roof-type (or stepwise) profile as reported in bilayered media with exponential material nonlinearity [177]. Clearly, the complex nonlinear wave dynamics is an effect of how nonlinearity is embedded and interacts with the underlying phononic system.

5.2 Objective: The role of continuum and strong discrete nonlinearity

In this part of the dissertation, the wave dynamics of a layered phononic material where the linear continua (or layers) are nonlinearly coupled are analyzed. The focus of the study is to understand the role of strongly nonlinear coupling on the elastodynamic behavior of linear layers and the existence and propagation of localized traveling waves in such media. Additionally, how energy is distributed and exchanged within this architecture, where nonlinearity exists only at discrete locations separated by linear continua, is studied. Such understanding is crucial for these materials to be used for controlling the propagation of mechanical wave energy.

The *uncompressed* contacts, considered in this study, exhibit strong nonlinearity stemming from their inability to support tensile loads. This is in addition to nonlinear contact response under compressive loads arising from nonlinear mechanical deformation of roughness. The evolution of propagating waves, excited in the form of Gaussian tone burst at frequencies in the same order as the modal frequencies of individual layers, is studied using time-domain finite element (FE) simulations. Particularly, the elastodynamics effects arising from the nonlinearly-coupled layers are illustrated and the existence and properties of localized traveling waves in such phononic materials are investigated. The main objective is to report novel nonlinear wave phenomena of energy transfer through acoustic resonances and the emergence of stegotons in continuum phononic materials with discrete contact nonlinearity, and present some insights through extensive numerical simulations.

A non-dimensional frequency, Ω, is introduced in this chapter and it is defined as the ratio of the excitation frequency, f, to the first fixed-free resonance frequency of layers, $f_{fixed-free}$. All the numerical simulations presented correspond to $\Omega = 0.52$ ($f = 0.25$ MHz and $f_{fixed-free} = 0.484$ MHz), unless explicitly specified. This particular frequency is chosen for simulation as it captures the elastic deformation of the layers (and therefore elastodynamic response of the layers due to the strong nonlinearity of contacts) within a reasonable computational cost. All the simulations were conducted with $\zeta = 12.5/f$, $\psi = 2.5/f$ of Eq. (3.8) and at excitation amplitude, $U = 5$ nm, corresponding to strain, ϵ, of 1.25×10^{-6} in layers of width, $s = 3.175$ mm, unless explicitly specified.

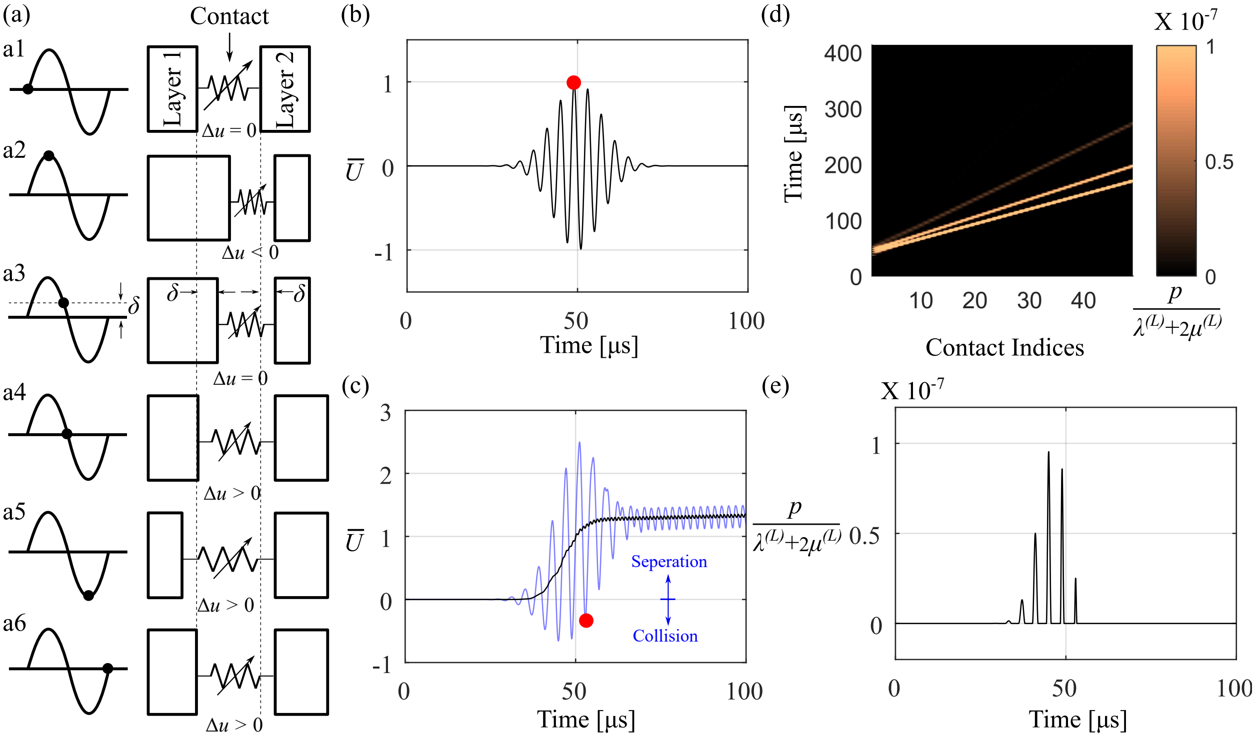

Figure 5.1: Contact clapping under wave excitation. (a) Schematic demonstration of contact collision and separation under the first wave cycle of the Gaussian tone burst of (b). Black markers show specific instants of the wave cycle and corresponding contact conditions (a1-a6). Dashed lines are the initial interface location. The red marker in (b) is the maximum amplitude of the tone burst. (c) Displacement-time profile of the contact surface of layer 2 (black) and spring deformation of the rough contact between layers 1 and 2 (light blue). The last instance of clapping is associated with the maximum amplitude of the tone burst. Displacement profile, $\overline{U}$, is normalized by the excitation displacement amplitude, U. (d) Spatiotemporal plot of the contact pressure, and (e) temporal plot of the contact pressure at the first rough contact. Contact pressure is normalized by the uniaxial modulus of the layer material, where $\lambda^{(L)}$ and $\mu^{(L)}$ are the material Lame parameters.

5.3 Energy transfer through layer resonances

The interaction of the excited wave with rough contacts results in clapping (or breathing), which is a collision and separation of contacting rough surfaces. This section first explains the mechanics of such collision and separation and then the complex wave dynamics of resonance activation from it.

5.3.1 Wave-induced contact clapping

Consider a wave cycle propagating from layer 1 to layer 2 [Fig. 5.1(a)] such that layer 1 is the first layer of the phononic material in the direction of excitation. The rough contact between these layers is at an uncompressed initial condition, thus, the deformation, Δu, of the nonlinear spring representing the contact is initially zero [Fig. 5.1(a1)]. A collision occurs at the contact when the spring deformation is less than zero; otherwise, contact separation will take place. As a result, only a fraction of a full-wave cycle is transmitted across the contact [Fig. 5.1(a)]. This fraction of the cycle consists of a portion of the compressive part of the wave cycle [Figs. 5.1(a2) and 5.1(a3)]. This can be explained as follows - when the displacement of the wave cycle increases from 0 to its peak amplitude, the rough surface of layer 1 is forced to move toward the rough surface of layer 2 causing the contact spring to deform and transmit the forces across the contact [Fig. 5.1(a2)]. At the same time, layer 2 deforms under the action of transmitted force causing the rough surface at the contact to move to the right. During the next part of the wave cycle from its peak amplitude to 0, the rough surface of layer 1 retracts, releasing the spring deformation. The forces are still transferred across the contact during this stage until the rough surface of layer 1 retracts to position δ to account for the deformation of layer 2 [Fig. 5.1(a3)]. At this instant, the spring is back to the uncompressed state. As the cycle progresses, the lack of tensile force at the contact results in a contact loss ($\Delta u > 0$), and the rough surface of layer 2 cannot be pulled back [Fig. 5.1(a4)]. It should be noted that the wave transmitted across the contact now propagates through layer 2 and thus moves the right boundary (or surface) of layer 2 further toward the right. As expected, the tensile part of the wave cycle further increases the gap between the two rough surfaces at the contact [Fig. 5.1(a5)]. At the end of the cycle, layer 1 stays at the original position whereas layer 2 has moved to the right from its original position [Fig. 5.1(a6)].

This same clapping-separation behavior is repeated with each cycle of the tone burst until the tone burst reaches its maximum amplitude [red marker in Fig. 5.1(b)]. Note that the strongly nonlinear behavior of contact causes a change in the position of subsequent layers [for example, layer 2, see Fig. 5.1(c) - black line]. Also, recall that due to the Gaussian profile, the amplitudes of the later cycles of the tone burst are larger than the previous ones – refer to the Gaussian tone burst in Fig. 5.1(b). Thus, wave cycles of the tone burst can cause clapping as long as their amplitudes are larger than the gap between the contacting surfaces generated from the previous cycles [compare black and light blue lines of Fig. 5.1(c)]. Wave cycles beyond the maximum amplitude of the tone burst do not result in clapping, as they do not cause the rough surfaces to come in contact [wave cycles beyond the red marker in Fig. 5.1(c)]. This contact loss remains in place at all times due to the lack of external precompression and the system's inability to support any tensile forces [Figs. 5.1(d) and 5.1(e)]. The forces transmitted across the contact during tone burst interaction propagate through the phononic material and subsequently cause the separation of surfaces at each contact [Fig. 5.1(d)].

5.3.2 Emergence of acoustic resonances

Interestingly, the normalized displacement profile, $\overline{U}$, inside the first layer of the phononic material shows a harmonic response for all times after tone burst excitation [inset of Fig. 5.2(a)]. Similar observations are made in layer 2 [inset of Fig. 5.2(b)] and so on. The wavelet transform reveals that the frequency content of these harmonic responses is different from the tone burst excitation frequency of $\Omega = 0.52$. The frequency spectrum shows that these oscillations, in fact, correspond to the acoustic resonances of the corresponding layers. Layer 1 exhibits the first acoustic resonance under fixed-free BC. This is because the tone burst interaction with the rough contact causes a separation between surfaces of layer 1 and layer 2 (as illustrated in Fig. 5.1), which ultimately creates a free BC on the right side of layer 1, and the excitation boundary is held fixed in its original position after the excitation (a physical BC as seen in the experiments [178]). These BCs of the layer activate acoustic resonances given by $jc_L/4s$, where j is the order of resonance i.e. first, third, fifth, and so on. Thus, a fraction of the excited energy is now localized in layer 1 at its resonance frequencies. Higher-order resonances of this layer also exist but their amplitudes are much smaller than the first resonance. On the other hand, layer 2 experiences free BCs on either side because of loss of contact due to wave interaction with corresponding rough contacts. This results in acoustic resonances of layer 2 as given by $jc_L/2s$. Owing to free-free resonance, the center point inside layer 2 is a node while boundary points are antinodes [Fig. 5.2(d)]. Thus, wave responses shown in Fig. 5.2(b) are from a point close to the boundary in layer 2. Due to the separation of surfaces at each contact as the wave propagate [Fig. 5.2(d)], the later layers

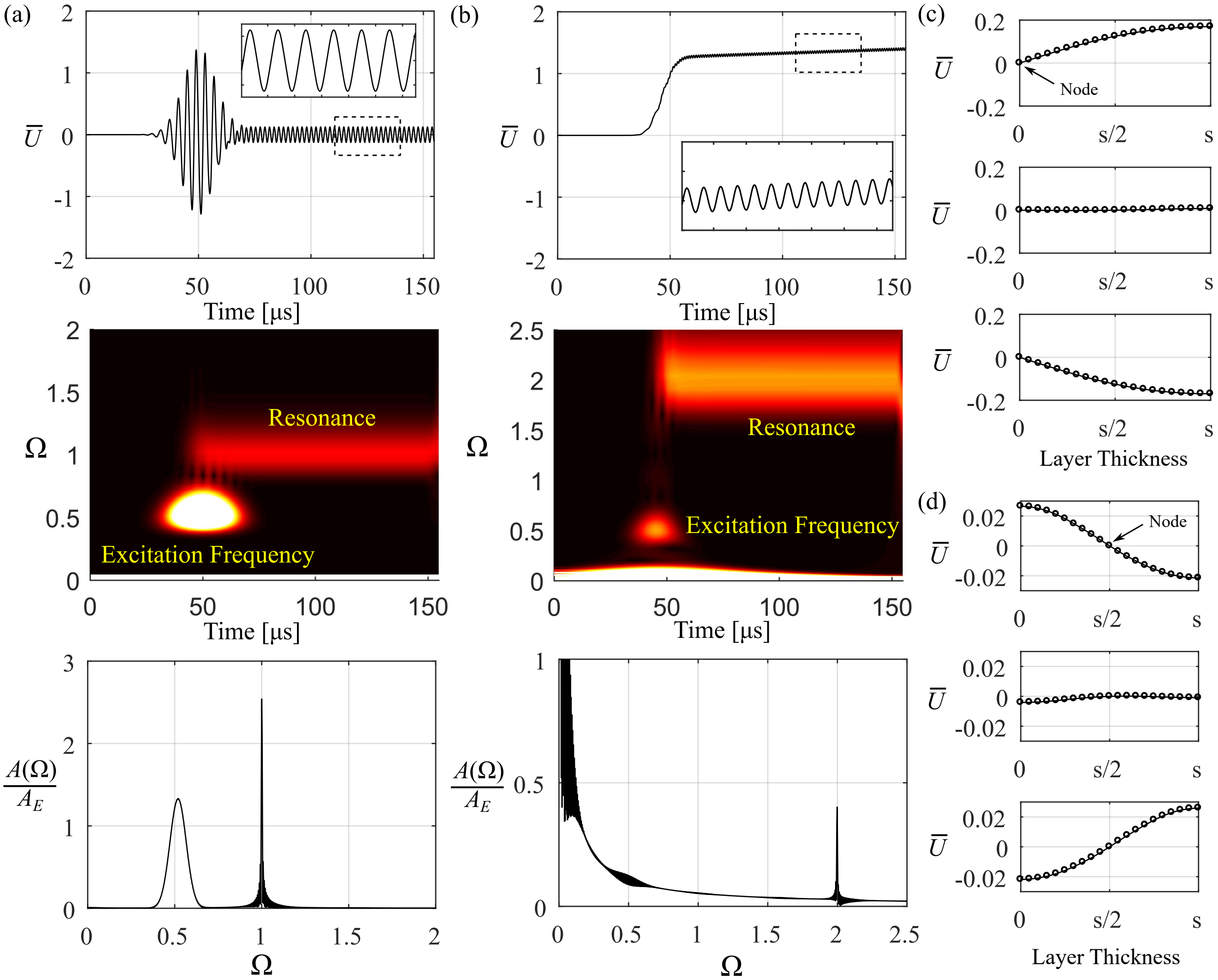

Figure 5.2: Energy transfer through activated layer resonances due to strong contact nonlinearity. Dynamic response of (a) layer 1 and (b) layer 2. The response is extracted at the center point for layer 1 and near the contact boundary for layer 2. Time-domain normalized displacement (top), corresponding wavelet transform (middle) and 2D FFT of the entire time-domain signal (bottom) are plotted for both points. Insets are zoomed views of dashed rectangles indicating resonant oscillations. Wavelet amplitudes are normalized by their maximum amplitude whereas 2D FFT amplitudes are normalized by FFT amplitude of the excitation signal, A_E. Normalized modal deformations of (c) layer 1 and (d) layer 2 under fixed-free and free-free acoustic resonances, respectively. The deformations are plotted for 3 different time instants during resonant oscillations.

also oscillate in a free-free resonance [discussed in terms of energy-frequency dependence later in Fig. 5.3(c)], however, their amplitudes are very small due to relatively weaker excitation energy at later contacts.

This indicates that the combined effects of strong nonlinearity, continuum layers, and dynamic excitations result in the nonlinear energy transfer between frequencies. While many other nonlinear energy transfer mechanisms have been reported, such as sub- [179] and super- [102], [180] harmonics generation, self-demodulation [102], [132], and nonlinear wave mixing [103], [158], the mechanism in continuum phononic materials with contacts is different in that it is fundamentally based on activating *acoustic* resonances of elastic elements (for example, layers in this case). This behavior has been not reported so far, as studies of unconsolidated phononic media were focused at frequencies much lower than modal frequencies of individual elastic elements (for example, particles in granular crystals [62], [162]). At such low frequencies, elastic media between contacts has been considered as point masses. As a result, there exists a lack of coupling between these masses after contact loss, and no resonances are activated. While granular metamaterials [181] and woodpile structures [176] have shown spectral energy transfer through resonances, the mechanism is based on *local* resonances. These studies considered lumped-mass elements, where resonators are only coupled directly to an oscillator at each site. On the other hand, the system studied in this dissertation is not set up as a locally resonant system, in fact, the layers are coupled and modeled as continua. As a result, the resonances observed inside the phononic material correspond to the acoustic resonances of these layers. Further, these acoustic resonances capture the physical deformation of the layers in the form of modes of finite bodies [Figs. 5.2(c) and 5.2(d)] and can also capture higher-order resonances of the layers for high-frequency excitations.

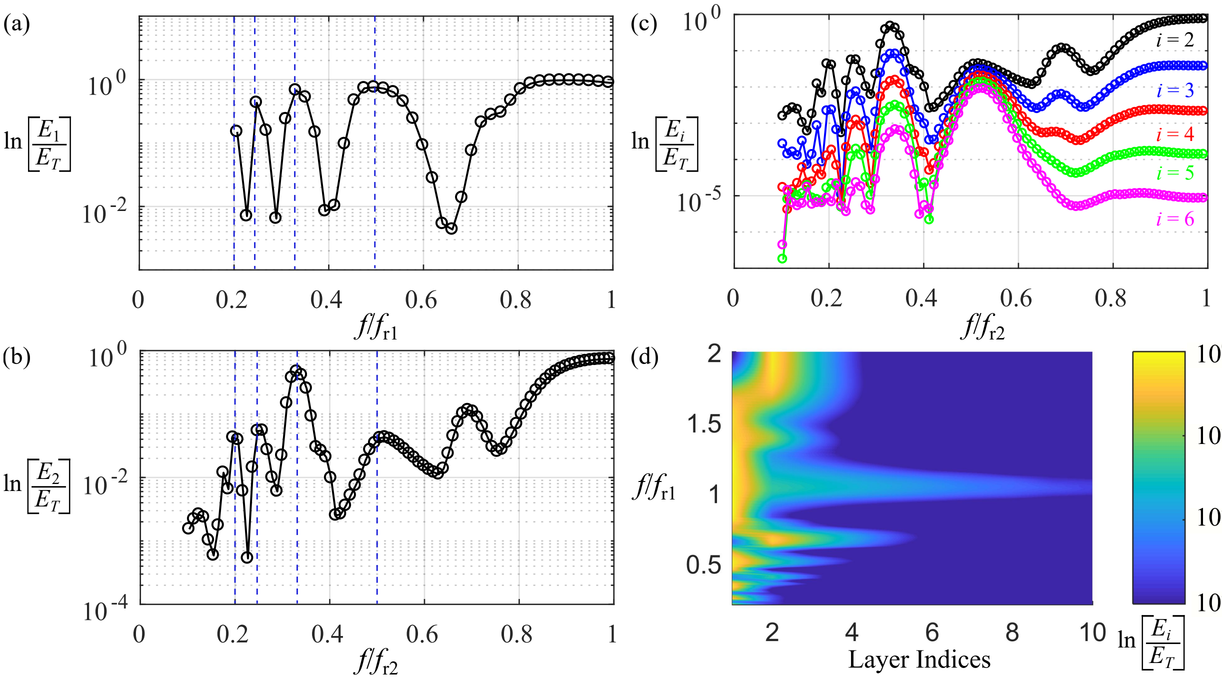

Figure 5.3: Energy distribution within the phononic material due to layer acoustic resonances. Dependence of the energies trapped in (a) layer 1 (E_1) due to fixed-free resonance (f_{r1}) and (b) layer 2 (E_2) due to free-free resonance (f_{r2}) on excitation frequency, f. Vertical dashed lines correspond to when the excitation frequency is a fraction multiple of resonances. (c) Energy stored in the resonances of subsequent layers (E_i), where i indicates layer index from the excitation boundary. (d) Resonance energy distribution in the first 10 layers of the phononic material for different excitation frequencies. The colorbar indicates energy inside the layers normalized by the total energy in the system.

Further, the distribution and dependencies of the energies (normalized by the total energy, E_T) trapped in these layers due to their resonances on the excitation frequency, f, is evaluated (Fig. 5.3). Parametric numerical simulations were conducted by sweeping excitation frequencies from far away from the layer resonances to the layer resonance frequencies. As the excitation frequency approaches the resonance of layer 1, f_{r1}, almost all the energy of the system is stored in layer 1 [Fig. 5.3(a) as $f/f_{r1} \rightarrow 1$]. Interestingly, even when the excitation frequency is a fraction multiple of resonance frequency ($f/f_{r1} = 1/5, 1/4, 1/3, 1/2$), a significant portion of the total energy is stored in layer 1. This is because of higher harmonic responses arising from the nonlinear rough contact. As the wave interacts with the quadratically nonlinear rough contacts, higher harmonics are generated at the contact, which activates the resonances of layer 1. Layer 1 stores more energy when lower-order harmonics, such as the second (for $f/f_{r1} = 1/2$) and third (for $f/f_{r1} = 1/3$), of the excitation frequency fall close to the resonance, compared to other higher-order harmonics (for $f/f_{r1} = 1/4, 1/5$). As expected, the energy stored in layer 2 also increases as the excitation frequency approaches the resonance of layer 2 [Fig. 5.3(b) as $f/f_{r2} \to 1$]. Similarly, fractional multiples of the excitation frequency contribute to activating the resonance of layer 2. Since harmonics with increasing order are associated with reduced amplitudes, the energies stored in layer resonances are increasingly weaker from harmonics with increasing order. For example, the free-free resonances of layer 2 activated for $f/f_{r2} \sim 0.125$ [left-most peak in Fig. 5.3(b)] are much weaker than for other fractional frequencies; particularly, the energy in the layer resonance for $f/f_{r2} \sim 0.125$ is almost three orders of magnitude smaller than the total energy. As the excitation frequency decreases further ($f/f_{r2} \to 0$), corresponding higher-order harmonics become significantly less effective in exciting the free-free resonances of layer 2. At excitation frequency $f/f_{r2} \sim 0.7$, the generated third harmonic is close to the 2$^{\text{nd}}$ order free-free resonance of the layer ($2f_{r2}$). Thus, layer 2 stores more energy at this excitation frequency and shows a local maximum. The energy stored in layer 2 for an excitation frequency of $f/f_{r2} = 0.5$ is much smaller compared to other adjacent fractional frequencies. This is contradictory to the dependence of layer 1 energy on excitation frequency. This difference in the energy dependence of these two layers can be attributed to the relation between their resonance frequencies. Recall that the resonant frequency of layer 2, f_{r2}, is twice the resonant frequency of layer 1, f_{r1}. Thus, most of the total energy is localized in layer 1 when $f = f_{r1} = 0.5f_{r2}$, leaving only a small amount of energy in layer 2.

The energy dependence of the subsequent layers ($i = 3, 4, ...$) on excitation frequency is identical to layer 2 as all these layers oscillate under free-free resonance [Fig. 5.3(c)]. However, energy stored in these layers gradually reduces away from the excitation boundary [Fig. 5.3(d)]. While the reduction in stored energy with propagation distance is also frequency-dependent, energy localization primarily happens in the first few layers ($i < 6$) only [Fig. 5.3(d)]. Clearly, a portion of the wave energy is localized in each of these layers as a wave propagates through them. Specifically, for frequencies that significantly contribute to activating the resonances of these layers. In other words, wave energy at these frequencies sharply reduces as it propagates. Therefore, wave interactions with subsequent contacts do not excite the resonances of the subsequent layers as effectively as previous layers. This can be seen through a monotonic reduction in the energy stored in layers with layer indices [Fig. 5.3(d)]. This is the reason for the reduction in the resonant oscillations of the later layers. The remaining portion of the total energy, which is not stored in these layers, propagates through the phononic material (discussed in Section 5.4). Remarkably, the percentage of total energy propagating through the material is frequency-dependent [Fig. 5.3(d)]. For example, the energy localized near the excitation boundary for $f/f_{r1} \sim 0.5$ and $f/f_{r1} \sim 1$ is almost same as the total energy, whereas for $f/f_{r1} < 0.25$, $0.33 < f/f_{r1} < 0.5$, and $0.5 < f/f_{r1} < 0.6$, only a small portion of the energy is localized and the remaining energy propagates through the material. Clearly, the elastic media between nonlinear contacts contributes to complex dynamics due to the overlapping effects of harmonic responses of contacts and resonances of layers. The energy dependencies presented here further inform that the proposed phononic material can be used for both acoustic attenuation and signal propagation by carefully selecting the excitation frequency with respect to layer acoustic resonances.

5.4 Propagation of localized traveling waves

An interplay between nonlinearity and dispersion gives rise to solitary waves in periodic media [62], [162]. A study of such waves in layered media with exponential material nonlinearity revealed a new type of solitary-like wave [177]. Unlike classical solitons, this new wave exhibited a roof- or ridge-type spatial profile and thus was named a "stegoton". This wave, however, satisfied the other properties of solitons, which are propagation at a constant speed, and speeds being proportional to the wave amplitude. Later, stegotons were observed mathematically in the context of hyperbolic partial differential equations with spatially varying coefficients [182] and in a spring dimer configuration of Fermi-Pasta-Ulam-Tsingou lattices [183]. Still, it is not well understood what role nonlinearity plays in the propagation characteristics of stegotons. Moreover, stegotons have not been reported in a phononic system with physically-motivated nonlinearity, such as contact nonlinearity. In the phononic materials studied here, the combined effects of strong nonlinearity of rough contacts, dispersion from their periodic arrangement, and the presence of elastic layers, give rise to the propagation of stegotons. In this section, these waves and their characteristics in rough contact-based phononic materials are reported.

5.4.1 Formation of stegotons

For a tone burst at excitation frequency, $\Omega = 0.52$, trains of stegotons are observed [Fig. 5.4(a)]. Such trains are generated because of two simultaneous effects: 1) multiple collisions of contacting rough surfaces due to multiple wave cycles in the tone burst excitation, and 2) layer internal reflections (such as seen in the dynamics of an impact of a striker on a Hopkinson bar [184]). Three dominant stegotons observed in the simulations are a result of three strong collisions of rough surfaces during the tone burst interaction with the first rough contact [Figs. 5.1(c) and 5.1(e)]. The loss of contact after these collisions results in a gap between the layers preventing any further collision from the later cycles of the tone burst [Fig. 5.1(c)]. Additional stegotons due to other weaker collisions from tone burst cycles and internal layer reflections are also generated but their amplitudes are relatively negligible (two orders smaller).

The stegotons in these phononic materials are localized traveling waves yet due to the continuum between successive nonlinear contacts, they show a stepwise wave profile [Fig. 5.4(a)] that is different from the continuous shape of classical solitons. This is because displacements are discontinuous across the contact causing steps in the spatial profile, whereas displacements inside layers vary smoothly due to layer deformation. This stepwise profile that consists of both jumps and continuous variation has not been seen in solitary waves in granular crystals, as these systems have thus far been modeled as spring-mass chains. Further, the stegoton spatial profiles continuously change while propagating through a collection of 3 layers, as can be seen at two representative time instants [Fig. 5.4(a)]. Note that the stegotons are propagating through the same 3 layers at both of these time instants. At t_1, the leading part of the stegoton (between 44^{th} and 45^{th} contact) is lower compared to the trailing part (between 42^{nd} and 43^{rd} contact) [Fig. 5.4(a1)]. The opposite is the case at $t_1 + 20\Delta t$ [Fig. 5.4(a2)]. The same change in profile is repeated as the wave propagates to the next layers. Clearly, two simultaneous effects are happening inside the phononic material – 1) macroscopic dynamics of phononic material and 2) localized dynamics within the layers. Macroscopic dynamics means the dispersion from periodicity that counteracts that of the contact nonlinearity, which gives rise to the propagation of compact waves. This is similar to the mechanics of the formation of solitary waves in, e.g., nonlinear granular media. As a result, stegotons propagate with a constant spatial profile between layers despite exhibiting changing profiles within a collection of 3 layers. Additionally, the local dynamics of the continuum layers cause elastic deformations [Inset of Fig. 5.4(a1)]. These localized effects have typically not been considered in nonlinear granular media, where masses are modeled as point masses. In that case, the displacement profile across the particles is constant, and no local effects are seen [62], [162].

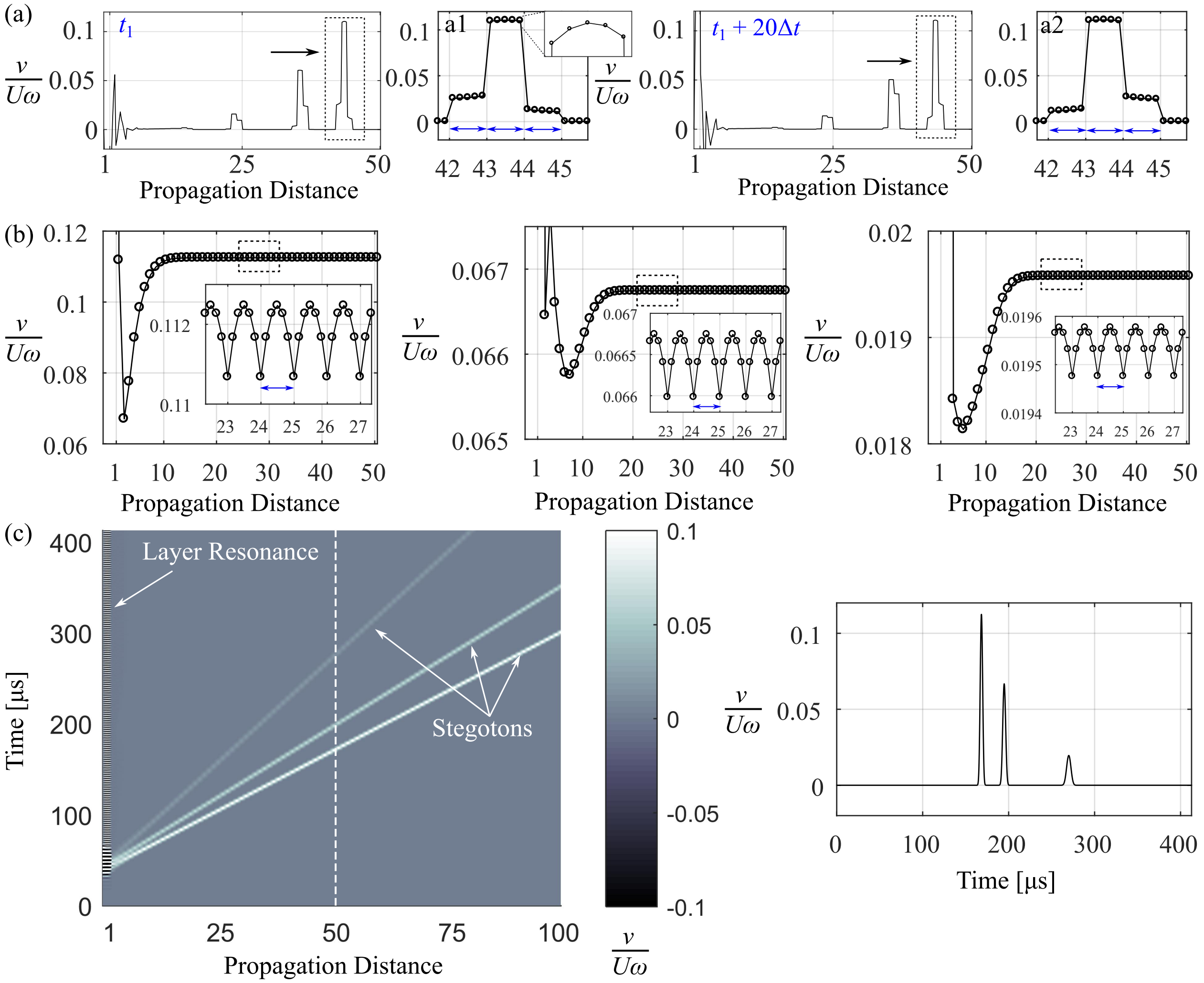

Figure 5.4: Propagation of stegotons. (a) Formation of stegoton trains under tone burst excitation. Results at two different time instants, when stegotons are within the same layers, are shown indicating changing spatial profile of stegotons within these layers. Magnified views of the stegotons in dashed rectangles are to the right (a1-a2). Layer width is marked through blue arrows. Inset of a1 shows stegoton amplitude variation inside a layer between 43rd and 44th contacts. Arrows indicate wave propagation direction. Propagation distance is marked in terms of contact indices. (b) Stegoton amplitude dependence on propagation distance. The three plots correspond to the three stegotons of (a) with amplitudes evaluated at the center point in each layer. Insets show amplitudes evaluated at multiple locations inside each layer, in the neighborhood of the 25th contact (dashed rectangles), highlighting their local variation. The amplitudes are extracted from the temporal wave profile for each spatial point. Results are shown for the first 50 contacts only. (c) Spatiotemporal amplitude plot showing constant propagation speed of the generated stegotons. The temporal profile of the stegotons on the right corresponds to a location near the 50th contact (dashed vertical line).

5.4.2 Characteristic features of stegotons

The spatial width of the stegotons in this phononic material is equal to 3 layers [Fig. 5.4(a)]. This is in contrast to the spatial width of solitary waves arising due to Hertzian contact nonlinearity, which is equal to 5 particle diameters [162], and due to exponentially nonlinear bilayer media, which is equal to 10 layers [177]. As demonstrated in [185], the width of a solitary wave in granular crystal in terms of the particle

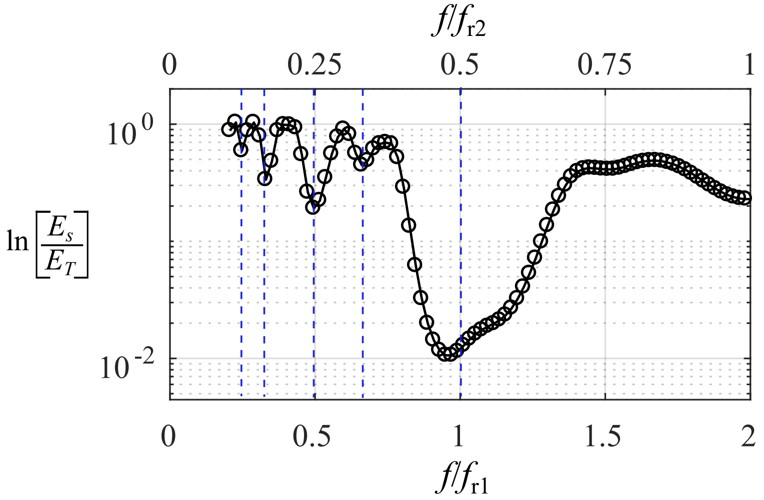

Figure 5.5: Dependence of the energies carried by stegotons, E_S, on the excitation frequency, f. Vertical dashed lines correspond to when the excitation frequency is a fraction multiple of layer resonances.

size depends upon the coefficient resulting from the power-law of contact nonlinearity. Solitary wave width narrows as the exponent of power-law nonlinearity increases. Based on this theory, it can be determined that the rough contact nonlinearity between elastic layers generates more compact localized waves compared to other forms of nonlinearities explored thus far.

The amplitudes of the stegotons, in terms of particle velocity, v, normalized by $U\omega$, (where ω is angular excitation frequency such that $\omega = 2\pi f$, and U is the excitation displacement amplitude), varies within the layer [insets of Fig. 5.4(b)] yet remains constant with propagation distance for a given point inside each layer. Note that the amplitudes shown in Fig. 5.4(b) are evaluated at the center point inside each layer, whereas amplitudes in the insets are evaluated at 5 locations inside each layer. Interestingly, these waves propagate at a constant speed when traced at a particular point [e.g. center point in Fig. 5.4(c)] in each layer. The temporal profile highlights that the temporal width of these localized traveling waves is inversely proportional to their amplitude [Fig. 5.4(c)].

Next, the energy carried by these stegotons (normalized by the total energy, E_T) as a function of excitation frequency, f, is analyzed (Fig. 5.5). The plotted energies, E_S, are of all the stegotons such that $E_S = \sum_1^k E_{Sk}$, where k is the number of stegotons generated in the phononic material. There exist certain frequencies for which stegotons carry very low energy (two orders smaller than the total energy), for example, $f/f_{r1} \sim 1$. This is because most of the total energy at these excitation frequencies is localized in layer 1 (refer Fig. 5.3). Similarly, when the excitation frequency is a fraction multiple of the layer resonances, there exists a drop in the energy carried by the stegotons (refer to the dashed vertical lines in Fig. 5.5). For all other frequencies, stegotons carry a large portion of the energy through the phononic material. This characteristic demonstrates possible applications of this phononic material from filtering to signal propagation. This is because only a small amount of energy propagates through the material for certain frequencies (specifically for $f/f_{r1} \sim 1$) while for others, excited wave energy can travel through the material.

The dependence of stegoton propagation speed (c) on stegoton amplitude (v) [Fig. 5.6(a)], and on the contact pressure between layers (p) is further evaluated [Fig. 5.6(b)]. These relationships are determined at the excitation frequency of $\Omega = 0.52$. A long tone burst ($\zeta = 50/f$ and $\sigma = 10/f$) was used to generate multiple stegotons to find both the $c - v$ and $c - p$ relation. Stegoton amplitudes are evaluated at the center

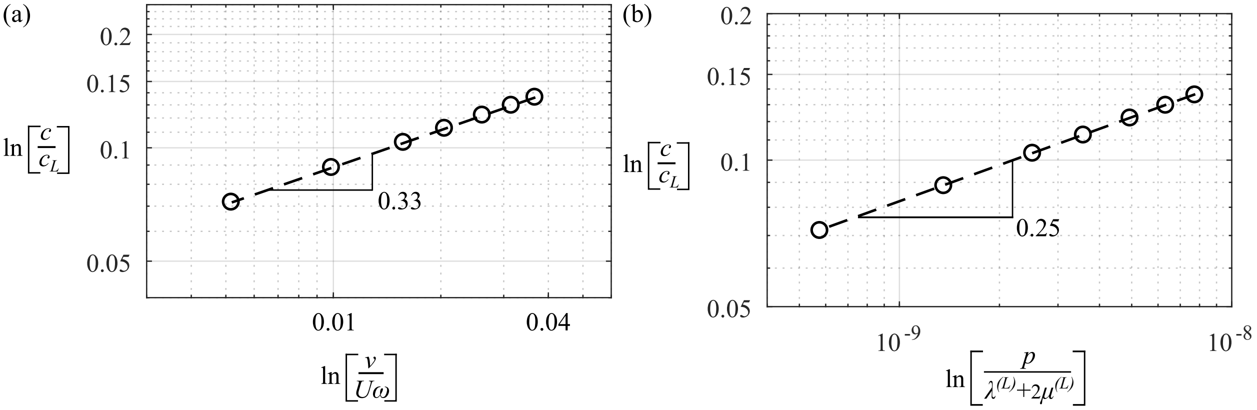

Figure 5.6: Stegoton characteristics due to rough contact nonlinearity. Stegoton wave speed dependence on (a) its amplitude and (b) contact pressure. Dashed lines are linear fit of the normalized variables in log scale. Solid lines indicate slopes of the fitted lines along with corresponding values.

point in the 50th layer and the speed is determined through propagation time delay between two points separated by a distance equal to five layers. The dependence of the speed of stegotons on their amplitudes is found to be a power-law relation with an exponent equal to $\sim 1/3$ [Fig. 5.6(a)]. The dependence of the speed of stegotons on the contact pressure follows a power-law relation with an exponent equal to $\sim 1/4$ [Fig. 5.6(b)].

It is interesting to compare these results to those of stegotons and solitary waves studied in prior work. For example, the dependence of the speed of stegotons on their amplitudes was found to be linear in a bilayer material with exponential nonlinearity [177]. These differences in dependencies potentially arise from the differences in the phononic materials of [177] and in this work, which are the form and type of nonlinearity (material vs contact), nature of nonlinearity (exponential vs quadratic), type of excitation (pulse vs tone burst), and impedance mismatch at the interfaces. In the case of Hertzian contact nonlinearity, the solitary wave speed has a power-law dependence on its amplitude with an exponent equal to $1/5$ and on contact force between particles with an exponent equal to $1/6$ [162]. Clearly, the phononic material with rough contact nonlinearity shows a stronger relationship between 1) the speed and amplitude of the stegotons, and 2) the speed of stegotons and contact pressure, compared to Hertzian contact. This suggests that localized traveling waves of equal amplitudes will propagate faster in continuum phononic material with rough contact nonlinearity compared to granular crystal with Hertzian contact nonlinearity.

Further, the wave speed of stegotons can be tuned through system parameters, such as excitation amplitude, frequency, and layer thickness. As discussed in Fig. 5.6(a), the stegoton speed is proportional to its amplitude. Thus, the speed of stegotons can be tuned by controlling the amplitude of the generated stegotons. This can be achieved by changing the excitation amplitude - a larger excitation amplitude causes stronger collisions at the rough contacts forming stegotons with higher amplitudes, and vice versa. Similarly, as discussed in Fig. 5.5, the amount of energy carried by the stegotons depends upon the frequency of excitation. In other words, the properties of stegoton propagation (i.e. their amplitude and wave speed) can be changed by changing the excitation frequency. The speed of stegotons also depends upon the layer thickness. The speed-amplitude relation of stegotons for different layer thicknesses is evaluated by following the method of Fig. 5.6(a). For all the simulated cases, excitation frequency was appropriately selected to account for the change in layer resonance frequencies, i.e. to keep normalized frequency ($\Omega = 0.52$) the same. Increasing the layer thickness in phononic material increases the wave speed of the stegotons for a given amplitude, however, the relationship

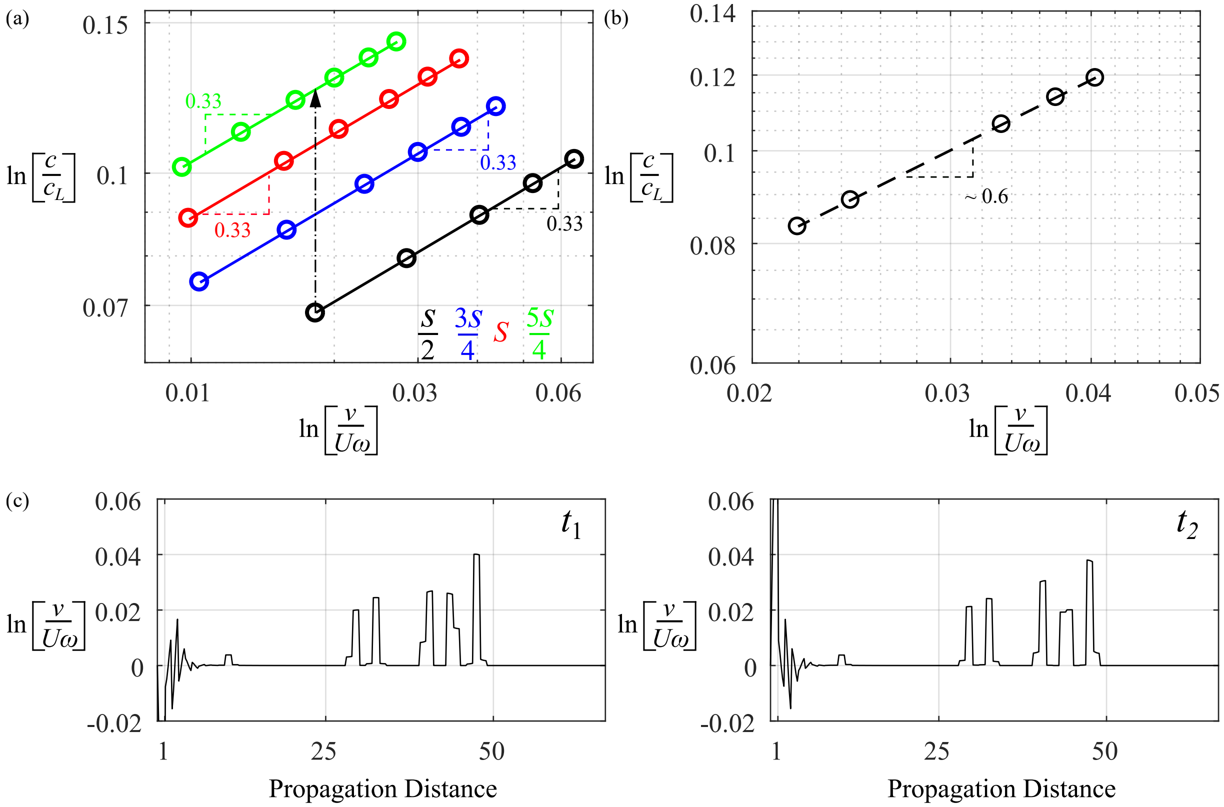

Figure 5.7: Stegoton tunability. (a) Stegoton wave speed dependence on its amplitude for different layer thicknesses ($s/2, 3s/4, s$, and $5s/4$). Dashed lines indicate slopes of the fit (solid lines) along with corresponding values. The arrow shows speeds increase with layer thickness for a given amplitude. (b) Stegoton speed-amplitude relation when contact power-law exponent is 4 (i.e. $\beta = 0.75$). (c) Snapshots of propagation of stegotons in (b) for two different time instants t_1 and t_2.

between the speed and amplitude remains unchanged [Fig. 5.7(a)]. This is likely because the relationship is governed by contact law, which depends only on the contacts and not the layer thickness. However, changing the layer thickness changes the overall dispersion and thus affects the speed of the stegotons. Finally, stegotons are generated from the counterbalance between nonlinearity and dispersion, hence, their speed-amplitude relation would depend upon the exponent of rough contact law. Rough contacts with different power-law exponents are achievable through different roughness topographies between contacting layers [115]–[117]. Therefore, stegoton properties can be potentially tuned through appropriate roughness selection as well. To briefly validate this, a phononic material with a larger exponent, specifically, contact power law exponent of 4 (corresponding to $\beta = 0.75$) is considered. The coefficient of proportionality is modified through the trial and error method to ensure the convergence of the problem. By following the method of Fig. 5.6(a), the obtained speed-amplitude relation for this increased exponent is 0.59, i.e. ~ 0.6 [Fig. 5.7(b)], which confirms that increasing the exponent of the power law increases the speed-amplitude relation. Further, the snapshots of stegoton propagation for this increased exponent case [Fig. 5.7(c)] highlights that the spatial width of the stegotons is 2 layers, which is more compact than the width observed when the power-law exponent is 2, which is 3 layers [refer to Fig. 5.4(a)]. This is consistent with the trend that increasing the power-law exponent reduces the spatial width of the localized traveling waves.

5.4.3 Collision dynamics of stegotons

Studies of collision dynamics of solitary waves formed in granular crystals have shown that these waves escape frontal collision, however, they generate additional weaker solitary waves [186], [187]. This is because the collision process releases some energy, owing to the squeezing of solitary waves during a collision, which eventually contributes to the generation of secondary solitary waves [186]. Surprisingly, the collision of stegotons in layered material with exponential nonlinearity did not result in the generation of additional waves [177]. In contrast, the collision of counter-propagating stegotons of equal amplitude in phononic materials with rough contacts generates a train of secondary stegotons, as shown in this section.

To study collision dynamics, a tone burst ($\zeta = 2.5/f$ and $\psi = 0.5/f$) is excited from each end of the phononic material at frequency $\Omega = 0.52$ such that the excited signal results in a single dominant stegoton propagating from both ends towards each other. Two cases of phononic material are studied - with odd ($n = 101$) and even ($n = 100$) numbers of layers. In the case of an odd number of layers [Fig. 5.8(a)], the collision takes place inside the elastic layer at the center ($i = 51$) of the phononic material. Upon collision, the formation of secondary stegotons is observed with an amplitude (and therefore speed) much (two orders) smaller than primary stegotons [Figs. 5.8(a) and 5.8(b)]. In the case of an even number of layers ($i = 100$) [Fig. 5.8(c)], the collision takes place at a rough contact (between $i = 50$ and $i = 51$). Generation of secondary stegotons is observed in this case as well, however, the amplitudes of these generated stegotons are significantly higher than the secondary stegotons from the collision inside the layer [Figs. 5.8(b) and 5.8(d)]. In both cases, a phase shift in propagating stegotons post-collision is observed [Figs. 5.8(e) - results shown for an even number of layers case only] - an observation consistent with the collision dynamics of solitary waves in granular crystals [187]. The dependence of the amplitudes of secondary stegotons on the amplitudes of primary stegotons in both collision cases is further evaluated [Fig. 5.8(f)]. There is an order of magnitude difference between the amplitudes of secondary stegotons generated at contact and within a layer.

To understand the role of the number of layers on the generation of secondary stegotons, the displacements and energies of the layers at and in the vicinity of collision are studied. When the collision of stegotons takes place inside a layer, the layer does not move before, during, or after the collision [Fig. 5.9(a) - refer i_c]. On the other hand, adjacent layers first move towards the center layer and then away from it post-collision, resulting in a contact loss [Fig. 5.9(a) - refer i_{c-1} and i_{c+1}]. This is because the stegoton propagating from left to right forces the layer i_{c-1} to initially move to the right, which eventually ceases due to the stegoton propagating in the opposite direction. This backward (right to left) propagating stegoton, when coming through the collision, forces the same layer to move to the left. The reverse is the case for the layer i_{c+1}. Despite these surrounding motions, the center layer is always at rest. As a result, the total kinetic energy in the center layer ($i_c = 51$) is ~ 0 unlike adjacent layers [$i_{c-1} = 50$ and $i_{c+1} = 52$], refer to Fig. 5.9(c). However, there exists a non-zero potential energy inside the center layer, which is significantly larger than the potential energy in other layers [Fig. 5.9(c) - red lines]. This excess potential energy is a result of the squeezing of the stegotons, equivalent to the squeezing of solitary waves in granular crystals [186], during the collision. This squeezing can be physically understood as follows - when two identical stegotons propagating towards each other collide, the layers that came in contact due to leading fronts of the stegotons start to move in the reverse direction due to repelling forces. At the same time, the trailing fronts of the stegotons are moving in the direction of the wave propagation, eventually causing them to squeeze. Note that stegotons have a spatial width of 3 layers and therefore the trailing front is not affected by the dynamics of the leading front for a certain duration of time, allowing such squeezing. The potential energy released from this dynamics, however, is temporarily transferred to the center layer during the collision [Fig. 5.9(c)] and thus only generate weaker

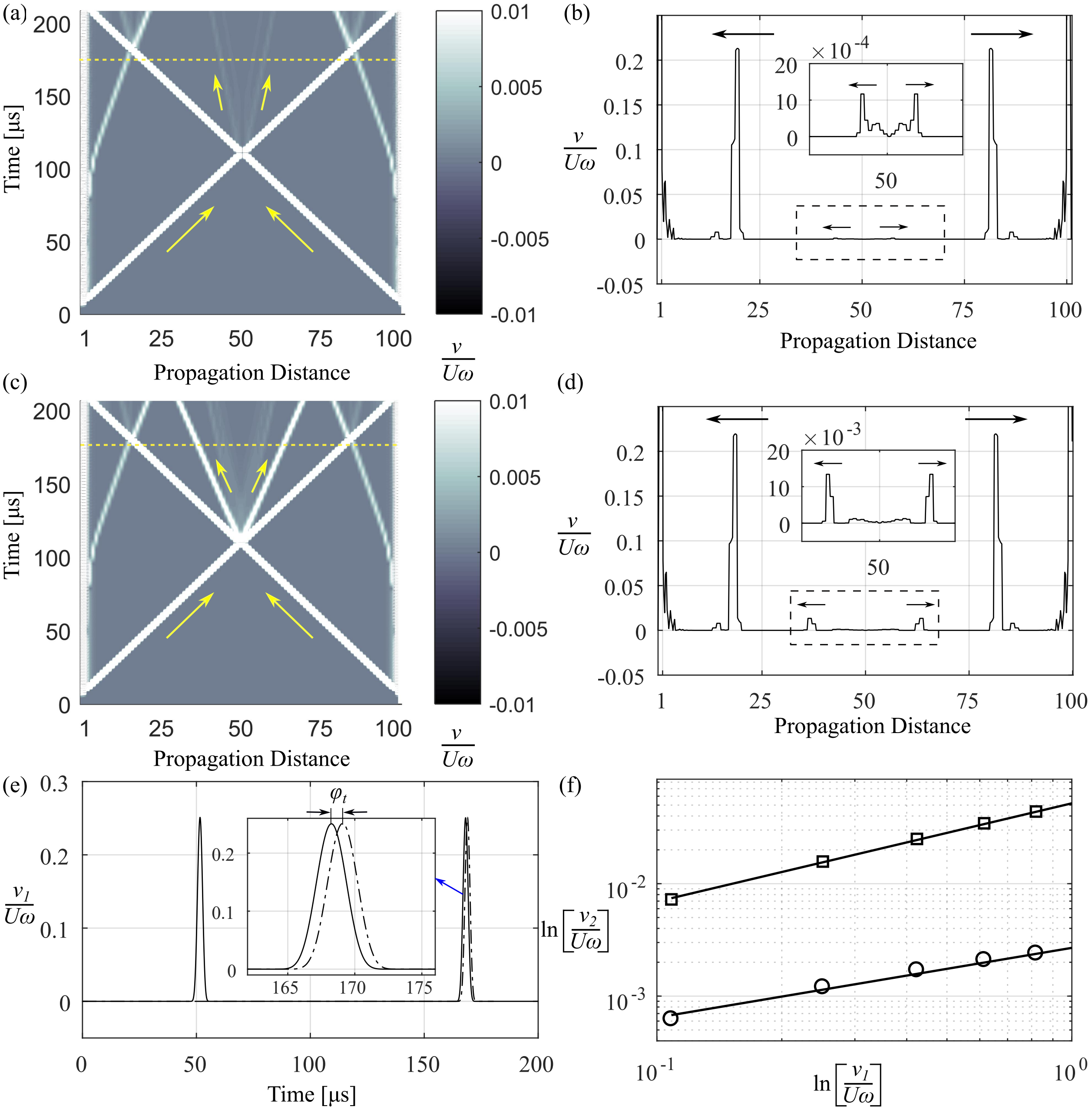

Figure 5.8: Collision dynamics of stegotons. Spatiotemporal amplitude plot of stegotons when the collision happens (a) inside a layer (for an odd number of layers) and (c) at a rough contact (for an even number of layers). (b) and (d) are snapshots of (a) and (c), respectively, at a time equal to 175 μs [dashed yellow line in (a)-(c)]. Arrows indicate the direction of propagation with longer and shorter arrows correspond to primary and collision-induced secondary stegotons, respectively. Insets in (b)-(d) are zoomed views of dashed rectangles. Propagation distances are in terms of contact indices. (e) Phase shift due to the collision of stegotons. Stegotons are recorded inside the 80th layer in the system with $n = 100$ when a stegoton is excited from each end (solid) and left end only (dashed). Inset is a zoomed view of the overlapped stegotons. (f) Dependence of the amplitudes of secondary stegotons, v_2, on primary stegotons, v_1 when the collision happens at a rough contact (squares) and inside a layer (circles).

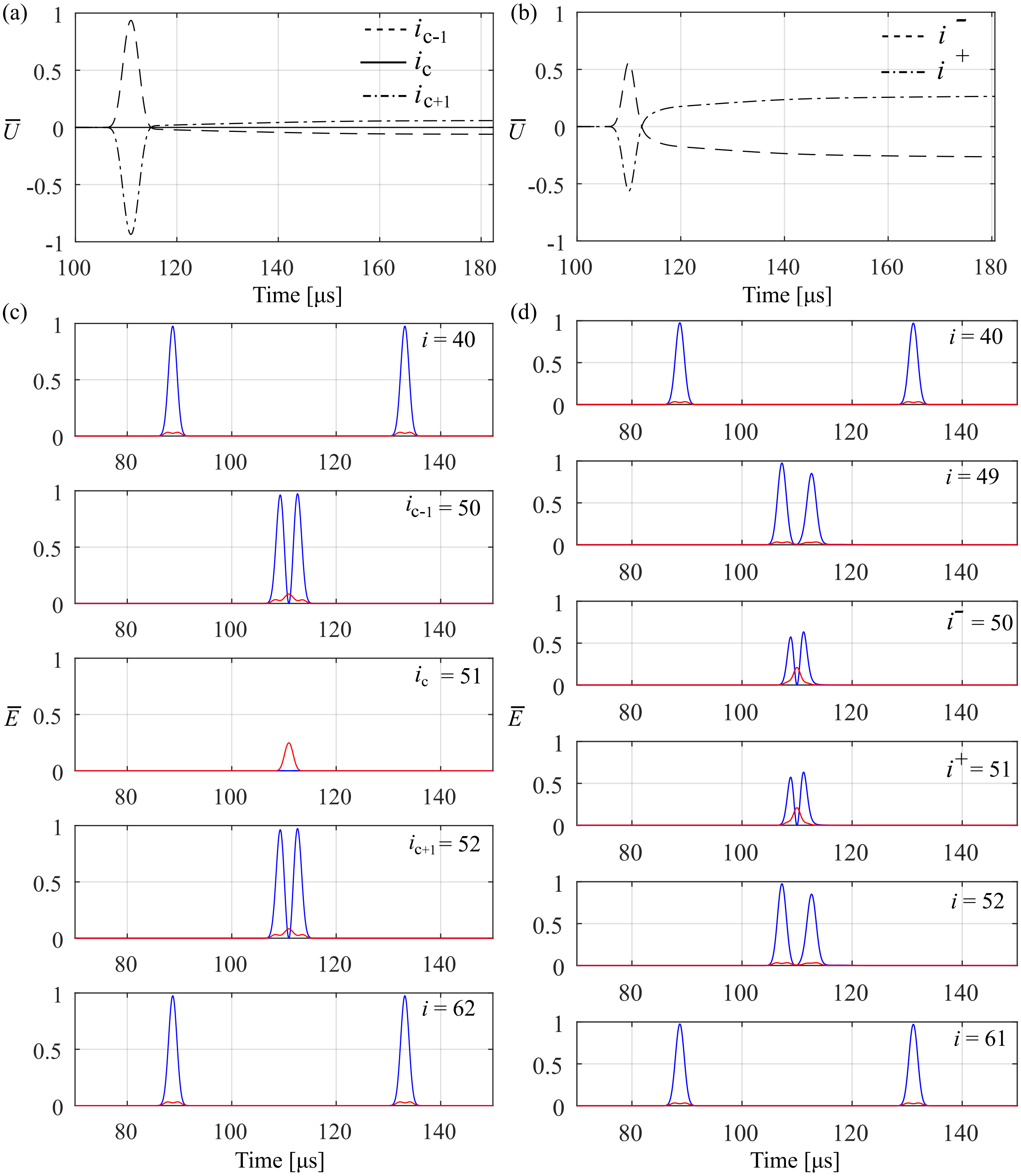

Figure 5.9: Normalized displacement profile of the layers in the vicinity of collision in phononic material with an (a) odd and (b) even number of layers. For an odd number of layers, i_c is the layer index in which collision is taking place, while i_{c-1} and i_{c+1} are the layers before and after i_c, respectively. For an even number of layers, i^+ and i^- are the layers before and after the contact where collision is taking place. Signals are recorded at the center point inside layers. Normalized kinetic (blue) and potential (red) energy of the layers in systems with an (c) odd and (d) even number of layers. $\bar{E}$ are energies normalized by the total energy of the stegoton. The layer indices are located at the top-right corner of each subplot.

secondary stegotons [Figs. 5.9(a) and 5.8(b)]. As stegotons propagate through the collision, they regain their kinetic energy [Fig. 5.9(c) - refer $i = 40$ and $i = 62$]. This can also be confirmed by the fact that the kinetic energy in the stegotons post-collision is only $\sim 0.005\%$ smaller than the pre-collision ones.

When stegotons collide at a contact, both the layers adjacent to the contact (i^- and i^+) change their position causing separation of contacting surfaces post-collision [Fig. 5.9(b)]. This can be understood in the same way as the motion of the adjacent layers in an odd number of layers. The squeezing of the stegotons in this case also releases potential energy [Fig. 5.9(d)], which cannot be stored at an interface and needs to be released. The phononic material considered here can only support localized traveling waves, hence, the energy is released in the form of (secondary) stegotons [Figs. 5.8(c) and 5.8(d)]. It is observed that some of this potential energy is temporarily stored in the adjacent layers [Fig. 5.9(d) - refer $i = 50$ and $i = 51$]. The energy in the layers in the vicinity of the collision also shows an evolving difference pre- and post-collision [Fig. 5.9(d) - refer $i = 49$ and $i = 52$], which is likely because of the overlapping effects of the leading and trailing fronts of the forward and backward propagating stegotons. Eventually, the stegotons attain a stable energy [Fig. 5.9(d) - refer $i = 40$ and $i = 61$]. Specifically, we observe that the energy in the stegotons post-collision is 0.4% smaller than pre-collision, indicating a stronger percentage of energy being utilized during the collision for the generation of secondary stegotons, compared to the case with an odd number of layers. In the absence of contact nonlinearity, it is possible that the energy imbalances upon collision in the system of [177] were stored inside the layers and thus no secondary stegotons were seen. Clearly, the dynamics of stegotons in phononic materials with rough contacts not only depend on the contact nonlinearity and elastic layers, but they also depend on the finite dimensions of the phononic material that can result in complex collision dynamics.

5.5 Physical constraints: Effects of light external precompression

While zero precompression exhibits interesting wave dynamics, such phononic material is an ideal system. From a physical perspective, a light precompression needs to be applied for interfaces to stay in contact. Interestingly, such a system still exhibits strong nonlinearity if the wave amplitude is larger than predeformation. This condition still leads to contact separation and collision, ensuring contact clapping. In the previous section, nonlinear responses of uncompressed systems were discussed. These responses include the propagation of stegotons and activation of layer resonances. In this section, how these responses are affected when light precompression is applied is studied. Further, light precompression may in fact support additional nonlinear responses not possible with uncompressed or strongly compressed media. Overall, two key questions are explored: (1) the changes in reported nonlinear responses of these phononic media (acoustic resonances, stegotons, and harmonic generation) when non-zero precompression and high amplitude excitation are involved, and (2) the coexistence of strongly and weakly nonlinear wave responses.

In this study, the numerical simulations are conducted in two stages: first, the model solves the static problem of external precompression to determine the deformed state of the phononic material and predeformation in the springs. Then, a wave propagation study as explained in Chapter 3 is conducted. The output of the static analysis is considered as the initial conditions for the wave propagation problem. A longitudinal wave pulse [wave schematic in Fig. 5.10(a)] of amplitude, U, and center frequency, f, with a Gaussian modulation (parameters, $\zeta = 2/f$, $\psi = 0.5/f$ for Eq. 3.8 was excited. Note that the maximum displacement of the input pulse [$\max(\mid +u \mid, \mid -u \mid)$] is smaller than excitation amplitude, U, due to Gaussian modulation yet larger than predeformation to cause contact clapping (i.e. $U > |u| > \delta_0$). This specific wave profile corresponds to the typical response of a broadband ultrasonic contact transducer. Importantly, using a single cycle input simplifies the nonlinear study and enables isolating the effects from light precompression. This would not have been achievable with an excitation comprising numerous cycles as investigated in the previous section.

5.5.1 Nonlinear wave disintegration

In this section, the evolution of the input wave profile in the phononic material with light external precompression and high amplitude excitation is studied. Specifically, an example case of $u/\delta_0 \approx 1.2$ ($U = 5$ nm and $p_0 = 10$ kPa), which activates strong nonlinearity as well as facilitates the study of the effect of external compression is presented. Here, a non-dimensional frequency, Ω, is introduced such that the frequencies are normalized by the lower-edge frequency of the first band gap of the linearized phononic media for the applied p_0 (i.e. band gap starts at $\Omega = 1$ or $f = 0.258$ MHz). Two representative cases of input pulse are studied: (1) with center frequency in pass band ($\Omega = 0.5$ or $f = 0.129$ MHz) and (2) with center frequency at band edge ($\Omega = 1$ or $f = 0.258$ MHz). The first pulse, consisting of a wide band of frequencies within $0 < \Delta\Omega < 1$, was excited to analyze nonlinear wave propagation in a highly dispersive frequency regime of the linearized phononic media. On the other hand, the second pulse, consisting of a wide band of frequencies within $0 < \Delta\Omega < 2.5$, was excited to analyze the effect of band gaps on nonlinear wave propagation.

The wave profile changes as the wave propagates through the phononic material [Fig. 5.10(a)]. Particularly, the input pulse that originally consists of both compression and extension displacement, gradually transforms to a profile that is predominantly in compression only [compare wave profile in layer 1 vs in layer 20 in Fig. 5.10(a)]. As the wave propagates, the tensile portion of the pulse vanishes with each layer [note a gradual reduction in negative displacements from layer 2 to 20 in Fig. 5.10(a)]. Moreover, the transmitted compressional part is followed by small-amplitude oscillatory waves. In fact, the Gaussian input pulse eventually evolves into a waveform that contains three distinct features: (1) a steep increase in profile at the wave front, followed by (2) a gradual amplitude reduction, and (3) an oscillatory tail. This transformation can be understood as follows: The profile of the pulse transmitted across a contact is a combined effect of contact nonlinearity and weak compression. The contacts transmit all compressive forces, whereas only tensile forces that are just enough to counteract the light precompression are transmitted. As a result, once tensile forces exceed precompression, contact loss occurs. Therefore, the only harmonic waves supported inside the phononic material are those that contain small amplitude displacements.

This wave evolution also causes energy transfer within the spectral domain, encompassing both strongly and weakly nonlinear effects in the phononic material. Specifically, layer 1 resonates at a frequency, $\Omega = 2$ [note resonant oscillations in Fig. 5.10(a) and a spectral peak in Fig. 5.10(b) for layer 1]. This resonance corresponds to the mode of the layer under the fixed-forced BC. Note that layer 1 is held fixed at the left end by virtue of the excitation profile whereas the right end is a rough contact. This mode is at a frequency slightly higher compared to the first fixed-free mode of the layer, i.e. acoustic resonance given by $\Omega_r = 1.876$ ($\Omega_r = c_L/4s$). This is because, unlike the uncompressed system, the lightly compressed system experiences a non-zero spring force at the contact end, which pushes the mode of the layer to a higher frequency. Surprisingly, layer 2 also displays a spectral peak at the same frequency [refer to inset in Fig. 5.10(b) for layer 2]. In an uncompressed system, the second layer resonates at a frequency twice that of layer 1 [104], as it loses contact with adjacent layers after wave interaction. However, in the current system, both layers (1 and 2) remain in contact due to external precompression, a state unachievable in an uncompressed system. Consequently, a portion of the resonant energy from layer 1 is possibly transmitted

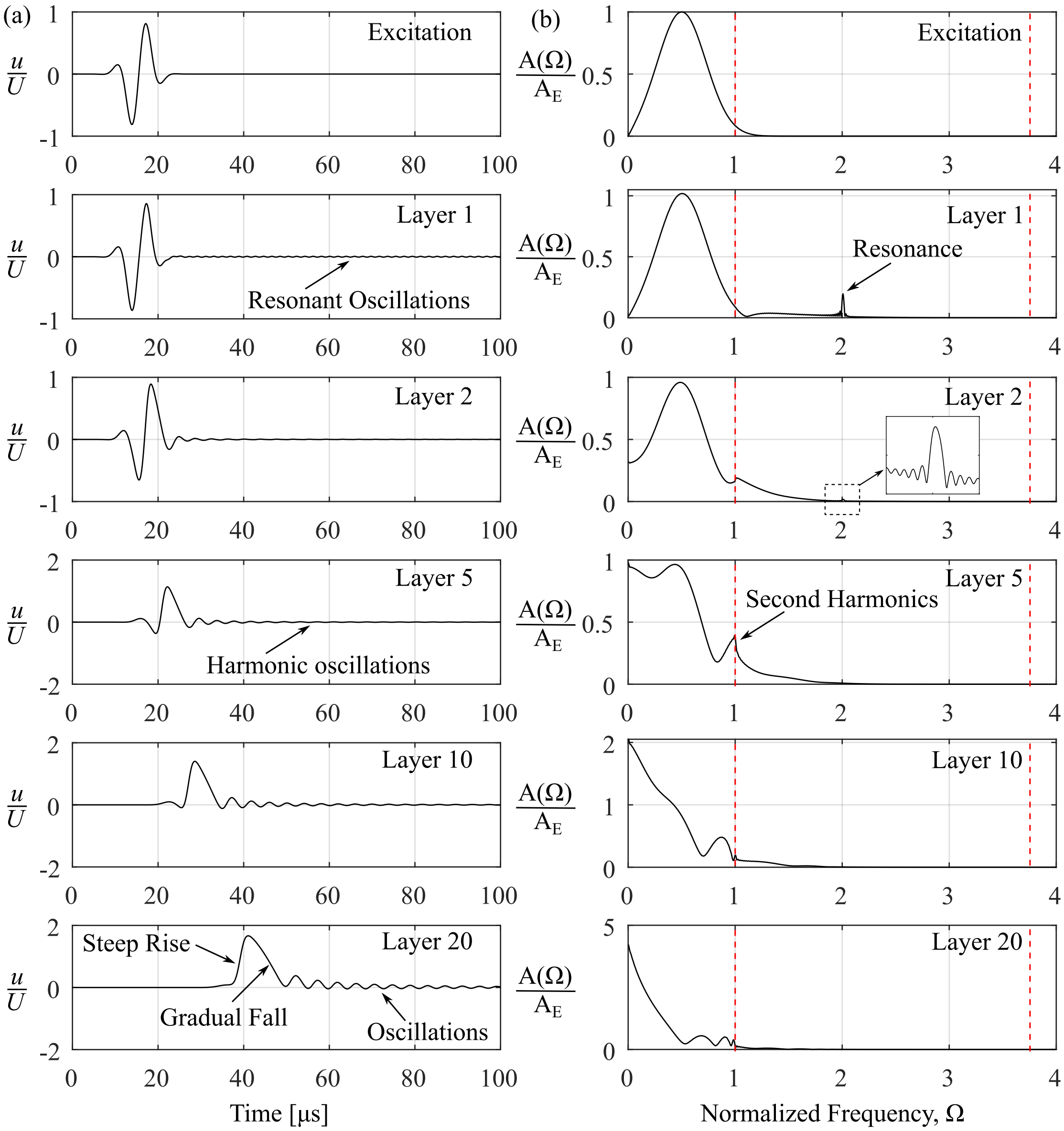

Figure 5.10: Evolution of input pulse with center frequency at $\Omega = 0.5$. (a) Displacement-time profile and (b) frequency content of the propagating wave at multiple locations inside the phononic material. Wave displacements, u, are normalized by pulse excitation amplitude, U, and spectral amplitudes are normalized by spectral excitation amplitude, A_E. The signals are recorded at the center point in the corresponding layers and the layer indices are numbered from the excitation boundary. Red dashed lines are band gap edges.

to layer 2, resulting in a spectral peak at $\Omega = 2$. In subsequent layers, second harmonics are generated, i.e. $\Omega = 1$ [refer to the spectral peak at Fig. 5.10(b) for layer 5] - a feature typical of weakly nonlinear systems. These harmonics, however, lie on the band gap edge and beyond, prohibiting their propagation and causing their spectral amplitude to diminish in later layers (e.g., layers 10 and 20). Frequencies within the pass band propagate while those close to the band gap edge propagate at extremely slow speed. Eventually, the propagating frequency components consist primarily of low frequencies close to 0 Hz, forming a localized traveling wave.

One can think of the transformation of the input wave profile and its frequency content as a “disintegration”

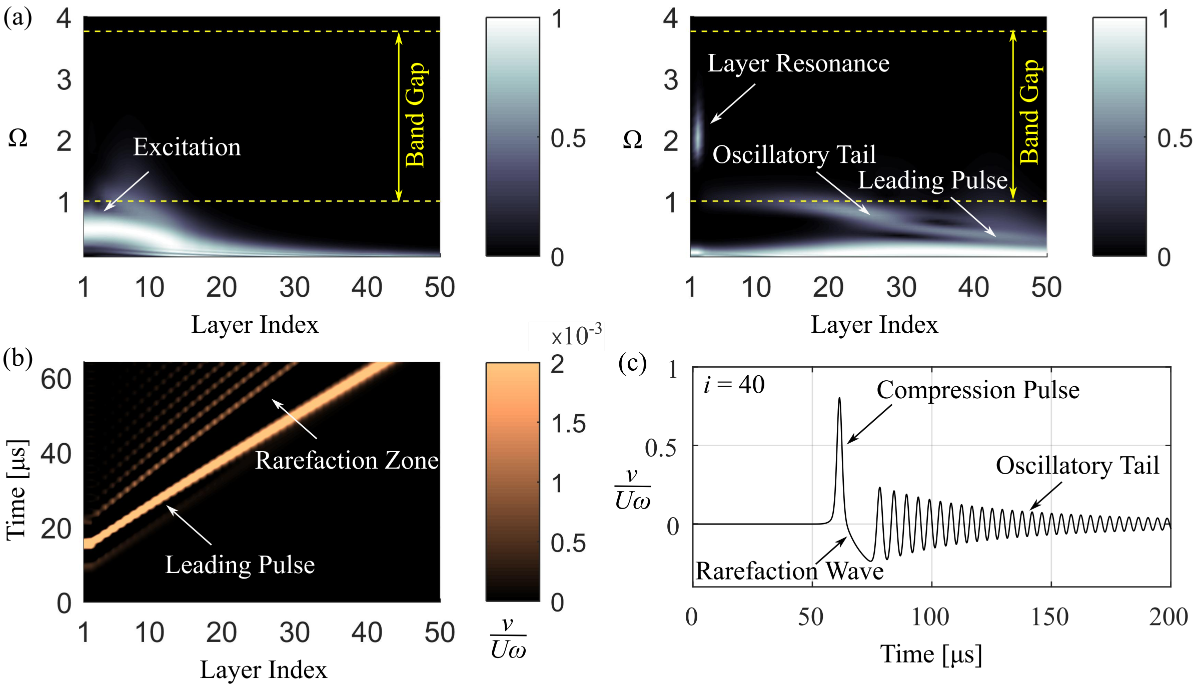

Figure 5.11: (a) Spatio-spectral and (b) spatiotemporal plots of nonlinear wave propagation for excitation at $\Omega = 0.5$. Spatio-spectral plot (normalized by its maximum value) is shown at an instant when the leading pulse is between the 10th and 20th layers (left) and between the 40th and 50th layers (right). Dashed yellow lines are band gap edges. Layer indices are marked from the excitation boundary. (c) Temporal profile of the disintegrated wave inside the 40th layer. Wave amplitude is denoted in terms of particle velocity, v, normalized by excitation amplitude, U, and angular frequency, ω.

of the input pulse. Here, disintegration is referred to as a transformation of the input pulse into (1) leading pulses of compressive nature, (2) transitioning zone of a rarefaction nature, and (3) tails of decaying amplitudes of harmonic nature. This can be seen in terms of the spatial distribution of frequency content [Fig. 5.11(a)] and temporal dependence of particle velocity [Figs. 5.11(b) and (c)]. Despite exciting energy in the system around $\Omega = 0.5$, the energy content within phononic material spreads spatially due to dispersion while some remains trapped in the form of layer resonances [Fig. 5.11(a)]. The oscillations correspond to frequencies near the band edge that propagate at a much slower speed. The leading pulse propagates faster than the oscillatory tails and thus overtakes them, causing disintegration, which is clearly visible away from the excitation boundary. The pulse and oscillatory wave profiles are linked through a rarefaction front [Fig. 5.11(c)]. As a result, the duration over which a rarefaction wave exists in a layer increases with propagation distance [Fig. 5.11(b)]. This shows that phononic material with contact nonlinearity can support rarefaction waves given non-zero external precompression. Interestingly, similar wave disintegration has been reported in nonlinear metamaterials but with softening-type nonlinearity, i.e. where the exponent of power-law nonlinearity is < 1 [76], [80]. Specifically, these studies reported that an excited compression pulse transforms into a leading rarefaction pulse in tensegrity [76] and origami metamaterials [80].

A similar wave disintegration occurs even in the case when the center frequency of the excited pulse is at the linearized band gap edge, i.e. $\Omega = 1$ (Fig. 5.12). Importantly, the frequencies $\Omega > 1$ do not propagate through the phononic material, indicating that the band gap exists at these frequencies in this strongly nonlinear regime. In this case, oscillatory tails consist of frequencies within the pass band only. Since the excitation frequency is closer to the resonance frequency of layer 1, there are stronger resonant oscillations of layer 1 compared to when the excitation center frequency is $\Omega = 0.5$ [Compare oscillations at layer index $= 1$ in Fig. 5.11(b) and Fig. 5.12(b)].

The leading compression pulses in these phononic materials are in fact localized traveling waves that propagate with constant speed and amplitude. Due to the hybrid nature of the phononic material, which is continua connected through discrete nonlinearity, these compression pulses are in the form of stegotons showing a step-wise spatial profile [104]. Due to light precompression, the material support two additional types of waves: rarefaction and oscillatory waves.

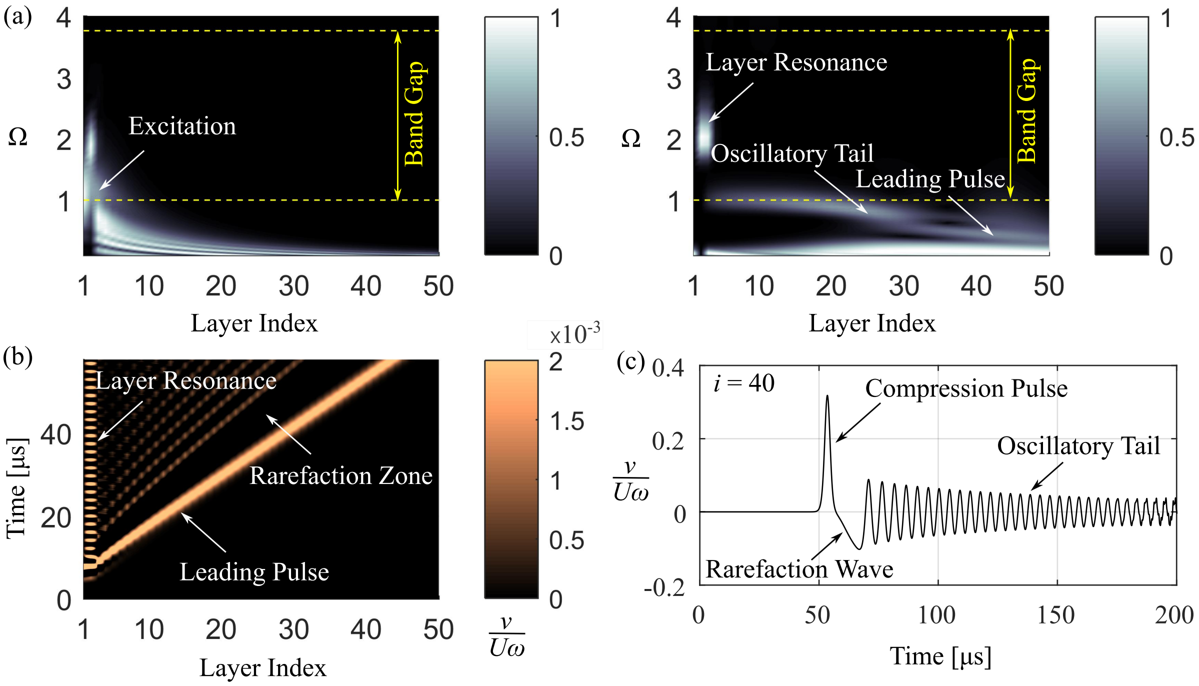

Figure 5.12: (a) Spatio-spectral and (b) spatiotemporal plots of nonlinear wave propagation for excitation at $\Omega = 1$. Spatio-spectral plot (normalized by its maximum value) is shown at an instant when the leading pulse is between the 1st and 10th layers (left) and between the 40th and 50th layers (right). Dashed yellow lines are linearized band gap edges. Layer indices are marked from the excitation boundary. (c) Temporal profile of the disintegrated wave inside the 40th layer.

5.5.2 Tunability of compression pulses

In this section, the dependence of these nonlinear waves on external precompression is characterized. Specifically, how light precompression can be used to tune and control the leading compression pulses is discussed, which offers greater flexibility and feasibility in utilizing these phononic materials for engineering applications.

For the same input amplitude, the amplitude of the generated compression pulse can be controlled through external precompression. Particularly, the amplitude of these pulses increases with an increase in precompression [Fig. 5.13(a)]. This contradicts the expectation that increasing precompression should result in a decrease in the ratio between predeformation and wave amplitude (δ_0/u), leading to weaker nonlinearity and relatively less momentum transfer across the contacts. Consequently, it would be anticipated that increasing precompression would yield compression pulses with diminishing amplitudes. However, keeping

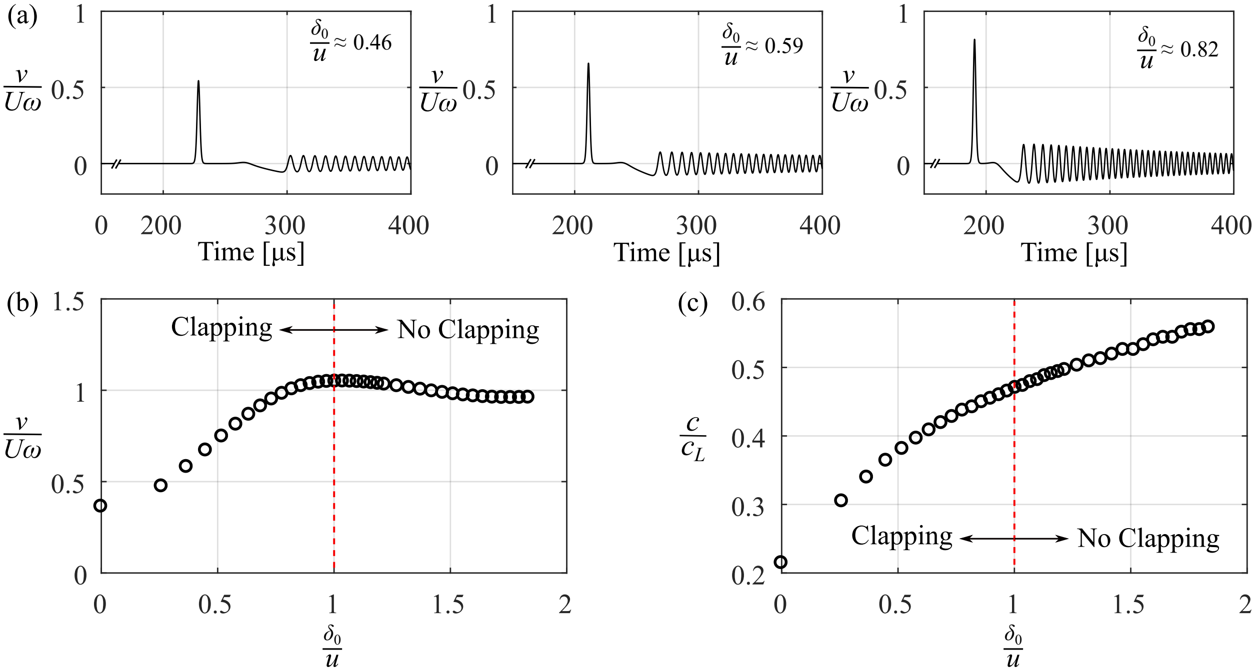

Figure 5.13: Tunability of nonlinear waves through precompression. (a) Disintegrated wave profile inside the 150th layer for three different precompressions: $\delta_0/u = 0.46$ ($p_0 = 3$ kPa), $\delta_0/u = 0.59$ ($p_0 = 5$ kPa), and $\delta_0/u = 0.82$ ($p_0 = 10$ kPa). Dependence of pulse (b) amplitude and (c) wave speed on precompression. Red dashed line is the precompression threshold below which contact clapping occurs.

the same excitation displacement amplitude in the analysis requires larger external work to be done on the system for larger precompressions. This is due to the dynamic excitation having to overcome the stronger contact forces resulting from increased precompressions. Overall, increasing precompression draws more input energy for the same excitation frequency and amplitude, which subsequently generates compression pulses with larger amplitudes. Moreover, the rarefaction and harmonic wave amplitudes also increase with compression pulse amplitudes. In other words, stronger precompression supports tensile waves of high amplitudes. These observations lead to the conclusion that lightly compressed systems exhibit nonlinear wave responses that combine features of uncompressed and strongly compressed systems, offering control over these responses. Specifically, the high amplitude portion of the excitation contributes to strongly nonlinear responses (i.e., compression pulses of stegoton-type) similar to those observed in the uncompressed system, while low amplitudes contribute to weakly nonlinear responses (i.e., frequency filtering and harmonic waves) resembling those in strongly compressed systems. Nonetheless, the transition zone from compression pulse to harmonic oscillations is only observed in weakly compressed systems. As waves propagate, compression pulses separate from the rarefaction waves. It is worth noting that the time delay between the compression pulse and rarefaction front can also be controlled through precompression [Fig. 5.13(a)].

As discussed, the compression pulses are in fact solitary waves as these pulses propagate with constant speed and amplitude. How the amplitude and speed of these pulses depend on precompression is discussed next and the threshold value of precompression that can still generate these strongly nonlinear responses is informed. Interestingly, the compression pulses are generated even for the cases where contact clapping is restricted, i.e. when predeformation is larger than the excitation amplitude ($\delta_0/u > 1$) [Fig. 5.13(b)]. Despite the lack of clapping, this regime is not necessarily weakly nonlinear since excitation amplitudes are not small

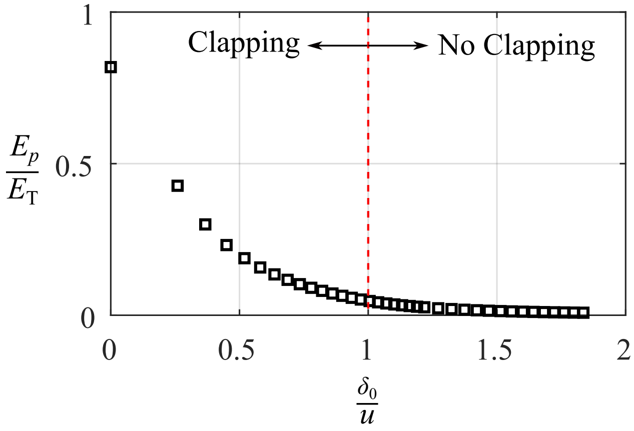

Figure 5.14: Dependence of the energy carried by the compression pulses (E_p) as a fraction of total energy (E_T) on precompression.

enough. Note that there exists quadratic nonlinearity between contact force and displacement due to the deformation of rough asperities. This nonlinearity is possibly sufficient to counterbalance the dispersion to form compression pulses. Further, the amplitude of generated pulses decreases beyond $\delta_0/u > 1$ - a threshold beyond which no clapping is possible. The change in amplitude of compression pulses is less sensitive to $\delta_0/u > 1$ compared to $\delta_0/u < 1$ [note the change in pulse amplitude dependence on precompression before and after the red dashed line in Fig. 5.13(b)]. The maximum amplitude of the compression pulse is attained at $\delta_0/u = 1$. This is the threshold where clapping is possible and energy added to the system is more than the energy added for $\delta_0/u < 1$. These observations indicate that the characteristics of the generated pulses undergo a transformation when the type of nonlinearity at the contact changes.

Contrary, the wave speed of the compression pulses, c, (normalized by bulk wave dilatational wave speed, c_L) increases monotonically with precompression [Fig. 5.13(c)]. This is consistent with Fig. 5.13(b) for $\delta_0/u < 1$ since the amplitude and speed of these waves are proportional to each other. Another observation is that the wave speed changes dramatically for low precompression and depends linearly on precompression at larger values. For $\delta_0/u > 1$, wave speed increases despite a decrease in amplitude. This indicates that the pulses generated beyond $\delta_0/u > 1$ have a different speed-amplitude relationship than solitary waves generated from contact clapping.

As expected, the fraction of energy carried by the compression pulses as a function of total energy in the system decreases with an increase in precompression (Fig. 5.14). In fact, the energy carried by the pulses is almost negligible (two orders smaller) for precompressions $u/\delta_0 > 1.5$. This indicates the region of precompression where the phononic material behavior potentially changes into a weakly compressed system.

5.6 Physical constraints: Effects of disorder

A fundamental feature of phononic media is their periodic architecture. The proposed continuum phononic materials in this research demonstrate periodicity through the arrangement of rough contacts, with each contact possessing identical properties. Particularly, all these contacts follow a specific nonlinear power law relation, which governs the discussed nonlinear wave responses. However, achieving perfect periodicity in a practical system is nearly impossible. In other words, real phononic material exhibit disorder, which refers to the presence of irregularities or variations. These irregularities can arise due to imperfections in the manufacturing process, inherent material heterogeneities, or external perturbations. In the context of continuum phononic material with rough contacts, the disorder can manifest as variations in layer size, shape, material properties, or contact interactions. Among these factors, contact interactions are the most likely sources of disorder due to the complex challenges associated with fabricating and aligning contacts with microscale asperities. This section explores how contact disorder impacts the propagation of stegotons through these phononic materials.

Granular crystals with disorders have been studied extensively over the years. Introducing defects or impurities within these materials has been proposed as an approach to enhance the dynamics of the material. This enhancement can be achieved by incorporating either light [188]–[190] or heavy [190] masses, placed either internally or at the ends [141], or by directly exciting defects [141]. These defects have led to intriguing wave responses in granular media, including energy trapping [188], long-lived nonlinear localized modes [189], bifurcations, and antisymmetric modes [141], [189], as well as wave fragmentation [190]. In contrast to single-site defects, random disorders have also been investigated, encompassing random variations in mass distribution, density, material properties, particle size, and power exponent [191]–[193]. These studies have demonstrated that solitary waves can still propagate through disordered granular media, albeit with reduced amplitude or energy due to energy loss during reflections at each bead/contact caused by property differences [191], [192].

To study how disorder from contact nonlinearity affects stegoton propagation in continuum-layered media studied in Section 5.4, two different types of disorders are considered: uniform and random. The uniform disorder is applied to a portion of the phononic material of $n = 200$ which allows the study of the effect of disorder on stegotons generated in an ideal system. The uniform disorder of the exponent, β, of contact power-law is defined as,

$$\beta(i) = \begin{cases} \beta_0, & 1 \leq i \leq 50, \\ \beta_0(1 + r\epsilon), & 50 < i < 150, \\ \beta_0 \pm \epsilon, & 150 \leq i \leq 200, \end{cases} \tag{5.1}$$

where i is the contact index from the excitation boundary, β_0 is ideal contact-law exponent, ϵ is the degree of disorder, and r takes values from 0 to ± 1 in the interval $50 < i < 150$. $+r$ correspond to gradual increasing exponent of contact nonlinearity and vice versa for $-r$ [Fig. 5.15(a)-(b)]. On the other hand, random disorder over the entire phononic material of $n = 100$ informs the effect of disorder on both the generation and propagation of stegoton. The random disorder of the exponent, β, of contact power-law is defined as,

$$\beta(i) = \beta_0(1 + \epsilon r_i), 1 \leq i \leq 100, \tag{5.2}$$

where r_i contains normally distributed values with mean = 0 and standard deviation = 1/3 such that the mean value of β_i is the same for both ideal and disordered systems.

A tone burst ($\zeta = 2.5/f$ and $\psi = 0.5/f$) is excited at frequency $\Omega = 0.52$ ($f = 0.25$ MHz) such that the excited signal would result in a single dominant stegoton propagating in an ideal in the phononic material. In the case of uniform disorder with $\epsilon = 10\%$ (Fig. 5.15), stegotons generated in an ordered section of the phononic material propagate through the disordered system [see black lines in the bottom plots of Figs. 5.15(c) and 5.15(d)]. However, their amplitude and speed experience a slight attenuation [red and black curves in the bottom plots of Figs. 5.15(c) and 5.15(d) do not overlap]. Moreover, at the interface between the ordered and disordered systems, stegotons are reflected, leading to the backward propagation of a portion of energy [negative humps in the inset of Figs. 5.15(c) and 5.15(d)]. Inside the disordered section, oscillatory

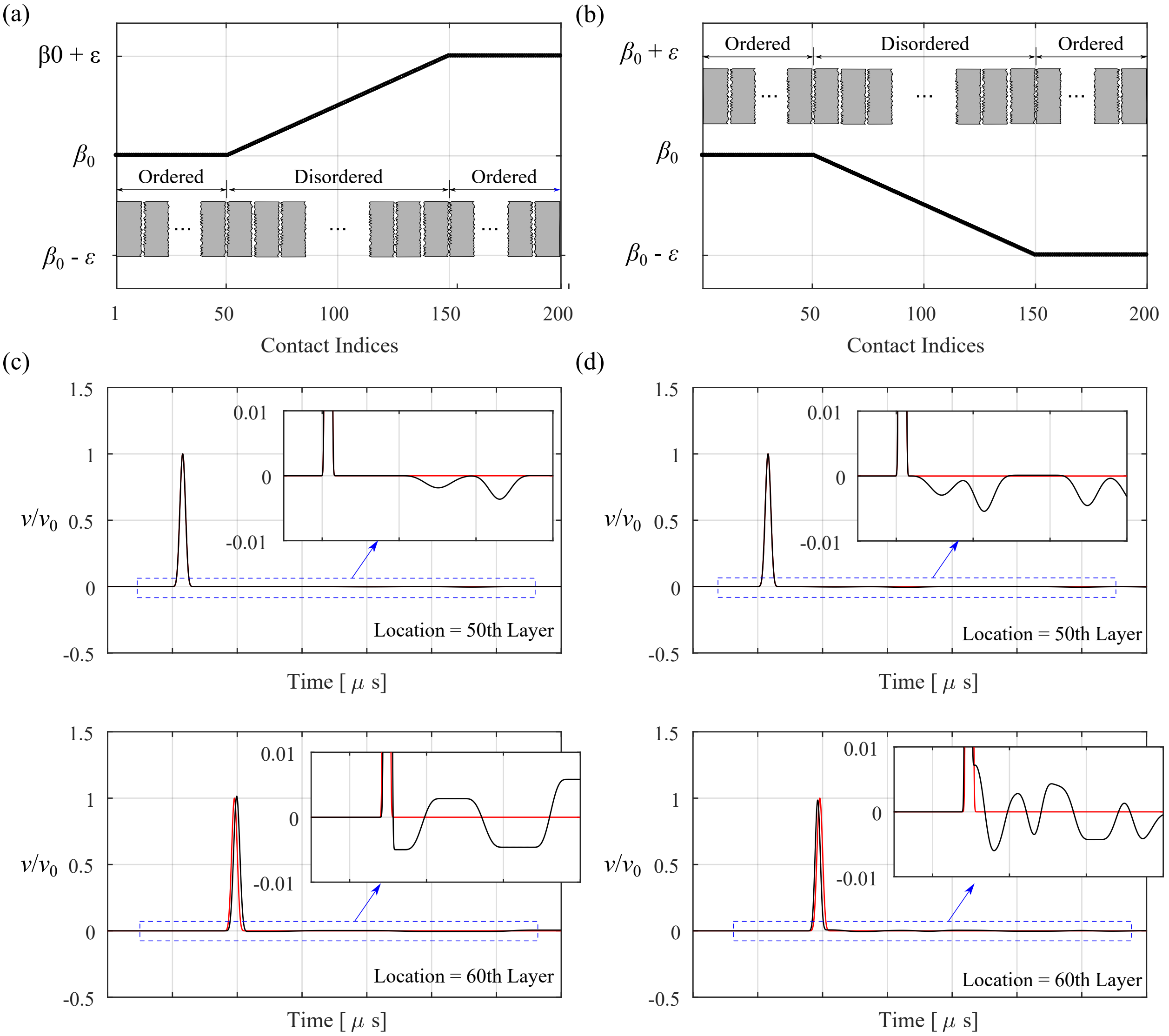

Figure 5.15: Stegoton propagation through phononic material with a uniform disorder of contact nonlinearity. Gradual (a) increasing and (b) decreasing disorder of the power-law exponent of contact nonlinearity. Disorder exists in the middle 100 layers of the phononic material. (c) and (d) are the temporal profiles of waves propagating through systems (a) and(b), respectively. These profiles are recorded inside the 50th layer (top) and 60th layer (bottom). Red and black lines correspond to fully ordered and disordered [as shown in (a)-(b)] phononic materials, respectively. Insets are zoomed views of dashed blue rectangles. v_0 is the amplitude of stegoton in an ordered phononic material.

trails are also observed due to wave reflections at each interface, as the contact properties are not strictly periodic.

In the case of random disorder (Fig. 5.16), stegoton propagation through the phononic material is highly sensitive to the disorder in contact nonlinearity. When the coefficient of variation (COV) is 1.5%, stegotons are generated and propagate through the material. However, their amplitude is smaller compared to the ordered system, resulting in slower propagation. This reduction in amplitude is caused by the fragmentation of energy into smaller oscillations left behind due to wave reflections at each contact, caused by the disordered contact nonlinearity. With propagation, oscillations increase while stegotons decay in amplitude. As the

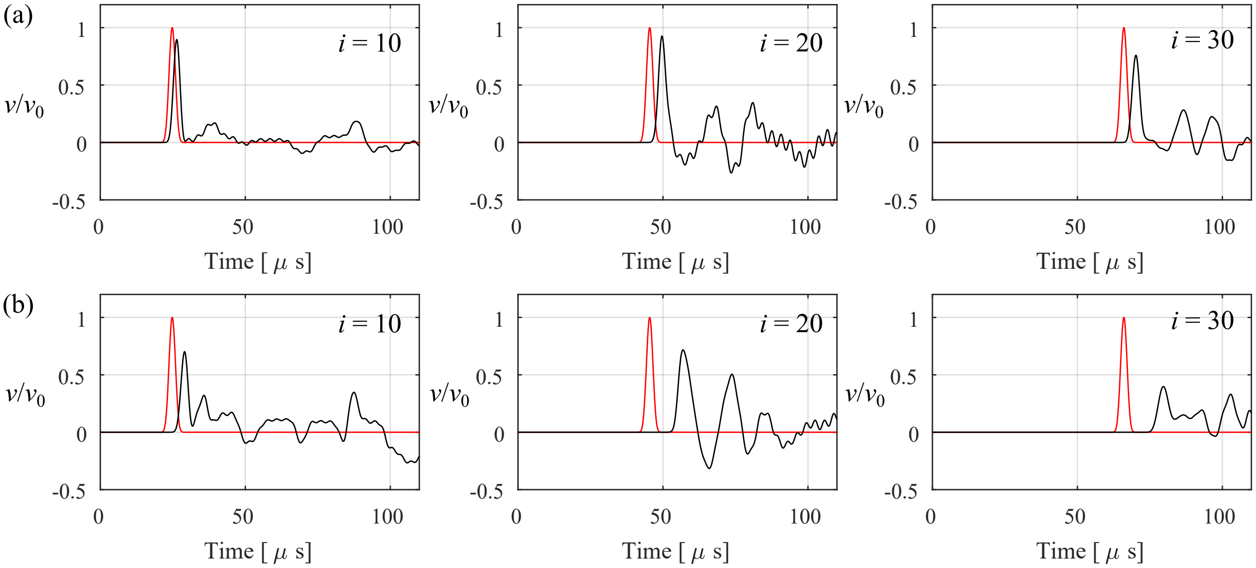

Figure 5.16: Stegoton propagation through phononic material with a random disorder of contact nonlinearity for a coefficient of variance of (a) 1.5% and (b) 3%. The temporal profiles of waves propagating through systems at 3 different locations are shown. Red and black lines correspond to fully ordered and disordered phononic materials, respectively.

degree of disorder increases (for example, with COV = 3%), stegotons cannot be formed in the disordered system. This indicates that stricter criteria for the variation in contact nonlinearity exponent are necessary to sustain stegotons in a continuum phononic material with rough contacts.

Overall, the presence of disorder often leads to the scattering, energy localization/trapping, or attenuation of stegotons. The degree of disorder determines the extent of these effects, with stronger disorders causing more pronounced changes in wave behavior. Moreover, the disorder can induce the formation of complex wave patterns, including decaying stegotons, slower energy travel, and wave scattering, which are absent in ordered systems.

5.7 Physical constraints: Effects of finite lateral size

The phononic material studied so far correspond to the uniaxial strain case, where each layer is assumed to be infinite in $y-$direction. This effectively generates only one-directional strain (in the $x-$ direction) in the system. While it is feasible to practically achieve such a phononic material when the material cross-section is much larger than the probed wavelength and wavefront, other scenarios with finite lateral dimensions are expected to introduce additional effects on stegoton propagation. Here, a brief numerical analysis is conducted to report what are the effects of finite lateral dimension on energy propagation and whether stegotons are still observed in such a system.

Numerical analysis is conducted on the same phononic material discussed in this chapter with only one difference: the top and bottom boundaries are left free instead of applying symmetry boundary conditions [refer to the insets in Figs. 5.17(a) and 5.17(b)]. This configuration simulates the effects of finite size on wave propagation within the phononic material, not limiting strains to one direction. The results reveal that waves are reflected away from the finite boundaries into the phononic material, creating scattered waves that manifest as trailing oscillations [Fig. 5.17(b) - top and bottom plots]. Despite these spurious waves, a localized

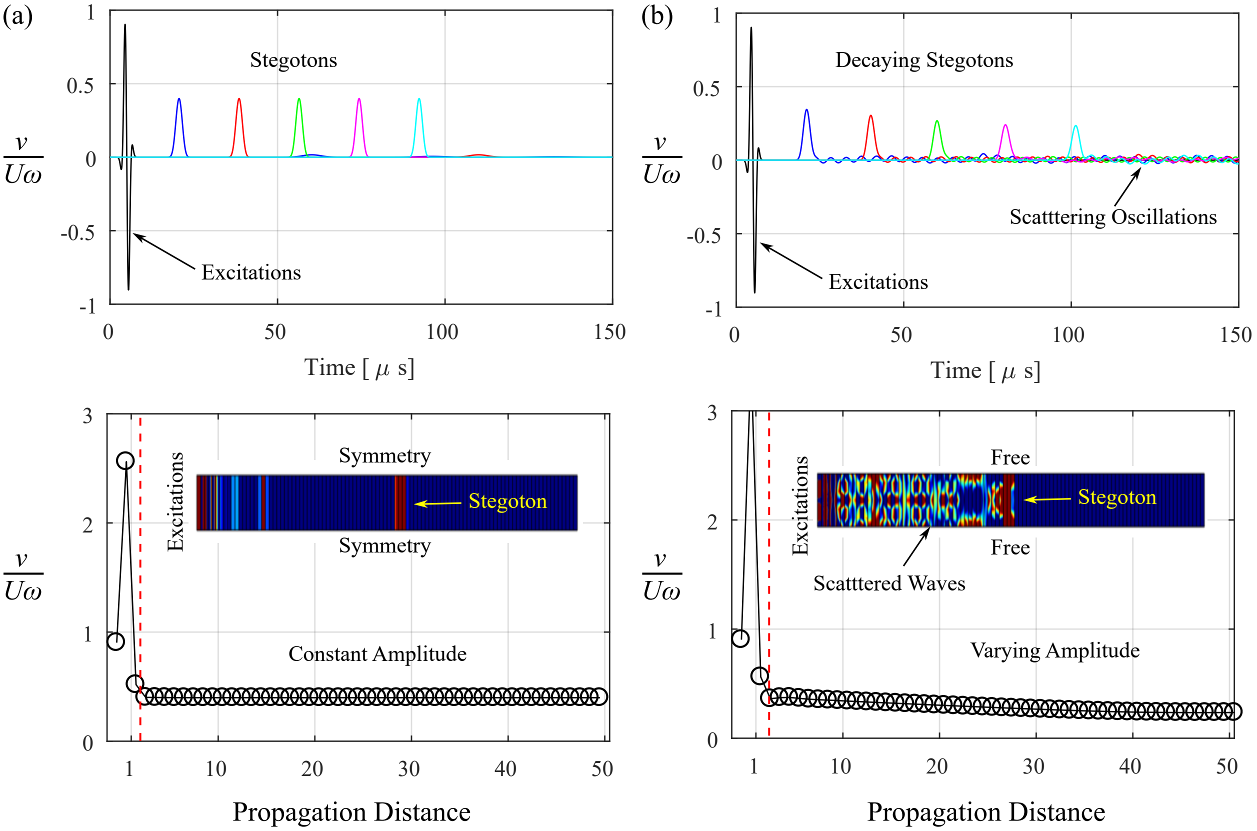

Figure 5.17: Stegoton propagation through phononic material with (a) infinite and (b) finite lateral dimensions. Top - Temporal profile of propagating wave measured at the excitation boundary (black) and inside the 11th (blue), 21st (red), 31st (green), 41st (magenta), and 51st (cyan) layers of the phononic material. Bottom - Amplitude variation of stegotons with propagation distance. Red dashed lines indicate the spatial location at which stegotons are clearly formed. Insets are snapshots of wave propagation at the same instant for both simulations indicating the presence of scattered waves in the phononic material with finite boundaries.

wave in the form of stegotons is still supported in the material. However, as energy is dispersed and reflected by the scattered waves, the amplitude of the localized wave gradually diminishes with increasing propagation distance [Fig. 5.17(b) - bottom plot]. There seems to be a threshold beyond which the amplitude change is saturating, which probably is an effect of phononic material effectively behaving as a 1D system. In contrast, the ideal uniaxial strain case exhibits no scattering or decay in amplitude [Fig. 5.17(a)]. These findings demonstrate that even in physically realized phononic materials with finite lateral dimensions, stegoton-like localized waves can be sustained, and their amplitude variation can be characterized by measuring amplitudes at various locations within the material.

5.8 Summary

In this chapter, strongly nonlinear dynamics of continuum phononic material with rough contacts is studied. The strong nonlinearity stems from the inability of these contact to support tensile loads under zero precompression. A noteworthy aspect of this setup is the local presence of strong nonlinearities, which are interconnected through linear elastic media. The chapter explored the behavior of wave propagation in this intricate configuration, specifically emphasizing the occurrence and properties of localized traveling waves associated with contact clapping. The studies yield significant insights, including:

1. Wave-contact interactions generate stegotons, which are localized traveling waves categorized as solitary waves. These stegotons effectively transport wave energy without experiencing dispersion, maintaining a constant speed and amplitude as they propagate. Particularly notable is the spatial characteristic of these waves, exhibiting a roof-like or stepwise profile owing to the periodic configuration of continua-discrete nonlinearity in the phononic material.

2. Wave-contact interactions additionally induce acoustic resonances within the layers. These layer resonances allow spectral energy transfer and localization near the excitation boundary. The amount of energy transmitted through the phononic material relies on the proximity of the excitation frequency to the acoustic resonances of the layers. When the input frequencies align with the layer resonances, a considerable amount of energy becomes trapped within these layers. Consequently, stegotons carry significantly lower energy, resulting in a wave attenuation reminiscent of a band-gap effect.

3. Due to a higher exponent of the power-law of rough contact nonlinearity (where exponent $= 2$), stegotons show a much stronger interrelationship between amplitude, speed, and contact pressure compared to solitary waves in granular crystals (where exponent $= 3/2$). Further, results show that the speed-amplitude relationship exponent is independent of the layer thickness and is likely governed by the contact power law only.

4. When stegotons collide, it leads to the formation of secondary stegotons. Notably, the amplitudes of these secondary waves are one order greater when the collision occurs at a contact, as opposed to collisions within a layer.

5. Stegotons emerge and propagate within the phononic material, even when subject to physical constraints such as light precompression, disorder, and finite lateral dimensions. However, the characteristics of these stegotons differ from those in an ideal system. Due to finite lateral dimensions, stegotons exhibit attenuation-like characteristics, i.e. reducing amplitudes with propagation distance, due to interference from scattered waves. Moreover, as the degree of disorder of the exponent of contact nonlinearity increases, the material ceases to support stegotons. These physical limitations also give rise to various additional wave phenomena, such as wave disintegration. Wave disintegration refers to the transformation of an input pulse into localized compression pulses, a rarefaction transition zone, and oscillatory trails. The disorder-induced effects encompass energy trapping, wave attenuation, and fragmentation of stegotons.

Chapter 6

Hysteretic nonlinear wave dynamics

This chapter investigates the nonlinear shear wave propagation through continuum phononic materials with externally precompressed rough contacts. In contrast to previous chapters, the focus here is on the tangential interactions of the contacts, specifically wave-induced frictional instability. It begins by highlighting the limited research on exploiting hysteretic nonlinearity in phononic media, with only a few anecdotal studies available. Subsequently, the effect of hysteresis on wave propagation through a single contact is studied, followed by an analysis of a periodic contact system. Two key results are observed: eigenstrain generation and energy dissipation. The chapter then demonstrates acoustically-governed mechanical programmability by exploiting eigenstrains and passive, wide-band attenuation from frictional dissipation. Some of the sections of this chapter have been adapted from my published article, [106], which was written as part of the research for this dissertation.

6.1 Knowledge gap: Hysteretic nonlinearity in phononic materials

As discussed in Chapter 1, phononic materials have been predominantly studied in the linear regime [12]. Recent studies have shown that nonlinearity yields unprecedented wave responses such as solitary waves [67], discrete breathers [71], amplitude-dependent band gaps [59], [179], energy transfer between frequencies/modes [179], among others, as detailed in a review by Patil and Matlack [44]. Yet, the focus so far has been on the propagation of *longitudinal* waves and nonlinear mechanisms, either weakly or strongly, that govern these wave responses. On the other hand, *shear* waves have received very less attention despite being the fundamental type of wave supported by solid materials. It remains an open question of how shear waves evolve in the presence of nonlinearities in phononic materials. Addressing this question is of foundational significance and could open opportunities for developing novel acoustic devices with advanced functionalities, such as mechanical programmability, surface reconfigurability, and passive wave attenuation, simply by employing shear waves.

Furthermore, the types of nonlinearities explored in phononic materials are thus far largely limited to *reversible* nonlinear laws, where nonlinear forces (or stresses) depend only on the current displacements (or strains). Such memory-independent nonlinearity typically stems from material constitutive laws under elastic limit [179], finite strains [61], and normal contact laws [67]. On the other hand, *hysteretic* (or irreversible) nonlinearity, where current forces also depend on their history, offers the potential to obtain nonlinear wave responses typically not possible with reversible nonlinearity. Although the effects of hysteresis on wave propagation have been considered, either through viscous damping [194]–[197] or elastic-plastic law [198], there still exists a lack of knowledge of how wave interacts when nonlinearity itself is memory-dependent. Such knowledge could provide a new platform to control wave-energy propagation in materials by introducing hysteretic nonlinearity and intentionally programming loading history.

One of the physical sources of hysteretic nonlinearity is friction between contacting surfaces. Coulomb's law, which is postulated to model friction between two surfaces with a coefficient of friction (μ), dictates the existence of two physical states of contact - stick ($T < \mu N$, where T and N are tangential and normal forces acting at the contact, respectively) and slip ($T = \mu N$). As a result, applied forces trigger hysteresis that physically correspond to surface wearing [199] and heat generation [200] at the contact. Consequently, friction between surfaces is widely researched in tribology [199], nonlinear dynamics [201], structural health monitoring [202], and nondestructive evaluation [122], [129], [203]. It has been traditionally studied to control its effects and increase component life [201], but it is now being explored as a tool to enable soft robotic devices that latch onto objects [204] and design mechanical metamaterials that absorb energy under quasi-static loading [205], [206]. However, it is yet to be explored how friction can be utilized to control wave propagation and enable smart functionalities.

Despite extensive studies on phononic materials with contacts (or interfaces), the effects of friction have been studied only in a limited capacity. Granular crystals have majorly focused on normal contact interaction only, i.e. Hertzian law [62]. A few of those studies analyzed torsional (or rotational) and transverse waves but modeled the tangential interactions through Hertz-Mindlin theory, which assumes no sliding at the contacts [134], [159], [207]. Only a few studies have incorporated friction to study dissipation [194], [208] and hysteretic torsional coupling [209] in granular crystals. Recently, an array of frictional disks [210] and an acoustic metamaterial with internal frictional contacts [211] have been studied to report the transition from static to dynamic friction [210] and low-frequency attenuation bands [211], respectively. These limited studies demonstrate the potential of the hysteretic nonlinearity of friction in enriching the wave dynamics of phononic materials.

Overall, there is a noticeable lack of emphasis on shear waves in nonlinear phononic materials, and limited studies have been conducted to comprehend the impact of hysteretic nonlinearity. In most cases, the exploration of contact friction in phononic materials remains uncharted territory. Consequently, further research is required to address these knowledge gaps and examine the influence of shear waves and hysteretic nonlinearity, particularly in relation to friction, within the realm of phononic materials. Such research possesses the potential to propel the advancement of acoustic devices and materials with enhanced functionalities.

6.2 Objective: Responses from shear wave-induced contact friction

To address the knowledge gap in the field, this chapter continues the investigation of continuum phononic materials but shifts the focus to shear wave propagation and tangential interaction at the contact. Particularly, the aim is to (1) illustrate nonlinear shear wave responses arising from hysteretic nonlinearity of frictional contact and (2) harness these responses to enable advanced acoustic/mechanical functionalities with programmable and adaptable characteristics. To this end, shear wave propagation through rough contacts with single and array configurations, which are externally precompressed is studied (refer to Section 2.2). The frictional instability of the contacts gives rise to strong nonlinearity within the system. To solve this problem, an interactive numerical framework that couples a finite element model solving 1D wave motion and an analytical model with contact friction law is employed (refer to Section 3.3.2). Specifically, the Jenkins friction model with experimentally-obtained properties at the contacts is considered. First, how contact instability gives rise to amplitude-dependent eigenstrains is discussed, and then programmable functions are illustrated by extending the analysis to complex configurations with multiple contacts. Finally, wave transmission through finite phononic material is studied to report the combined effects of periodicity and hysteretic nonlinearity.

For a general understanding of the nonlinear responses, two normalized parameters are defined:

1. $\xi = \tau_i/\mu\sigma_0$ is the normalized excitation, where τ_i is the maximum incident shear stress generated by the excitation wave. Accordingly, ξ increases with increasing excitation amplitude. Note that $\xi < 1$ corresponds to contact always being in the stick regime (linear case) as $\tau_i < \mu\sigma_0$, whereas $\xi > 1$ corresponds to the nonlinear case where contacts switch between the stick and slip zones. All the simulations presented herein correspond to external precompression, $\sigma_0 = 50$ MPa, unless explicitly specified.

2. $\Lambda = \lambda/s$ is the normalized wavelength, where λ is the wavelength in the bulk aluminum at excitation frequency, f (i.e. $\lambda = c_s/f$, where c_s is shear wave speed). This work focuses on two wavelength regimes - long-wavelength (or low frequency), i.e. $\lambda \gg s$, and short-wavelength (or high frequency), i.e. $\lambda \sim s$. The long-wavelength regime is used to illustrate programmable functionality from an array of contacts as this condition allows us to reduce the lag between the wavefront and trailing reflections. On the other hand, the short-wavelength regime captures the Bragg-scattering effects and thus, is used to analyze attenuation zones and band gap frequencies of the phononic material. Note that the studied wavelengths are still much larger than the asperity size to ensure the validity of the quasi-spring modeling of the contacts.

6.3 Eigenstrain generation from wave-induced friction

In this section, shear wave propagation through a single rough contact [Fig. 3.2(d) with $n = 0$] is studied, and the emergence of eigenstrains within the system is presented. A shear wave consisting of 15 cycles of amplitude $\xi = 2.76$ ($U = 4$ μm), at a frequency of 0.5 MHz, was excited. The shear wave interaction with the contact fundamentally affects wave transmission and causes distortion of waveform [Figs. 6.1(a)-(b)]. This is because when the excited wave interacts with a contact, it partially reflects and transmits due to the acoustic impedance. If the wave amplitude exceeds the friction limit, then the contact surfaces slide. This limits the maximum tangential force that can be transmitted and leads to the stress amplitude being clipped at τ_c [Fig. 6.1(a)]. Such clipping effectively generates odd-order harmonics of the input frequency, as previously reported in the nondestructive evaluation of microcracks [122], [129], [203].

Interestingly, the wave interaction with the contact also causes a total tangential static deformation, Δ, at the end of the wave propagation. Note the transmitted wave measured in the Γ_R waveguide [black in Fig. 6.1(b)] corresponds to $u/U = 0$ before wave-contact interaction and now at an offset $u/U > 0$ (i.e. $\Delta_T \neq 0$). The same offset is created in the reflected wave (Δ_R) in Γ_L waveguide but with the opposite sign (results not shown). This offset physically corresponds to the change in the relative position of the contact interface, and therefore of the elastic media that the wave occupies [Fig. 6.1(c)]. The system where both Γ_L and Γ_R were aligned before wave-contact interaction are now offset by $\Delta = \|\Delta_R\| + \|\Delta_T\|$. This effect is analogous to the permanent static deformation (or residual strain) of an elastic-perfectly plastic body under cyclic loading. In fact, the physical mechanisms of these two phenomena are indeed the same. They

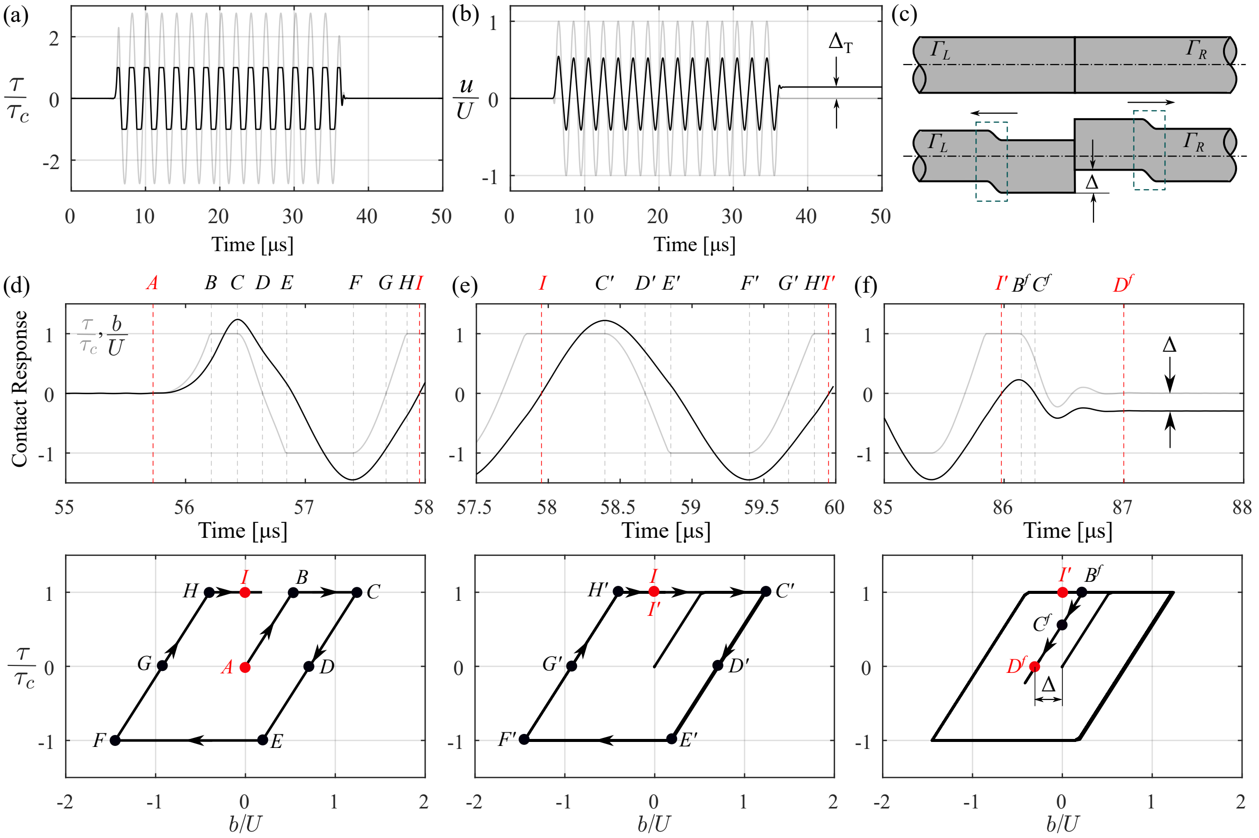

Figure 6.1: Wave evolution through a rough contact. Wave profile for $\xi = 2.76$, as an example, in terms of normalized shear (a) stress, τ, and (b) displacement, u, for the incident (gray) and transmitted (black) waves. Time on the x-axis is adjusted to overlap both waves for comparison. (c) Schematics with amplified deformation illustrating the emergence of shear-polarized eigenstrains, Δ, after wave-contact interaction. Dashed rectangles indicate the reflected and transmitted waves in the waveguides carrying the static deformations with them. (c)-(e) Hysteresis loops during wave-contact interaction. Top row - contact deformation (black) and stresses (gray), and bottom row - accumulative hysteresis loops for the (c) first, (d) subsequent, and (e) last cycle of contact deformation. Markers indicate transition points of the hysteresis loops and their instances are depicted as dashed lines with labels in the time domain. Red color indicates the start and end state of each hysteresis loop.

both are due to the hysteretic response and cause a change in the equilibrium state of the system at the end of loading. Further, the system attains a stress-free state at the end of wave propagation despite the presence of the static deformation [correlate the stresses in Fig. 6.1(a) with displacements in Fig. 6.1(b) for $t > 35\mu s$]. Previously, Qu et al. [212] have discussed that acoustic-radiation-induced strains in nonlinear material produce no stresses and can be viewed as eigenstrains. Similarly, shear deformations generated by wave-contact interaction are observed in this study, but without shear stresses. Therefore, these deformations are referred to as “shear-polarized eigenstrains”. While eigenstrains can also be generated in non-hysteretic systems with even-order nonlinearities, for example, materials with quadratic nonlinearity [212]–[215], they are only enabled by longitudinal waves. This is because shear wave self-interaction is not supported in isotropic nonlinear material [216], [217]. Thus, the interaction of shear waves with a frictional contact causes the unique response of a shear-polarized eigenstrain.

The role of hysteretic nonlinearity in generating eigenstrains can be clearly understood through hysteresis loops between contact forces and deformations. These loops occur when wave cycles transition contact between the stick and slip state, and evolve as subsequent wave cycles propagate through the contact [Fig. 6.1(d)-(f)]. The loop starts at the stress-free ($\tau/\tau_c = 0$) and undeformed ($b/U = 0$) condition (i.e. state A) during the first cycle of contact deformation [Fig. 6.1(d)]. Initially, elastic deformations of rough asperities transmit forces as dictated by the contact stiffness, κ_t, until the friction limit is reached (i.e. state B). Further deformation from the wave causes contact sliding while the force remains constant (path $B - C$). Note, the sliding of the contact in the positive y-direction is referred to as "up" sliding (i.e. $\dot{\tau} = 0$ and $\dot{b} > 0$). Once the maximum contact displacement is reached (state C), the contact starts deforming in the reverse direction owing to the oscillatory nature of the wave. Since the contact forces at each instant depend on their previous values, the contact response now takes a different path (path $C - D - E$). During this reverse motion, the contact first recovers the elastic deformation that occurred during the path $A - B$ and then starts deforming asperities in the negative direction (path $D - E$). Eventually, when the friction limit is reached, the contact starts sliding in the other direction (path $E - F$), which is "down" sliding (i.e. $\dot{\tau} = 0$ and $\dot{b} < 0$). Due to oscillatory excitation, the contact returns to its initial configuration of $b = 0$ (i.e. point I) at the end of the one full cycle but with stress, τ_c. This is because the second cycle of the wave packet now initiates its interaction with the contact even before the system attains its original stress-free state. Effectively, the first cycle contributes to changing the state of the system by undergoing different sliding in the up (path $B - C$) and down (path $E - F$) directions. Note that during the path $E - F$, the contact first has to work against the up-sliding ($B - C$) to reach the initial configuration and then create additional sliding in the opposite direction. However, the last path $H - I$ does not fully recover the sliding that occurred in the down direction, ultimately changing the equilibrium state of the system.

Unlike the first cycle, the subsequent cycles [Fig. 6.1(e)] use the final state of the first cycle (state I) as the initial state and follow a hysteresis loop $I - C' - D' - E' - F' - G' - H' - I'$, where the prime denotes transition points in the subsequent cycles. Therefore, the sliding in both directions (up and down) is the same for the later cycles ($H'C' = E'F'$). Finally, the instant beyond which the contact does not transition between stick-slip regimes governs the final state of the system. For example, state B_f is the instant of the final cycle of the contact deformation beyond which contact deformation oscillates with small amplitudes only, i.e. within the stick regime [Fig. 6.1(f)]. This state returns to its stress-free state (state D^f) by recovering the elastic deformation at the contact (path $B^f - C^f - D^f$), resulting in a shear-polarized eigenstrain, Δ.

The generation of eigenstrain is also amplitude-dependent [Fig. 6.2(a)]. The eigenstrain is zero when $\xi < 1$ (i.e. contact stays in the stick regime) and non-zero for $\xi > 1$ (i.e. when contacts undergo stick-slip transition) with a maximum eigenstrain for a specific excitation amplitude of $\xi = 1.58$. To get insights into how excitation amplitude governs eigenstrain generation, two representative cases of hysteresis loops are presented [Fig. 6.2(b)]. These loops highlight that despite the same initial condition [green marker], the last instant of contact sliding [blue marker] is much closer to the first instant of contact sliding [black marker] for $\xi = 4$ than $\xi = 1.95$. These differences are due to the different amount of hysteresis that occurs at the contact for a given excitation amplitude. For $\xi = 4$, the amount of sliding in both the "up" and "down" directions during the first cycle are relatively closer compared to that of $\xi = 1.95$ for the same friction limit. Consequently, the static offset at the end of the last sliding is smaller for $\xi = 4$ and therefore corresponding eigenstrain.

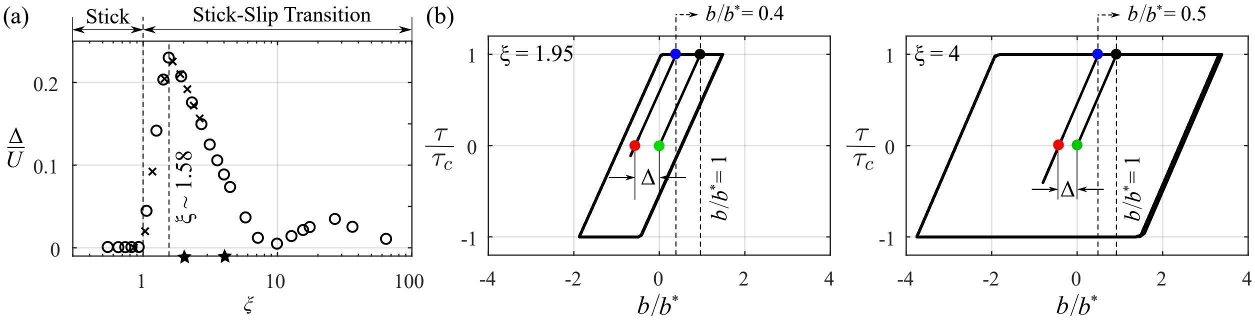

Figure 6.2: Amplitude-dependent eigenstrain generation. (a) Normalized eigenstrains for different excitation amplitudes when $\mu = 0.77$ (circle) - as obtained through experiments and $\mu = 0.5$ (cross) - as an alternate example. (b) Hysteresis loops for two different representative cases of ξ as shown in (a) with star markers. Contact deformations are normalized by the maximum deformation before the first sliding (b^*) such that $b/b^* = 1$ on the onset of the first contact sliding. Green, black, blue, and red dots are the instances corresponding to the start, first sliding, last sliding, and end states of the system, respectively.

6.4 Leveraging eigenstrains for acoustically-programmable responses

Next, the analysis is extended to two and four contacts, and those with gradients in their coefficients of friction. The generation of eigenstrains in these systems is exploited to enable advanced mechanical functions that are controlled by acoustic pulses through the system. Particularly, acoustically-programmable responses of a mechanical switch, precision position control, and surface reconfigurability are demonstrated.

First, the focus is on the generation of eigenstrains in a configuration with two rough contacts separated by a distance, s, referred to as a "layer" hereafter. To illustrate the system behavior, a single-cycle incident shear pulse with an amplitude $\xi = 2.76$ ($U = 4$ μm) at $f = 0.5$ MHz is simulated. To reduce the number of trailing reflections between the contacts, s is defined as approximately 6 times smaller than the incident wavelength (i.e., $\Lambda = 6.2$ or $s = 1$ mm). This enables a smaller delay in the programmed output relative to the wave input. While the magnitude of eigenstrain depends on the input wave frequency and amplitude, and the relation between λ and s, the qualitative nonlinear response of the system remains the same.

The wave-induced contact sliding generates eigenstrains in the semi-infinite waveguides, Γ_L and Γ_R, as well as in the layer [Fig. 6.3(a)]. These eigenstrains have different relative values and directions. The sign of the eigenstrains in the transmitted wave depends on the direction of the first contact sliding, which, in this simulated case, occurs in the positive (up) direction. Consequently, the transmitted wave across the first (left) contact contains a positive eigenstrain [red in Fig. 6.3(a)], which moves the layer up as the wave propagates through it. The reflected wave carries a negative eigenstrain [black in Fig. 6.3(a)] to balance out the effects in the transmitted wave, causing Γ_L to deform downward. As the transmitted wave propagates through the second (right) contact, the eigenstrain carried with it deforms the waveguide Γ_R upward as well. Since the amplitude of the wave transmitted across the first contact is capped to the friction limit, it prevents sliding at the second contact [Fig. 6.3(b)]. Accordingly, the relative eigenstrain between the layer and Γ_R is zero, while the relative eigenstrain between the layer and Γ_L is Δ.

To enable programmable functionalities, the generation of eigenstrains is isolated to the layer and the eigenstrains in the semi-infinite waveguides are canceled out by exciting identical wave pulses from both ends of the system [Fig. 6.3(c)]. The pulse propagating left-to-right generates a positive deformation in the transmitted wave, causing Γ_R to move *up*, and the wave propagating right-to-left generates a negative deformation in the reflected wave, causing Γ_R to move *down*. These deformations cancel each other, maintaining the initial state

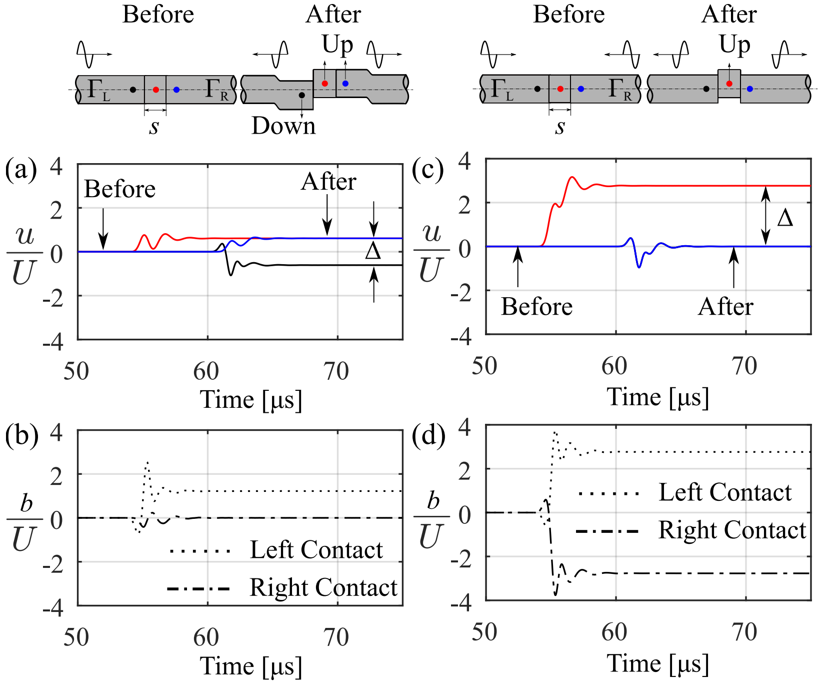

Figure 6.3: Generation of eigenstrains in a dual-contact system for (a)-(b) uni-directional and (c)-(d) bi-directional pulse excitation. (a) and (c) are wave displacements recorded in reflected (black), transmitted (blue) waveguides, and inside the layer (red), whereas (b) and (d) are corresponding contact deformations. Schematics with amplified deformations show system reconfiguration from its initial state.

of Γ_R. The same dynamics occur in Γ_L waveguide [Fig. 6.3(c)].

However, the eigenstrain remains in the layer when waves are excited from both ends, resulting in an amplified effect [compare red curves in Figs. 6.3(a) and (c)]. This is due to three simultaneous effects: (1) sliding of both contacts [Fig. 6.3(d)], (2) a change in the boundary conditions of the contacts, and (3) subsequent interactions of the reflected and transmitted waves. When waves propagate from each direction, they cause the sliding of the first contact in their path once they exceed the friction limit, and the wave transmitted through the first contact interferes with the wave propagating backward as it approaches the second contact. This wave mixing inside the layer changes the overall dynamics at the contact, leading to a non-zero eigenstrain in the layer. This demonstrates that acoustic pulses can control the position of the layer without affecting the state of the end waveguides.

6.4.1 Mechanical switch

The idea of controlling the offset of the layer from two-sided wave excitation is leveraged to enable a mechanical switch function by programming the input pulses and their phases. Since the phase of the pulses dictates the direction of contact sliding and therefore the eigenstrain, it is possible to control whether the layer shifts up or down using the input pulse phase. The versatility of this system is further highlighted by controlling the instances of pulse generation, which allow varying the duration of the specific state of the mechanical switch.

This functionality is numerically demonstrated by exciting a sequence of four single-cycle pulses with programmed phases [Fig. 6.4(a)]. Overall, the approach is to excite a pulse to change the switch's state and use subsequent pulses with the same amplitude but opposite phases to reverse the change. The first pulses

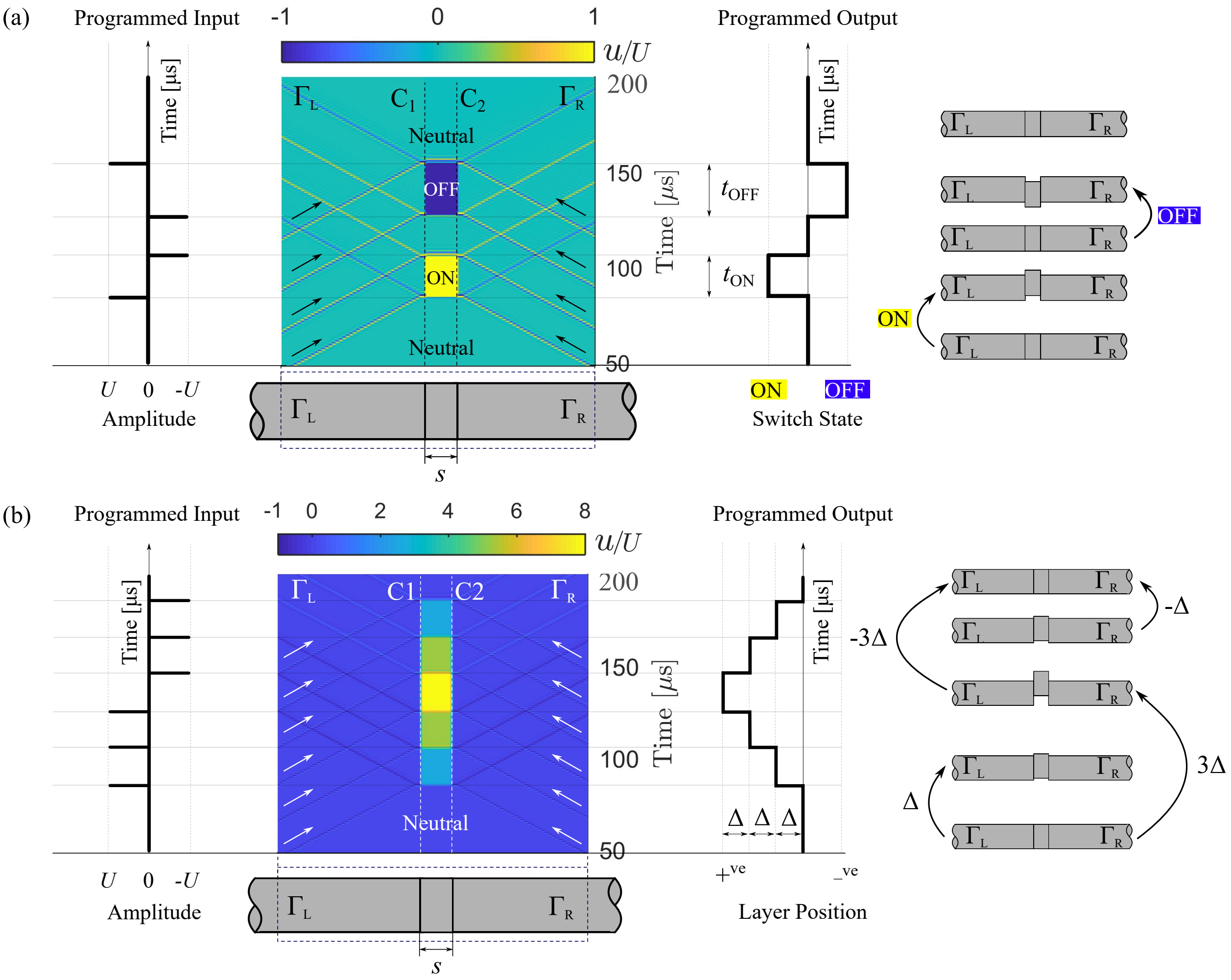

Figure 6.4: Leveraging friction-induced eigenstrains for programmable (a) mechanical switch and (b) precision position control functionalities. Each subplot contains programmed temporal patterns of input and output. Inputs are acoustic pulses with programmed amplitudes, where positive and negative values correspond to 0° and 180° phases, respectively while outputs are (a) switch states and (b) physical positions of the layer. System schematics with amplified deformations are also shown for representative time instants. Numerically-obtained spatiotemporal plots are shown for the region in the vicinity of two contacts, denoted by C_1 and C_2. The sets of parallel arrows show input pulses propagating toward the contacts.

with phase 0° move the layer to the up (ON) position as contacts slides in the positive direction generating a positive eigenstrain. The second and third pulses with a phase of 180° return the layer to the initial (Neutral) position and move it further down in the opposite direction, respectively. The switch is now in its OFF state. The final pulses with a phase 0° bring the layer back to its original state. This is an instantaneous activation as eigenstrain is generated in the layer as soon as the wave interacts with the contacts, and is potentially advantageous in reducing the time lag between actuation and response. Additionally, the switch is remotely tailored using shear waves, which makes it useful in extreme environments where electronic switches often malfunction. By controlling the time gap between pulses, the duration of a specific state of the switch can also be adjusted, providing more versatile control [note $t_{\mathrm{OFF}} > t_{\mathrm{ON}}$ in Fig. 6.4(a)].

6.4.2 Precision position control

By programming a sequence of pulses, it is possible to generate eigenstrains in series and precisely control the position of the layer by incrementally increasing or decreasing the eigenstrains. This is numerically demonstrated by exciting two groups of pulses of the same amplitude, where pulses within the same group have the same phase but are opposite that of the other group. [Fig. 6.4(b)]. The first group of pulses with 0° phases generates eigenstrain in the positive direction, causing the layer to increase its position incrementally (Δ), where Δ depends on the pulse amplitude. When the second group of pulses of 180° phases is excited, these pulses counteract the effects of the previous group of pulses and return the layer to its initial state. Note that the generated static deformation is of the order of input wave amplitude, which for the simulated case is of the order of micrometers. Therefore, despite the permanent reconfiguration, the contact area does not change considerably. Thus, we assume that the acoustic impedance at the contacts does not change for the subsequent pulses.

6.4.3 Surface reconfigurability

This section demonstrates how shear-polarized eigenstrains can serve as a platform for programmable surface reconfigurability. Surface reconfigurability, or morphing, has applications in soft robotics and fluid-structure interactions. Examples include designing soft robots capable of gripping arbitrary-shaped objects and tuning the aerodynamic response by modulating turbulent drag. Here, a more complex system consisting of an array of four contacts with a gradient in their coefficient of friction is explored. How this gradient in μ allows control over the position of an arbitrary layer between successive contacts is illustrated, highlighting the potential for precise surface manipulation.

A system with four contacts (or three layers) is considered [schematic of Fig. 6.5(a)]. This configuration is chosen to show how the position of the inner layer (I), which is not directly accessible from either side, can be controlled by programming the input pulses. To do so, The gradient of frictional properties is leveraged by setting the coefficient of friction at the outermost contacts (μ_O) smaller than the one at the innermost contacts (μ_I), i.e. $\mu_O < \mu_I$. More specifically, $\mu_O = 2/3\mu_I$ is considered as a test case. The gradient is expected to cause different responses at the inner and outer contacts, and therefore different eigenstrains at the inner (I) and outer (O) layers. Further, note that the wave interaction with an array of contacts results in multiple reflections and transmissions at each contact. All these waves interfere with each other and depending upon their phase difference, the effective contact deformation is either amplified or truncated. Therefore, the eigenstrains generated in these layers are studied first for different excitation amplitudes [Fig. 6.5(a)].

For the studied range of amplitudes, $U/U_{max} = 0.125$ to 1 (i.e. $U = 1$ μm to 8 μm), an increasing excitation amplitude increases the eigenstrains of both inner and outer layers [square and circle markers in Fig. 6.5(a), respectively]. As expected, larger eigenstrains are generated in the outer layers (Δ_O) compared to the inner layer (Δ_I) under the same excitation. This is because of the lower stick limit of the outer contacts, which results in a stronger hysteresis response. More importantly, the difference between their eigenstrains ($\Delta_O - \Delta_I$) also grows with excitation amplitude [cross markers in Fig. 6.5(a)]. At low amplitude, sliding occurs only at the outer contacts, resulting in zero relative eigenstrain between the inner and outer layers. However, as wave amplitude is increased, the friction limit of inner contact is also exceeded, causing sliding at both inner and outer contacts but of different magnitudes. This results in non-zero relative eigenstrains between the inner and outer layers. By taking advantage of this difference in their static deformation, only

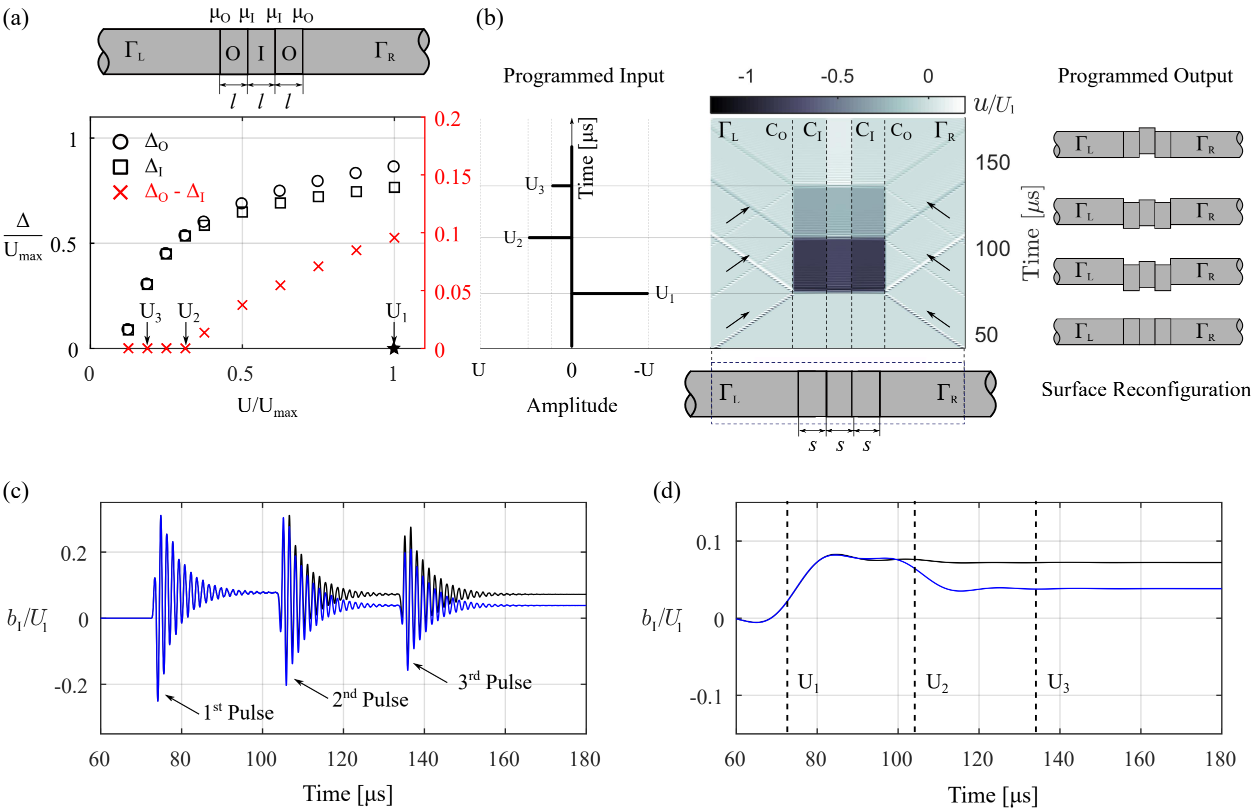

Figure 6.5: Leveraging friction-induced eigenstrains for programmable surface reconfigurability in a four-contact system with a gradient of coefficients of friction. (a) Generated eigenstrains in outer (Δ_O) and inner (Δ_I) layers, and their relative difference ($\Delta_O - \Delta_I$) for different excitation amplitudes. The plot is normalized by the maximum amplitude ($U_{\max}$) of the simulated range (star marker). (b) Numerical validation of programmed input to shift the inner layer only. Inputs are acoustic pulses with programmed amplitudes [marked in (a)], where positive and negative values correspond to 0° and 180° phases, respectively, while outputs are the physical positions of the layers. System schematics with amplified deformations are also shown for representative time instants. The spatiotemporal plot is shown for the region adjacent to the contacts, denoted by C_O and C_I as outer and inner contacts, respectively. The sets of parallel arrows show input pulses propagating toward the contacts. (c) Inner contact deformation (b_I) for two different programmed inputs, where U_2 corresponds to $\Delta_O - \Delta_I = 0$ (black) and $\Delta_O - \Delta_I \neq 0$ (Blue). In both cases, U_1 is the same, and U_3 is different but corresponds to $\Delta_O - \Delta_I = 0$. (d) Low-pass filtered response of (c) illustrating eigenstrains. Dashed lines indicate approximate time instances when input pulses interact with the inner contacts.

the inner layer can be shifted while keeping the outer layers aligned with the semi-infinite waveguides. The principle here is to (1) first excite a pulse with an amplitude high enough to cause sliding at all contacts, and (2) then excite relatively low amplitude pulses with opposite phases in at least two steps to bring back the outer layers to their initial state. Due to varying differences between the relative eigenstrains for different excitation amplitudes, the inner layer is expected to be at an offset with the entire system despite outer layers returning to their original position.

To demonstrate this approach, numerical simulations are conducted on an array of four contacts with programmed input pulses of varying amplitudes (U_1, U_2, U_3) and phases ($180°, 0°, 0°$) [Fig. 6.5(b)]. The amplitudes were selected based on two conditions: (1) the eigenstrains generated in the outer layers by the first pulses (U_1) should be equal to the total strains generated by the second (U_2) and third (U_3) pulses, i.e., $\Delta_O^{(1)} = \Delta_O^{(2)} + \Delta_O^{(3)}$, where the superscripts denote the pulse indices, and (2) the relative eigenstrain between the inner and outer layers for U_1 should be greater than the total relative eigenstrain for U_2 and U_3, i.e., $|\Delta_O - \Delta_I|^{(1)} > |\Delta_O - \Delta_I|^{(2)} + |\Delta_O - \Delta_I|^{(3)}$. The required pulse amplitudes for numerical simulations are obtained by best-fitting the data points of Fig. 6.5(a) such that $U_1/U_{max} = 1$ (i.e. $U_1 = 8$ μm), $U_2/U_{max} = 0.3125$ (i.e. $U_2 = 2.5$ μm), and $U_3/U_{max} = 0.2$ (i.e. $U_3 = 1.583$ μm). The outcome of the simulation confirms that only the inner layer is shifted with respect to the rest of the system after wave propagation, as seen in the system configuration at $t > 140\mu s$ in Fig. 6.5(b).

Additionally, the magnitude of the offset of the inner layer can also be controlled by programming the amplitudes of the subsequent pulses only [Figs. 6.5(c)-(d)]. Two cases are presented, where U_1 is the same, i.e. $U_1/U_{max} = 1$ (or $U_1 = 8$ μm), but U_2 is selected such that it causes sliding either at the outer contacts only [black where $U_2/U_{max} = 0.3125$ (i.e. $U_2 = 2.5$ μm)] or at both inner and outer contacts [blue where $U_2/U_{max} = 0.5$ (i.e. $U_2 = 4$ μm)]. The temporal deformation patterns of inner contacts reveal that the eigenstrain generated from U_1 is reduced only when U_2 can cause sliding at inner contacts as well [blue in Figs. 6.5(c)-(d)]. While U_3 is different for these two cases [$U_3/U_{max} = 0.2$ (i.e. $U_3 = 1.583$ μm) for black and $U_3/U_{max} = 0.15$ (i.e. $U_3 = 1.181$ μm) for blue], it generates no strain in the inner layer as it corresponds to sliding of outer contacts only. Hence, the final offset of the inner layer differs for both cases. This demonstration illustrates the potential of contact-based materials and friction-induced eigenstrains to achieve a variety of remotely-actuated surface reconfigurations by selecting appropriate combinations of input pulse amplitudes and phases. For example, fluid flow along the surface of an object can be obstructed or altered by protruding a part of the surface in its flow path or reconfiguring the surface to an optimized profile. Further, this could be used to deploy or modify the spacing of riblets [218], [219], which have been shown to reduce turbulent drag by resisting cross-flow and displacing vortices away from the wall of wall-bounded aerodynamic flows, or deploy surface textures that have been shown to delay separation [220].

6.5 Passive and wide band wave attenuation

In this section, the focus is on the canonical properties of phononic materials - “band gaps”. Recall from Section 1.2 that band gaps are the range of frequencies for which phononic materials do not support any propagating modes [12]. As a result, wave transmission in the band gaps is significantly lower, hence referred to as “attenuation zones”. These band gaps and therefore the attenuation zones are formed by Bragg-scattering and their width is typically narrow as it depends on the periodicity constant and unit cell properties. Therefore, several other mechanisms such as externally attached linear viscoelastic dampers [221], [222], inertial amplification [15], and Bridging-coupling [223] have been proposed to widen these zones, and several other external stimuli have been used to tune these zones *in situ* [26]. Here, how the hysteretic nonlinearity of frictional contacts serves as a passive mechanism to widen the attenuation zone of finite phononic materials is investigated. Specifically, the role of amplitude-dependent energy dissipation and wave coefficients in widening the attenuation zones is illustrated. The effectiveness of the periodic arrangement of contacts in reducing wave transmission is also characterized.

Linearized band gaps of the pure shear wave propagation through the phononic material are evaluated using Eq. (3.6). A normalized frequency parameter is defined such that, $\Omega = f/f_{\text{Bragg}}$, where f_{Bragg} is the Bragg scattering frequency of the bulk aluminum unit cell of length, $s = 3$ mm, (i.e. $f_{\text{Bragg}} = c_s/2s = 0.5167$ MHz). Specifically, the focus is on the two lowest band gaps of the system (Band Gap 1: $0.7 \leq \Omega \leq 1$ and Band Gap 2: $1.47 \leq \Omega \leq 2$).

Transmission characteristics of a phononic material with 3 unit cells (i.e. 4 contacts) are numerically

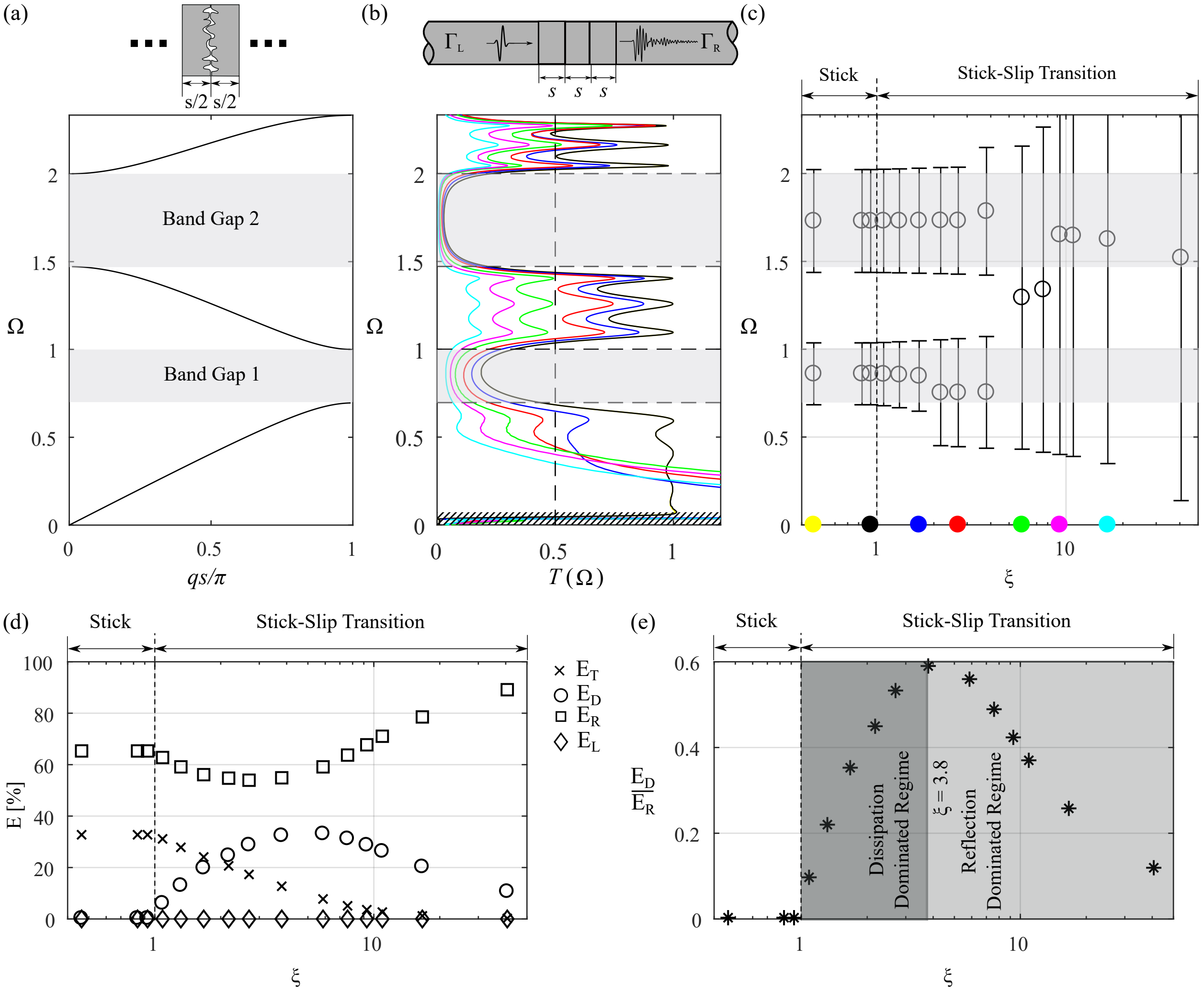

Figure 6.6: Passive wave attenuation through phononic material due to hysteretic nonlinearity of frictional contacts. (a) Linear dispersion of shear waves. Schematic is the unit cell of the phononic material. (b) Transmission, $T(\Omega)$ and (c) attenuation zone width of finite phononic material for different excitation amplitudes, ξ. Shaded regions are linear band gaps. Transmission curves plotted for different ξ values are shown by filled markers with corresponding colors in (c). The hatched regions correspond to filtered frequencies in post-processing. Hollow markers in (c) are the center frequencies of the attenuation zones and bars represent zone width. The width is evaluated at the 50% drop in transmission [dashed vertical line in (b)]. Amplitude-dependent (d) energy distribution and (e) the ratio of the dissipated to reflected energy in the phononic material.

evaluated. The three-unit cell system can capture the effects of periodicity-induced dispersion along with strongly nonlinear effects with reasonable computational cost. The transmission, $T(\Omega)$, is defined as the ratio of the amplitudes of the transmitted wave (in the Γ_R waveguide) to the incident wave in the frequency domain. A Gaussian modulation [102] with $\zeta = 2/f$ and $\psi = 0.5/f$ is applied to the input wave packet of Eq. (3.9) of center frequency, $\Omega = 1.16$ (i.e. $f = 0.6$ MHz) to only excite the frequencies of interest (i.e. $0 \leq \Omega \leq 2.33$). The static offsets (or eigenstrains) generated in the transmitted wave from frictional nonlinearity introduce leakage in the frequency spectrum. To avoid this, a high pass Chebyshev Type-II filter (with ripple values of 10 dB for the pass band and 50 dB for the stop band) at $\Omega = 0.05$ is applied before taking FFT. Thus, the transmission plots in Fig. 6.6(b) are hatched out for the range $0 \leq \Omega \leq 0.05$. For low-amplitude linear waves ($\xi < 1$), the transmission curves are amplitude-independent while the attenuation zones correlated well with the predicted linear band gaps of the system [note, yellow and black curves overlap each other in Fig. 6.6(b)]. Further increase in excitation amplitude results in the widening of the attenuation zones. Specifically, two effects are seen: (1) the transmission ratio in the band gap further reduces, and (2) propagating modes of the system are suppressed. In fact, the entire 1st optical branch ($1 \leq \Omega \leq 1.47$), and the boundary modes of the acoustic (as $\Omega \to 0.7$) and 2nd optical branch (as $\Omega \to 2$) that are close to band gap edges are also suppressed. The sharp increase in the transmission curve in the vicinity of $\Omega = 0.05$ is a result of the generation of DC and self-modulated frequency [102] in the presence of nonlinearity.

As excitation amplitude is further increased, the two attenuation zones eventually merge [Fig. 6.6(c)]. This results in a wide band attenuation region compared to the attenuation capacity of the underlying linear system. This characteristic of passively widening the attenuation zones with increasing excitation amplitude of the periodic frictional contacts highlights an effect equivalent to adding a nonlinear metadamping to the system. Thus, the frequencies that were originally carrying mechanical energy across the linear material, now, can not support energy travel. We further highlight that, in addition to widening the zone, the zone boundaries themselves have reduced to low-frequency values compared to the linear attenuation zone. This demonstrates the ability of frictional contacts to mitigate damaging low-frequency vibrations without requiring unit cells with large sizes.

To further understand the underlying mechanism behind the widening of the attenuation zones, energy distribution, as a fraction of input energy, in the phononic material is evaluated [Figs. 6.6(d) and (e)]. The energies are evaluated after all the internal reflections come out of the phononic material. This is confirmed by evaluating the energies in all the layers in between the contacts (E_L), which are ~ 0 for all ξ [refer to diamond markers in Fig. 6.6(d)]. As $\xi \to \infty$, % dissipated energy (E_D) reduces after reaching a peak, whereas, % reflected energy (E_R) drastically increases. The attenuation zone, on the other hand, monotonically widens as $\xi \to \infty$ [Fig. 6.6(c)]. This highlights that the two friction-induced nonlinear effects - (1) amplitude-dependent energy dissipation and (2) amplitude-dependent reflection, together, govern the attenuation zone widening. Interestingly, the competition between these two effects results in dissipation-dominated and reflection-dominated regimes as a function of ξ [Fig. 6.6(e)]. As ξ increases beyond 1, the energy dissipation increases at a rate larger than the change in reflected energy. This indicates that as energy is added into the system, in the form of increased amplitudes, a larger portion of the energy is used in contact sliding. Thus, the widening of the attenuation zones for $1 \leq \xi \leq 3.8$ is primarily caused by contact friction. On the contrary, reflected energy increases rapidly compared to dissipation for $\xi > 3.8$. Since energy dissipation has now reached a cap, any added energy is now reflected from the interface between the left waveguide, Γ_L, and effective phononic material. Thus, reflection is the primary reason for increasing the attenuation zone for $\xi > 3.8$.

Finally, the role of the periodic arrangement of rough contacts in reducing mechanical energy propagation is explained. As the input wave energy propagates through the material with an array of contacts, it is primarily dissipated at the first contact, i.e. the contact with which the propagating wave interacts first [Fig. 6.7(a)]. Since the first contact restricts the transfer of forces beyond the stick limit, the wave transmitted across the first contact propagates forward with an amplitude equal to the stick limit. When this transmitted wave interacts with the subsequent contacts, it is incapable of causing further sliding. Thus, the total contribution of later contacts in energy dissipation from the incident wave is zero. However, note that despite the low amplitudes of the waves, the tangential forces generated at the later contacts depend on the

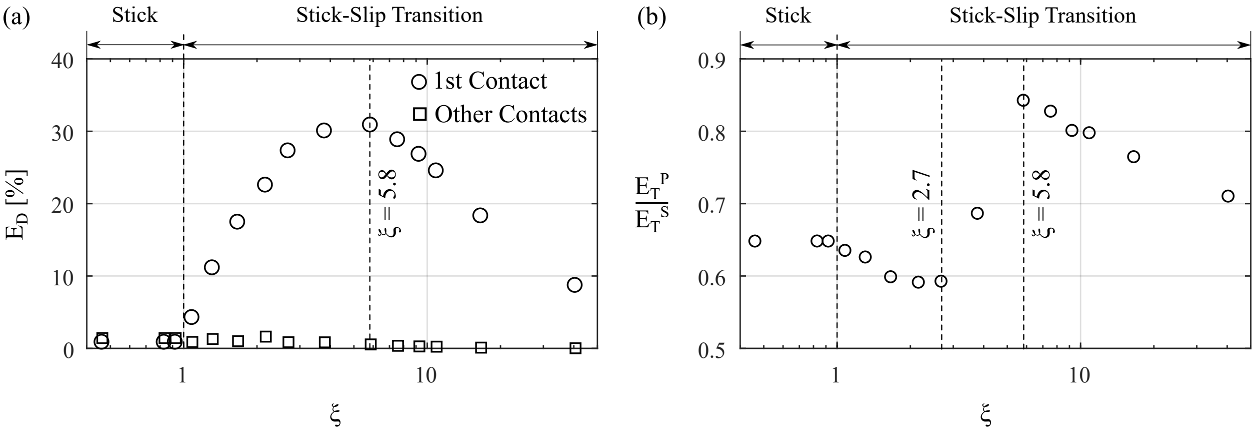

Figure 6.7: The effects of contact-periodicity on wave propagation. (a) Energy dissipation, as a fraction of input energy, for different contacts of the finite phononic material. (b) The ratio of normalized transmitted energy in the case of periodic contact (E_T^P) to a single contact (E_T^S) system. E_T^S results are obtained for the same input excitation as that of E_T^P to facilitate comparison.

interference of the forward propagating waves and reflected waves from each contact. This complex wave dynamics, enabled by the periodic arrangement, cause later contacts to undergo a limited amount of sliding resulting in non-zero but relatively much smaller energy dissipation.

More importantly, the later contacts enable phononic effects by causing multiple reflections and transmission, and their destructive interference (or Bragg scattering). Thus, the energy transmitted in the case of periodic contact is considerably smaller compared to a single rough contact for the same excitation amplitudes [note that $E_T^P/E_T^s < 1$ in Fig. 6.7(b)]. For $\xi < 1$, the energy transmitted across the contacts depends only on the acoustic impedance at the contact. Thus, the only mechanism to suppress the propagation of energy is through Bragg-scattering, caused by the periodic arrangement of contacts. This eventually reduces the energy transmission by about 35%, which is amplitude-independent. For $\xi > 1$, contact sliding and phononic effects both contribute to reducing energy propagation in the phononic material. As a result, the effectiveness in reducing energy propagation increases for phononic material compared to single rough contact (note the drop in E_T^P/E_T^s up to 0.6 for $\xi = 2.7$). With a further increase in excitation amplitude, sliding becomes more prominent and the effect of the phononic process in suppressing wave propagation is overshadowed by the energy loss in dissipation. This is clear when the dissipation at the contact is maximum ($\xi = 5.8$), and the difference between energy transmitted for the single and periodic case is the minimum. As $\xi \to \infty$, the energy dissipation saturates, and the contribution of the phononic effects on reducing wave propagation again increases (note the gradual drop in E_T^P/E_T^s as $\xi \to \infty$). This effect can be attributed to the stronger reflection at the interface between the waveguide (Γ_L) and phononic material compared to the reflection from a single contact. This is because there exists a significant difference in the acoustic properties of the waveguide and effective phononic material, unlike the impedance mismatch in the single contact system.

Overall, these results illustrate that frictional contact is a passive mechanism to control wave transmission through phononic materials. In fact, the periodic arrangement of the contacts couples the phononic and hysteretic effects to enhance the typical properties of linear periodic media. Particularly, the propagation of mechanical energy can be mitigated significantly over a wide range of frequencies, without employing any additional mechanisms or increasing the unit cell size.

6.6 Summary

In this chapter, strongly nonlinear shear wave propagation through single and arrays of rough contacts with friction is studied. Specifically, how shear waves drive the frictional instability at the contacts and give rise to memory-dependent (hysteretic) nonlinear responses are explained, which has remained an unexplored territory in the field of phononic materials. These responses are then harnessed to demonstrate advanced wave control and the ability to enable smart mechanical functionalities. The key findings and demonstrations of wave control are as follows:

1. Wave-induced friction at contact generates shear-polarized eigenstrains, which are residual strains in the stress-free system. Physically, the eigenstrains correspond to the repositioning of the initially aligned contact interfaces (and therefore the waveguides) so that there exists an offset between them.
2. Eigenstrain generation can be isolated only to a certain section of the system, particularly between successive contacts, by exciting identical wave pulses from both sides simultaneously. These pulses negate each other's effects in the end waveguides but not in the layers between contacts.
3. Nonlinearly-generated eigenstrains were utilized to demonstrate acoustically-controlled smart mechanical functionalities, including a mechanical switch, precision position control, and surface reconfigurability.
4. Furthermore, wave-induced contact sliding results in energy dissipation. The underlying physics of how this amplitude-dependent energy dissipation passively widens the attenuation zones of finite contact-based phononic materials is explained. The optical band of the phononic material is suppressed from the combined effect of energy dissipation at the contact and energy reflection at the first interface, which eventually merges two band gaps and results in a wide band attenuation zone.

Chapter 7

Preliminary ultrasonic experiments

This chapter presents experimental investigations of ultrasonic wave propagation through rough contacts. It begins with the acoustic characterization of bulk materials through underwater acoustic measurements. This provides information on the wave speed and frequency-dependent attenuation coefficient, which are essential for the precise analysis of ultrasonic wave propagation. Subsequently, the longitudinal and shear ultrasonic wave propagation through single rough contacts is examined. The measurements indicate nonlinear behaviors at the contacts and offer insights into challenges, potential solutions, and guidelines for future research. These experimental setups and preliminary measurements lay the groundwork for realizing continuum phononic materials with contacts and validating their nonlinear wave responses.

7.1 Acoustic characterization of bulk material

Wave propagation through bulk materials can be described through their acoustic properties, namely wave speed, and attenuation. Wave speed refers to the velocity at which a wave travels through a medium, whereas attenuation refers to the reduction in the amplitude or intensity of a wave as it propagates through a medium [224]. Attenuation typically occurs due to one or combinations of - (1) diffraction or spreading of an excited wave from a finite-width source (e.g. transducer), (2) scattering from (wave interaction with) grains, dislocations, inclusions, and pores, and (3) damping/absorption/dissipation from crystalline defects, dislocation motion, grain boundary sliding, elastothermodynamic, friction, and magnetoelastic effects. Due to these inherent mechanisms, wave attenuation is often unavoidable, even in bulk materials that seem homogeneous at the macroscale. Moreover, the wave speed and attenuation of the material often exhibit frequency dependence, particularly at ultrasonic frequencies. At these frequencies, the wavelengths are small enough to be influenced by the material microstructure and defects, which cause wave scattering and hence frequency-dependent acoustic response.

Wave speed and attenuation have traditionally been employed in nondestructive evaluation to predict the state of material and damage [225]–[227]. Typically, materials with higher modulus exhibit greater wave speed, while increased attenuation is indicative of more damage or the presence of microcracks and dislocations [225]–[227]. In general, attenuation tends to rise with frequency [228], [229]. Consequently, meticulous consideration of these acoustic properties is necessary to experimentally observe the nonlinear wave responses of the proposed continuum phononic material. This is due to the fact that weakly nonlinear phenomena, such as DC and harmonic generation, as well as strongly nonlinear effects, such as variations in stegoton amplitude within a layer, are at least an order smaller than the input amplitude. By accounting for variations in attenuation and wave speed arising from manufacturing, defects, and handling, it becomes possible to isolate and investigate the effects of nonlinear phenomena induced by rough contacts. In this dissertation, aluminum was chosen as the base material for the phononic material under investigation. Although the attenuation coefficient of aluminum alloys is relatively small compared to other metals [224] and non-metals [228], [229], it should be noted that the absolute amplitudes of waves generated by ultrasonic transducers in metallic materials are on the order of nanometers. Therefore, even the smaller attenuation coefficients can play a significant role when wave propagation is studied over longer propagation distances, as expected in a periodic contact phononic material. Further, the effects of attenuation and variation in wave speed can not be ignored while working with other metals and non-metals. Thus, accurate measurement of responses necessitates the consideration of the frequency-dependent acoustic properties of the parent material. Additionally, additive manufacturing can be employed to produce controlled roughness at contacts for the physical realization of these phononic materials. However, the acoustic properties of additively manufactured materials cannot be assumed and must be evaluated through nondestructive means. In this section, ultrasonic measurements in an immersion tank are conducted to evaluate wave speed and attenuation. While aluminum samples are used, the experimental framework is presented so that it can be carefully applied to complex materials as well.

7.1.1 Ultrasonic pulse-echo immersion measurements

To characterize the acoustic properties of the material, ultrasonic pulse-echo measurements were conducted in an immersion tank. This method involves capturing multiple echoes from the sample. The estimation of wave speed relies on analyzing the time intervals between different echoes, while variations in echo amplitudes provide information about the attenuation coefficient. Immersion methods offer enhanced reliability due to the consistent coupling between the transducer and sample facilitated by the presence of water (or fluid, in general). In contrast, contact-based measurements often encounter difficulties in reproducing a consistent interface between the sample and transducer. Consequently, the complexities and errors associated with calculating and correcting the reflection coefficient [228] at the transducer-sample interface can be avoided.

7.1.1.1 Sample preparation

Three samples in the form of rectangular blocks of 10 mm X 40 mm X 40 mm were machined from an extruded square bar of aluminum alloy 6061-T6511 (vendor: OnlineMetals). This particular shape was selected for its ease of fabrication and mounting. However, it is worth noting that other shapes can also be utilized, as wave speed and attenuation are intrinsic material properties that are not dependent on sample shape. All the surfaces of the samples were surface finished using a milling process leading to an average roughness value $\sim$ 0.25 μm. This level of smoothness ensures that unwanted scattering from the sample surface is minimized. The thickness of the sample ($L_s = 10$ mm) is chosen such that echoes from the rear end of the sample do not overlap the incident pulse at the probed frequencies. A sample size with a side length four times larger than the thickness was selected to mitigate any effects of side reflections on the pulse-echo measurements. Moreover, the chosen side length exceeds the transducer size based on diffraction calculations discussed in the subsequent section, ensuring maximum beam intensity focusing on the sample.

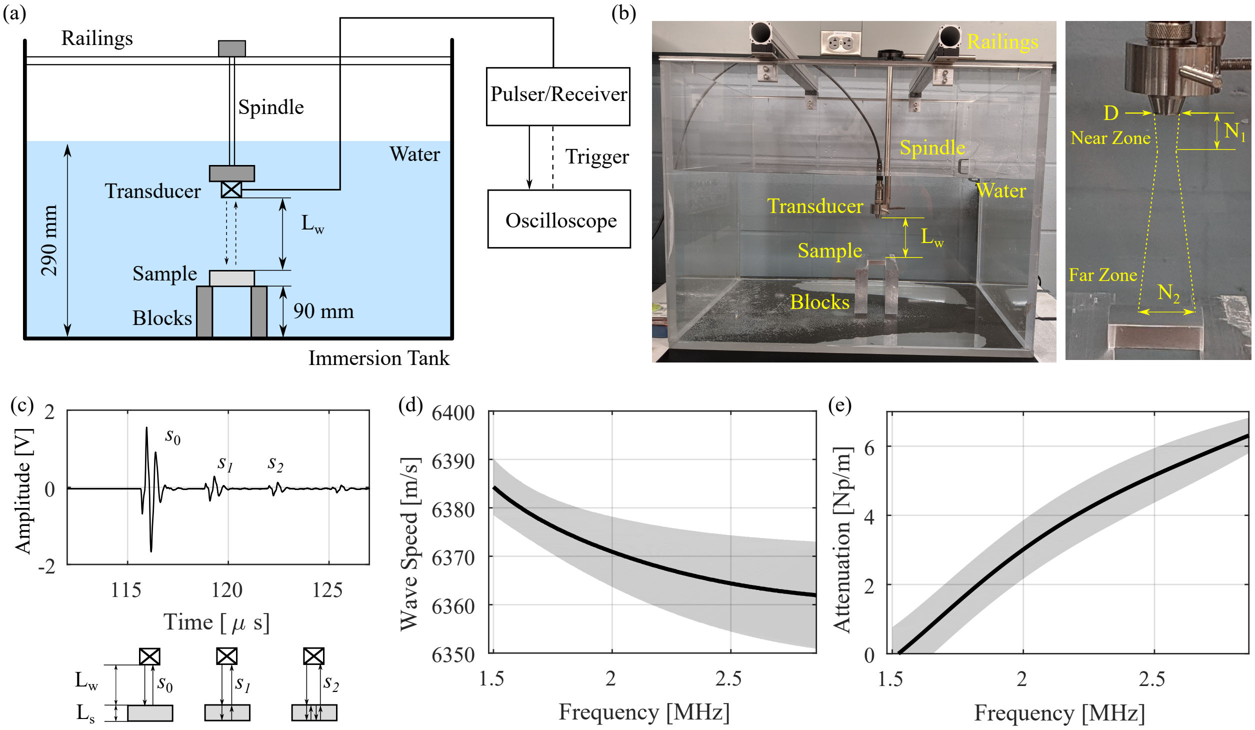

Figure 7.1: Ultrasonic pulse-echo immersion measurements for acoustic characterization of aluminum. Experimental (a) schematic and (b) physical setup. Inset in (b) illustrates the beam spreading from the transducer toward the sample. (c) Typical recorded time signal with the surface (S_0), first back-wall (S_1), and second (S_2) back-wall echoes. Estimated (d) wave speed and (e) attenuation coefficient of aluminum over the transducer bandwidth. Solid lines and shaded stripes are mean values and standard deviations, respectively.

7.1.1.2 Experimental setup and parameters

Fig. 7.1 shows the experimental schematic [Fig. 7.1(a)] and the actual setup [Fig. 7.1(b)] of the ultrasonic pulse-echo immersion measurement. The tank was filled with water that has been purified using a portable filter, and the water level was kept consistent throughout all measurements. To hold the immersion transducer in water, a spindle with a transducer seat at its end was employed. This spindle was attached to railings that facilitate the positioning of the transducer inside the tank. The sample was rested on two blocks, aligned with the transducer axis, and their parallel alignment was ensured using a spirit level during the experiment. The measurements were conducted in a vertical orientation to simplify alignment. The specific distances highlighted in the setup serve the following purposes: (1) preventing double reflections of the first surface echo from interfering with other reflections, (2) avoiding interference between reflections from the bottom surface of the tank and the first and second back wall reflections, and (3) eliminating any impact of reflections from the tank walls on the measurement.

For frequencies < 10 MHz, the contact properties of microns-scale roughness do not exhibit frequency dependence, and the quasi-spring model assumption is applicable [113]. As a result, ultrasonic measurements involving rough contacts (Sections 7.2 and 7.3) were conducted at frequencies < 3 MHz. Therefore, the acoustic properties of the material were also evaluated within these frequency ranges. Particularly, pulse-echo measurements were conducted using an immersion transducer with a center frequency of 2.25 MHz (Olympus, V323) and a bandwidth range of 1.48-2.86 MHz.

The distance between the sample and transducer (L_w) was carefully selected by considering the effects of near-field fluctuations and beam spread at a far-field [refer to the inset of Fig. 7.1(b)]. In the near-field regime, the wavefront generated by the transducer is not fully developed, leading to distortion and uneven distribution of acoustic energy. It is advised that the measurement should be done outside the near-field regime. A near-field distance, N_1, is given by,

$$N_1 = \frac{D^2}{4\lambda}, \tag{7.1}$$

where, D is transducer diameter and λ is the wavelength of excited frequency in water, all in meters. While the wave speed in water can be evaluated from the measured signals, it is assumed to be 1500 m/s for simplicity. The beam spread, N_2, is calculated as

$$N_2 = 2L_w \left\{ \tan \left[\sin^{-1} \left(\frac{Kc_w}{Df} \right) \right] \right\}, \tag{7.2}$$

where, L_w is the distance between the transducer face and the sample front wall. K is the constant beam divergence factor which was taken as 0.56 for 6dB. c_w and f are wave speed in water and frequency of excitation, respectively. Distance, L_w, in the experimental setup was selected as 85 mm, which is larger than N_1 and results in N_2 smaller than the side length of the sample, for the used transducer. This way the concentration of the excited transducer beam on the sample was ensured.

7.1.1.3 Measurement and post-processing

First, the density of the material was evaluated through Archimedes's method where sample weights were measured both in the air and in water such that

$$\rho = \frac{W|_{Air}}{W|_{Air} - W|_{Water}} \rho|_{Water}, \tag{7.3}$$

where, W is weight of the sample in respective medium and ρ is density. The mean value of measured density is 2708.25 kg/m^3.

Ultrasonic measurements were performed in a pulse-echo mode such that the same transducer was used for sending and receiving the signal [Fig. 7.1(a)]. A pulse was emitted into the water, which reflects from the water-sample interface generating a surface echo (S_0). Subsequently, the first (S_1) and second (S_2) back-wall reflections arise and were captured by the transducer. The pulse was generated using a pulser/receiver (JSR Ultrasonics, DPR300, 475V, 50MHz Bandwidth) and recorded using an oscilloscope (Tektronix MSO44). Both pulser and oscilloscope were set at 50Ω terminal load and therefore BNC connection cables of grade 58U were used. The pulse was characterized by the following settings: gain = 30 dB, low Pass Filter = 10 MHz, pulse amplitude = 325V, damping = 5, and pulse energy = high Z4. A representative recorded signal (averaged over 256 points, bandwidth limit = 350 MHz, and sampling rate = 3.125 Gs/s) with corresponding reflections is shown in Fig. 7.1(c). To ensure comprehensive data collection, three different measurements were conducted, with each measurement involving three additional sets of measurements. This approach involved removing and remounting the sample in the tank before each set, resulting in a total of nine measurements.

As mentioned earlier, wave speed may exhibit frequency dependence as a result of scattering from the material's microstructure and defects if the probed wavelengths are small enough to be influenced by them. Therefore, to estimate the phase velocity of the waves propagating through the sample at the probed frequencies (1.48-2.86 MHz), the phase shift of the propagating frequencies is considered. The phase velocity is then estimated using the following equation:

$$c_p(f) = \frac{2L_s}{\Delta t + \frac{\Delta\phi(f)}{2\pi}}, \tag{7.4}$$

where L_s is sample thickness, Δt is the time difference between the two echoes (first and second back wall), and $\Delta\phi$ is the phase difference between propagating frequencies of the pulse.

The attenuation coefficient, α, is evaluated as [228]–[230],

$$\alpha = \frac{1}{2L_s}\left\{ ln\left|\frac{S_1(f)}{S_2(f)}\right| - ln\left|\frac{D_L(f, 2L_w + 2L_s)}{D_L(f, 2L_w + 4L_s)}\right| + ln(|R_{ws}|^2)\right\}, \tag{7.5}$$

where S_1 and S_2 are first and second back-wall reflections respectively, R_{ws} is reflection coefficient at sample-water interface such that, $R_{ws} = \frac{Z_w - Z_s}{Z_w + Z_s}$, where $Z = \rho c$ is acoustic impedance with subscript w and s correspond to water and sample material, respectively. The density of water is considered as 1000 kg/m^3. D_L in Eq. 7.5 is a Lommel diffraction correction valid for $\sqrt{qD} \gg 1$ and given by [229], [231],

$$|D_L(f, z)| = \left\{\left[\cos\frac{2\pi}{\Pi(f, z)} - J_0\left(\frac{2\pi}{\Pi(f, z)}\right)\right]^2 + \left[\sin\frac{2\pi}{\Pi(f, z)} - J_1\left(\frac{2\pi}{\Pi(f, z)}\right)\right]^2\right\}^{\frac{1}{2}}, \tag{7.6}$$

where J_0 and J_1 are Bessel functions and $\Pi = \frac{\lambda z}{D^2}$. In these experiments, for the selected transducer ($D = 6.35$ mm and $f = 2.25$ MHz), $\sqrt{q_w a} = 7.73 \gg 1$ and $\sqrt{q_s a} = 3.76 \gg 1$. This ensures the validity of Eq. (7.6). Further, $\Pi = 4.3 > 3$ confirms that the calculations are conducted outside the fluctuation zone of the Lommel diffraction correction.

7.1.2 Estimated phase velocity and attenuation

Fig. 7.1(d) shows obtained phase velocities and their relationship with frequency. The measured values of the phase velocity are comparable to the known standard value (6400 m/s [232]) for wave speed in aluminum. However, there is a slight difference, indicating possible variations in material alloy composition and manufacturing effects. The measured phase velocity is consistently slightly smaller than the standard value. Furthermore, the experimental data reveals that the phase velocity only marginally decreases as the frequency increases. Over a frequency range of 1.5 MHz, the reduction in phase velocity is approximately 0.4% only. This means wave propagation speed within the aluminum material is frequency-independent for the probed frequencies. Thus, an average value of wave speed over these frequencies is obtained (6375 m/s) and used for further calculations. The variability in the experimental measurements and across trials is less than 0.1%, indicating good consistency and reproducibility of the results.

Fig. 7.1(e) shows the wave attenuation coefficient and its dependence on frequency. The attenuation coefficient represents the rate at which the wave amplitude decreases as it propagates through the material. Based on the obtained data, the experiment indicates an almost negligible or even negative wave attenuation coefficient for frequencies below 1.5 MHz. This means that at these frequencies, the wave amplitude does not change significantly during propagation, or at least not enough to be captured by the sensitivity of the experimental setup. As the frequency increases, the attenuation coefficient starts to increase as well. At 2.86 MHz, it reaches a maximum value of ~6 Np/m. This measured range of coefficients aligns with the literature values reported for different aluminum alloys using various measurement techniques [224], [233]. Moreover, the standard deviation is very small, indicating the reliability and precision of the experimental setup.

The acquired acoustic properties of aluminum are utilized in the subsequent experiments to ensure precise measurement and estimation of the contact response. To physically realize the phononic materials discussed in this study, it becomes necessary to fabricate contacts with controlled roughness in order to reduce disorder. However, it is important to note that 3D printed materials often exhibit inherent microstructural defects or features, such as soft phases, porosities, and loosely jointed interfaces or powders, which depend on the specific fabrication method employed. Consequently, the acoustic properties of these materials can significantly deviate from those of their parent material. In such cases, the developed experimental setup can be utilized to assess the acoustic properties of these complex and intricate materials.

7.2 Longitudinal wave propagation through rough contact

The traditional method for investigating the nonlinear response of rough contacts involves analyzing load-deformation data obtained from two contacting bodies [234]. However, this approach is susceptible to errors due to the significantly smaller interfacial deformation compared to bulk deformations [235]. An alternative method that overcomes these limitations is the use of ultrasonic techniques for characterizing rough contacts [113], [236], [237]. The key advantage of the ultrasonic method is that the signal reflected from the interface can be separated in time from those originating from the boundaries of the bulk material. As a result, the accuracy of the measurement remains unaffected by the bulk deformations or specimen dimensions. Both linear and nonlinear ultrasound approaches have been employed for contact characterization. In the linear approach, the contact is treated as a linear spring, and the measured reflection or transmission is directly correlated with the spring stiffness using analytical methods. Thus, this method is primarily suitable for strongly compressed rough contacts [113], [236], [237] only. On the other hand, the nonlinear approach utilizes either the second harmonic [238] or wave mixing [136] to quantify the linear and nonlinear stiffness, limited to quadratic order. However, these studies have primarily focused on weakly nonlinear regimes, where the precompression exceeds the wave amplitudes. It is important to note that the behavior of rough asperities under light precompression, particularly when predeformations are smaller than wave amplitudes, is expected to exhibit distinct characteristics (namely coefficient and exponent of power-law) compared to what has been previously reported.

This section focuses on longitudinal wave propagation through rough contact. For the future realization of phononic material with rough contacts, this study establishes an initial experimental framework, including an ultrasonic setup that potentially informs nonlinear behavior at rough contact through wave measurements. First, linear wave propagation is employed to characterize contact nonlinearity as a means to develop and validate an in-house ultrasonic setup. The method relies on measuring the transmission and reflection coefficients at a rough contact. These coefficients are determined by measuring the incident and transmitted waves through contact. The contact is then treated as a linear spring with stiffness analytically formulated as a function of wave coefficients [239], [240]. However, the nonlinearity of the contact is captured when the coefficients are measured for different external precompressions. Effectively, contact stiffness evaluated from these coefficients exhibits a nonlinear dependence on precompression that inform the power-law relationship at the contact. While these contact laws may be used for weakly nonlinear studies, the limitation of this method for characterizing contact responses for light precompression is also discussed. Finally, a hybrid numerical-experimental approach for contact characterization in a strongly nonlinear regime is proposed as future work. This approach may provide insights into the stegoton properties based on the strongly nonlinear responses of the contact.

7.2.1 Contact characterization using linear ultrasonic waves

7.2.1.1 Sample preparation

Four samples in the form of rectangular blocks of 20 mm X 30 mm X 30 mm were machined from an extruded square bar of aluminum alloy 6061-T6511 (vendor: OnlineMetals). This particular shape was selected for its ease of fabrication and mounting. To ensure better and consistent alignment, all surfaces of the samples underwent surface finishing using a milling process. The thickness of the sample ($L_s = 20$ mm) is chosen such that reflections from the contact surface of the sample do not overlap the incident wave at probed frequencies. A larger side length was chosen to avoid side reflection affecting measurements. Additionally, the side length is larger than the transducer size, as per the diffraction calculation presented in the section 7.1.1.2, to ensure the focusing of most of the excited energy on the sample.

7.2.1.2 Roughness generation and measurement

Wave propagation is studied in the thickness (L_s) direction of the sample. To prepare the samples for experimentation, one surface of each sample, perpendicular to the thickness direction, was manually polished using sandpapers of varying grits. Initially, P240 sandpaper (Buehler, CarbiMet) was used, which provides the roughest abrasion, followed by P400. The polishing process was continued until the surfaces exhibited a lack of specific directionality in roughness, and any prominent patches, grooves, or cracks were no longer visible. Subsequently, these polished surfaces were thoroughly cleaned using a compressed air gun, gently washed under water, and finally treated with Isopropyl alcohol (IPA) to eliminate any remaining dirt, loose particles, or microscale stains that may persist after the polishing stage. These meticulously polished surfaces served as the rough contacts in the experimental setup.

To accurately assess and ensure uniform roughness on the mating surfaces, optical imaging was employed for quantifying the rough surfaces. In comparison to traditional stylus profilometers, optical profilers offer superior resolution, contrast, and provide areal measurements. Consequently, roughness measurements become less susceptible to directional surface features. Furthermore, optical profilers enable the generation of 3D images, facilitating a comprehensive understanding and visualization of surface texture. These instruments operate as non-contact and non-destructive tools, ensuring that the sample surface remains unaltered and free from marks, which is crucial for preserving the integrity of rough surfaces. In this study, a 3D laser scanning confocal microscope (Keyence, VK-X1000) was utilized due to its exceptional resolution of 20 nm in the vertical direction and focus variation ranging from 1-10 micrometers. A 20x objective lens was employed, and roughness values were measured at five different locations on each surface. The field of view for each measurement was set at 0.5 mm X 0.7 mm. Since the nonlinearity of rough contacts at the frequency of interest (~ 1.7 MHz) is associated with the mesoscale response (given that $\lambda > \delta$), the field of view was selected to be approximately 100 times larger than typical rough features (a few microns). Additionally, the wavelength of the frequencies of interest was around seven times larger than the field of view, ensuring the experimental validity within an effective spring model of contact for subsequent post-processing. The mean and variation of the measurements at all five sites were then evaluated and reported as quantitative mesoscale parameters representing the surface roughness.

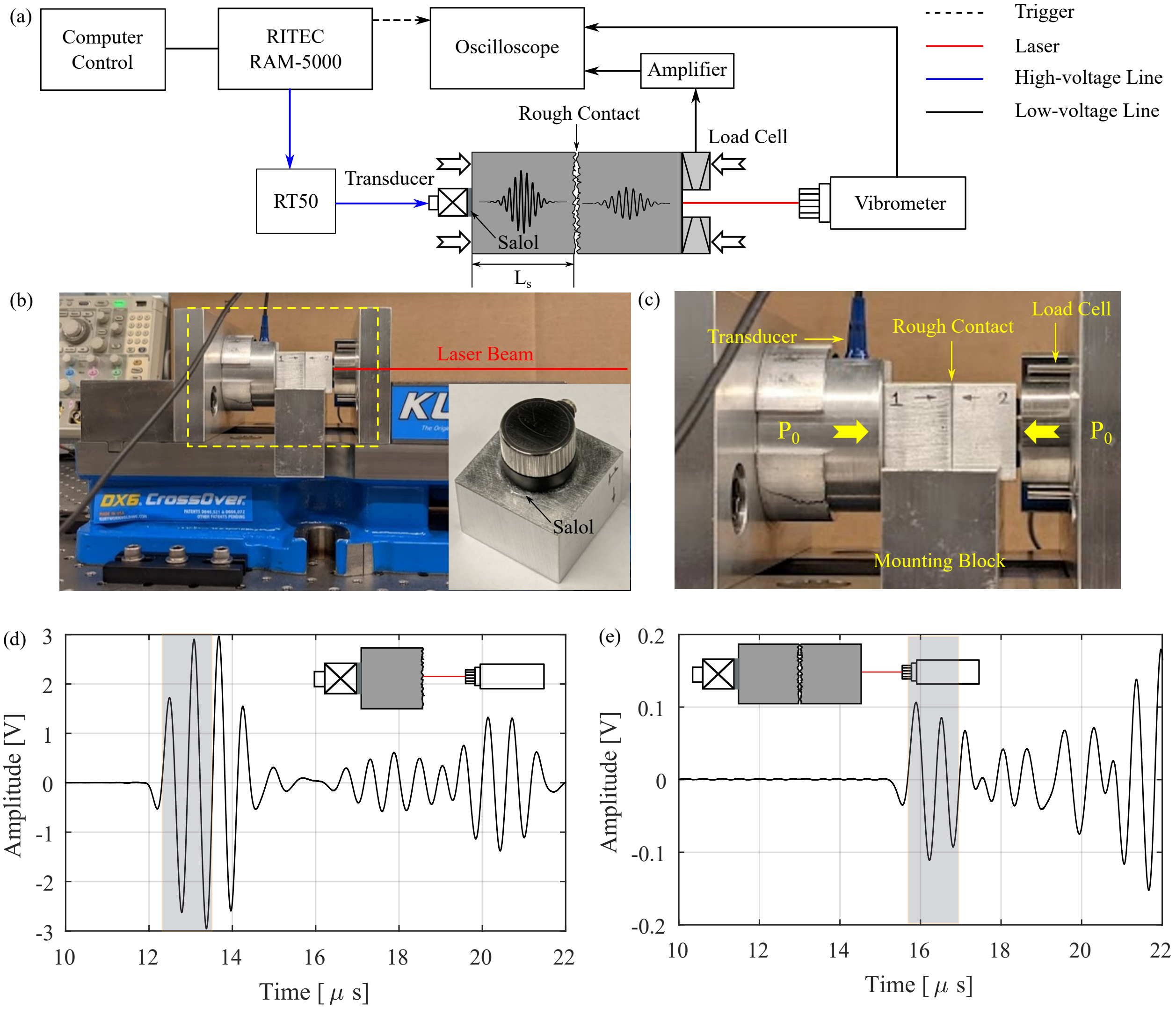

Figure 7.2: Ultrasonic characterization of rough contact. Experimental (a) schematic and (b)-(c) physical setup. Inset in (b) shows transducer-sample coupling through Salol. (c) Zoomed view of the yellow dashed rectangle in (b). Typical recorded time signal of (d) incident and (e) transmitted wave. Inset schematic show the corresponding experimental setup and shaded regions are the main wave packets used for postprocessing.

7.2.1.3 Experimental setup

Fig. 7.2 shows the experimental schematic [Fig. 7.2(a)] and the actual setup [Fig. 7.2(b)] of the ultrasonic wave propagation through a rough contact. Two aluminum blocks were mounted on a manually operated pressure vice (Kurt DX6) to form a rough contact such that the polished surfaces face each other [Fig. 7.2(c)]. The vice was mounted on an optical table to isolate ground vibrations and mounting fixtures were meticulously designed to ensure precise alignment of the two blocks. An ultrasonic contact transducer (ndtXducer, CMP01.54) with a nominal frequency of 1.7 MHz, narrow bandwidth of 1.5-1.9 MHz, and a piezo element diameter of 0.25” was attached to the left surface of the left sample using a thermal adhesive – Phenyl Salicylate (salol). This particular thermal adhesive, salol, ensured a robust and consistent coupling between the transducer and the sample, eliminating variations during measurements. Salol is available in powder form, with a melting temperature of 45°C and solidification occurring at room temperature. Consequently, the transducer can be easily attached to and detached from the sample using a low-capacity heat gun, without compromising the integrity of the adhesive bond. Solidifying within the operating temperature limit of the transducer (60°C), salol did not cause any damage to the transducer. The second sample was in contact with the load cell (Transducer Techniques, THC-5K-T), which measured the force applied to the samples. The low voltage signals of the load cell were amplified through a power amplifier (FUTEK IAA100). Fixtures were designed carefully to ensure that the pressure exerted by the vice was transmitted solely to the sample blocks and load cell.

7.2.1.4 Measurement and postprocessing

A high-power ultrasonic measurement system (RITEC RAM-5000) was used to excite a wave. To compensate for the lower conversion efficiency of the transducer and potential energy loss at the contact, a high-power exciter was utilized, enabling a higher energy input into the system. The output port of RITEC system was terminated with a 50Ω load to reduce fluctuation in the input signal. The wave consisted of 3 cycles at a frequency of 1.7 MHz, with an output level set at 50% of the full-scale power of the RITEC system. The length of the signal was carefully chosen to ensure it could be effectively separated from the reflected and transmitted waves, while still providing enough cycles for accurate data processing in the frequency domain. The power level was limited to 50% to prevent any potential damage to the transducer. During the experimentation, it was observed that the signal exhibited a slight variation in peak amplitude of approximately 0.5% over a period of 3 hours. This variation could potentially be attributed to thermal fluctuations in the electronics. The wave was detected using a Doppler vibrometer (Polytec, OFV505) equipped with a velocity decoder (VD09) at 200mm/s/V range. To facilitate the laser beam projection onto the sample's surface, a hollow cylinder load cell was employed. The vibrometer signals were then transferred to an oscilloscope (Tektronix MSO44) with the termination of 1MΩ for maximum voltage transfer.

First, wave incident to the rough contact was measured. To do this, only the left sample was mounted on the vice, and the laser beam was focused on the right (polished) surface of the sample. The measured signal was used as an incident wave $[S_A(t)]$ to calculate wave coefficients. Then, the second sample was loaded on the vice, and the wave was measured on the right surface of the second sample $[S_B(t)]$. The measured signal was corrected for attenuation and diffraction in the right sample and used as a signal transmitted through the contact. Typical recorded signals of the incident and transmitted waves (averaged over 256 points, bandwidth limit = 350 MHz, and sampling rate = 3.125 Gs/s) are shown in Figs. 7.2(d) and 7.2(e), respectively.

These time signals were transformed into the frequency domain by taking an FFT. A Hanning window was used over the main wave packet to isolate other reflections in processing the data. Then, the transmission coefficient, $T(f)$, was evaluated in the frequency domain as,

$$T(f) = \frac{S_B(f)}{S_A(f)} \frac{1}{2D_L(f,z)\alpha_c(f,z)}, \tag{7.7}$$

where $D_L(f,z)$ is diffraction correction as given by Eq. (7.6) and α_c is attenuation correction as given by $\alpha_c = e^{[-(\alpha z - ikz)]}$ with $z = L_s$. The measurements were repeated for multiple loading and unloading precompression. The reflection coefficients were evaluated as $R(f) = 1 - T(f)$.

To evaluate the contact properties, the contact is treated as a linear spring with stiffness, K_N. An analytical expression of K_N as a function of R is obtained essentially on similar lines as [239], [240]. Considering a 1D wave propagation through the contact and force continuity at the contact interface leads to,

$$\sigma(X_-, t) = \sigma(X_+, t) = F_s, \tag{7.8}$$

where X_- and X_+ are the contact interfaces in spatial coordinate x and F_s is contact spring force. This can be further rewritten in terms of material and contact properties as,

$$E\frac{\partial u(X_-, t)}{\partial x} = E\frac{\partial u(X_+, t)}{\partial x} = K_N[u(X_+, t) - u(X_-, t)]. \tag{7.9}$$

It is worth noting that the stresses in bulk material depend on the derivative of displacement whereas contact forces depend directly on displacement, which eventually leads to frequency-dependent relation between stiffness and wave coefficients. However, recall that due to the underlying modeling of contact as a quasi-spring, the contact stiffness itself is frequency independent.

Considering wave propagating of a function, Φ, leads to: $u_i = \Phi$, $u_r = R(\omega)\Phi$, and $u_t = T(\omega)\Phi$, where i, r, and t denotes incident, reflected and transmitted waves. Replacing these waves in Eq. (7.9) results in,

$$i\omega\rho c[R(\omega) - 1]\Phi = -i\omega\rho c T(\omega)\Phi = K_N[T(\omega) - R(\omega) - 1]\Phi. \tag{7.10}$$

Effectively, the contact stiffness as a function of the reflection coefficient is:

$$K_N = \frac{\omega\rho c}{2}\sqrt{\frac{1}{[R(\omega)]^2} - 1}. \tag{7.11}$$

Note that by definition, the contact stiffness, K_N, must be frequency independent, which informs that the reflection coefficient, $R(\omega)$, and frequency, ω, in Eq. (7.11) should counterbalance each other.

7.2.2 Estimated contact characteristic

As discussed, one surface of each of the four samples was polished. This allowed for the examination of two rough contacts formed by pairing samples 1 and 2 and samples 3 and 4 (Fig. 7.3). To assess the roughness, the polished surfaces were measured both before and after applying precompression using an optical microscope [example results of sample 1 polished surface is shown in Fig. 7.3(a)]. The maximum peak and valley of the rough features are found to be approximately from 4 - 5 μm. The results indicate that the average roughness is uniform across the measured locations for each surface [Figs. 7.3(b) and 7.3(c)]. Additionally, the roughness values exhibit remarkable consistency, ranging from 0.46-0.49 μm indicating a coefficient of variation of merely 0.04. Moreover, these roughness values are higher than 0.3 μm - expected of machined samples. This indicates that the polishing procedure rendered the surfaces rougher. Interestingly, despite manual polishing, the roughness is found to be isotropic. When considering the effect of precompression on the surface roughness, minimal changes are observed across all samples [compare blue vs black data points in Figs. 7.3(b) and 7.3(c)]. While the roughness values remained relatively stable, it is worth noting that sample 3 exhibits a larger spread in roughness values at different locations after precompression. While further measurements are required, specifically on other statistics such as peaks and valleys, these results indicate that the precompression values used in the measurements did not significantly alter the average surface roughness.

Wave propagation was measured and contact stiffness was estimated for three loading-unloading cycles

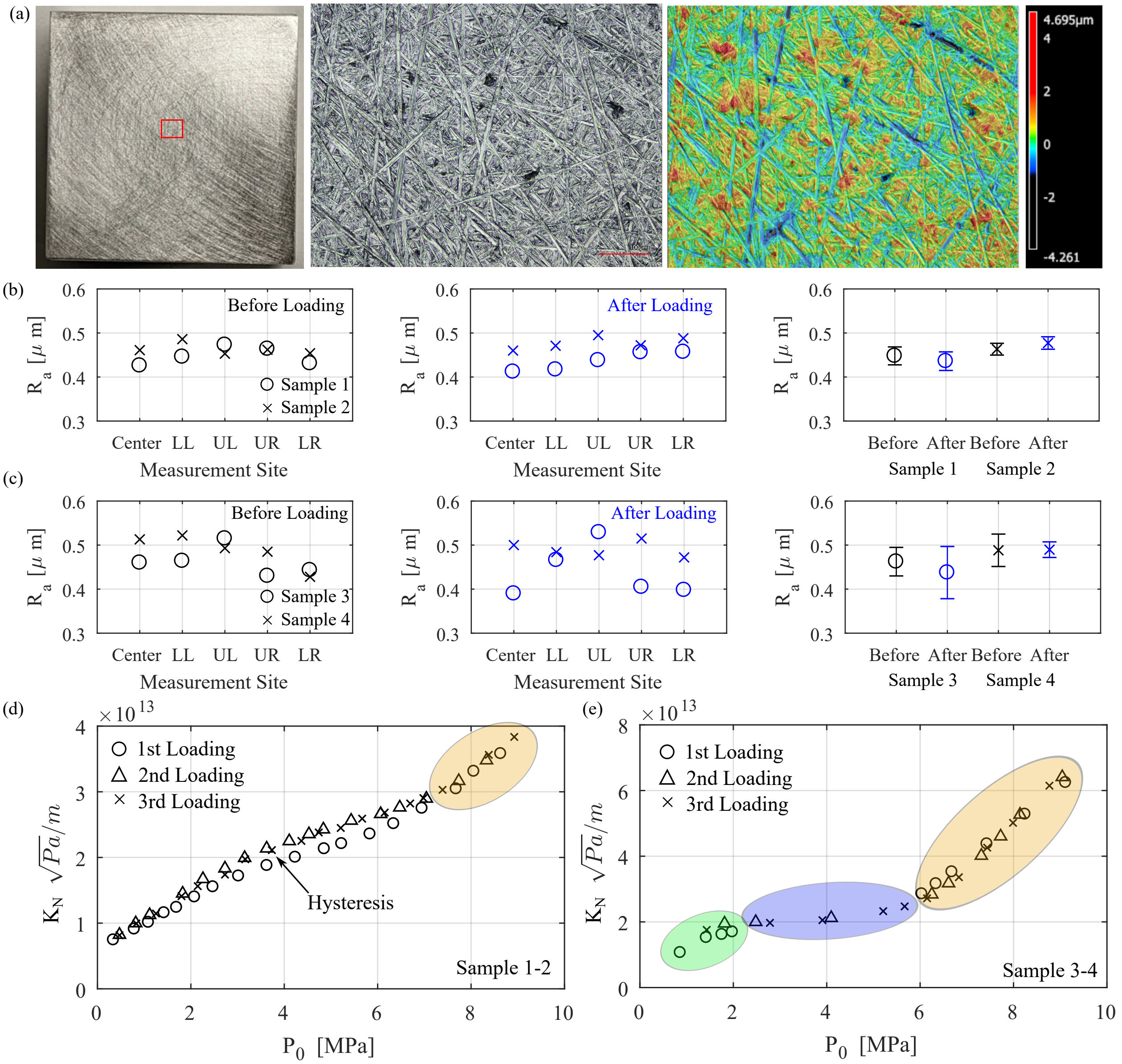

Figure 7.3: Estimated contact characteristics from ultrasonic measurements. (a) Sample 1 polished surface and corresponding surface texture. An optical microscope image and colormap with roughness height distribution of the region (red rectangle) of the surface are also shown. Average roughness of (b) sample 1-2 and (c) sample 3-4 before (black) and after (blue) precompression is applied. The measurement is done at five different approximate locations on the surfaces: Center, Lower-left (LL), Upper-left (UL), Upper-right (UR), and Lower-right (LR). Markers and error bars in the right plot show the mean and variation among these locations, respectively. Estimated $K_N - p_0$ nonlinear relationship for (d) sample 1-2 and (e) sample 3-4. Colored patches show different trends.

of external precompression [Figs. 7.3(d) and 7.3(e)]. Measurements were taken for each incremental load, while none were done during unloading due to a lack of control over decreasing precompression values in the manually-operated vice. The results for samples 1 and 2 pairings [Fig. 7.3(d)] consistently demonstrate an increasing and nonlinear trend of stiffness with precompression. This behavior can be attributed to the deformation of rough asperities. As the precompression is increased, the increasing deformation of asperities leads to an increase in the contact area, and therefore contact stiffness. The maximum load applied for each loading cycle was the same, resulting in a hysteresis but only during the first loading cycle. This indicates plastic deformation of asperities occurred only during the first cycle. Although this plastic deformation may not be evident in the average roughness measurements [Fig. 7.3(b)], it is possible that plastic deformation mainly occurred at asperities with peak roughness values. The lower percentage of roughness peaks on the surfaces possibly did not affect the overall average roughness value. No additional plastic deformation was observed during the subsequent 2nd and 3rd loading cycles, as evidenced by their overlapping nature. The data points from these subsequent loading cycles were fitted with a power law relation, yielding an exponent of 0.5, which has been proposed to be associated with asperities with a uniform height distribution [115]. This hypothesis is further supported by the roughness measurement, which indicates that the average roughness on these samples is in fact uniform. Interestingly, for the precompression, 7 MPa$< p_0 <$11 MPa (yellow shaded region), no hysteresis is seen between the 3 loadings, and the slope of the $K_N - p_0$ seems to have shifted. This behavior is more clearly seen for samples 3-4 pairing discussed next.

An additional set of samples (pairs of samples 3 and 4) was subjected to the same ultrasonic measurements [Fig. 7.3(e)]. Similar to the previous set of measurements, an increasing and nonlinear trend of contact stiffness with precompression is observed. However, two distinct trends have emerged based on the magnitude of precompression: for low precompression (green shaded region), the slope of the contact stiffness is relatively smaller, while for higher precompression (yellow shaded region), the slope becomes steeper. In the steeper portion of the contact stiffness (higher precompression values), no hysteresis is observed. All the loading cycles overlap, suggesting minimal plastic deformation. In the low precompression zone, the first loading differs slightly from the second and third loading. This difference could be attributed to the plastic deformation of rough asperities. These asperities, likely to be sharp or spike-like, experienced stress concentration for low precompression and underwent plastic deformation during the first loading cycle. This effect is expected to be pronounced in the low precompression zone, where the contact area is relatively smaller. However, lack of hysteresis at high precompression could be a result of a larger contact area, where deformation of sharp asperities does not contribute significantly. The fact that average roughness is fairly constant before and after precompression [Fig. 7.3(c)] support these results with a lack of noticeable hysteresis. Further experiments, at much higher precompression may be conducted to induce a stronger plastic deformation and validate the hypothesis outlined here.

The results also show an intermediate precompression zone (blue-shaded region), where contact stiffness remains relatively unchanged. This suggests that precompression applied within this range may not be effectively transmitted to the actual contact area probed by the propagating wave. The shift in the trend around 6 MPa may be attributed to the alignment of asperities and/or the interaction between neighboring asperities. It is plausible that at relatively higher precompression levels, the lateral deformation of asperities encounters increased resistance from surrounding asperities. This resistance could lead to a sudden rise in contact stiffness. Notably, the power-law fitting of data points at high precompression yields an exponent of less than 1, resulting in a force-displacement relationship with a softening nonlinearity. Although further experiments are required to validate this relationship, it is conceivable that rough contacts exhibit both hardening and softening nonlinearities within different precompression ranges.

7.2.3 Contact characterization in the strongly nonlinear regime

The current method employed for contact characterization assumes that the frequency content of the wave remains unchanged during its interaction with the contact. This assumption holds true for highly

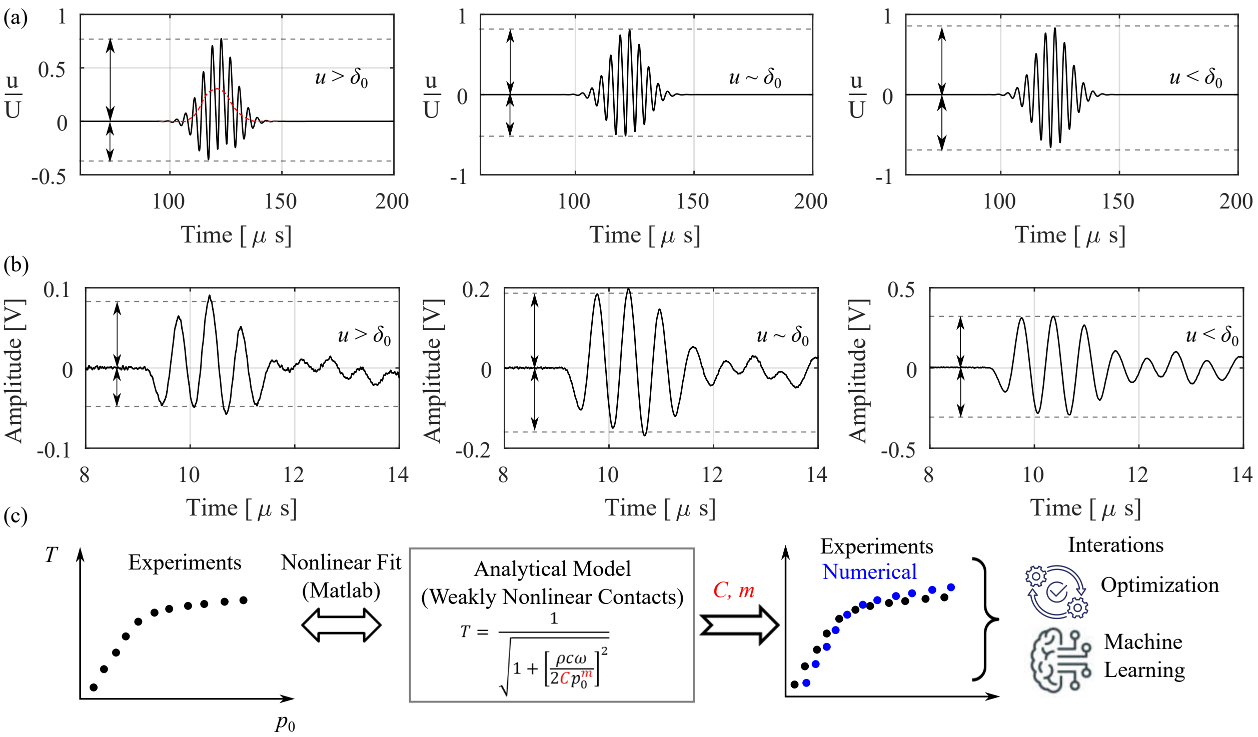

Figure 7.4: Contact characterization in a strongly nonlinear regime. Transmitted wave obtained from (a) numerical simulations and (b) experiments for strongly nonlinear (left and center) and weakly nonlinear regimes (right). Arrows indicate asymmetry in the wave profile. The Red dashed line indicates a long-wavelength component generated from contact nonlinearity. (c) Proposed hybrid experimental-numerical approach to characterize contact law in the strongly nonlinear regime.

precompressed systems and even weakly nonlinear cases where the amplitudes of generated higher harmonics are two orders of magnitude smaller than the fundamental wave. Therefore, any drop in the amplitude of the transmitted wave is attributed to the reflection at the contact, indicating an increased reflection coefficient. However, for lightly compressed contacts, where wave amplitudes are larger than the predeformation, contact clapping takes place and much stronger harmonics are generated [241]. In addition to that, asymmetric nonlinearity also generates low-frequency components. As a result, a portion of energy from the fundamental waves is transferred to other frequencies within the transmitted wave, instead of being solely reflected from the contact. These prominent nonlinear effects involving frequency conversion from wave-contact interaction lead to incorrect contact properties if the measured signals are post-processed using linear wave theory. In this section, the limitation of the approach presented in the previous section is elaborated and a hybrid method consisting of numerical-experimental parts is proposed for characterizing contact nonlinearity in the strongly nonlinear regime.

A prominent feature of strongly nonlinear wave-contact interaction in time domain signals is asymmetry. Due to contact clapping, wave transmission across contact is restricted when the contact surfaces separate. This generates asymmetry in the transmitted wave profile. Wave propagation through a single rough contact is simulated using finite element analysis as discussed in Chapter 3 for contact clapping. When wave amplitude is larger than predeformation, the displacement profile of the transmitted wave is asymmetric with a strong long-wavelength component [Fig. 7.4(a)]. As precompression is increased for the same wave amplitude, the asymmetry reduces and the wave becomes relatively more symmetric [compare wave for $u > \delta_0$ with $u < \delta_0$

in Fig. 7.4(a)]. The measured signals in the experiments of the previous section show the same behavior [Fig. 7.4(b)]: significant asymmetry at low precompression, which reduces as precompression is increased, i.e. when contact clapping is restricted. Clearly, nonlinear effects are substantial for low precompression, and an analytical model relating reflection coefficient and contact stiffness based on linear wave propagation is not applicable. While wave propagation through weakly nonlinear rough contacts has been studied analytically, the closed-form equations obtained through perturbation analysis are valid for low-amplitude waves only. Thus, these models can not be used to obtain contact characteristics under clapping behavior.

Alternatively, a hybrid experimental-numerical approach can be employed to determine the contact power-law relationship in the strongly nonlinear regime [Fig. 7.4(c)]. This approach involves estimating approximate contact law parameters and iteratively adjusting these parameters in finite element simulations to match experimentally obtained data. Specifically, the approach begins with the experimental acquisition of a transmission-precompression ($T - p_0$) relationship, as discussed in the previous section. This relation can then be nonlinearly fitted with the analytical model [115] of weakly nonlinear wave propagation, yielding potential values for the power-law exponent and proportionality constant. These estimated parameters can be subsequently utilized in the contact law within finite element simulations. Through iterative modification, the contact law parameters are adjusted to ensure that the transmission coefficient obtained from numerical analysis aligns with the experimental data across all precompression levels. This iterative process can be facilitated by developing a comprehensive understanding of the relationships between contact law parameters and transmission characteristics. Alternatively, advanced techniques like optimization and machine learning may be employed to expedite this method. This hybrid approach offers numerous benefits: Firstly, it does not rely on linear wave propagation. Secondly, it uses fundamental wave measurements instead of harmonics, which are often sensitive and prone to errors unless carefully measured. Finally, it enables the determination of contact properties within the strongly nonlinear regime, where analytical solutions are unavailable, and contact characterization remains an ongoing exploration.

7.3 Shear wave propagation through rough contact

This section focuses on ultrasonic wave propagation of shear polarization through rough contact. The objective of this study is to establish an initial experimental framework for realizing shear wave responses in phononic materials with rough contact. Preliminary studies suggest wave-induced friction at contact generates eigenstrains and results in energy dissipation, both of which may be captured experimentally.

7.3.1 Eigenstrain generation

Acoustic-radiation-induced strains, also known as eigenstrains, have been experimentally measured in materials with quadratic nonlinearity in their constitutive law, particularly for longitudinal waves. These strains have been looked at as static (or low-frequency) displacements in wave profiles. The first experimental measurements of these strains were conducted on samples of single-crystal silicon and vitreous silica [213]. It was observed that ultrasonic tone bursts generate static displacement pulses having the shape of a right-angled triangle. This shape was obtained by isolating the low frequencies of the measured signals using a low-pass filter. However, later studies highlighted the influence of detector bandwidth on the triangular shape [214], [215]. Jacob *et al.* [214] conducted careful experiments using an optical probe to measure the wave profile for different bandwidths. Their study revealed that the quasistatic displacement pulse, obtained by filtering the signal with a low-pass filter, exhibited a flat-top shape with an amplitude independent of the tone burst duration. Similar experiments conducted by Narasimha et al. [242] confirmed the flat-top shape of the detected quasistatic pulse, with its amplitude remaining unaffected by the duration of the tone burst. While these studies confirm the generation and presence of eigenstrains from longitudinal wave propagation, shear wave-induced eigenstrains are yet to be experimentally captured. A preliminary experimental framework has been developed here that possibly indicates the presence of friction-governed eigenstrains.

Finite element simulations were conducted to inform appropriate sample dimensions and experimental parameters for experimental validation of eigenstrain generation. To simulate 1D shear wave propagation and isolate scattering waves reaching the contact, samples with varying cross-sections were designed [Fig. 7.5(a)]. The main sources of scattered waves are typically the (1) edges of the transducer and (2) side boundaries of the samples. Enlarging the end sections of waveguides ($h_1 > h_0$ and h_2) minimize the interference of scattered waves from transducer edges and side boundaries with the main signal by the time measurements were done. Conversely, having a smaller cross-section (h_2) for the waveguide compared to the transducer element diameter (h_0) facilitates the replication of 1D wave propagation through the waveguide. The numerical results of high-amplitude shear wave propagation at 1 MHz frequency confirm the generation of eigenstrain even in a waveguide with finite lateral dimensions [Fig. 7.5(b)]. Note that the static displacements are generated in the waveguide only after $t = 15\mu$s, i.e., when the wave interacts with contact and triggers sliding. This static displacement is seen only when the wave amplitude is larger enough to cause sliding [Compare black vs red lines in time signal of Fig. 7.5(b)].

Two samples of the aforementioned geometry of dimensions $H = 40$ mm, $L = L_w = H$, and $H_w = \lambda$ were machined from an extruded square bar of aluminum alloy 6061-T6511 (vendor: OnlineMetals). These dimensions were carefully selected to minimize the impact of scattered waves, as previously discussed, and to prevent overlap between the main pulse and reflections from contacts at the chosen frequency of 1 MHz. The selection of this specific frequency enables working with sample sizes that are small enough to simulate 1D wave propagation while still being feasible to fabricate using conventional machining. Additionally, waveguide thickness similar to the wavelength approximates 1D wave propagation as informed by finite element simulations. The thickness is also four times smaller than the transducer, which approximates plane wave propagation through the waveguide, i.e. finite size effects in the lateral direction can be reduced. The cross-section of the sample is rectangular, simplifying fabrication and alignment processes and facilitating laser beam focusing on the surface. All the surfaces of the samples were surface finished using a milling process. No additional polishing at contact was done. The attenuation and diffraction effects and calculations were omitted for simplicity. However, incorporating these effects would facilitate a more accurate analysis.

The experimental schematic [Fig. 7.5(c)] and the actual setup [Fig. 7.5(d)] of the shear wave propagation through a rough contact is as follows: Two samples were mounted on a manually operated pressure vice (Kurt DX6) to form a rough contact [Fig. 7.5(d)]. The vice was securely mounted on an optical table to isolate ground vibrations and mounting fixtures were carefully designed to align the two blocks. An ultrasonic shear-polarized contact transducer (Olympus, V153-RM) of nominal frequency of 1 MHz, broad bandwidth of 0.5-1.5 MHz, and piezo element diameter of 0.25” was attached to the left surface of the left sample using a thermal adhesive – Phenyl Salicylate (salol). The polarization direction of the transducer was in the vertical direction, i.e. perpendicular to the waveguide axis. The second sample was in contact with the load cell (Transducer Techniques, THC-5K-T) which measured the force applied to the samples. The low voltage signals of the load cell were amplified through a power amplifier (FUTEK IAA100).

A pulse was generated using a pulser/receiver (JSR Ultrasonics, DPR300, 475V, 50MHz Bandwidth) with the settings of gain = 70 dB, low Pass Filter = 5 MHz, pulse amplitude = 475V, damping = 1, and pulse

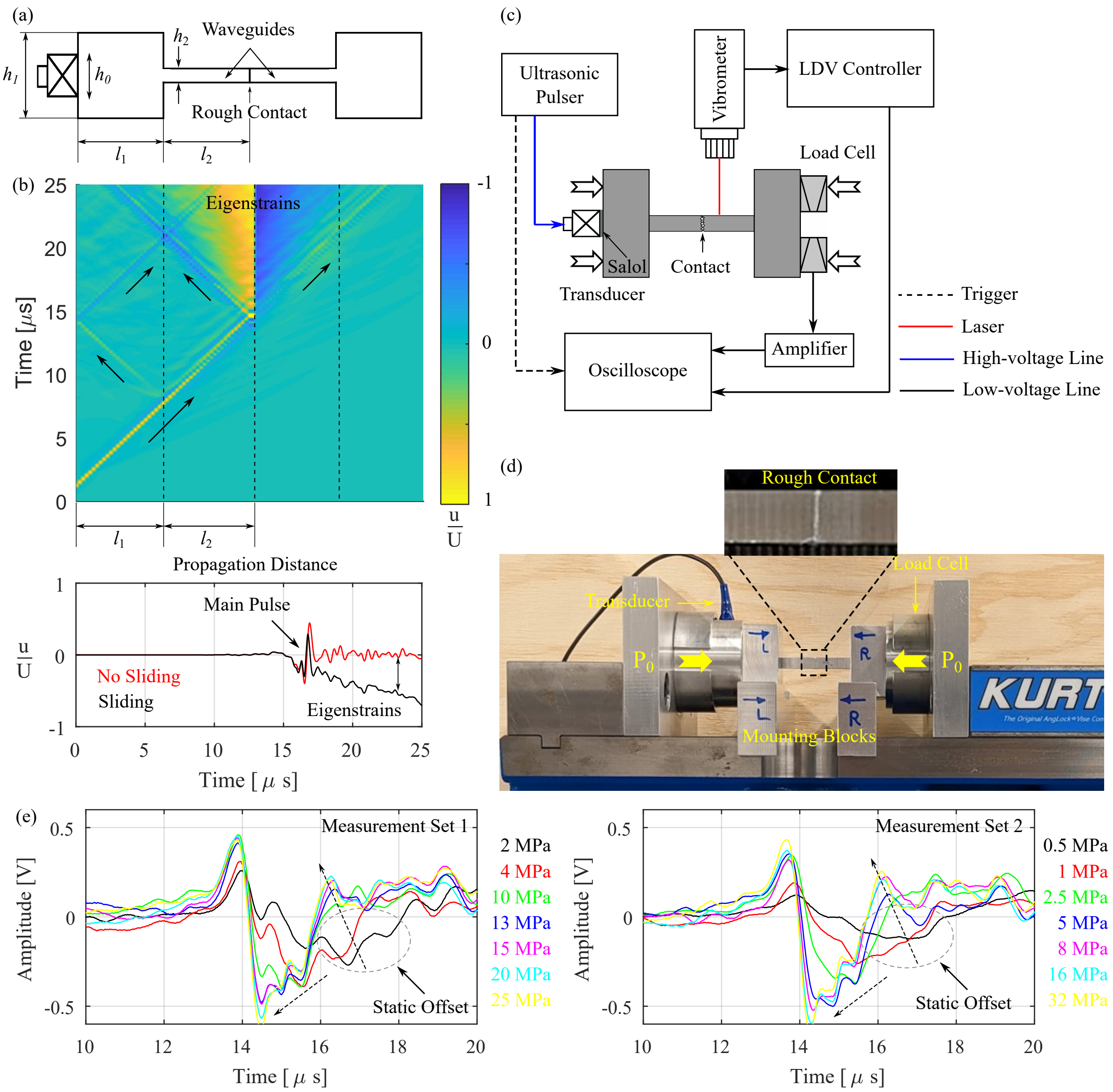

Figure 7.5: Measurement of shear-polarized eigenstrain from wave-induced frictional sliding. (a) Geometry of samples with a rough contact at the center. (b) Numerical results of high-amplitude shear wave propagation through (a) when excited from the left end. Spatiotemporal plots of wave displacements indicate static offset generation when the wave interacts with contact. Arrows indicate wave propagation directions. The time domain signal of the transmitted wave indicates eigenstrain generation only when contact sliding is activated. Experimental (c) schematic and (d) actual setup. (e) Two different measurements for the same samples. Displacement amplitudes of transmitted waves for different precompressions (colors) show static offset for low precompression only (dashed ellipse). Arrows indicate changing trend of signals with increasing precompression.

energy = low Z4. This setting represents the maximum limit of the pulser, enabling the generation of a pulse with the highest attainable wave amplitude. The wave transmitted through the contact was detected using a Doppler vibrometer (Polytec, OFV505) using a displacement decoder (DD300) at 50 nm/V range. The vibrometer was positioned such that the laser was aligned parallel to the transducer's polarization direction, allowing for accurate detection of wave-particle displacement. The vibrometer signals were then transferred to an oscilloscope (Tektronix MSO44) with the termination of 1MΩ. The signals were averaged over 256 points, with a bandwidth limit = 350 MHz, and a sampling rate = 3.125 Gs/s.

Two measurements were conducted on the same samples, which involved disassembling and reassembling the setup to ensure repeatability [Fig. 7.5(e)]. Throughout both measurements, the same input wave amplitude was maintained as the precompression was gradually increased. Measurements show that transmitted waves obtained for low precompression cases in both measurements exhibit a persistent offset in wave amplitude for an extended period after the main wave pulse [refer to both black and red curves in Fig. 7.5(e)]. Interestingly, as the precompression is increased, this negative offset gradually diminishes [refer to the upward arrow in Fig. 7.5(e)], eventually disappearing entirely. It is expected that higher levels of precompression prevent sliding and hence the generation of eigenstrains. Therefore, the static offsets seen in the low-precompression cases, similar to numerical simulations [time signals in Fig. 7.5(b)], are suggestive of eigenstrains. This qualitative behavior of the signals, wherein the negative offset vanishes with increasing precompression, is consistent across both measurements. However, it should be noted that the exact onset of precompression required to eliminate the offset differs between the two measurements. For example, a static offset is seen for $p_0 = 4$ MPa or lower in measurement Set 1 but for Set 2 it is seen for $p_0 < 2.5$ MPa. Several factors could contribute to this difference, including variations in pairs of asperities in contact, potential measurement inaccuracies in probing the same location using a vibrometer, and the evolving nature of contacts under applied precompression. Additionally, the results reveal a shift in the signal in the time domain. While the positive peaks of the pulses were consistently measured at $\sim 14\mu$s, the negative peaks show a significant shift with an increase in precompression [refer to the downward arrow in Fig. 7.5(e)]. For instance, the maximum shift observed in the valley point (negative peak) between the lowest and highest precompression levels studied is approximately 2μs. The exact mechanism causing this shift in the time domain is unclear, as such a substantial time shift cannot be solely attributed to asperity and bulk deformation. However, it is reasonable to hypothesize that scattered waves may play a role and need to be studied further.

7.3.2 Energy dissipation

This section presents experimental work on another feature of wave-induced frictional sliding, namely the dissipation of energy (Fig. 7.6). The experimental setup, sample configuration, and measurement procedure remain the same as described in the section 7.3.1, except RITEC is used for input excitation control [Fig. 7.6(a)]. The RITEC system enables the excitation of a wave packet consisting of a finite number of cycles. In this case, 10 cycles were excited, of which 5 cycles in the approximate steady-state region were used for converting the time domain data into the frequency domain and obtaining transmission across the contact. The measurements were conducted for different combinations of wave amplitude (Ritec power level from 10% to 40%) and precompression, while the frequency of excitation (1 MHz) is kept the same. It is anticipated that at low precompression and high wave amplitude, a stronger nonlinear effect of frictional sliding and, consequently, higher energy dissipation will be observed. Conversely, for high precompression and low amplitude, the nonlinear effects of frictional sliding and energy dissipation are expected to be less pronounced. The wave is detected using a Doppler vibrometer (Polytec, OFV505) equipped with a velocity decoder (VD09) at 200mm/s/V range. Both, incident waves entering the contact and transmitted waves through the contacts were measured using the vibrometer. Fig. 7.6(b) shows a typical incident and transmitted signal (averaged over 256 points, bandwidth limit = 350 MHz, and sampling rate = 3.125 Gs/s) and corresponding FFT.

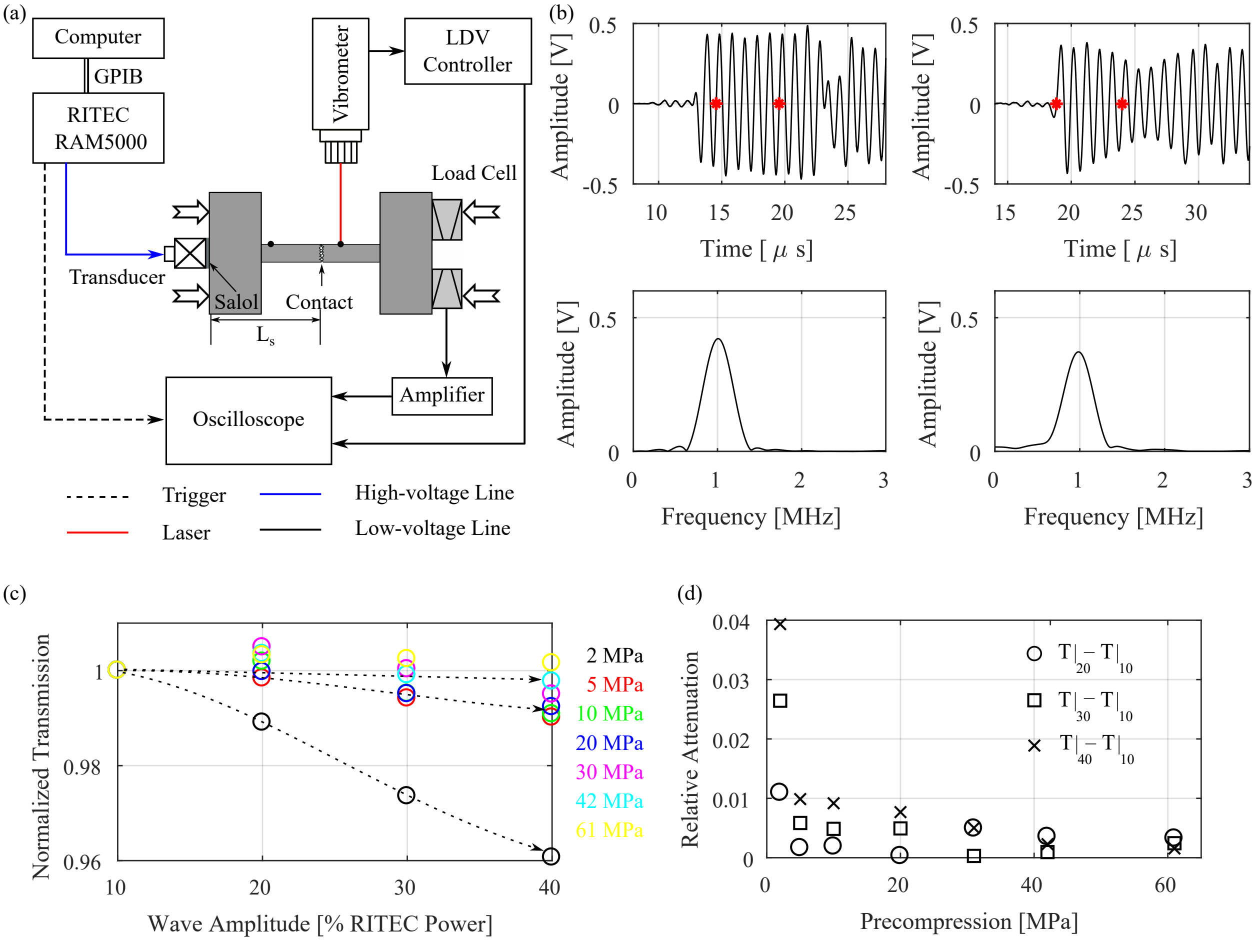

Figure 7.6: Measurement of energy dissipation from wave-induced frictional sliding. (a) Experimental schematics. (b) Typical incident (left) and transmitted (right) time domain signal. These signals were probed on the sample surfaces as denoted by block dots in (a). A nearly steady-state portion of the signal, denoted by two red dots, is considered to convert to the frequency domain. Peak amplitudes of FFT plots at fundamental frequency were used to evaluate transmission. (c) Transmission for different precompression and wave amplitudes. Wave amplitudes are denoted in terms of % of RITEC power level. Marker colors correspond to precompression values. (d) Relative attenuation as a function of precompression.

Wave transmission through contact is evaluated as the ratio of FFT amplitudes of the transmitted wave to the incident wave at the fundamental frequency. These transmission values are normalized by the transmission at the lowest wave amplitude (10% power level). The results show a clear trend: for low precompression, an increase in wave amplitude leads to a reduction in transmission [refer to black markers in Fig. 7.6(c)]. This reduction in transmission can be attributed to energy loss at the contact interface from sliding, which is expected to increase with increasing wave amplitudes. As precompression is increased, the friction limit of the contacts is also increased. Therefore, the frictional sliding and energy dissipation are restricted up to a certain extent. This causes only a small gradual drop in transmission for the same range of wave amplitudes [refer to red, green, and blue markers in Fig. 7.6(c)]. When precompression is increased further, the transmission does not change substantially as wave amplitudes are increased [refer to cyan and yellow markers in Fig. 7.6(c)], suggesting that the contacts are in a stick state (linear case) and the response becomes amplitude-independent. To better visualize these results, the drop in transmission, referred to as attenuation, is plotted as a function of precompression [Fig. 7.6(d)]. The relative attenuation is evaluated as the difference between transmission at different input power levels. For the lowest precompression, relative attenuation increases with an increase in wave amplitude. This suggests that increasing wave input results in more contact sliding and hence a reduction in the transmitted wave. As precompression is increased, the difference in relative attenuation reduces. Eventually, for the highest precompression applied, the relative attenuation is almost the same for all wave amplitudes tested and is close to zero. This suggests that at this precompression contact was in a fully stick state and transmission is essentially amplitude-independent. Since the change in transmission, even for the lowest precompression, is only up to 4%, the variation and repeatability of these experiments need to be verified in future studies.

7.4 Troubleshooting ultrasonic experiments and guidelines for future experimentations

While ultrasonic setups have been developed and preliminary measurements show promising results, these experiments suffer from a lack of repeatability. Consequently, extensive investigations have been conducted and a range of potential factors that impact the precision of the measurements have been identified. Focused attention on these factors is warranted in forthcoming studies. Therefore, this section provides a concise overview of some of the significant challenges/issues and proposes prospective solutions to effectively mitigate these concerns.

1. *Lack of uniform contact*: Fig. 7.7(a) displays images obtained from a pressure film placed between the two samples. It is observed that at low precompression, the real contact area does not occur at the central part of the samples (i.e. area aligned to the transducer face). Even for large precompressions, the real contact area is skewed to one side of the apparent area. This occurrence is likely due to surface irregularities resulting from machining or manual polishing. Three potential improvements can be done to address this issue: (1) Controlled roughness generation through micro grooving, micro dimples, and microchannels instead of using sandblasting and manual polishing, (2) Reducing the contact area on one of the mating samples, limiting contact to a region smaller than the diameter of the transducer element, and (3) modifying end fixtures to incorporate spherical joints (gimbal fixtures) in contact with samples, which allow contact surfaces to parallelize themselves by unconstraining degrees of freedom. Additionally, surface inclination and long-wavelength components of surface waviness can be measured immediately after sample fabrication, which can serve as a checkpoint. Advanced surface treatment methods such as chemical itching, Laser ablation, and electroplating may also be explored to assess the control over fabricated roughness parameters.

2. *Variation between measurements*: For consistent and reliable qualitative measurements, it is necessary to ensure that most of the asperities in contact are reproduced for every new measurement on the same sample. However, achieving this may be challenging if the roughness of other interfaces and clearances between mating parts of the setup are comparable. In the current setup, four interfaces exist in addition to the rough contact to be tested [Fig. 7.7(b)]: (1) Left vice plate and transducer seat, (2) transducer seat and left sample, (3) right sample and load cell, and (4) load cell and right vice plate. These interfaces have their own tolerances and surface textures, both typically on the micron scale, which might introduce variations in the setup. Additionally, the mounting fixtures used to align the samples in the direction perpendicular to the page themselves have manufacturing tolerances of the

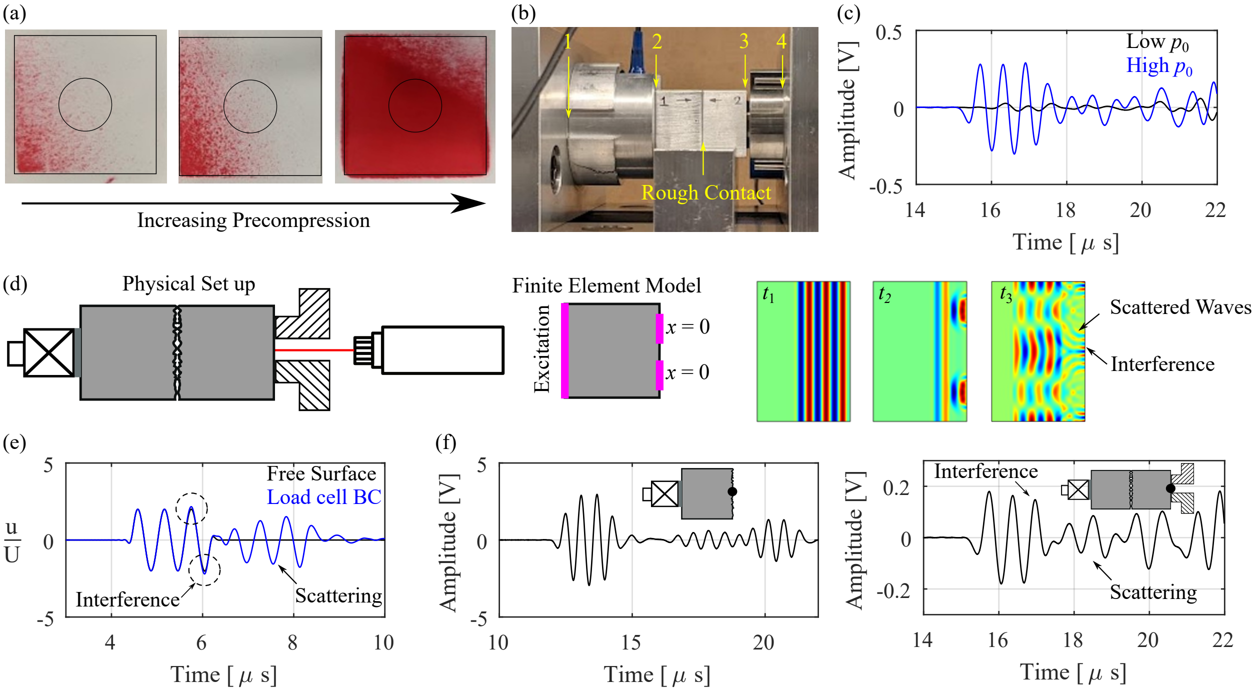

Figure 7.7: Troubleshooting ultrasonic experiments with rough contacts. (a) Pressure films at contact for difference precompression indicating non-uniform real contacts. Rectangular and circular borders are apparent contact and transducer element area, respectively. (b) The number of interfaces in the experimental setup apart from the rough contact to be tested. (c) Extremely weak measured signal (of the order of scattering) of the transmitted wave for low precompressions. (d) Actual setup and corresponding finite element setup to simulate mixed boundary conditions. Total wave displacements at three different time instants indicate the scattering of waves from the edges of sample-load cell contact. Transmitted waves obtained (e) numerically and (f) experimentally clearly highlight the interference of scattered waves with the main wave at the probed location. Black dots in the insets of (f) are the probed locations of measurement.

orders of a few micrometers. One approach to minimize measurement variations is to reduce the number of interfaces in the setup to only the rough contact between the samples under investigation. This can be achieved by redesigning the fixtures as a unified assembly instead of separate parts. In fact, even the samples could be integrated with the end fixtures to minimize the number of interfaces in the setup. Alternatively, if the contact being studied is designed with larger-sized asperities (at least an order larger than those of other interfaces and manufacturing tolerances), this issue may be circumvented.

3. *High impedance mismatch at low precompression*: For low precompressions, the real contact area is significantly small [Fig. 7.7(a)] resulting in a very high impedance mismatch at the contact interface. As a result, only a small amount of energy is transmitted across the contact leading to an extremely lower signal-to-noise ratio [Black signal in Fig. 7.7(c)]. This is even more problematic for ultrasonic frequencies, where wave attenuates with propagation distance and the ultrasonic transducers themselves have a very low conversion efficiency. These issues can be addressed by reducing the frequency of excitation. Low frequencies can be generated more efficiently and can penetrate material with low energy loss. Such low frequencies may be excited using piezoelectric patches, low-frequency transducers, or high-frequency vibration shakers.

4. *Interference from scattered waves*: The transmitted signals measured on the end surface of the right

sample are influenced by scattered waves, as evident in both simulated and measured signals [Figs. 7.7(d)-(f)]. This interference arises from scattered waves generated due to a mixed boundary condition on the surface where the transmitted wave is measured. In the physical setup [Fig. 7.7(d)], the right surface of the right sample is in contact with the load cell. This generates a mixed boundary condition on the sample surface: (1) the annular region in contact with the load cell experiences displacement boundary conditions ($x = 0$) whereas (2) the inside region is stress-free ($\sigma = 0$). Thus, the boundary of the load cell edges generates scattered waves [note the scattering in the wave propagation plots at t_2 and t_3 in Fig. 7.7(d)]. These scattered waves interfere with the signal measured at the center of the surface, which can be seen in both numerical simulations [Figs. 7.7(e)] and experiments [Figs. 7.7(f)]. Increasing the number of cycles in a wave packet exacerbates the scattering interference, impeding accurate analysis of wave propagation. To mitigate this issue, one potential solution is to reduce the wavelength, although it contradicts the need for increased energy input. Alternatively, appropriate fixtures can be designed to ensure that most of the sample surface remains free while forces are still transmitted through the load cell and sample end boundaries.

7.5 Summary

This chapter presented experimental work on ultrasonic wave propagation through a single rough contact. The experiments performed include: (1) Immersion pulse-echo measurements for acoustic characterization of aluminum material, (2) Longitudinal ultrasonic wave propagation through rough contact for characterizing contact nonlinearity, and (3) Shear ultrasonic wave propagation through rough contact to observe nonlinear effects of eigenstrain generation and friction dissipation. Key results and insights from these measurements are -

1. Acoustic characterization of aluminum revealed wave speed and frequency-dependent attenuation coefficient. This experiment can also be used to characterize the acoustic properties of additively manufactured materials, paving the way for utilizing 3D printing to generate controlled roughness.

2. Uniform roughness can be generated through manual polishing. Using P400 sandpaper results in average surface roughness of $\sim 0.45\ \mu$m for aluminum samples. The average roughness of the contact surface remains unchanged after applying multiple loading-unloading cycles within the studied precompression range.

3. Measurements of longitudinal ultrasonic waves can capture contact nonlinearity in the normal direction. Contact response indicates hysteresis only during the first loading cycle, indicating plastic deformation occurs solely during the initial loading. The contact stiffness-precompression relationship changes from low to high precompression but the underlying cause behind this shift is unclear. This suggests that the contact power-law obtained at higher precompression [115] may not be applicable at low precompression values. Consequently, a hybrid experimental-numerical method is proposed as an alternative to the erroneous linear wave propagation-based approach for contact characterization in the strongly nonlinear regime.

4. For low precompression, shear waves exhibit a static offset that diminishes with higher precompression, indicating the generation of eigenstrains. Additionally, the shear pulses shift in time as precompression is increased. At low precompression, increasing wave amplitudes reduce the transmission of shear waves

through contact, implying energy loss from contact sliding. In contrast, at high precompression, wave transmission remains fairly amplitude-independent.

5. These preliminary experiments offer valuable insights while also presenting opportunities for improvement. Some areas requiring attention include achieving uniform contact, increasing energy transfer across the contact, ensuring consistent results for identical sample sets and experimental parameters, as well as minimizing the presence of scattered waves. By addressing these aspects, future studies can enhance the overall quality and reliability of the findings.

Overall, the developed experimental framework represents significant progress toward physically realizing continuum phononic materials with contact nonlinearity, as explored in this dissertation.

Chapter 8

Conclusion

This concluding chapter provides a concise summary of the research covered in preceding chapters, encompassing phononic material designs, methodologies employed, and key findings. Drawing upon this research, potential directions for future investigations are also proposed. Moreover, it emphasizes the contribution of this dissertation to the scientific community and its impact on advancing the engineering field, in general.

8.1 Summary

This dissertation is focused on mechanical wave propagation and the development of tailored materials for wave control. The research is motivated by the pervasive existence of waves and their fundamental significance in technological advancements and environmental challenges. The dissertation particularly exploited nonlinear phononic materials due to their ability to exhibit unprecedented wave characteristics. The primary question studied is how waves propagate in continuum phononic materials with discrete (or local) nonlinearities, as recent research predominantly examined either *discrete* nonlinearity in the form of spring-mass chains or *continuous* nonlinearities in continuous periodic materials.

The primary aim is to understand the role of the continuum and the distribution of discrete nonlinearities in governing energy propagation. Taking inspiration from geomaterials, the research investigated 1D nonlinear continuum phononic materials that incorporate microcracks (or rough contacts) - a geomaterial microstructure - as discrete nonlinearities. Two key factors are examined: (1) the influence of the periodic arrangement of rough contacts on wave propagation and (2) the role of local contact nonlinearity between successive continuum layers in shaping nonlinear wave responses. The analysis is restricted to cases where wavelengths are much larger than the size of asperities at contact, but on the same order as the width of layers of phononic material. Therefore, the contacts are treated as nonlinear springs that are independent of frequency.

To analyze nonlinear wave propagation, finite element models were employed, considering various levels of contact nonlinearity ranging from weak to strong, including friction. Nonlinear laws at contacts are informed through experimental contact characterization. Nonlinearity at the contacts arises from three sources: (1) Large deformation of asperities (unevenness on contacting surfaces) under compressive loads, (2) the inability of externally uncompressed contacts to support tensile loads, and (3) frictional sliding of the surfaces under tangential loads. The normal interaction of contacts is modeled using a power-law relationship between contact pressure and displacement, with a power exponent of 2, while tangential interaction is modeled using Jenkins friction law. Various configurations are studied, including systems with single and periodic contacts, semi-infinite and finite phononic materials, and contacts with infinite-length and embedded nature. Furthermore, configurations with and without precompression are examined, along with longitudinal and shear wave excitations, to gain a comprehensive understanding of nonlinear wave propagation through these phononic materials. Weak nonlinearity is obtained when precompression is applied, whereas contacts exhibit strong nonlinearity in the absence of precompression. Under shear wave propagation, contacts demonstrate frictional instability, resulting in a hysteresis response. Through a careful examination of wave evolution within the material, the research has uncovered the underlying physics behind the emergence of novel nonlinear responses. Noteworthy wave responses and insights about them are as follows:

1. In *weakly nonlinear* systems [102], [103], two nonlinear phenomena are studied: wave self-interactions and wave-wave interactions. Wave self-interactions give rise to the DC component, self-demodulated low frequency in the vicinity of the DC component, and second harmonics. The amplitude of these nonlinearly-generated frequencies depends on the dispersion zone in which they fall. Moreover, the relative phase between the second harmonic and fundamental wave determines how the second harmonic amplitude depends on propagation distance, resulting in either continuous increase or spatial beating. The treatment of elastic layers as continua changes the response of the nonlinearly-generated waves, e.g. they locally reduce the DC component and cause variations in second harmonic amplitudes inside the layers, even though the layers are linear. The nonlinear responses of the phononic material can be tuned through external precompression as dispersion is a function of applied precompression. The study of embedded contacts reveals that the coupling between the contact and surrounding continuum changes the nonlinear contact response. Thus, DC and second harmonic wave amplitudes depend on the arrangement of embedded contacts in a continuum. Wave-wave interactions generate the sum and difference frequencies of the propagating frequencies, complementing the capabilities of wave self-interactions. This wave mixing phenomenon is combined with band gaps of phononic materials to achieve broadband and tunable nonreciprocity. A phononic diode is designed based on the global asymmetry, local nonlinearity, and periodicity of precompressed rough contacts. Numerical demonstration confirmed nonreciprocal wave propagation upon excitation of a frequency pair. The uniqueness of this diode lies in its ability to tune the frequency and propagating mode of nonreciprocal waves through an appropriate selection of input frequencies, surpassing the limitations of existing diodes. Further, wave propagation can be switched to support reciprocity or nonreciprocity, allowing unidirectional, bidirectional, or no propagation of energy at all. Finally, the presence of rough contacts also enables *in-situ* control of energy propagation through precompression.

2. In *strongly nonlinear* systems [104], [105], the occurrence and properties of localized traveling waves associated with contact clapping (separation and collision of contacting surfaces) are explored. Contact clapping, dispersion, and discrete-continuum architecture, together, give rise to stegotons, which are localized traveling waves categorized as solitary waves. Notably, stegotons exhibit distinct spatial characteristics, displaying a roof-like or stepwise profile due to the periodic configuration of continua-discrete nonlinearity present in the phononic material. Additionally, wave-contact interactions induce acoustic resonances within the layers, allowing for spectral energy transfer and localization near the excitation boundary. Thus, energy transmission through the phononic material relies on the proximity of the excitation frequency to the acoustic resonances of the layers. When the input frequencies align with the layer resonances, a considerable amount of energy is trapped within these layers. Consequently, stegotons carry significantly lower energy, resulting in a wave attenuation reminiscent of band gaps

in linear periodic media. Owing to rough contact nonlinearity with a power exponent of 2, stegotons show a much stronger dependence of speed on amplitude and contact pressure compared to solitary waves in granular crystals. When stegotons collide, secondary stegotons are formed. Notably, the amplitudes of these secondary waves are one order of magnitude greater when the collision occurs at a contact compared to collisions within a layer. Stegotons can emerge and propagate within the phononic material, even when subjected to physical constraints such as light precompression, disorder, and finite lateral dimensions. However, the characteristics of these stegotons differ from those in an ideal system, as they exhibit attenuation-like properties and tend to disintegrate over time.

3. In *hysteretic nonlinear* systems [106], how frictional instability at the contacts changes shear wave propagation is studied, which has remained an unexplored territory in the field of phononic materials. Wave-induced friction at contact generates shear-polarized eigenstrains, which are residual strains in the stress-free system. Physically, these eigenstrains represent the repositioning of initially aligned contact interfaces (and thus waveguides), resulting in an offset between them. By selectively inducing eigenstrain generation in a specific section of the system through two-way excitation, the capability to achieve smart mechanical functionalities is demonstrated. This includes acoustically-controlled features such as a mechanical switch, precision position control, and surface reconfigurability. Furthermore, wave-induced contact sliding results in energy dissipation. The underlying physics of how this amplitude-dependent energy dissipation passively widens the attenuation zones of finite contact-based phononic materials is explained. Results show that the optical band of the phononic material is suppressed by the combined effect of energy dissipation at the contact and energy reflection at the first interface. As a result, the two band gaps merge and exhibit a wide band attenuation zone.

In addition to numerical analysis, the dissertation performed pilot experimental studies on ultrasonic wave propagation as follows: (1) Immersion pulse-echo measurements were conducted for acoustic characterization of aluminum material. The results revealed wave speed and frequency-dependent attenuation coefficients. This experimental framework holds implications for the acoustic characterization of complex multiscale materials achieved through additive manufacturing for the future realization of precisely designed phononic materials. (2) Longitudinal ultrasonic wave propagation through a single rough contact was measured for characterizing contact nonlinearity. This experiment informed the nonlinear relationships between contact pressure and displacement at contact. It also highlighted the limitations of existing approaches and outlined a proposed approach to characterize contacts in the strongly nonlinear regime. (3) Shear ultrasonic wave propagation through a single rough contact was measured to observe the nonlinear effects of eigenstrain generation and friction dissipation. While these preliminary experiments offered valuable insights, they also revealed areas that require attention and improvement. These areas include improving control over surface texture, ensuring uniform contact area, increasing energy transfer across contacts, achieving consistent results for identical sample sets and experimental parameters, as well as minimizing the scattering of waves. By addressing these aspects, future studies can enhance the overall quality and reliability of the findings. Overall, the developed experimental framework represents significant progress toward physically realizing continuum phononic materials with contact nonlinearity.

The research presented in this dissertation has resulted in 5 journal publications, 1 conference proceeding, 1 web editorial, and 5 conference presentations. The details of these scholarly outputs are listed below:

Nonlinear Study	Journal Articles	Proceedings/Editorials	Presentations
Weak (Numerical)	Self-interactions [102] Phononic diode [103]	Self-interactions [243] -	Self-interactions [244] -
Strong (Numerical)	Stegotons [104] -	- Wave disintegration [105]	Stegotons [245] Wave disintegration [105]
Hysteretic (Numerical)	Eigenstrains [106]	-	Eigenstrains [246]
Experiments	-	-	Contact Characterization [247]
-	Review article [44]	-	-

Table 8.1: Scholarly research output

8.2 Outlook: future research directions

Despite the comprehensive investigations and understanding of complex wave phenomena, the current work relies on several assumptions, includes reduced-order models, and is limited to relatively simplified configurations. Further, numerous aspects of the intricate problem of wave propagation through periodic local nonlinearity remain unexplored and require further understanding. These unanswered aspects act as catalysts for promising future research. Here are some noteworthy avenues to explore:

8.2.1 Exploring stegoton characteristics

This study revealed stegotons - a special type of localized traveling wave that belongs to the family of solitary waves. However, further exploration of stegotons is necessary to gain a better understanding of their characteristics and their dependence on various system parameters. Unanswered questions remain, such as the speed-amplitude relationship of stegotons with frequency excitations and their convergence into solitary waves under low-frequency excitations. Since layer deformations are negligible at low frequencies and can be treated as rigid bodies, it would be intriguing to explore the relationship between solitary waves in granular crystals with Hertzian contacts and stegotons in layered media with rough contacts. The study also found that stegoton amplitudes vary within a layer while remaining constant as they propagate when observed at a fixed location. Investigating the correlation between this variation and mean amplitude for different excitation frequencies can illuminate the influence of layer deformation and mode on propagation properties. Further, examining how different contact laws resulting from varying asperity height distributions affect stegotons can inform the design of surface textures for a wide range of propagation properties. Finally, the phononic material studied here assumed perfect periodicity. However, studying the role of disorder and uncertainties in layer material, thickness and, specifically, in the contact law, on stegotons propagation could pave the way toward their practical realization.

8.2.2 Wavelengths comparable to asperities

Expanding the current study to investigate wave-contact interactions at wavelengths that are of the same order as the size of asperities ($\lambda \sim \delta$) is another potential future research direction. Currently, the research focuses on wavelengths much larger than the asperity size ($\lambda \gg \delta$), where the contact properties are frequency-independent and can be formulated using a quasi-spring model. Additionally, the interfacial mass (or inertia) can be neglected due to their small magnitudes under these conditions. However, when the wavelength approaches the scale of the asperities, these assumptions and modeling approaches break. In such cases, the contact properties are expected to be frequency-dependent, and the inertial mass could have a significant influence [248]. For example, Thomas et al. [249] reported that the contact response at high frequencies is dependent on the size, shape, and distribution of the scatterers (asperities). This gives rise to several intriguing questions that could shape future research scope: How can rough contacts be characterized when the wavelength and asperities are of the same order? What is the nature of the frequency-dependent contact response? How can this nonlinear response be accurately modeled using analytical or numerical methods? Furthermore, exploring the effect of frequency dependence on the observed nonlinear wave responses in phononic materials, such as on stegotons and eigenstrain generation, would be of great interest. Addressing these questions represents an exciting research direction for the future, as it holds the potential to enhance our understanding of contact behavior and wave-contact interactions at scales that have not been studied before.

8.2.3 Architected rough contacts

Another potential future research direction builds upon the current study, which is focused on a 1D phononic material with a relatively simple periodic arrangement. The arrangement involved contacts that were periodically placed perpendicular to the direction of wave propagation. While this system facilitated a fundamental understanding of wave propagation in such materials, it resulted in the decoupling of normal and tangential interactions at the contacts. However, exploring configurations where these interactions are coupled presents new opportunities for novel wave responses. Such coupling could be achieved by exciting a wave at an angle to contact interfaces. The current research has already developed and implemented numerical models that account for both normal and tangential interactions at the contact, which could serve as a platform to explore the coupling effects. Such configurations hold the potential for intriguing wave responses, including the generation of higher harmonics with different polarizations [180], nonlinear mode conversion [180], and mode hopping [74]. Moreover, previous studies on complex lattice materials have demonstrated that geometric architecture profoundly influences propagation properties [16], [17]. For instance, auxetic lattices exhibit faster shear wave propagation compared to longitudinal waves, which is not feasible in conventional materials [16], [17]. Therefore, an exciting research direction would involve combining the features of contact nonlinearity and geometric architecture. By exploring such material configurations, it may be possible to generate harmonics with speeds that can be adjusted to be higher or lower than the fundamental waves that generate them.

8.2.4 Frictional mechanisms at play

The current study of incorporating friction into the phononic material is based on certain assumptions. Specifically, the study assumed rate independence, the absence of adhesion and partial slip, and a steady-state contact response. While these assumptions may hold true under specific conditions, moving beyond them actually present new opportunities to gain a deeper understanding of how realistic frictional mechanisms affect wave propagation. There are several intriguing questions to address: how does the wave propagation response evolve as contact surfaces undergo wear? What role does contact adhesion play in shaping the wave profile, particularly in the context of soft materials and their contact clapping? How eigenstrain generation and energy dissipation is influenced when partial slip is incorporated into the current model? Finally, how significant is the frequency of the wave when the contact response exhibits rate dependence? Additionally, the current study employed the Jenkins friction model to capture stick-slip transition at contact. However, there are several other frictional models proposed in the community that imitate other physical phenomena that occur at contacts, for example, Coulomb's friction model with Stribeck effect [250], the Bouc–Wen model of hysteresis [251], among others [252]. Recently, comprehensive graphical methods - Methods of Memory Diagrams [114], [128] - have also been developed that can capture the evolution of contact state under both normal and tangential transient loading including partial slip. Investigating how these alternative models affect wave propagation could inform designing contact-based phononic materials for targeted applications.

8.2.5 Surface-interactions at small-scales

The contacting surfaces are idealized in this work such that the surfaces themselves do not have any wavelength. However, microcracks in geomaterials are in fact fractal, i.e. they have repeating profiles at multiple length scales. Therefore, future studies could investigate controllable fractal geometries and enhance our understanding of wave-contact interactions. Further, scaling down the asperities may involve additional physical phenomena not considered in this study. Notably, at the nanoscale, van der Waals forces [253], [254] become more dominant, leading to stronger adhesive forces between surface asperities. These forces can result in increased adhesion and stiction between surfaces, affecting friction behavior. As asperity sizes decrease, the ratio of surface area to volume also increases significantly. This may lead to changes in surface energy and wettability, affecting the contact angle and capillary forces, which is another source that could influence friction and adhesion. Further, the contact area between asperities becomes smaller at nanoscales, leading to higher contact pressures. This may cause elastic and plastic deformations as waves propagate through the contacts. Finally, thermal fluctuations and temperature-induced changes in material properties become more significant at the nanoscale. This could influence the effective stiffness of the surfaces and therefore the wave propagation responses. Thus, exploring these distinctive surface interactions on a small scale holds promise for enriching our insights into the feasibility of miniaturizing these phononic materials.

8.2.6 Experimental validation

The current study primarily utilized numerical analysis to investigate the properties of continuum phononic materials with rough contacts. The next logical step in this research is to experimentally validate the reported phenomena. Preliminary measurements have already demonstrated promising results, laying the foundation for further experiments. While there are challenges in physically realizing the studied phononic materials, as discussed in chapter 7, it may be possible to sidestep these obstacles by up-scaling the asperities at the contact and reducing the frequencies to be probed. The nonlinear wave responses presented in this research rely on the local contact nonlinearity between adjacent elastic media. The size and scale of the roughness only determine the frequencies for which the obtained results are valid. Therefore, a potential research direction could involve conducting experimental investigations with large-scale and controlled asperities (for example, spherical asperities of equal radii [109] or hierarchical asperities such as small spherical bumps on large spherical curvature [109]) to explore and validate results presented in this dissertation on a broader scale. Moreover, the numerical models did not account for the plastic deformation of asperities or frictional sliding of adjacent asperities under longitudinal wave excitation. These physical effects are expected to cause energy dissipation at the contact, leading to wave amplitude attenuation [194]. However, by experimentally measuring wave amplitudes, these effects could be captured and used to develop empirical relations of dissipation at contacts, enhancing the predictive capability of numerical models.

8.2.7 Expanding sources of local nonlinearity

The core objective of this research is to understand the role of local or discrete contact nonlinearity in a continuum and its impact on wave propagation. While the current research employed microcrack-inspired rough contacts as a representative example, there are several other physical sources that can be explored to expand the available space of local nonlinearities. Geomaterials, for instance, possess porosities filled with fluids [96], interfaces between soft and hard phases [97], and delaminations [255], each expected to potentially exhibit distinct nonlinear characteristics. By incorporating these nonlinear sources in the research framework developed in this dissertation, it could be possible to uncover new properties and opportunities for controlling wave propagation.

8.3 Significance and impact

This dissertation makes valuable contributions to the scientific community in three distinct categories. Firstly, it develops fundamental knowledge of wave propagation through phononic materials that uniquely incorporate discrete nonlinearities. Secondly, it integrates concepts and research themes from different subdomains of the mechanics community. Lastly, it showcases the potential of the designed phononic materials for advanced engineering applications.

1. *Fundamental knowledge*: This research makes significant contributions to the field of wave mechanics by enhancing our understanding of mechanical wave propagation through a continuum with periodic and discrete nonlinearity. Additionally, it demonstrated the manipulation of global wave responses through local nonlinearity, offering a unique platform for designing phononic materials. The research further advances state-of-the-art knowledge by reporting a new type of solitary wave (stegotons) and friction-induced shear-polarized eigenstrain, unraveling the underlying physics behind these phenomena. Finally, this research pioneers the concept of utilizing hysteretic nonlinearity for wave control and programmable functionality, addressing an untapped area within the field.

2. *Interconnecting subfields*: While rough contacts are known to exhibit nonlinear properties in nondestructive evaluation, their application for wave control remained unexplored until now. By connecting the two distinct fields of wave mechanics – nondestructive evaluation and phononic media, this research not only filled a crucial gap but also broadened the horizons of both disciplines. Furthermore, it sets the foundation for further exploration of various microstructural features found in geomaterials, which can serve as additional sources of inspiration for designing phononic materials, extending beyond the realm of bio-inspiration. Additionally, the introduction of hysteretic nonlinearity in this study establishes a connection between tribology and phononic materials. Overall, this research demonstrates how interdisciplinary research contributes to the advancement of wave control techniques.

3. *Towards applications*: The findings of this research have implications for various engineering applications, encompassing vibration mitigation, energy harvesting, signal processing, nondestructive evaluation, and fluid-structure interaction. These phononic materials, characterized by their periodicity, possess band gaps (or attenuation zones) that are also dependent on both amplitude and precompression due to contact nonlinearities. Consequently, these materials offer both active and passive adaptability, rendering them suitable for vibration mitigation even in fluctuating environments. Notably, unlike soft metamaterials, the developed phononic materials can be integrated into load-bearing components,

making them valuable for structural applications. The strong nonlinearity of contact clapping gives rise to layer resonances, which effectively localize energy near the excitation boundary. This property can be harnessed for impact mitigation, energy absorption, and harvesting purposes. Moreover, stegotons, characterized by their ability to transfer signals over long distances without dispersion in conservative material, hold promise for the development of advanced sensors and energy propagators. Eigenstrains emerge as a potential tool for crack detection, while contact-based programmable switches can be employed in the design of acoustic sensors and actuators. Controlling the position of periodic layers via waves may be used for remote tuning of the surface topology of aerodynamic objects such as turbine blades, riblets, and airfoils in extreme and inaccessible environments. Overall, the novel wave responses of these phononic materials and unprecedented control capabilities hold immense potential for technological innovation in the field of acoustics.

References

[1] K. Chandrashekhara and A. Agarwal, "Active vibration control of laminated composite plates using piezoelectric devices: A finite element approach," *Journal of Intelligent Material Systems and Structures*, vol. 4, no. 4, pp. 496–508, 1993. DOI: `10.1177/1045389X9300400409`.

[2] R. Panneton and N. Atalla, "Numerical prediction of sound transmission through finite multilayer systems with poroelastic materials," *The Journal of the Acoustical Society of America*, vol. 100, no. 1, pp. 346–354, 1996. DOI: `10.1121/1.415956`.

[3] M. Strasberg and D. Feit, "Vibration damping of large structures induced by attached small resonant structures," *The Journal of the Acoustical Society of America*, vol. 99, no. 1, pp. 335–344, 1996. DOI: `10.1121/1.414545`.

[4] J. O. Vasseur, P. A. Deymier, B. Chenni, B. Djafari-Rouhani, L. Dobrzynski, and D. Prevost, "Experimental and theoretical evidence for the existence of absolute acoustic band gaps in two-dimensional solid phononic crystals," *Physical Review Letters*, vol. 86, no. 14, p. 3012, 2001. DOI: `10.1103/PhysRevLett.86.3012`.

[5] A. Khelif, B. Aoubiza, S. Mohammadi, A. Adibi, and V. Laude, "Complete band gaps in two-dimensional phononic crystal slabs," *Physical Review E*, vol. 74, no. 4, p. 046 610, 2006. DOI: `10.1103/PhysRevE.74.046610`.

[6] K. H. Matlack, A. Bauhofer, S. Krödel, A. Palermo, and C. Daraio, "Composite 3D-printed metastructures for low-frequency and broadband vibration absorption," *Proceedings of the National Academy of Sciences*, vol. 113, no. 30, pp. 8386–8390, 2016. DOI: `10.1073/pnas.1600171113`.

[7] G. Hu, L. Tang, A. Banerjee, and R. Das, "Metastructure with piezoelectric element for simultaneous vibration suppression and energy harvesting," *Journal of Vibration and Acoustics*, vol. 139, no. 1, p. 011 012, 2017. DOI: `10.1115/1.4034770`.

[8] O. Abdeljaber, O. Avci, and D. J. Inman, "Optimization of chiral lattice based metastructures for broadband vibration suppression using genetic algorithms," *Journal of Sound and Vibration*, vol. 369, pp. 50–62, 2016. DOI: `10.1016/j.jsv.2015.11.048`.

[9] B. Assouar, M. Oudich, and X. Zhou, "Acoustic metamaterials for sound mitigation," *Comptes Rendus Physique*, vol. 17, no. 5, pp. 524–532, 2016. DOI: `10.1016/j.crhy.2016.02.002`.

[10] A. Khelif, A. Choujaa, S. Benchabane, B. Djafari-Rouhani, and V. Laude, "Guiding and bending of acoustic waves in highly confined phononic crystal waveguides," *Applied physics letters*, vol. 84, no. 22, pp. 4400–4402, 2004. DOI: `10.1063/1.1757642`.

[11] J.-H. Sun and T.-T. Wu, "Propagation of surface acoustic waves through sharply bent two-dimensional phononic crystal waveguides using a finite-difference time-domain method," *Physical Review B*, vol. 74, no. 17, p. 174 305, 2006. DOI: 10.1103/PhysRevB.74.174305.

[12] M. I. Hussein, M. J. Leamy, and M. Ruzzene, "Dynamics of phononic materials and structures: Historical origins, recent progress, and future outlook," *Applied Mechanics Reviews*, vol. 66, no. 4, p. 040 802, 2014. DOI: 10.1115/1.4026911.

[13] X. Zhou, X. Liu, and G. Hu, "Elastic metamaterials with local resonances: An overview," *Theoretical and Applied Mechanics Letters*, vol. 2, no. 4, p. 041 001, 2012. DOI: 10.1063/2.1204101.

[14] Z. Liu, X. X. Zhang, Y. Mao, *et al.*, "Locally resonant sonic materials," *Science*, vol. 289, no. 5485, pp. 1734–1736, 2000. DOI: 10.1126/science.289.5485.1734.

[15] C. Yilmaz, G. M. Hulbert, and N. Kikuchi, "Phononic band gaps induced by inertial amplification in periodic media," *Physical Review B*, vol. 76, no. 5, p. 054 309, 2007. DOI: 10.1103/PhysRevB.76.054309.

[16] G. U. Patil and K. H. Matlack, "Effective property evaluation and analysis of three-dimensional periodic lattices and composites through bloch-wave homogenization," *The Journal of the Acoustical Society of America*, vol. 145, no. 3, pp. 1259–1269, 2019. DOI: 10.1121/1.5091690.

[17] G. U. Patil, A. B. Shedge, and K. H. Matlack, "3D auxetic lattice materials for anomalous elastic wave polarization," *Applied Physics Letters*, vol. 115, no. 9, p. 091 902, 2019. DOI: 10.1063/1.5116687.

[18] G. Patil, "Influence of geometric parameters on 3D periodic lattice effective properties," 2019. [Online]. Available: `http://hdl.handle.net/2142/105092`.

[19] O. Babatola, G. U. Patil, D. Hsieh, K. H. Matlack, and S. Sinha, "Independently Tunable Thermal Conductance and Phononic Band Gaps of 3D Lattice Materials," *Advanced Engineering Materials*, vol. 22, no. 2, p. 1 901 004, 2020. DOI: 10.1002/adem.201901004.

[20] J. M. Kweun, H. J. Lee, J. H. Oh, H. M. Seung, and Y. Y. Kim, "Transmodal Fabry-Pérot resonance: theory and realization with elastic metamaterials," *Physical review letters*, vol. 118, no. 20, p. 205 901, 2017. DOI: 10.1103/PhysRevLett.118.205901.

[21] R. Zhu, X. N. Liu, G. K. Hu, C. T. Sun, and G. L. Huang, "Negative refraction of elastic waves at the deep-subwavelength scale in a single-phase metamaterial," *Nature Communications*, vol. 5, no. 1, p. 5510, 2014. DOI: 10.1038/ncomms6510.

[22] X. Zhang and Z. Liu, "Superlenses to overcome the diffraction limit," *Nature materials*, vol. 7, no. 6, pp. 435–441, 2008. DOI: 10.1038/nmat2141.

[23] S. Zhang, L. Yin, and N. Fang, "Focusing ultrasound with an acoustic metamaterial network," *Physical review letters*, vol. 102, no. 19, p. 194 301, 2009. DOI: 10.1103/PhysRevLett.102.194301.

[24] R. V. Craster and S. Guenneau, *Acoustic metamaterials: Negative refraction, imaging, lensing and cloaking*. Springer Dordrecht, 2012, vol. 166. DOI: 10.1007/978-94-007-4813-2.

[25] D. Beli, M. I. N. Rosa, C. De Marqui Jr, and M. Ruzzene, "Wave beaming and diffraction in quasicrystalline elastic metamaterial plates," *Physical Review Research*, vol. 4, no. 4, p. 043 030, 2022. DOI: 10.1103/PhysRevResearch.4.043030.

[26] Y.-F. Wang, Y.-Z. Wang, B. Wu, W. Chen, and Y.-S. Wang, "Tunable and active phononic crystals and metamaterials," *Applied Mechanics Reviews*, vol. 72, no. 4, p. 040 801, 2020. DOI: 10.1115/1.4046222.

[27] J.-F. Robillard, O. B. Matar, J. O. Vasseur, *et al.*, “Tunable magnetoelastic phononic crystals,” *Applied Physics Letters*, vol. 95, no. 12, p. 124 104, 2009. DOI: `10.1063/1.3236537`.

[28] A. Bergamini, T. Delpero, L. D. Simoni, L. D. Lillo, M. Ruzzene, and P. Ermanni, “Phononic crystal with adaptive connectivity,” *Advanced Materials*, vol. 26, no. 9, pp. 1343–1347, 2014. DOI: `10.1002/adma.201305280`.

[29] E. Walker, D. Reyes, M. M. Rojas, A. Krokhin, Z. Wang, and A. Neogi, “Tunable ultrasonic phononic crystal controlled by infrared radiation,” *Applied Physics Letters*, vol. 105, no. 14, p. 143 503, 2014. DOI: `10.1063/1.4894489`.

[30] K. Jim, C. W. Leung, S. Lau, S. Choy, and H. Chan, “Thermal tuning of phononic bandstructure in ferroelectric ceramic/epoxy phononic crystal,” *Applied Physics Letters*, vol. 94, no. 19, p. 193 501, 2009. DOI: `10.1063/1.3136752`.

[31] P. Wang, J. Shim, and K. Bertoldi, “Effects of geometric and material nonlinearities on tunable band gaps and low-frequency directionality of phononic crystals,” *Physical Review B*, vol. 88, no. 1, p. 014 304, 2013. DOI: `10.1103/PhysRevB.88.014304`.

[32] T. Vasileiadis, J. Varghese, V. Babacic, J. Gomis-Bresco, D. N. Urrios, and B. Graczykowski, “Progress and perspectives on phononic crystals,” *Journal of Applied Physics*, vol. 129, no. 16, p. 160 901, 2021. DOI: `10.1063/5.0042337`.

[33] J. Ma, “Phonon engineering of micro- and nanophononic crystals and acoustic metamaterials: A review,” *Small Science*, vol. 3, no. 1, p. 2 200 052, 2023. DOI: `10.1002/smsc.202200052`.

[34] X. Yao and A. Belyanin, “Giant optical nonlinearity of graphene in a strong magnetic field,” *Physical Review Letters*, vol. 108, no. 25, p. 255 503, 2012. DOI: `10.1103/PhysRevLett.108.255503`.

[35] I. R. Epstein and K. Showalter, “Nonlinear chemical dynamics: Oscillations, patterns, and chaos,” *Journal of Physical Chemistry*, vol. 100, no. 31, pp. 13 132–13 147, Aug. 1996. DOI: `10.1021/JP953547M`.

[36] O. Bolmin, J. J. Socha, M. Alleyne, A. C. Dunn, K. Fezzaa, and A. A. Wissa, “Nonlinear elasticity and damping govern ultrafast dynamics in click beetles,” *Proceedings of the National Academy of Sciences*, vol. 118, no. 5, e2014569118, 2021. DOI: `10.1073/PNAS.2014569118`.

[37] L. Zhang, J. Thingna, D. He, J.-S. Wang, and B. Li, “Nonlinearity enhanced interfacial thermal conductance and rectification,” *Europhysics Letters*, vol. 103, no. 6, p. 64 002, 2013. DOI: `10.1209/0295-5075/103/64002`.

[38] C. S. Wojnar, J.-B. le Graverend, and D. M. Kochmann, “Broadband control of the viscoelasticity of ferroelectrics via domain switching,” *Applied Physics Letters*, vol. 105, no. 16, p. 162 912, 2014. DOI: `10.1063/1.4899055`.

[39] V. A. De Lorenci, R. Klippert, M. Novello, and J. M. Salim, “Nonlinear electrodynamics and FRW cosmology,” *Physical Review D*, vol. 65, no. 6, p. 063 501, 2002. DOI: `10.1103/PhysRevD.65.063501`.

[40] B. Gleich and J. Weizenecker, “Tomographic imaging using the nonlinear response of magnetic particles,” *Nature*, vol. 435, no. 7046, pp. 1214–1217, 2005. DOI: `10.1038/nature03808`.

[41] A. Rosario Hamann, C. Müller, M. Jerger, *et al.*, “Nonreciprocity Realized with Quantum Nonlinearity,” *Physical Review Letters*, vol. 121, no. 12, p. 123 601, 2018. DOI: `10.1103/PhysRevLett.121.123601`.

[42] X. Zhao, G. Duan, K. Wu, S. W. Anderson, and X. Zhang, "Intelligent metamaterials based on nonlinearity for magnetic resonance imaging," *Advanced Materials*, vol. 31, no. 49, p. 1 905 461, 2019. DOI: 10.1002/ADMA.201905461.

[43] G.-L. Dai, "Designing nonlinear thermal devices and metamaterials under the Fourier law: A route to nonlinear thermotics," *Frontiers of Physics*, vol. 16, no. 5, p. 53 301, 2021. DOI: 10.1007/S11467-021-1048-Y.

[44] G. U. Patil and K. H. Matlack, "Review of exploiting nonlinearity in phononic materials to enable nonlinear wave responses," *Acta Mechanica*, vol. 233, no. 1, pp. 1–46, 2022. DOI: 10.1007/s00707-021-03089-z.

[45] C. Truesdell, "General and exact theory of waves in finite elastic strain," *Archive for Rational Mechanics and Analysis*, vol. 8, no. 1, pp. 263–296, 1961. DOI: 10.1007/BF00277444.

[46] A. E. Green, "A note on wave propagation in initially deformed bodies," *Journal of the Mechanics and Physics of Solids*, vol. 11, no. 2, pp. 119–126, 1963. DOI: 10.1016/0022-5096(63)90059-0.

[47] M. A. Breazeale and D. O. Thompson, "Finite-amplitude ultrasonic waves in aluminum," *Applied Physics Letters*, vol. 3, no. 5, pp. 77–78, 1963. DOI: 10.1063/1.1753876.

[48] G. L. Jones and D. R. Kobett, "Interaction of elastic waves in an isotropic solid," *The Journal of the Acoustical Society of America*, vol. 35, no. 1, pp. 5–10, 1963. DOI: 10.1121/1.1918405.

[49] A. A. Gedroits and V. A. Krasil'nikov, "Finite-amplitude elastic waves in solids and deviations from Hooke's law," *Soviet Phys. JETP*, vol. 16, no. 5, pp. 1122–1126, 1963.

[50] P. Bhatnagar, *Nonlinear waves in one-dimensional dispersive systems*. Oxford University Press, USA, 1979.

[51] R. Ogden, *Non-linear elastic deformations*. Ellis Harwood Ltd., Chichester, England, 1984.

[52] M. Hamilton and D. Blackstock, *Nonlinear acoustics*. Academic press, San Diego, USA, 1998.

[53] A. M. Samsonov, "Nonlinear strain waves in elastic waveguides," in *Nonlinear Waves in Solids*, ser. CISM Courses and Lectures, A. Jeffrey and J. Engelbrecht, Eds., vol. 341, Springer Vienna, 1994, pp. 349–382. DOI: 10.1007/978-3-7091-2444-4_6.

[54] M. Deng, "Cumulative second-harmonic generation of Lamb-mode propagation in a solid plate," *Journal of Applied Physics*, vol. 85, no. 6, pp. 3051–3058, 1999. DOI: 10.1063/1.369642.

[55] A. P. Mayer, "Surface acoustic waves in nonlinear elastic media," *Physics Reports*, vol. 256, no. 4-5, pp. 237–366, 1995. DOI: 10.1016/0370-1573(94)00088-K.

[56] A. H. Nayfeh and D. T. Mook, *Nonlinear oscillations*. John Wiley & Sons, Inc., 1995.

[57] G. Chakraborty and A. K. Malik, "Dynamics of weakly non-linear periodic chain," *International Journal of Nonlinear Mechanics*, vol. 36, no. 2, pp. 375–389, 2001. DOI: 10.1016/S0020-7462(00)00024-X.

[58] K. Manktelow, M. J. Leamy, and M. Ruzzene, "Multiple scales analysis of wave-wave interactions in a cubically nonlinear monoatomic chain," *Nonlinear Dynamics*, vol. 63, no. 1, pp. 193–203, 2011. DOI: 10.1007/s11071-010-9796-1.

[59] R. K. Narisetti, M. J. Leamy, and M. Ruzzene, "A perturbation approach for predicting wave propagation in one-dimensional nonlinear periodic structures," *Journal of Vibration and Acoustics*, vol. 132, no. 3, p. 031 001, 2010. DOI: 10.1115/1.4000775.

[60] B. S. Lazarov and J. S. Jensen, "Low-frequency band gaps in chains with attached non-linear oscillators," *International Journal of Non-Linear Mechanics*, vol. 42, no. 10, pp. 1186–1193, 2007. DOI: 10.1016/j.ijnonlinmec.2007.09.007.

[61] R. Khajehtourian and M. I. Hussein, "Dispersion characteristics of a nonlinear elastic metamaterial," *AIP Advances*, vol. 4, no. 12, p. 124 308, 2014. DOI: 10.1063/1.4905051.

[62] G. Theocharis, N. Boechler, and C. Daraio, "Nonlinear periodic structures and granular crystals," in *Acoustic Metamaterials and Phononic Crystals*, ser. Springer Series in Solid-State Sciences, P. A. Deymier, Ed., vol. 173, Springer-Verlag Berlin Heidelberg, 2013, pp. 217–251. DOI: 10.1007/978-3-642-31232-8_7.

[63] C. Chong, M. A. Porter, P. G. Kevrekidis, and C. Daraio, "Nonlinear coherent structures in granular crystals," *Journal of Physics: Condensed Matter*, vol. 29, no. 41, p. 413 003, 2017. DOI: 10.1088/1361-648X/aa7672.

[64] K. L. Manktelow, M. Ruzzene, and M. J. Leamy, "Wave propagation in nonlinear lattice materials," in *Dynamics of Lattice Materials*, S. Phani and M. I. Hussein, Eds., John Wiley & Sons, 2017, pp. 107–137. DOI: 10.1002/9781118729588.ch5.

[65] B. Deng, J. R. Raney, K. Bertoldi, and V. Tournat, "Nonlinear waves in flexible mechanical metamaterials," *Journal of Applied Physics*, vol. 130, no. 4, p. 040 901, 2021. DOI: 10.1063/5.0050271.

[66] H. Nassar, B. Yousefzadeh, R. Fleury, *et al.*, "Nonreciprocity in acoustic and elastic materials," *Nature Review Materials*, vol. 5, no. 9, pp. 667–685, 2020. DOI: 10.1038/s41578-020-0206-0.

[67] V. F. Nesterenko, "Propagation of nonlinear compression pulses in granular media," *Journal of Applied Mechanics and Technical Physics*, vol. 24, no. 5, pp. 733–743, 1983. DOI: 10.1007/BF00905892.

[68] A. Rosas and K. Lindenberg, "Pulse velocity in a granular chain," *Physical Review E*, vol. 69, no. 3, p. 037 601, 2004. DOI: 10.1103/PhysRevE.69.037601.

[69] Y. Starosvetsky and A. F. Vakakis, "Traveling waves and localized modes in one-dimensional homogeneous granular chains with no precompression," *Physical Review E*, vol. 82, no. 2, p. 026 603, 2010. DOI: 10.1103/PhysRevE.82.026603.

[70] C. Daraio, V. F. Nesterenko, E. B. Herbold, and S. Jin, "Strongly nonlinear waves in a chain of Teflon beads," *Physical Review E*, vol. 72, no. 1, p. 016 603, 2005. DOI: 10.1103/PhysRevE.72.016603.

[71] N. Boechler, G. Theocharis, S. Job, P. G. Kevrekidis, M. A. Porter, and C. Daraio, "Discrete breathers in one-dimensional diatomic granular crystals," *Physical Review Letters*, vol. 104, no. 24, p. 244 302, 2010. DOI: 10.1103/PhysRevLett.104.244302.

[72] J. Cabaret, V. Tournat, and P. Béquin, "Amplitude-dependent phononic processes in a diatomic granular chain in the weakly nonlinear regime," *Physical Review E*, vol. 86, no. 4, p. 041 305, 2012. DOI: 10.1103/PhysRevE.86.041305.

[73] V. J. Sánchez-Morcillo, I. Pérez-Arjona, V. Romero-García, V. Tournat, and V. E. Gusev, "Second-harmonic generation for dispersive elastic waves in a discrete granular chain," *Physical Review E*, vol. 88, no. 4, p. 043 203, 2013. DOI: 10.1103/PhysRevE.88.043203.

[74] R. Ganesh and S. Gonella, "From modal mixing to tunable functional switches in nonlinear phononic crystals," *Physical Review Letters*, vol. 114, no. 5, p. 054 302, 2015. DOI: 10.1103/PhysRevLett.114.054302.

[75] F. Fraternali, L. Senatore, and C. Daraio, "Solitary waves on tensegrity lattices," *Journal of the Mechanics and Physics of Solids*, vol. 60, no. 6, pp. 1137–1144, 2012. DOI: 10.1016/j.jmps.2012.02.007.

[76] F. Fraternali, G. Carpentieri, A. Amendola, R. E. Skelton, and V. F. Nesterenko, "Multiscale tunability of solitary wave dynamics in tensegrity metamaterials," *Applied Physics Letters*, vol. 105, no. 20, p. 201 903, 2014. DOI: 10.1063/1.4902071.

[77] J. R. Raney, N. Nadkarni, C. Daraio, D. M. Kochmann, J. A. Lewis, and K. Bertoldi, "Stable propagation of mechanical signals in soft media using stored elastic energy," *Proceedings of the National Academy of Sciences*, vol. 113, no. 35, pp. 9722–9727, 2016. DOI: 10.1073/pnas.1604838113.

[78] M. J. Frazier and D. M. Kochmann, "Band gap transmission in periodic bistable mechanical systems," *Journal of Sound and Vibration*, vol. 388, pp. 315–326, 2017. DOI: 10.1016/j.jsv.2016.10.041.

[79] B. Deng, J. R. Raney, V. Tournat, and K. Bertoldi, "Elastic vector solitons in soft architected materials," *Physical Review Letters*, vol. 118, no. 20, p. 204 102, 2017. DOI: 10.1103/PhysRevLett.118.204102.

[80] H. Yasuda, C. Chong, E. G. Charalampidis, P. G. Kevrekidis, and J. Yang, "Formation of rarefaction waves in origami-based metamaterials," *Physical Review E*, vol. 93, no. 4, p. 043 004, 2016. DOI: 10.1103/PhysRevE.93.043004.

[81] M. Gonzalez, J. Yang, C. Daraio, and M. Ortiz, "Mesoscopic approach to granular crystal dynamics," *Physical Review E*, vol. 85, no. 1, pp. 1–6, 2012. DOI: 10.1103/PhysRevE.85.016604.

[82] P. Gélat, J. Yang, O. Akanji, *et al.*, "The dynamic excitation of a granular chain: Contact mechanics finite element analysis and experimental validation," *The Journal of the Acoustical Society of America*, vol. 141, no. 6, pp. 4240–4248, 2017. DOI: 10.1121/1.4983466.

[83] R. W. Musson and W. Carlson, "Simulation of solitary waves in a monodisperse granular chain using COMSOL multiphysics: Localized plastic deformation as a dissipation mechanism," *Granular Matter*, vol. 16, no. 4, pp. 543–550, 2014. DOI: 10.1007/s10035-014-0499-z.

[84] N. Jain and J. Shim, "Numerical study on the phononic band-structure of soft granular crystals," *International Journal of Solids and Structures*, vol. 191-192, pp. 173–186, 2020. DOI: 10.1016/j.ijsolstr.2019.12.007.

[85] R. A. Guyer and P. A. Johnson, *Nonlinear mesoscopic elasticity: The complex behaviour of granular media including rocks and soil*. WILEY-VCH Verlag GmbH & Co. KGaA, Weinheim, 2009. DOI: 10.1002/9783527628261.

[86] M. Lott, M. C. Remillieux, P.-y. L. Bas, T. J. Ulrich, V. Garnier, and C. Payan, "From local to global measurements of nonclassical nonlinear elastic effects in geomaterials," *Journal of Acoustical Society of America*, vol. 140, no. 3, EL231–235, 2016. DOI: 10.1121/1.4962373.

[87] M. C. Remillieux, R. A. Guyer, C. Payan, and T. J. Ulrich, "Decoupling nonclassical nonlinear behavior of elastic wave types," *Physical Review Letters*, vol. 116, p. 115 501, 11 2016. DOI: 10.1103/PhysRevLett.116.115501.

[88] C. Payan, V. Garnier, J. Moysan, and P. Johnson, "Applying nonlinear resonant ultrasound spectroscopy to improving thermal damage assessment in concrete," *The Journal of the Acoustical Society of America*, vol. 121, no. 4, EL125–EL130, 2007. DOI: 10.1121/1.2710745.

[89] K. E. Van Den Abeele, A. Sutin, J. Carmeliet, and P. A. Johnson, "Micro-damage diagnostics using nonlinear elastic wave spectroscopy (NEWS)," *NDT & E International*, vol. 34, no. 4, pp. 239–248, 2001. DOI: `10.1016/S0963-8695(00)00064-5`.

[90] G. Renaud, P. Y. L. Bas, and P. A. Johnson, "Revealing highly complex elastic nonlinear (anelastic) behavior of Earth materials applying a new probe: Dynamic acoustoelastic testing," *Journal of Geophysical Research: Solid Earth*, vol. 117, B06202, 2012. DOI: `10.1029/2011JB009127`.

[91] J. Jin, M. G. Moreno, J. Riviere, and P. Shokouhi, "Impact-based nonlinear acoustic testing for characterizing distributed damage in concrete," *Journal of Nondestructive Evaluation*, vol. 36, no. 3, p. 51, 2017. DOI: `10.1007/s10921-017-0428-2`.

[92] T. Ulrich, P. Johnson, and A. Sutin, "Imaging nonlinear scatterers applying the time reversal mirror," *The Journal of the Acoustical Society of America*, vol. 119, no. 3, pp. 1514–1518, 2006. DOI: `10.1121/1.2168413`.

[93] P.-Y. Le Bas, M. Remillieux, L. Pieczonka, J. Ten Cate, B. Anderson, and T. Ulrich, "Damage imaging in a laminated composite plate using an air-coupled time reversal mirror," *Applied physics letters*, vol. 107, no. 18, p. 184 102, 2015. DOI: `10.1063/1.4935210`.

[94] P. A. Johnson and X. Jia, "Nonlinear dynamics, granular media and dynamic earthquake triggering," *Nature*, vol. 437, no. 7060, pp. 871–874, 2005. DOI: `10.1038/nature04015`.

[95] L. A. Ostrovsky and P. A. Johnson, "Dynamic nonlinear elasticity in geomaterials," *La Rivista Del Nuovo Cimento*, vol. 24, no. 7, pp. 1–46, 2001. DOI: `10.1007/BF03548898`.

[96] W. F. Murphy, K. W. Winkler, and R. L. Kleinberg, "Acoustic relaxation in sedimentary rocks: Dependence on grain contacts and fluid saturation," *Geophysics*, vol. 51, no. 3, pp. 757–766, 1986. DOI: `10.1190/1.1442128`.

[97] C. Madonna, B. S. Almqvist, and E. H. Saenger, "Digital rock physics: Numerical prediction of pressure-dependent ultrasonic velocities using micro-CT imaging," *Geophysical Journal International*, vol. 189, no. 3, pp. 1475–1482, 2012. DOI: `10.1111/j.1365-246X.2012.05437.x`.

[98] H. Davis, "On the fractal character of the porosity of natural sandstone," *Europhysics Letters*, vol. 8, no. 7, pp. 629–632, 1989. DOI: `10.1209/0295-5075/8/7/008`.

[99] Y. Zhang and M. N. Toksoz, "Impact of the cracks lost in the imaging process on computing linear elastic properties from 3D microtomographic images of Berea sandstone," *Geophysics*, vol. 77, no. 2, R95–R104, 2012. DOI: `10.1190/geo2011-0126.1`.

[100] B. Bera, S. K. Mitra, and D. Vick, "Understanding the micro structure of Berea Sandstone by the simultaneous use of micro-computed tomography (micro-CT) and focused ion beam-scanning electron microscopy (FIB-SEM)," *Micron*, vol. 42, no. 5, pp. 412–418, 2011. DOI: `10.1016/j.micron.2010.12.002`.

[101] D. T. Zeitvogel, K. H. Matlack, J.-Y. Kim, L. J. Jacobs, P. M. Singh, and J. Qu, "Characterization of stress corrosion cracking in carbon steel using nonlinear Rayleigh surface waves," *NDT & E International*, vol. 62, pp. 144–152, 2014. DOI: `10.1016/j.ndteint.2013.12.005`.

[102] G. U. Patil and K. H. Matlack, "Wave self-interactions in continuum phononic materials with periodic contact nonlinearity," *Wave Motion*, vol. 105, p. 102 763, 2021. DOI: `10.1016/j.wavemoti.2021.102763`.

[103] G. U. Patil, S. Cui, and K. H. Matlack, "Leveraging nonlinear wave mixing in rough contacts-based phononic diodes for tunable nonreciprocal waves," *Extreme Mechanics Letters*, vol. 55, p. 101 821, 2022. DOI: 10.1016/j.eml.2022.101821.

[104] G. U. Patil and K. H. Matlack, "Strongly nonlinear wave dynamics of continuum phononic material with periodic rough contacts," *Physical Review E*, vol. 105, no. 2, p. 024 201, 2022. DOI: 10.1103/PhysRevE.105.024201.

[105] G. U. Patil and K. H. Matlack, "Nonlinear wave disintegration in phononic material with weakly compressed rough contacts," in *Proceedings of 10th European Nonlinear Dynamics Conference (ENOC2022)*, 2022, p. 382 267. [Online]. Available: https://enoc2020.sciencesconf.org/382267.

[106] G. U. Patil, A. Fantetti, and K. H. Matlack, "Shear wave-induced friction at periodic interfaces for programmable mechanical responses," *Journal of Applied Mechanics*, vol. 90, no. 9, p. 091 002, 2023. DOI: 10.1115/1.4062494.

[107] K. L. Johnson, *Contact mechanics*. Cambridge University Press, Cambridge, 1985.

[108] B. N. J. Persson, *Sliding friction: Physical principles and applications*, ser. NanoScience and Technology. Springer Berlin, Heidelberg, 2000. DOI: 10.1007/978-3-662-04283-0.

[109] J. Archard, "Elastic deformation and the laws of friction," *Proceedings of the royal society of London A*, vol. 243, no. 1233, pp. 190–205, 1957. DOI: 10.1098/rspa.1957.0214.

[110] J. A. Greenwood and J. P. Williamson, "Contact of nominally flat surfaces," *Proceedings of the royal society of London A*, vol. 295, no. 1442, pp. 300–319, 1966. [Online]. Available: https://www.jstor.org/stable/2415421.

[111] A. Bush, R. Gibson, and T. Thomas, "The elastic contact of a rough surface," *Wear*, vol. 35, no. 1, pp. 87–111, 1975. DOI: 10.1016/0043-1648(75)90145-3.

[112] G. Zavarise, M. Borri-Brunetto, and M. Paggi, "On the resolution dependence of micromechanical contact models," *Wear*, vol. 262, no. 1-2, pp. 42–54, 2007. DOI: 10.1016/j.wear.2006.03.044.

[113] B. Drinkwater, R. Dwyer-Joyce, and P. Cawley, "A study of the interaction between ultrasound and a partially contacting solid—solid interface," *Proceedings of the Royal Society of London A*, vol. 452, no. 1955, pp. 2613–2628, 1996. DOI: 10.1098/rspa.1996.0139.

[114] V. Aleshin, S. Delrue, A. Trifonov, O. Bou Matar, and K. Van Den Abeele, "Two dimensional modeling of elastic wave propagation in solids containing cracks with rough surfaces and friction – Part I: Theoretical background," *Ultrasonics*, vol. 82, pp. 11–18, 2018. DOI: 10.1016/j.ultras.2017.07.002.

[115] S. Biwa, S. Nakajima, and N. Ohno, "On the acoustic nonlinearity of solid-solid contact with pressure-dependent interface stiffness," *Journal of Applied Mechanics*, vol. 71, no. 4, pp. 508–515, 2004. DOI: 10.1115/1.1767169.

[116] R. Pohrt and V. L. Popov, "Contact stiffness of randomly rough surfaces," *Scientific Reports*, vol. 3, no. 1, p. 3293, 2013. DOI: 10.1038/srep03293.

[117] C. Zhai, Y. Gan, D. Hanaor, G. Proust, and D. Retraint, "The role of surface structure in normal contact stiffness," *Experimental Mechanics*, vol. 56, no. 3, pp. 359–368, 2016. DOI: 10.1007/s11340-015-0107-0.

[118] S. Bograd, P. Reuss, A. Schmidt, L. Gaul, and M. Mayer, "Modeling the dynamics of mechanical joints," *Mechanical Systems and Signal Processing*, vol. 25, no. 8, pp. 2801–2826, 2011. DOI: 10.1016/j.ymssp.2011.01.010.

[119] S. Medina, D. Nowell, and D. Dini, "Analytical and numerical models for tangential stiffness of rough elastic contacts," *Tribology Letters*, vol. 49, no. 1, pp. 103–115, 2013. DOI: 10.1007/s11249-012-0049-y.

[120] J. O'connor and K. Johnson, "The role of surface asperities in transmitting tangential forces between metals," *Wear*, vol. 6, no. 2, pp. 118–139, 1963. DOI: 10.1016/0043-1648(63)90125-X.

[121] A. Fantetti and C. Schwingshackl, "Effect of friction on the structural dynamics of built-up structures: An experimental study," in *Proceedings of the ASME Turbo Expo 2020: Turbomachinery Technical Conference and Exposition*, American Society of Mechanical Engineers, vol. 11, 2020, V011T30A021. DOI: 10.1115/GT2020-14945.

[122] X. Li and R. S. Dwyer-Joyce, "Measuring friction at an interface using ultrasonic response: Measuring Friction at an Interface," *Proceedings of the Royal Society A*, vol. 476, no. 2241, p. 20 200 283, 2020. DOI: 10.1098/rspa.2020.0283.

[123] W. Jiao and S. Gonella, "Mechanics of inter-modal tunneling in nonlinear waveguides," *Journal of the Mechanics and Physics of Solids*, vol. 111, pp. 1–17, 2018. DOI: 10.1016/j.jmps.2017.10.008.

[124] W. Jiao and S. Gonella, "Doubly nonlinear waveguides with self-switching functionality selection capabilities," *Physical Review E*, vol. 99, no. 4, pp. 1–15, 2019. DOI: 10.1103/PhysRevE.99.042206.

[125] J. Zhao, V. K. Chillara, B. Ren, H. Cho, J. Qiu, and C. J. Lissenden, "Second harmonic generation in composites: Theoretical and numerical analyses," *Journal of Applied Physics*, vol. 119, no. 6, p. 064 902, 2016. DOI: 10.1063/1.4941390.

[126] M. B. Morlock, J.-Y. Kim, L. J. Jacobs, and J. Qu, "Mixing of two co-directional Rayleigh surface waves in a nonlinear elastic material," *The Journal of the Acoustical Society of America*, vol. 137, no. 1, pp. 281–292, 2015. DOI: 10.1121/1.4904535.

[127] D. Broda, W. J. Staszewski, A. Martowicz, T. Uhl, and V. V. Silberschmidt, "Modelling of nonlinear crack-wave interactions for damage detection based on ultrasound - A review," *Journal of Sound and Vibration*, vol. 333, no. 4, pp. 1097–1118, 2014. DOI: 10.1016/j.jsv.2013.09.033.

[128] S. Delrue, V. Aleshin, K. Truyaert, O. B. Matar, and K. V. D. Abeele, "Two dimensional modeling of elastic wave propagation in solids containing cracks with rough surfaces and friction – Part II: Numerical implementation," *Ultrasonics*, vol. 82, pp. 19–30, 2018. DOI: 10.1016/j.ultras.2017.07.003.

[129] P. Blanloeuil, A. J. Croxford, and A. Meziane, "Numerical and experimental study of the nonlinear interaction between a shear wave and a frictional interface," *The Journal of the Acoustical Society of America*, vol. 135, no. 4, pp. 1709–1716, 2014. DOI: 10.1121/1.4868402.

[130] A. Mehrem, N. Jiménez, L. J. Salmerón-Contreras, *et al.*, "Nonlinear dispersive waves in repulsive lattices," *Physical Review E*, vol. 96, no. 1, p. 012 208, 2017. DOI: 10.1103/PhysRevE.96.012208.

[131] R. Ganesh and S. Gonella, "Invariants of nonlinearity in the phononic characteristics of granular chains," *Physical Review E*, vol. 90, no. 2, p. 023 205, 2014. DOI: 10.1103/PhysRevE.90.023205.

[132] V. Tournat, V. E. Gusev, and B. Castagnède, "Self-demodulation of elastic waves in a one-dimensional granular chain," *Physical Review E*, vol. 70, no. 5, p. 056 603, 2004. DOI: 10.1103/PhysRevE.70.056603.

[133] T. Devaux, V. Tournat, O. Richoux, and V. Pagneux, "Asymmetric acoustic propagation of wave packets via the self-demodulation effect," *Physical Review Letters*, vol. 115, no. 23, p. 234 301, 2015. DOI: 10.1103/PhysRevLett.115.234301.

[134] F. Allein, V. Tournat, V. Gusev, and G. Theocharis, "Linear and nonlinear elastic waves in magnetogranular chains," *Physical Review Applied*, vol. 13, no. 2, p. 024 023, 2020. DOI: 10.1103/PhysRevApplied.13.024023.

[135] Y. Ishii, S. Biwa, and T. Adachi, "Second-harmonic generation in a multilayered structure with nonlinear spring-type interfaces embedded between two semi-infinite media," *Wave Motion*, vol. 76, pp. 28–41, 2018. DOI: 10.1016/j.wavemoti.2017.07.009.

[136] X. Guo, D. Zhang, and J. Wu, "Quantitative evaluation of contact stiffness between pressed solid surfaces using dual-frequency ultrasound," *Journal of Applied Physics*, vol. 108, no. 3, p. 034 902, 2010. DOI: 10.1063/1.3465614.

[137] A. Maznev, A. Every, and O. Wright, "Reciprocity in reflection and transmission: What is a 'phonon diode'?" *Wave Motion*, vol. 50, no. 4, pp. 776–784, 2013. DOI: 10.1016/j.wavemoti.2013.02.006.

[138] R. Fleury, D. L. Sounas, C. F. Sieck, M. R. Haberman, and A. Alù, "Sound isolation and giant linear nonreciprocity in a compact acoustic circulator," *Science*, vol. 343, no. 6170, pp. 516–519, 2014. DOI: 10.1126/science.1246957.

[139] S. A. Cummer, "Selecting the direction of sound transmission," *Science*, vol. 343, no. 6170, pp. 495–496, 2014. DOI: 10.1126/science.1249616.

[140] S. Zhu, T. Dreyer, M. Liebler, R. Riedlinger, G. M. Preminger, and P. Zhong, "Reduction of tissue injury in shock-wave lithotripsy by using an acoustic diode," *Ultrasound in Medicine and Biology*, vol. 30, no. 5, pp. 675–682, 2004. DOI: 10.1016/j.ultrasmedbio.2004.03.008.

[141] N. Boechler, G. Theocharis, and C. Daraio, "Bifurcation-based acoustic switching and rectification," *Nature Materials*, vol. 10, no. 9, pp. 665–668, 2011. DOI: 10.1038/nmat3072.

[142] G. Trainiti and M. Ruzzene, "Non-reciprocal elastic wave propagation in spatiotemporal periodic structures," *New Journal of Physics*, vol. 18, no. 8, p. 083 047, 2016. DOI: 10.1088/1367-2630/18/8/083047.

[143] H. Nassar, H. Chen, A. N. Norris, M. R. Haberman, and G. L. Huang, "Non-reciprocal wave propagation in modulated elastic metamaterials," *Proceedings of the Royal Society A*, vol. 473, no. 2202, p. 20 170 188, 2017. DOI: 10.1098/rspa.2017.0188.

[144] B. M. Goldsberry, S. P. Wallen, and M. R. Haberman, "Non-reciprocal wave propagation in mechanically-modulated continuous elastic metamaterials," *The Journal of the Acoustical Society of America*, vol. 146, no. 1, pp. 782–788, 2019. DOI: 10.1121/1.5115019.

[145] K. J. Moore, J. Bunyan, S. Tawfick, *et al.*, "Nonreciprocity in the dynamics of coupled oscillators with nonlinearity, asymmetry, and scale hierarchy," *Physical Review E*, vol. 97, no. 1, p. 012 219, 2018. DOI: 10.1103/PhysRevE.97.012219.

[146] J. Vila, R. K. Pal, and M. Ruzzene, "Observation of topological valley modes in an elastic hexagonal lattice," *Physical Review B*, vol. 96, no. 13, p. 134 307, 2017. DOI: 10.1103/PhysRevB.96.134307.

[147] G. Ma and P. Sheng, "Acoustic metamaterials: From local resonances to broad horizons," *Science Advances*, vol. 2, no. 2, e150159, 2016. DOI: 10.1126/sciadv.1501595.

[148] B. Liang, B. Yuan, and J. C. Cheng, "Acoustic diode: Rectification of acoustic energy flux in one-dimensional systems," *Physical Review Letters*, vol. 103, no. 10, p. 104 301, 2009. DOI: 10.1103/PhysRevLett.103.104301.

[149] B. Liang, X. S. Guo, J. Tu, D. Zhang, and J. C. Cheng, "An acoustic rectifier," *Nature Materials*, vol. 9, no. 12, pp. 989–992, 2010. DOI: 10.1038/nmat2881.

[150] W. J. Zhou, X. P. Li, Y. S. Wang, W. Q. Chen, and G. L. Huang, "Spectro-spatial analysis of wave packet propagation in nonlinear acoustic metamaterials," *Journal of Sound and Vibration*, vol. 413, pp. 250–269, 2018. DOI: 10.1016/j.jsv.2017.10.023.

[151] P. P. Kulkarni and J. M. Manimala, "Realizing passive direction-bias for mechanical wave propagation using a nonlinear metamaterial," *Acta Mechanica*, vol. 230, no. 7, pp. 2521–2537, 2019. DOI: 10.1007/s00707-019-02415-w.

[152] Z. Wu, Y. Zheng, and K. W. Wang, "Metastable modular metastructures for on-demand reconfiguration of band structures and nonreciprocal wave propagation," *Physical Review E*, vol. 97, no. 2, p. 022 209, 2018. DOI: 10.1103/PhysRevE.97.022209.

[153] L. Fang, A. Darabi, A. Mojahed, A. F. Vakakis, and M. J. Leamy, "Broadband non-reciprocity with robust signal integrity in a triangle-shaped nonlinear 1D metamaterial," *Nonlinear Dynamics*, vol. 100, no. 1, pp. 1–13, 2020. DOI: 10.1007/s11071-020-05520-x.

[154] Q. Zhang, W. Li, J. Lambros, L. A. Bergman, and A. F. Vakakis, "Pulse transmission and acoustic non-reciprocity in a granular channel with symmetry-breaking clearances," *Granular Matter*, vol. 22, no. 1, p. 20, 2020. DOI: 10.1007/s10035-019-0982-7.

[155] Y. Zhai, H. S. Kwon, and B. I. Popa, "Active Willis metamaterials for ultracompact nonreciprocal linear acoustic devices," *Physical Review B*, vol. 99, no. 22, p. 220 301, 2019. DOI: 10.1103/PhysRevB.99.220301.

[156] B. I. Popa and S. A. Cummer, "Non-reciprocal and highly nonlinear active acoustic metamaterials," *Nature communications*, vol. 5, no. 1, p. 3398, 2014. DOI: 10.1038/ncomms4398.

[157] A. S. Gliozzi, M. Miniaci, A. O. Krushynska, *et al.*, "Proof of concept of a frequency-preserving and time-invariant metamaterial-based nonlinear acoustic diode," *Scientific Reports*, vol. 9, no. 1, p. 9560, 2019. DOI: 10.1038/s41598-019-44843-7.

[158] F. Li, P. Anzel, J. Yang, P. G. Kevrekidis, and C. Daraio, "Granular acoustic switches and logic elements," *Nature Communications*, vol. 5, no. 1, p. 5311, 2014. DOI: 10.1038/ncomms6311.

[159] Q. Zhang, O. Umnova, and R. Venegas, "Nonlinear dynamics of coupled transverse-rotational waves in granular chains," *Physical Review E*, vol. 100, no. 6, p. 062 206, 2019. DOI: 10.1103/PhysRevE.100.062206.

[160] X. Fang, J. Wen, L. Cheng, and B. Li, "Bidirectional elastic diode with frequency-preserved nonreciprocity," *Phys. Rev. Applied*, vol. 15, no. 5, p. 054 022, 2021. DOI: 10.1103/PhysRevApplied.15.054022.

[161] R. Ganesh and S. Gonella, "Nonlinear waves in lattice materials: Adaptively augmented directivity and functionality enhancement by modal mixing," *Journal of the Mechanics and Physics of Solids*, vol. 99, pp. 272–288, 2017. DOI: 10.1016/j.jmps.2016.11.001.

[162] V. F. Nesterenko, *Dynamics of heterogeneous materials*, ser. Shock Wave and High Pressure Phenomena. Springer-Verlag New York, Inc, 2001. DOI: 10.1007/978-1-4757-3524-6.

[163] J. S. Russell, "Report on waves," in *Report of the 14th Meeting of the British Association for the Advancement of Science*, 1844, pp. 311–390. [Online]. Available: https://www.biodiversitylibrary.org/item/47344#page/366/mode/1up.

[164] G. I. Stegeman and M. Segev, "Optical spatial solitons and their interactions: Universality and diversity," *Science*, vol. 286, no. 5444, pp. 1518–1523, 1999. DOI: 10.1126/SCIENCE.286.5444.1518.

[165] T. Heimburg and A. D. Jackson, "On soliton propagation in biomembranes and nerves," *Proceedings of the National Academy of Sciences*, vol. 102, no. 28, pp. 9790–9795, 2005. DOI: 10.1073/PNAS.0503823102.

[166] S. Shrivastava, K. H. Kang, and M. F. Schneider, "Solitary shock waves and adiabatic phase transition in lipid interfaces and nerves," *Physical Review E*, vol. 91, no. 1, p. 012 715, 2015. DOI: 10.1103/PhysRevE.91.012715.

[167] B. Deng, P. Wang, Q. He, V. Tournat, and K. Bertoldi, "Metamaterials with amplitude gaps for elastic solitons," *Nature Communications*, vol. 9, no. 1, p. 3410, 2018. DOI: 10.1038/s41467-018-05908-9.

[168] A. Spadoni and C. Daraio, "Generation and control of sound bullets with a nonlinear acoustic lens," *Proceedings of the National Academy of Sciences*, vol. 107, no. 16, pp. 7230–7234, 2010. DOI: 10.1073/pnas.1001514107.

[169] A. Leonard, L. Ponson, and C. Daraio, "Wave mitigation in ordered networks of granular chains," *Journal of the Mechanics and Physics of Solids*, vol. 73, pp. 103–117, 2014. DOI: 10.1016/j.jmps.2014.08.004.

[170] B. Deng, L. Chen, D. Wei, V. Tournat, and K. Bertoldi, "Pulse-driven robot: Motion via solitary waves," *Science Advances*, vol. 6, no. 18, eaaz1166, 2020. DOI: 10.1126/sciadv.aaz1166.

[171] E. Kim, F. Restuccia, J. Yang, and C. Daraio, "Solitary wave-based delamination detection in composite plates using a combined granular crystal sensor and actuator," *Smart Materials and Structures*, vol. 24, no. 12, p. 125 004, 2015. DOI: 10.1088/0964-1726/24/12/125004.

[172] C. Daraio, V. F. Nesterenko, E. B. Herbold, and S. Jin, "Tunability of solitary wave properties in one-dimensional strongly nonlinear phononic crystals," *Phys. Rev. E*, vol. 73, no. 2, p. 026 610, 2006. DOI: 10.1103/PhysRevE.73.026610.

[173] S. Katz and S. Givli, "Solitary waves in a bistable lattice," *Extreme Mechanics Letters*, vol. 22, pp. 106–111, 2018. DOI: 10.1016/j.eml.2018.06.003.

[174] R. Ziv and G. Shmuel, "Observation of vector solitary waves in soft laminates using a finite-volume method," *International Journal of Non-Linear Mechanics*, vol. 124, p. 103 502, 2020. DOI: 10.1016/j.ijnonlinmec.2020.103502.

[175] I. V. Andrianov, V. V. Danishevs'kyy, O. I. Ryzhkov, and D. Weichert, "Dynamic homogenization and wave propagation in a nonlinear 1D composite material," *Wave Motion*, vol. 50, no. 2, pp. 271–281, 2013. DOI: 10.1016/j.wavemoti.2012.08.013.

[176] E. Kim, F. Li, C. Chong, G. Theocharis, J. Yang, and P. G. Kevrekidis, "Highly nonlinear wave propagation in elastic woodpile periodic structures," *Physical Review Letters*, vol. 114, no. 11, p. 118 002, 2015. DOI: 10.1103/PhysRevLett.114.118002.

[177] R. J. Leveque and D. H. Yong, "Solitary waves in layered nonlinear media," *SIAM Journal on Applied Mathematics*, vol. 63, no. 5, pp. 1539–1560, 2003. DOI: 10.1137/S0036139902408151.

[178] C. Kim, H. Yin, A. Shmatok, B. C. Prorok, X. Lou, and K. H. Matlack, "Ultrasonic nondestructive evaluation of laser powder bed fusion 316L stainless steel," *Additive Manufacturing*, vol. 38, p. 101 800, 2021. DOI: 10.1016/j.addma.2020.101800.

[179] P. B. Silva, M. J. Leamy, M. G. Geers, and V. G. Kouznetsova, "Emergent subharmonic band gaps in nonlinear locally resonant metamaterials induced by autoparametric resonance," *Physical Review E*, vol. 99, no. 6, p. 063 003, 2019. DOI: 10.1103/PhysRevE.99.063003.

[180] V. Tournat, V. E. Gusev, V. Y. Zaitsev, and B. Castagnède, "Acoustic second-harmonic generation with shear to longitudinal mode conversion in granular media," *Europhysics Letters*, vol. 66, no. 6, pp. 798–804, 2004. DOI: 10.1209/epl/i2003-10264-2.

[181] L. Bonanomi, G. Theocharis, and C. Daraio, "Wave propagation in granular chains with local resonances," *Physical Review E*, vol. 91, no. 3, p. 033 208, 2015. DOI: 10.1103/PhysRevE.91.033208.

[182] D. I. Ketcheson, "High order strong stability preserving time integrators and numerical wave propagation methods for hyperbolic PDEs," Ph.D. dissertation, University of Washington, 2009.

[183] T. E. Faver, "Nanopteron-Stegoton traveling waves in mass and spring dimer Fermi-Pasta-Ulam-Tsingou lattices," Ph.D. dissertation, Drexel University, 2018.

[184] H. Kolsky, *Stress waves in solids.* Dover Publications, Inc., New York, 1963.

[185] D. Sun and S. Sen, "Nonlinear grain-grain forces and the width of the solitary wave in granular chains: A numerical study," *Granular Matter*, vol. 15, no. 2, pp. 157–161, 2013. DOI: 10.1007/s10035-013-0400-5.

[186] E. Avalos and S. Sen, "How solitary waves collide in discrete granular alignments," *Physical Review E*, vol. 79, no. 4, p. 046 607, 2009. DOI: 10.1103/PhysRevE.79.046607.

[187] F. Santibanez, R. Munoz, A. Caussarieu, S. Job, and F. Melo, "Experimental evidence of solitary wave interaction in Hertzian chains," *Physical Review E*, vol. 84, no. 2, p. 026 604, 2011. DOI: 10.1103/PhysRevE.84.026604.

[188] Y. Man, N. Boechler, G. Theocharis, P. Kevrekidis, and C. Daraio, "Defect modes in one-dimensional granular crystals," *Physical Review E*, vol. 85, no. 3, p. 037 601, 2012. DOI: 10.1103/PhysRevE.85.037601.

[189] G. Theocharis, M. Kavousanakis, P. Kevrekidis, C. Daraio, M. A. Porter, and I. Kevrekidis, "Localized breathing modes in granular crystals with defects," *Physical Review E*, vol. 80, no. 6, p. 066 601, 2009. DOI: 10.1103/PhysRevE.80.066601.

[190] E. Hascoët and H. J. Herrmann, "Shocks in non-loaded bead chains with impurities," *The European Physical Journal B-Condensed Matter and Complex Systems*, vol. 14, no. 1, pp. 183–190, 2000. DOI: 10.1007/s100510050119.

[191] M. Manciu, S. Sen, and A. J. Hurd, "Impulse propagation in dissipative and disordered chains with power-law repulsive potentials," *Physica D: Nonlinear Phenomena*, vol. 157, no. 3, pp. 226–240, 2001. DOI: 10.1016/S0167-2789(01)00302-5.

[192] M. Manjunath, A. P. Awasthi, and P. H. Geubelle, "Wave propagation in random granular chains," *Physical Review E*, vol. 85, no. 3, p. 031 308, 2012. DOI: 10.1103/PhysRevE.85.031308.

[193] B. P. Lawney and S. Luding, "Frequency filtering in disordered granular chains," *Acta mechanica*, vol. 225, no. 8, pp. 2385–2407, 2014. DOI: 10.1007/s00707-014-1130-4.

[194] R. Carretero-González, D. Khatri, M. A. Porter, P. Kevrekidis, and C. Daraio, "Dissipative solitary waves in granular crystals," *Physical Review Letters*, vol. 102, no. 2, p. 024 102, 2009. DOI: 10.1103/PhysRevLett.102.024102.

[195] P. Martakis, G. Aguzzi, V. K. Dertimanis, E. N. Chatzi, and A. Colombi, "Nonlinear periodic foundations for seismic protection: Practical design, realistic evaluation and stability considerations," *Soil Dynamics and Earthquake Engineering*, vol. 150, p. 106 934, 2021. DOI: 10.1016/j.soildyn.2021.106934.

[196] A. Fortunati, A. Bacigalupo, M. Lepidi, A. Arena, and W. Lacarbonara, "Nonlinear wave propagation in locally dissipative metamaterials via Hamiltonian perturbation approach," *Nonlinear Dynamics*, vol. 108, no. 2, pp. 765–787, 2022. DOI: 10.1007/s11071-022-07199-8.

[197] S. Sepehri, M. M. Mashhadi, and M. M. S. Fakhrabadi, "Wave propagation in nonlinear monoatomic chains with linear and quadratic damping," *Nonlinear Dynamics*, vol. 108, no. 1, pp. 457–478, 2022. DOI: 10.1007/s11071-021-07184-7.

[198] H. A. Burgoyne and C. Daraio, "Elastic-plastic wave propagation in uniform and periodic granular chains," *Journal of Applied Mechanics*, vol. 82, no. 8, p. 081 002, 2015. DOI: 10.1115/1.4030458.

[199] A. Fantetti, L. Tamatam, M. Volvert, *et al.*, "The impact of fretting wear on structural dynamics: Experiment and Simulation," *Tribology International*, vol. 138, pp. 111–124, 2019. DOI: 10.1016/j.triboint.2019.05.023.

[200] A. Yevtushenko and E. Ivanyk, "Effect of the rough surface on the transient frictional temperature and thermal stresses near a single contact area," *Wear*, vol. 197, no. 1-2, pp. 160–168, 1996. DOI: 10.1016/0043-1648(95)06916-X.

[201] M. R. Brake, *The mechanics of jointed structures: Recent research and open challenges for developing predictive models for structural dynamics*. Springer Cham, 2018. DOI: 10.1007/978-3-319-56818-8.

[202] I. Argatov and I. Sevostianov, "Health monitoring of bolted joints via electrical conductivity measurements," *International Journal of Engineering Science*, vol. 48, no. 10, pp. 874–887, 2010. DOI: 10.1016/j.ijengsci.2010.05.009.

[203] A. Meziane, A. N. Norris, and A. L. Shuvalov, "Nonlinear shear wave interaction at a frictional interface: Energy dissipation and generation of harmonics," *The Journal of the Acoustical Society of America*, vol. 130, no. 4, pp. 1820–1828, 2011. DOI: 10.1121/1.3628663.

[204] V. Vikas, E. Cohen, R. Grassi, C. Sözer, and B. Trimmer, "Design and locomotion control of a soft robot using friction manipulation and motor–tendon actuation," *IEEE Transactions on Robotics*, vol. 32, no. 4, pp. 949–959, 2016. DOI: 10.1109/TRO.2016.2588888.

[205] A. P. Garland, K. M. Adstedt, Z. J. Casias, *et al.*, “Coulombic friction in metamaterials to dissipate mechanical energy,” *Extreme Mechanics Letters*, vol. 40, p. 100 847, 2020. DOI: 10.1016/j.eml.2020.100847.

[206] J. Li, Z. Chen, Q. Li, L. Jin, and Z. Zhao, “Harnessing friction in intertwined structures for high-capacity reusable energy-absorbing architected materials,” *Advanced Science*, vol. 9, no. 13, p. 2 105 769, 2022. DOI: 10.1002/advs.202105769.

[207] A. Merkel, V. Tournat, and V. Gusev, “Experimental evidence of rotational elastic waves in granular phononic crystals,” *Physical Review Letters*, vol. 107, no. 22, p. 225 502, 2011. DOI: 10.1103/PhysRevLett.107.225502.

[208] C. Wang, Q. Zhang, and A. F. Vakakis, “Wave transmission in 2D nonlinear granular-solid interfaces, including rotational and frictional effects,” *Granular Matter*, vol. 23, no. 2, p. 21, 2021. DOI: 10.1007/s10035-021-01093-7.

[209] J. Cabaret, P. Béquin, G. Theocharis, V. Andreev, V. E. Gusev, and V. Tournat, “Nonlinear hysteretic torsional waves,” *Physical Review Letters*, vol. 115, no. 5, p. 054 301, 2015. DOI: 10.1103/PhysRevLett.115.054301.

[210] H. Charan, J. Chattoraj, M. P. Ciamarra, and I. Procaccia, “Transition from static to dynamic friction in an array of frictional disks,” *Physical Review Letters*, vol. 124, no. 3, p. 030 602, 2020. DOI: 10.1103/PhysRevLett.124.030602.

[211] A. Banerjee, M. Sethi, and B. Manna, “Vibration transmission through the frictional mass-in-mass metamaterial: An analytical investigation,” *International Journal of Non-Linear Mechanics*, vol. 144, p. 104 035, 2022. DOI: 10.1016/j.ijnonlinmec.2022.104035.

[212] J. Qu, L. J. Jacobs, and P. B. Nagy, “On the acoustic-radiation-induced strain and stress in elastic solids with quadratic nonlinearity (L),” *The Journal of the Acoustical Society of America*, vol. 129, no. 6, pp. 3449–3452, 2011. DOI: 10.1121/1.3583501.

[213] W. T. Yost and J. H. Cantrell, “Acoustic-radiation stress in solids. II. Experiment,” *Physical Review B*, vol. 30, no. 6, pp. 3221–3227, 1984. DOI: 10.1103/PhysRevB.30.3221.

[214] X. Jacob, R. Takatsu, C. Barrìre, and D. Royer, “Experimental study of the acoustic radiation strain in solids,” *Applied Physics Letters*, vol. 88, no. 13, p. 134 111, 2006. DOI: 10.1063/1.2191428.

[215] P. B. Nagy, J. Qu, and L. J. Jacobs, “Finite-size effects on the quasistatic displacement pulse in a solid specimen with quadratic nonlinearity,” *The Journal of the Acoustical Society of America*, vol. 134, no. 3, pp. 1760–1774, 2013. DOI: 10.1121/1.4817840.

[216] A. N. Norris, “Symmetry conditions for third order elastic rnoduli and implications in nonlinear wave theory,” *Journal of Elasticity*, vol. 25, no. 3, pp. 247–257, 1991. DOI: 10.1007/BF00040928.

[217] W. Jiang and W. Cao, “Second harmonic generation of shear waves in crystals,” *IEEE Transactions on Ultrasonics, Ferroelectrics and Frequency Control*, vol. 51, no. 2, pp. 153–162, 2004. DOI: 10.1109/tuffc.2004.1320763.

[218] D. M. Bushnell and J. N. Hefner, *Viscous drag reduction in boundary layers*, ser. Progress in Astronautics and Aeronautics. American Institute of Aeronautics and Astronautics, Inc. Washington, DC, 1990, vol. 123.

[219] R. Garcia-Mayoral and J. Jiménez, "Drag reduction by riblets," *Philosophical Transactions of the Royal Society A*, vol. 369, no. 1940, pp. 1412–1427, 2011. DOI: 10.1098/rsta.2010.0359.

[220] A. W. Lang, P. Motta, P. Hidalgo, and M. Westcott, "Bristled shark skin: A microgeometry for boundary layer control?" *Bioinspiration & Biomimetics*, vol. 3, no. 4, p. 046 005, 2008. DOI: 10.1088/1748-3182/3/4/046005.

[221] M. I. Hussein and M. J. Frazier, "Metadamping: An emergent phenomenon in dissipative metamaterials," *Journal of Sound and Vibration*, vol. 332, no. 20, pp. 4767–4774, Sep. 2013. DOI: 10.1016/j.jsv.2013.04.041.

[222] A. Arena, A. Bacigalupo, and M. Lepidi, "Wave propagation in viscoelastic metamaterials via added-state formulation," *International Journal of Mechanical Sciences*, vol. 228, p. 107 461, 2022. DOI: 10.1016/j.ijmecsci.2022.107461.

[223] X. Fang, J. Wen, D. Yu, and J. Yin, "Bridging-coupling band gaps in nonlinear acoustic metamaterials," *Physical Review Applied*, vol. 10, no. 5, p. 054 049, 2018. DOI: 10.1103/PhysRevApplied.10.054049.

[224] J. Krautkrämer and H. Krautkrämer, *Ultrasonic testing of materials*. Springer-Verlag Berlin Heidelberg GmbH, 1983.

[225] R. L. Smith, "The effect of grain size distribution on the frequency dependence of the ultrasonic attenuation in polycrystalline materials," *Ultrasonics*, vol. 20, no. 5, pp. 211–214, 1982. DOI: 10.1016/0041-624X(82)90021-X.

[226] A. Ruiz, N. Ortiz, A. Medina, J.-Y. Kim, and L. Jacobs, "Application of ultrasonic methods for early detection of thermal damage in 2205 duplex stainless steel," *NDT & E International*, vol. 54, pp. 19–26, 2013. DOI: 10.1016/j.ndteint.2012.11.009.

[227] A. P. Arguelles and J. A. Turner, "Ultrasonic attenuation of polycrystalline materials with a distribution of grain sizes," *The Journal of the Acoustical Society of America*, vol. 141, no. 6, pp. 4347–4353, 2017. DOI: 10.1121/1.4984290.

[228] M. Treiber, J.-Y. Kim, L. J. Jacobs, and J. Qu, "Correction for partial reflection in ultrasonic attenuation measurements using contact transducers," *The Journal of the Acoustical Society of America*, vol. 125, no. 5, pp. 2946–2953, 2009. DOI: 10.1121/1.3106125.

[229] M. A. Goñi and C. E. Rousseau, "On the validity and improvement of the ultrasonic pulse-echo immersion technique to measure real attenuation," *Ultrasonics*, vol. 54, no. 2, pp. 544–550, 2014. DOI: 10.1016/j.ultras.2013.08.008.

[230] T. Kang, H. H. Kim, S. J. Song, and H. J. Kim, "Characterization of fatigue damage of Al6061-T6 with ultrasound," *NDT & E International*, vol. 52, pp. 51–56, 2012. DOI: 10.1016/j.ndteint.2012.08.001.

[231] P. H. Rogers and A. L. V. Buren, "An exact expression for the Lommel-diffraction correction integral," *The Journal of the Acoustical Society of America*, vol. 55, no. 4, pp. 724–728, 1974. DOI: 10.1121/1.1914589.

[232] K. Vecchio and G. Gray III, "Shock-loading response of 6061-t6 aluminum-alumina metal-matrix composites," *Journal de Physique IV France*, vol. 4, pp. C8-231–C8-236, 1994. DOI: 10.1051/jp4:1994834.

[233] G. Zhang, X. Li, S. Zhang, and T. Kundu, "Investigation of frequency-dependent attenuation coefficients for multiple solids using a reliable pulse-echo ultrasonic measurement technique," *Measurement*, vol. 177, p. 109 270, 2021. DOI: 10.1016/j.measurement.2021.109270.

[234] D. M. Mulvihill, H. Brunskill, M. E. Kartal, R. S. Dwyer-Joyce, and D. Nowell, "A comparison of contact stiffness measurements obtained by the digital image correlation and ultrasound techniques," *Experimental Mechanics*, vol. 53, no. 7, pp. 1245–1263, 2013. DOI: 10.1007/s11340-013-9718-5.

[235] R. S. Dwyer-Joyce, B. W. Drinkwater, and A. M. Quinn, "The use of ultrasound in the investigation of rough surface interfaces," *Journal of Tribology*, vol. 123, no. 1, pp. 8–16, 2001. DOI: 10.1115/1.1330740.

[236] J. Y. Kim, A. Baltazar, and S. I. Rokhlin, "Ultrasonic assessment of rough surface contact between solids from elastoplastic loading-unloading hysteresis cycle," *Journal of the Mechanics and Physics of Solids*, vol. 52, no. 8, pp. 1911–1934, 2004. DOI: 10.1016/j.jmps.2004.01.006.

[237] M. Gonzalez-Valadez, A. Baltazar, and R. S. Dwyer-Joyce, "Study of interfacial stiffness ratio of a rough surface in contact using a spring model," *Wear*, vol. 268, no. 3-4, pp. 373–379, 2010. DOI: 10.1016/j.wear.2009.08.022.

[238] S. Biwa, S. Hiraiwa, and E. Matsumoto, "Experimental and theoretical study of harmonic generation at contacting interface," *Ultrasonics*, vol. 44, e1319–e1322, 2006. DOI: 10.1016/j.ultras.2006.05.010.

[239] H. G. Tattersall, "The ultrasonic pulse-echo technique as applied to adhesion testing," *Journal of Physics D: Applied Physics*, vol. 6, no. 7, pp. 819–832, 1973. DOI: 10.1088/0022-3727/6/7/305.

[240] J. M. Baik and R. B. Thompson, "Ultrasonic scattering from imperfect interfaces: A quasi-static model," *Journal of Nondestructive Evaluation*, vol. 4, no. 3-4, pp. 177–196, 1984. DOI: 10.1007/BF00566223.

[241] P. Blanloeuil, A. Meziane, L. R. Rose, and C. H. Wang, "Analytical and numerical 1D modelling of the nonlinear scattering at a rough-surface contact interface with clapping," *Journal of Sound and Vibration*, vol. 485, p. 115 519, 2020. DOI: 10.1016/j.jsv.2020.115519.

[242] K. T. Narasimha, E. Kannan, and K. Balasubramaniam, "Simplified experimental technique to extract the acoustic radiation induced static strain in solids," *Applied Physics Letters*, vol. 91, no. 13, p. 134 103, 2007. DOI: 10.1063/1.2793181.

[243] I. Arretche, G. U. Patil, and K. H. Matlack, "Phononic materials: Controlling elastic waves in solids," in *iMechanica: Web of Mechanics and Mechanicians*, ser. Journal Club, vol. September, 2021. [Online]. Available: https://imechanica.org/node/25398.

[244] G. U. Patil and K. H. Matlack, "Tunable bandgaps and second harmonic generation of a one-dimensional nonlinear phononic material with periodic rough interfaces," *The Virtual Meeting 2020 of the Society of Engineering Sciences*, 2020.

[245] G. U. Patil and K. H. Matlack, "Emergence of stegotons in phononic materials with strongly nonlinear rough contacts," *The Journal of the Acoustical Society of America*, vol. 150, no. 4, A147–A147, 2021. DOI: 10.1121/10.0007934.

[246] G. U. Patil, A. Fantetti, and K. H. Matlack, "Frictional instability: A nonlinear mechanism to control shear wave responses in rough contact-based metamaterials," *The Journal of the Acoustical Society of America*, vol. 152, no. 4, A38–A39, 2022. DOI: 10.1121/10.0015463.

[247] G. U. Patil and K. H. Matlack, “Experimental study of nonlinear waves in phononic materials with rough contacts,” *The Journal of the Acoustical Society of America*, vol. 151, no. 4, A41–A41, 2022. DOI: 10.1121/10.0010593.

[248] L. Zhang, W. Zhang, and F. Xin, “Broadband low-frequency sound absorption of honeycomb sandwich panels with rough embedded necks,” *Mechanical Systems and Signal Processing*, vol. 196, p. 110 311, 2023. DOI: 10.1016/j.ymssp.2023.110311.

[249] R. Thomas, B. W. Drinkwater, and D. Liaptsis, “The reflection of ultrasound from partially contacting rough surfaces,” *The Journal of the Acoustical Society of America*, vol. 117, no. 2, pp. 638–645, 2005. DOI: 10.1121/1.1835505.

[250] H. Olsson, K. J. Åström, C. C. De Wit, M. Gäfvert, and P. Lischinsky, “Friction models and friction compensation,” *European Journal of Control*, vol. 4, no. 3, pp. 176–195, 1998. DOI: 10.1016/S0947-3580(98)70113-X.

[251] N. Vaiana, S. Sessa, and L. Rosati, “A generalized class of uniaxial rate-independent models for simulating asymmetric mechanical hysteresis phenomena,” *Mechanical Systems and Signal Processing*, vol. 146, p. 106 984, 2021. DOI: 10.1016/j.ymssp.2020.106984.

[252] J. H. Porter and M. R. Brake, “Towards a predictive, physics-based friction model for the dynamics of jointed structures,” *Mechanical Systems and Signal Processing*, vol. 192, p. 110 210, 2023. DOI: 10.1016/j.ymssp.2023.110210.

[253] H. Margenau, “Van der waals forces,” *Reviews of Modern Physics*, vol. 11, no. 1, pp. 1–35, 1939. DOI: 10.1103/RevModPhys.11.1.

[254] R. Legtenberg, H. A. Tilmans, J. Elders, and M. Elwenspoek, “Stiction of surface micromachined structures after rinsing and drying: Model and investigation of adhesion mechanisms,” *Sensors and actuators A: Physical*, vol. 43, no. 1-3, pp. 230–238, 1994. DOI: 10.1016/0924-4247(93)00654-M.

[255] J. Fredrich, B. Menéndez, and T.-F. Wong, “Imaging the pore structure of geomaterials,” *Science*, vol. 268, no. 5208, pp. 276–279, 1995. DOI: 10.1126/science.268.5208.276.